

Euskal Herriko Unibertsitatea/Universidad del País Vasco

Faculty of Engineering

Department of Chemical and Environmental Engineering

Power-to-Gas: catalytic developments to store the surplus of renewable electricity as methane

A dissertation submitted to the University of the Basque Country

In partial fulfilments of the requirements for the degree of PhD in Chemical Engineering

By

Mr. Iker García García

Thesis Advisors:

Dr. Victoria Laura Barrio Cagigal

Prof. Dr. José Francisco Cambra Ibáñez

Bilbao, 2018.

Agradecimientos

Lo que debería ser lo más sencillo de todas estas páginas puede que al final sea lo más complicado, por no querer dejarme a nadie fuera, por querer ir más allá del típico familia-amigos y hacerlo además intentando que no ocupe más que el resto de la tesis.

A mis directores, José y Laura Por tener siempre un segundo, que acababa siendo más, para mí. Por buscar fuentes de financiación en todos lados para que no hiciese esta tesis por amor al arte. Por sus ideas, a veces locas, y por escuchar y comentar las mías. Esta tesis también es vuestra, más allá de la figura de directores.

A ese grupo que coincidimos durante la realización de mi proyecto de fin de carrera, Alain, Alba, David, Judit y Saioa, quizá de no haber coincidido con vosotros y haber formado un grupo tan unido hoy no estaría escribiendo esto.

Cómo no, a Esther y Jesús. Vosotros me dirigisteis y supervisasteis en mis primeros pasos en la investigación haciendo que me interesase por seguir unos años más. De no ser por vosotros no habría empezado este doctorado.

A todos los miembros del grupo SuPrEn. A mis compañeros del aula I+D, los becarios, y los que ya no lo son pero han pasado por ahí en algún momento: Ainhoa, Atiziber, Iker, Jess, Jon Solar, Jon García, Juan Luis, Leire, Mikel, Nere y Sara. Compartir el día a día con vosotros, las comidas, las cañas y los cafés ha hecho que hasta en los peores momentos de la investigación haya ido a trabajar con una sonrisa. A Miren y Naia, compañeras de mesa en distintos momentos, a las que seguramente haya distraído más de lo debido pero con las que he compartido tanto. A Kepa, por las incontables horas de charla en el laboratorio de catálisis, por tu ayuda en cada momento desde mi primer contacto con la investigación, por ser un gran amigo. No puedo olvidar aquí a Jaione, Josu y Miren. Sin vuestra ayuda durante la realización de vuestro proyecto de fin de carrera muchos de los resultados de esta tesis no habrían sido posibles, espero haber sido capaz de enseñaros algo.

A mi cuadrilla por ayudarme a cambiar de aires siempre que ha sido necesario, pese a que a día de hoy todavía no entendáis a qué me he dedicado estos años. A mi otra cuadrilla, la de Santa Pola, a los que conozco de hace muchísimos años y a los que cada

vez que acaba el verano echo todavía más de menos, a los que siguen preguntándome cuándo dejaré de estudiar.

To all my friends scattered throughout the world. To Nemanja, it was a pleasure to meet you and work with you. I still love our talks about basketball and hope to see you again soon. To Roberto, for making my stay in Australia way funnier and easier. To all the staff and friends I made at NCV, specially to Susan, Nitish, Leo and all the Level 3 Family: Dawn, best SR ever, Abishek, Ian and Josh. I miss you all!

To my supervisors at the UNSW: Jason “no worries” Scott and Rose Amal. You were even better than I could ever hope. I learnt a lot with you and I hope that I was somehow useful to PartCat too in exchange. To Lena and Victor, for helping me to be part of PartCat so fast. To all my mates from PartCat but specially to Jess, Shayan, Yoshi, Hendra and to the two friends sitting beside me: Channing and Saline. To the most important person during my stay at the UNSW: Emma. Working with you during six months was a experience that I will never forget.

En este caso sí se puede aplicar eso de “los últimos serán los primeros”. A mis padres, Isidoro e Irene. Sois los responsables de todas mis virtudes, mientras que mis defectos son sólo cosa mía. Me habéis dado los medios para llegar hasta aquí hoy, gracias a vosotros he tenido todas las oportunidades que vosotros no tuvisteis, con las que sin ninguna duda hubieseis llegado mucho más lejos todavía. Me habéis dado también algo mucho más importante, algo que no se puede medir. Gracias a los dos por vuestro cariño, por vuestro amor, por haberme educado así. Espero que estéis orgullosos de mí, os quiero. A mi hermana Lorena, porque toda mi vida ha sido más fácil teniendo un buen espejo en el que mirarme y a una persona que siempre sé que dará todo por mí. A mi abuela Irene, porque desde que tengo memoria siempre has estado ahí, por aguantar todas mis travesuras de la infancia cuando me cuidabas.

A ti, Marta. Porque aún no existen palabras con las que describir todo lo que te debo. Por estar a mi lado siempre, de manera incondicional. Por animarme, por aguantarme. Por ser tú, por ser nosotros, por la convicción de que lea cuando lea esto tú estarás a mi lado. Te quiero.

A mi padre, Isidoro. A mi madre, Irene. A mi hermana, Lorena. A mi abuela, Irene.

A mi otra mitad, Marta.

Por la suerte que he tenido con que seáis mi familia.

Table of contents

ABSTRACT	1
RESUMEN	3
CHAPTER I. INTRODUCTION	5
CHAPTER II. STATE OF THE ART	25
CHAPTER III. OBJECTIVE AND SCOPE	49
CHAPTER IV. EXPERIMENTAL	55
CHAPTER V. RESULTS	75
CHAPTER VI. DESIGN OF AN INDUSTRIAL PROCESS	213
CHAPTER VII. CONCLUSIONS	239
REFERENCES	245
RESUME	263

Abstract

This PhD thesis started in October 2014 with the support of the Sustainable Process Engineering (SuPrEn) research group from the Chemical and Environmental Engineering Department from the Faculty of Engineering of Bilbao, University of the Basque Country. This work has been carried out under the supervision of Professor José Francisco Cambra Ibáñez and Dr. Victoria Laura Barrio Cagigal. Moreover, during this PhD thesis a stay in the Particles and Catalysis (PartCat) research group from the University of New South Wales (UNSW) in Sydney, Australia, was carried out under the supervision of Dr. Jason Scott and Scientia Professor Rose Amal, and with the kind support of Dr. Emma Lovell.

Along these years, this work permitted to progress in the development of catalytic systems to produce methane from carbon dioxide and hydrogen, thus, enabling the integration of renewable electricity in the energy system and reducing carbon dioxide emissions. Furthermore, this PhD thesis permitted the publication of various scientific papers in different peer-reviewed journals and different publications in international conferences. This work has been divided in seven chapters.

Chapter I, consists in a brief introduction describing the context in which this work is framed within. The relationship of the human being with the energy and its unavoidable need is explained, together with the description of the actual energy system. This is linked with the issues related to the climate change and the energy dependence of the countries. Finally, the different technologies to store energy are described.

Chapter II, taking into account the energy storage technologies described in the Chapter I, Power-to-Gas (PtG) is selected as the most promising one. In this chapter an exhaustive review of the state of the art of the PtG technology is performed focusing specially on the carbon dioxide methanation process.

Chapter III, the objective of this PhD thesis is defined in this chapter. In order to fulfil the objective different partial goals or milestones are set.

Chapter IV, the experimental procedure carried out along the performing of this PhD thesis is summarized and described in this chapter. The different synthesis and

characterisation techniques are thoroughly described together with the procedure carried out during the activity tests. A summary of the employed materials and equipments is also included in this chapter.

Chapter V, consists in the presentation and discussion of all the results obtained during this PhD thesis. In order to ease the understanding, this chapter is divided in four main subsections including: I) Analysis of the most suitable operating conditions, II) Catalysts tested in fixed bed reactors, III) Stability tests and IV) Catalysts for photoreactors.

Chapter VI, a design of an industrial plan is proposed in this chapter. Not only all the needed equipment is sized but also an economic analysis is carried out, taking into account both the equipment cost and the labour cost needed.

Chapter VII, consists in the conclusions obtained after carrying out this PhD thesis. The physicochemical properties required by a catalyst to be efficient for the carbon dioxide methanation process are listed and promising catalytic systems are presented. Also, the feasibility of building an industrial plant is explained.

Resumen

Esta tesis doctoral comenzó en octubre de 2014 con el apoyo del grupo de investigación Sustainable Process Engineering (SuPrEn) del Departamento de Ingeniería Química y del Medio Ambiente de la Escuela de Ingeniería de Bilbao, Universidad del País Vasco/Euskal Herriko Unibertsitatea (UVP/EHU). El trabajo ha sido llevado a cabo bajo la supervisión del Profesor Dr. José Francisco Cambra Ibáñez y la Dr. Victoria Laura Barrio Cagigal. Durante la realización de esta tesis doctoral se realizó una estancia en el grupo de investigación Particles and Catalysis (PartCat) de la University of New South Wales (UNSW) en Sídney, Australia, bajo la supervisión del Dr. Jason Scott y la Profesora Rose Amal, junto a la inestimable ayuda de la Dr. Emma Lovell.

El trabajo realizado durante estos años ha permitido el desarrollo de sistemas catalíticos para producir metano a partir de dióxido de carbono e hidrógeno, permitiendo la integración de electricidad de origen renovable en el sistema energético y reduciendo las emisiones de dióxido de carbono. Esta tesis doctoral ha permitido la publicación de varios artículos en revistas científicas y en congresos internacionales. Este trabajo ha sido dividido en siete capítulos.

Capítulo I, se trata de una breve introducción del contexto en el que se enmarca el trabajo. Se describe la relación entre la raza humana y la energía, su necesidad inevitable, además del sistema energético actual. Esto se relaciona con el cambio climático, y sus problemas derivados, y la dependencia energética de los distintos países. Finalmente, se describen diferentes tecnologías para el almacenamiento de energía.

Capítulo II, partiendo de las tecnologías de almacenamiento de energía descritas en el Capítulo I, se selecciona Power-to-Gas (PtG) como una de las más prometedoras. En este capítulo se realiza una revisión exhaustiva del estado del arte en el campo del PtG, prestando especial atención a la proceso de metanación de dióxido de carbono.

Capítulo III, se define el objetivo de la presente tesis doctoral. Además, se definen los diferentes hitos necesarios para llevar a cabo de manera satisfactoria dicho objetivo.

Capítulo IV, se describe el procedimiento experimental empleado durante el desarrollo de la tesis. Se describen los procedimientos de síntesis y caracterización así como los de realización de los ensayos de actividad. Además, se enumeran los materiales y equipos utilizados.

Capítulo V, todos los resultados obtenidos durante la realización de la presente tesis doctoral se encuentran en este capítulo. Para facilitar la lectura del mismo, se encuentra dividido en cuatro sub-secciones principales, incluyendo: I) Análisis de las condiciones de operación idóneas, II) Catalizadores probados en reactores de lecho fijo, III) Tests de estabilidad y IV) Catalizadores para fotoreactores.

Capítulo VI, se propone el diseño de una planta de escala industrial. Además de dimensionar todo el equipamiento necesario, se realiza un análisis de la viabilidad económica teniendo en cuenta tanto el coste material como el del funcionamiento de la planta.

Capítulo VII, consiste en las conclusiones obtenidas tras la realización de esta tesis doctoral. Se enumeran las propiedades fisicoquímicas necesarias para que un catalizador sea eficiente en la reacción de metanación de dióxido de carbono y además se presentan algunos sistemas catalíticos con un rendimiento prometedor. Finalmente, se presentan las conclusiones sobre la viabilidad de construir una planta industrial para la realización de este proceso.

Chapter I

Introduction

Table of contents

1.1. HUMAN BEING AND ENERGY	9
1.1.1. ENERGY SYSTEM	10
1.1.1.1. <i>Fossil fuels</i>	12
1.1.1.2. <i>Nuclear energy</i>	14
1.1.1.3. <i>Hydropower</i>	15
1.1.1.4. <i>Renewable energy sources</i>	15
1.1.2. CLIMATE CHANGE	16
1.1.3. ENERGY DEPENDENCE	19
1.2. ANALYSING THE PROBLEM	20
1.3. ENERGY STORAGE.....	21
1.3.1. MECHANICAL ENERGY STORAGE	21
1.3.2. CHEMICAL ENERGY STORAGE	22
1.3.3. ELECTRICAL ENERGY STORAGE	23
1.3.4. MAGNETIC ENERGY STORAGE	23
1.3.5. BIOLOGICAL ENERGY STORAGE	24
1.3.6. THERMAL ENERGY STORAGE	24

1.1. Human being and energy

“Energy can neither be created nor destroyed; it can only be changed from one form to another”.

This famous quote not only is true but it probably is also the most important law that rules our life. We, as human beings, are used to a standard of living that requires huge amounts of energy. We cannot create this energy, we can just take advantage of different resources and transform them into energy.

Natural resources, those that usually are used and often wasted in order to obtain energy, will not always be available. Moreover, the emerging economies are, in their particular race to reach the same economic level as the most developed countries, really hunger for energy so the lifespan of our natural resources is being reduced at a worrying fast pace.

Looking at world overall energy consumption, comparing 1973 and 2014 using the data provided by the International Energy Agency (IEA), the increase in energy consumption in the last 30 years has been more than 100%, from 4661 Mtoe in 1973 to 9425 Mtoe in 2014. Looking closer at these numbers, it can be figured out that developing countries such as most of non-OCDE countries, a great part of Asia, Middle East, and China are the main responsible of this growth in energy consumption, as it can be seen in Figure 1.1 [1].

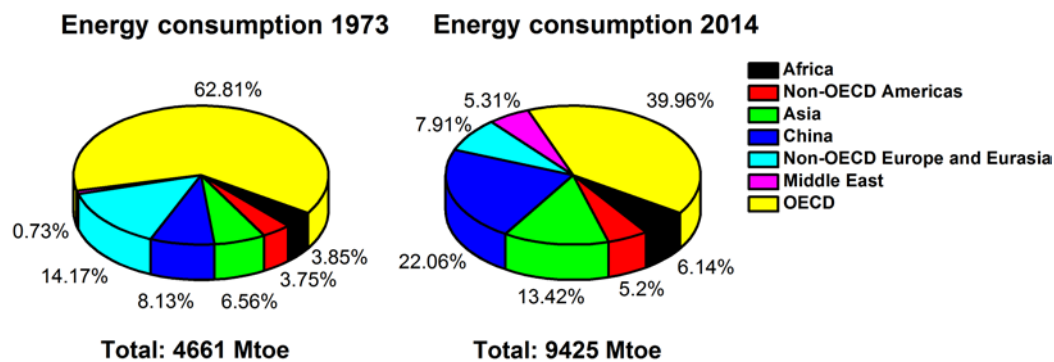


Figure 1.1. World energy consumption 1973-2014 [1]

The energy amount needed nowadays around the world and the trends in energy consumption are known, so how the future will look like can be projected. The last International Energy Outlook, by the U.S. Energy Information Administration (EIA), published in 2016 projects the total world energy consumption in the period of 28 years that goes since 2012 to 2040. According to this projections, the energy demand in 2040 will increase 48% from 2012. As it has been stated, most of the growth in the energy demand will be due to the fact that developing countries need a lot of energy to accomplish their economic growth, being the increase in the energy demand for non-OECD countries of 71% in the span of years previously mentioned, while in the case of OECD countries the growth will be just 18% [2].

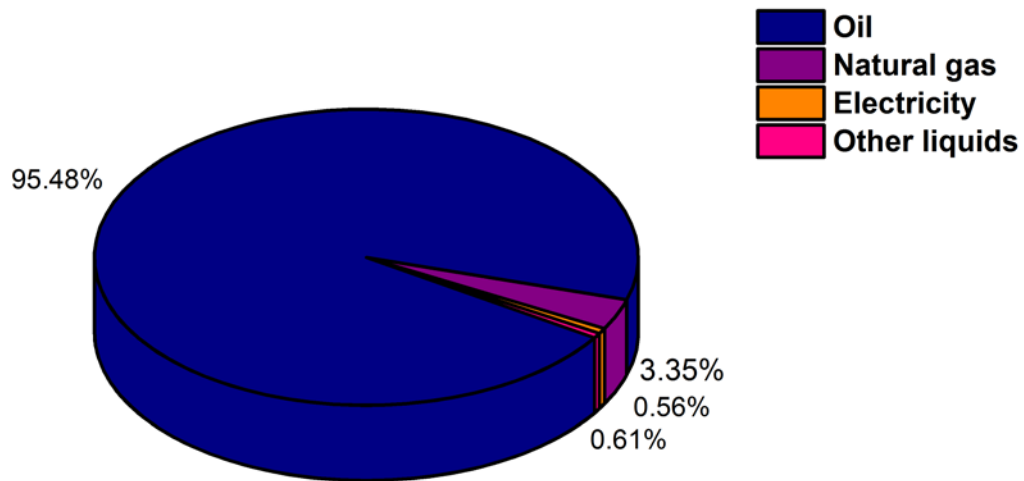
Ensuring future energy supply will be a serious issue. Furthermore, the increase in energy consumption not only leads to a faster depletion of natural resources but also to an increase in carbon dioxide and other greenhouse gas emissions, altering Earth's temperature and climate. There are several options that could ensure future energy supply while lowering to the minimum the impact on the environment. In order to fulfil this we need to change our mind and completely build again our energy system, using as a basis renewable energies and not fossil fuels. This way, we could ensure our future energy, with low environmental impact and without the need of spoiling another countries.

In order to analyse the situation there are key factors that we need to know as these are crucial to figure out how to solve our problem: energy system, climate change and energy dependence.

1.1.1. Energy system

Our energy system is based on fossil fuels, they are the most used resources both for electricity generation and as fuel for transportation. According to the data provided by the EIA, in 2014 oil (in its several forms) was the most used energy source as a fuel for transportation accounting for more than 95 % of the total use. The fuels used for transportation are shown in Figure 1.2 [2].

Energy sources for transportation 2014

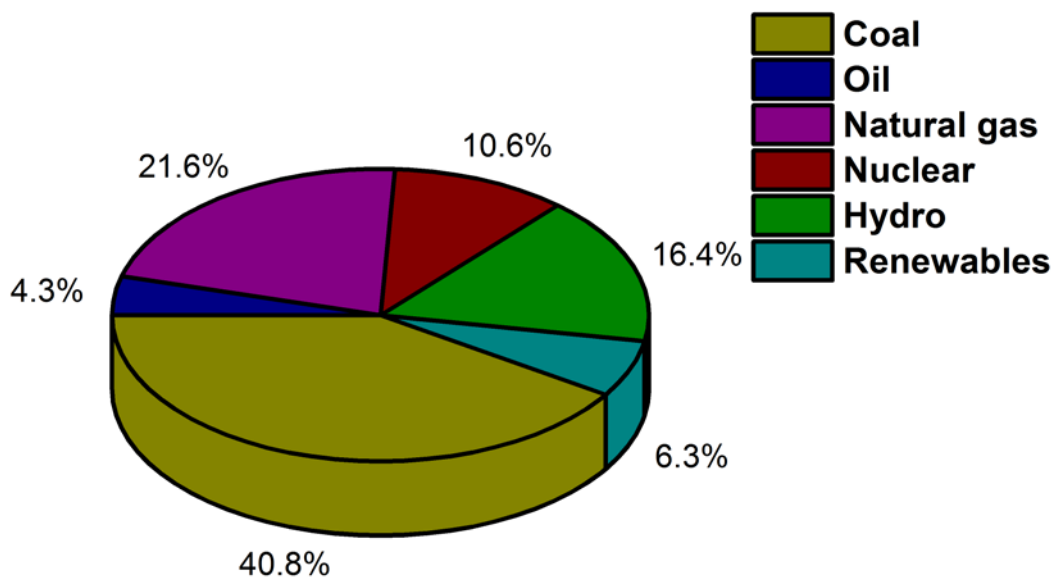


Total: 2675 Mtoe

Figure 1.2. Energy sources for transportation 2014 [2]

Regarding to electricity generation, coal is the most used energy source being responsible for approximately 40 % of the electricity generated while combined with oil and natural gas, makes fossil fuels responsible for more than 65 % of the electricity generated. This data is shown in Figure 1.3 [2].

Electricity generation by fuel 2014



Total: 23816 TWh

Figure 1.3. Electricity generation by fuel 2014 [2]

As it can be seen, fossil fuels have no competitors in the transportation sector. However, for electricity generation even if they are the most used fuels there are alternatives like nuclear energy, hydropower and renewables. All these kind of energy sources are explained with more detail below.

1.1.1.1. Fossil fuels

The fossil fuels that are nowadays were created million years ago, specifically about 300-360 million years ago. Different microscopic plants and animals that lived during the Carboniferous period, a geological period part of the Palaeozoic, formed the fossil fuels. The plants, which lived in the ocean, fixed the carbon from the atmosphere and once dead formed layers in the bottom of the ocean. These layers formed kerogen, a polymeric material, which was mixed with sand, clay and minerals and under great

pressure sedimentary rocks were formed with the kerogen inside. As time passed by, high temperature and massive pressure turned kerogen into oil or gas, depending on the specific properties of the kerogen and the ambient conditions. Usually, the highest the temperature the lightest the oil formed or natural gas was formed. These fossil fuels were then absorbed into the pores of the rocks, finally creating a reservoir. Fossil fuels are exploited from different kind of reservoirs and depending on the ease of extraction are called conventional, if easier, or unconventional fossil fuels [3]. The most abundant fossil fuels, conventional ones, are coal, natural gas and oil.

- Coal: a heterogeneous combustible rock formed by organic compounds that gained relevance during the Industrial Revolution. Can be used as fuel, for electricity generation and also as raw material for different processes like steel production. Its main advantages are that is ready to use without any previous treatment and that is the most abundant fossil fuel. However, its burning generates huge amounts of carbon dioxide [4].
- Natural gas: consisting mainly on methane, it can be found both in natural gas fields, oil fields or adsorbed in porous coals. Apart from methane, natural gas is formed by non-combustible components that lower down its heating value. It is extensively used for heating and electricity generation and it is gaining importance as a fuel for transport, due to the fact that has the lowest carbon content, hence, lowest carbon dioxide emissions among all the fossil fuels [4].
- Oil: the most common kind of oil is called crude oil, which consists in a mixture of hydrocarbon chains. Its properties vary according to the exploitation site, creating different categories of crude oil [4]. After refining, it has several uses being the main one as a fuel for transportation but it is also used as raw material, for example in the production of plastics.

Since the industrial era, fossil fuels have been the most used resource in order to produce energy. They can either just be burned to produce electricity or can be used as a fuel for transport. In both ways, they are really inefficient and, in the best case scenario, the thermal efficiency is 33%[5]. Moreover, fossil fuels are the main

accountable for carbon dioxide emissions to the atmosphere and they are also a resource that will disappear in the future. This last assertion has been polemic in the last few years since all the estimations of fossil fuel depletion have failed.

In 1956, M. King Hubbert predicted that oil would reach its maximum production in 1970. It seemed an accurate prediction, however several reservoirs have been discovered since then and the peak of oil production continues shifting in the time. The development of oil industry, with new exploitation methods in deepwater, deep layers and the Arctic Region seems to delay the peak in oil production at least until 2040. This peak for coal and natural gas will probably happen in 2050 and 2060 respectively [6]. Even if new reservoirs appear, and the depletion of fossil fuels is delayed, what is certainly true is that they will disappear one day as we are exploiting them at a higher rate than the one needed by the nature to create more fossil fuels.

The ease of the extraction with well-known methods, then lower prices, and makes fossil fuels the main option both for electricity generation and as a fuel for transport.

1.1.1.2. Nuclear energy

Nuclear energy is probably the oldest low-carbon energy source as the first nuclear power plant was developed in 1957. After 1966 the cost of energy generation for nuclear power plants was already lower than the one of thermal power plants. The continuous developing of this technology and the different energy crises resulted in an increase on energy generated by nuclear power plants from 400 TWh to 2400 TWh in 1977. After this date, nuclear energy continued its growth reaching a value of energy production of 4400 TWh in the first decade of this century. This growth was suddenly stopped by the Fukushima Daiichi incident and, as different countries are shutting down their nuclear power plants, current nuclear energy production values are close to those presented at the beginning of the 1990s [7].

Although nuclear fuel reserves are much higher than those of fossil fuels [5] raw materials are still needed and that does not ensure future energy supply, just delays the

problem. One of the benefits of nuclear energy is that it does not contribute directly to carbon dioxide emissions. However, nuclear energy has also different disadvantages as its high cost, being only a valuable energy generation method in developed countries, difficult disposal of the wastes produced and operation safety [7].

With different incidents related to nuclear energy in the last 30 years, being the one at Fukushima Daiichi (2011) responsible for 573 deaths and the one at Chernobyl (1986) responsible for 4056 deaths [8], probably the main challenge for nuclear energy is to convince public opinion about its value as a good alternative energy generation method. A difficult challenge as it is the energy source with less public support [9].

1.1.1.3. Hydropower

It is a mature technology for electricity generation, being the most used electricity source in Canada (more than 63 % of electricity produced) and experimenting an expansion in the United States while it is also widely used in Europe, Asia Pacific and Latin America [6]. Hydropower consists in the flow of water from a reservoir through a turbine, generating electricity with the movement of the turbine. Even if it can be considered a renewable energy source, it is usually removed from that category due to the fact that it has a huge environmental impact wherever it is built. Also its use is really limited by topography and land use conflicts [9]

1.1.1.4. Renewable energy sources

Unlike fossil fuels or nuclear energy, renewable energies can be used without the depletion of the resources. They can also be used in a decentralized way, therefore providing energy even to small locations. There are different renewable energy sources like solar, wind, biomass and geothermal, being the first three the most developed ones [10].

- Solar energy: is the most available renewable energy source, as the Sun emits approximately 3.8×10^{23} kW and 1.8×10^{14} kW reach the Earth. Due to the fact that electricity does not reach much areas but the Sun is available, although with

different intensity, everywhere it is possible to use it to produce electricity in a decentralized way. Direct solar energy to electricity conversion is achieved employing photovoltaic (PV) cells, which use the PV effect. Electricity is generated when the energy collected is, at least, the same as the band-gap of the materials of the PV cells. However, even if sunlight is free, the costs of this technology are high [10] and it is also needed to take into account that is an intermittent energy source, affected by day/night cycles and by the weather, as cloudy days would decrease solar energy production.

- Wind energy: one of the most applied renewable energy sources for electricity generation, it is experiencing a fast expansion. Wind energy converts the wind, potentially 9000 TWh/year, in electricity using turbines. However, as wind is not available everywhere, and even if available is an intermittent source, wind energy should be coupled with other energy sources for a reliable operation or used to generate electricity in small locations [10].
- Biomass energy: biogas is the most common way of biomass energy, produced by the anaerobic digestion of different wastes (animal manure, vegetal crops and wastewater). Biogas can be produced when needed and can be easily stored or transported using the existing natural gas grid [10]. However biogas has impurities that need to be removed before its use, increasing its cost. It is also a not reliable technology for large scale energy production.

This is the key fact of the energy system, with the problems associated with fossil fuels (depletion, contamination) and the risks associated to nuclear energy (waste management, safety, public support) renewable energy sources emerge as the best option for a future sustainable energy system.

1.1.2. Climate change

Although several compounds contribute to climate change, carbon dioxide is still its main responsible.

Even if its concentration in the atmosphere is very low, it absorbs infrared radiation at different wavelengths causing the increase in Earth's average temperature [11]. Climate change is a serious issue, being responsible of: extreme weather events (floods, windstorms and droughts), increase of infectious diseases and cardiovascular and respiratory problems [12].

The main human activity that emits carbon dioxide is the burn of fossil fuels, mainly for electricity production. Among these, coal is responsible of approximately 46% of the carbon dioxide emitted in order to produce energy, while oil accounts for approximately 34% of the emissions and natural gas for approximately 20% of the emissions [1].

Not only the burn of fossil fuels results in carbon dioxide emissions, also certain industrial processes emit carbon dioxide.

In addition to this, natural carbon dioxide sinks, as forests, have been destroyed by human activities. The combination of this two factors results in an increase in carbon dioxide concentration in the atmosphere, from 260×10^{-6} ppm during pre-industrial times to 400×10^{-6} ppm nowadays [11].

How can we reduce carbon dioxide emissions to the atmosphere? Knowing the estimated impact on carbon dioxide emissions of each energy source could help to answer this question. The estimated carbon dioxide emissions are divided in two groups: direct emissions, those produced during the energy generation, and indirect emissions that are associated to the building of the technology and its lifetime. Both direct and indirect carbon dioxide emissions for different energy sources are shown in Figure 1.4 [9].

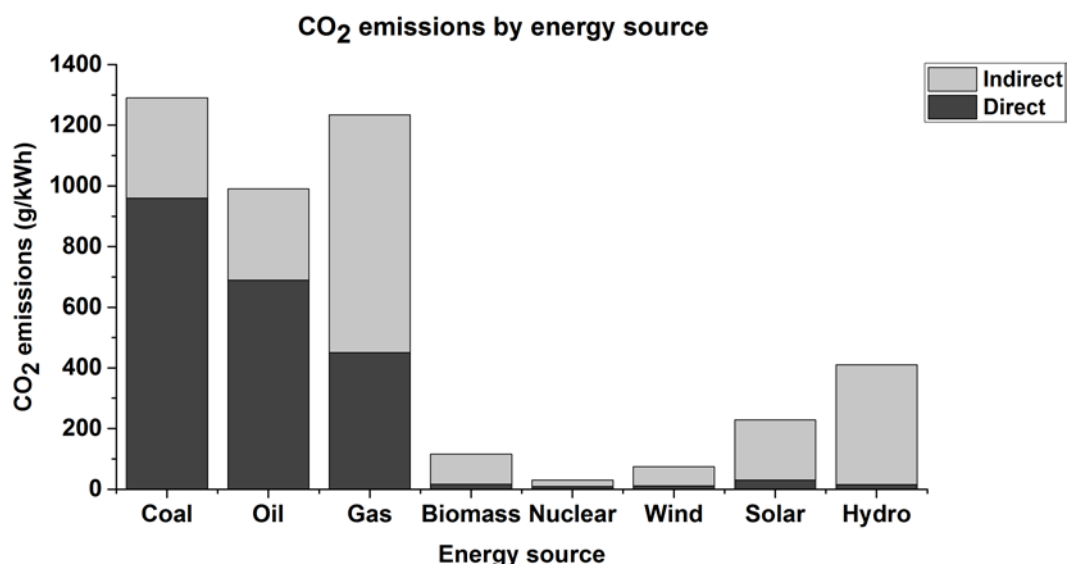


Figure 1.4. Estimated carbon dioxide emissions per energy source[9]

Using more natural gas, instead of coal or oil, in order to produce electricity could be an alternative in the short-term, as direct carbon dioxide emissions from natural gas are lower. Building nuclear power stations would have a huge impact in carbon dioxide emissions, but it would create another problem on how to deal with the residues. Increasing the amount of renewable energies in the power generation mix could be a good alternative to reduce carbon dioxide emissions.

However, there are some industrial processes as cement or steel production that emit a huge amount of carbon dioxide and, at least by now, they cannot be replaced by other processes. Carbon capture and sequestration would be answer to this problem but, is it carbon dioxide going to be stored forever? Would it not be better if we could take advantage of the huge carbon dioxide emissions we produce and generate useful products?

It is possible to transform carbon dioxide into valuable chemicals, both fuels and raw materials for the production of different products like plastics. That said, carbon dioxide is the most oxidised form of carbon being as a result a thermodynamically highly stable molecule and any transformation needs a high input of energy [11]. Being able to

transform carbon dioxide at a reasonable price is one of the challenges that needs to be faced by researchers worldwide.

This is the key fact of the climate change, in order to reduce carbon dioxide emissions we do not only need to fight against the source of those emissions, we can take advantage of them and produce valuable chemicals as feedstock.

1.1.3. Energy dependence

As it has been previously mentioned, energy usage is inherent to human being so energy plays a key role in any economy. Both energy imports and exports have an enormous impact in the economy of a country, being the cost of the energy an important factor in the rate of inflation of a country and determining how competitive that country is in the international scenario [13].

With the present energy system, being the most used resources located in well determined zones and not able to be produced locally, all the countries that do not have access to those resources depend on other countries and securing the external energy supply is a critical issue.

For the European Union, creating a common policy to secure the external energy supply became important after the Russian-Ukrainian gas dispute that took place in 2006, having as a consequence gas shortages in European Union's gas supply due to the fact that almost 80 % of this gas came through Ukrainian pipelines [14].

We can distinguish different policies to secure the energy supply depending on the energy source: oil or gas. In the case of the oil, most of the proven reserves are located in the Persian Gulf so the dependence of the European Union on that area will increase in the future. The case of the gas supply is completely different as a great part of the gas needed by the European Union is produced in countries that are part of the Union as Norway and Netherlands [13]. However, the reduction of the natural gas production rates in Netherlands, in order to avoid earthquakes [15] and concerns about the ability of Norway to maintain the production [16] make necessary to adopt measurements.

Natural gas supply within Europe could be ensured if all the possible supplying alternatives are maintained and the natural gas is buffered, for its use in case of disruptions in the supply [17].

Future will determine if the policies adopted by the European Union regarding to the energy supply security have been successful. This will strongly depend in the evolution of the international affairs but we can distinguish two scenarios: i) Markets and Institutions, which means a strong collaboration between countries or ii) Regions and Empire, which involves a division of the world into competing spheres of influence. Unfortunately, this last one looks like the most possible future [13].

There is a way to secure energy supply without the need of being dependent on another countries: renewable energies. Increasing the share of renewable energies will not only have a positive effect in the reduction of greenhouse gas emissions, it will also reduce the use of fossil fuels, which are geographically localized in some regions, and will allow the countries to obtain their energy locally.

This is the key fact of the energy dependence: renewable energies could ensure the energy supply.

1.2. Analysing the problem

All the sections described above concluded with a key fact as a summary. All the key facts together make a clear picture of how the future should be like: based on renewable energy sources.

An energy system based on renewable energy sources would not only be sustainable, it would also be efficient against the climate change and would ensure the energy supply worldwide, minimizing the need to be dependent of other countries to ensure the energy supply. The future path is clear and should be followed, renewable energies could ensure a sustainable future.

1.3. Energy storage

As set forth before, integrating renewable energies into the energy mix is limited by their intermittency and variability. Energy storage could make renewable energy sources a reliable option for the energy system, storing the excess generated when available could ensure the energy supply when renewable energy sources are not available [18].

Energy storage technologies can be sorted in mechanical, chemical, electrical, magnetic, biological and thermal energy storage [19].

1.3.1. Mechanical energy storage

Mechanical energy storage technologies convert electricity in different forms of energy, with losses due to efficiency up to 50 % [19]. The most common mechanical energy storage methods are:

- Pumped Hydroelectric Energy Storage (PHES): works depending on the energy demand. If demand is low, water is pumped from a river up to a reservoir to be released when the demand is high. Released water drives a turbine that generates electricity [19]. PHES can release stored energy in a short period of time (< 1 min), with a typical efficiency of 65-85 %. It is the most common energy storage installation [20].
- Flywheel Energy Storage (FES): energy is stored in kinetic form. During the storage a flywheel rotates and transfers angular momentum to a rotor, where the energy is stored. During the release of the energy, the rotating mass decelerates and generates electrical energy with a generator connected to the shaft. This method is cheap and has a long life cycle with low maintenance, but friction losses reduce its efficiency along the time [18]. Operating in vacuum is a suitable way to reduce friction losses [19].
- Gravity Energy Storage (GES): adapted from PHES, eliminates the constraints caused by the size of the reservoir. A piston is introduced in a shaft filled with water, which operates in closed loop so there is only need to fill it once. During

the storage, electricity is used to operate a pump that forces the water down the shaft, the piston is pushed upwards and held until the electricity is needed. During the release of the electricity, the piston is released and pushes the water through a turbine generating electricity [18].

- Compressed Air Energy Storage (CAES): during the storage, electricity is used to compress air that is stored in a reservoir. When electricity is needed, this compressed air is released and passed through a turbine, generating electricity. It can reach efficiencies about 70 % [18].
- Liquid-Piston Energy Storage (LPES): it is still under development. This system uses a liquid to compress a gas inside a vessel. When electricity is needed, the gas is expanded pushing the liquid through a pump/motor and generating electricity. It can reach efficiencies about 73 %, being the main drawback the possibility of leaks [18].

1.3.2. Chemical energy storage

Chemical energy storage technologies convert electricity in chemical compounds through reversible chemical reactions. Energy is absorbed and released using chemical reactions. A known example of chemical storage are batteries, which can store a large amount of energy in a small volume [19]. Most of the chemical compounds used (butanol, ethanol, hydrocarbons, hydrogen, methane or methanol) have higher energy density than the mechanical storage techniques, making chemical energy storage an ideal way to store energy [18]. The most common chemical energy storage methods are:

- Power-to-Gas (PtG): electricity is converted in an energy carrier that can be converted again back into electricity. PtG is a flexible system as the chemical energy carriers can be stored, used as a fuel for transportation or industry and as raw materials for chemical industry. PtG can convert electricity in hydrogen or methane, two well-known energy carriers [21].
- Power-to-Liquids (PtL): based in the same technology as PtG, PtL is used to produce methanol as energy carrier. The main objective of producing methanol,

a liquid fuel, is replacing fossil fuels. Other energy carriers can be produced as gasoline, kerosene, dimethyl ether, diesel and waxes [21].

- Solar-to-Fuels (StF): solar energy is converted in fuels using carbon dioxide and water. There are two different pathways i) a PtL process using solar energy and ii) carbon monoxide is generated that can be used to generate syngas for further synthesis processes [21].

1.3.3. Electrical energy storage

Electrical energy storage technologies store electricity in the form of electric charges between two conductive plates that are separated by an insulating or dielectric medium. The capacity of this system, thus, depends on the size of the plates, their distance and their material [19]. The most common electrostatic energy storage methods are:

- Supercapacitor Energy Storage: electricity is stored in two series capacitors. Large energy density can be stored with a fast response to any change in power demand. The main drawbacks of this method are its cost, and the discharge rate of 5% per day, so it is only useful for short term energy storage [18].
- Battery Energy Storage: is the oldest electrical energy storage device, electricity is stored as chemical energy. It is an electrochemical technique that delivers electricity generated by electrochemical reactions. There are different kind of batteries with an efficiency between 60-80 %. The most common batteries are: sodium sulphur battery, sodium nickel chloride battery, vanadium redox battery, iron chromium battery, zinc bromine battery, zinc air battery, lead acid battery, lithium ion battery and nickel cadmium battery [18].

1.3.4. Magnetic energy storage

Magnetic energy storage technologies store electricity in a magnetic field. Advances in material technologies have resulted in a development of this technique in the last years. The use of superconducting materials, which at low temperature have minimal electrical resistance, allows large currents to be transferred with minimal losses [19].

Superconducting Magnetic Energy Storage (SMES) is the most developed magnetic energy storage method. It uses a cryogenically cooled magnetic field, reaching a temperature of approximately 3 K. It has a high efficiency but also high capital and operating costs [18].

1.3.5. Biological energy storage

Biological energy storage technologies store energy in a bio-battery. Glucose is used as the main energy source, and it is converted using enzymes in protons and electrons, consequently, generating electricity [19].

1.3.6. Thermal energy storage

Thermal energy storage technologies store electricity as heat or cold [21]. It is an environmentally-friendly technology, being its main drawback that is not suitable for long-term storage [19]. The most common thermal energy storage methods are:

- **Sensible Energy Storage:** energy is stored as internal energy induced by temperature changes in the material. Energy is available as heat, both in liquids (hot water, oil based fluids and molten salts) and in solids (metals and rock filled storage). Its main disadvantage is the need of large storage volumes [18,19,21].
- **Latent Energy Storage:** energy is stored as heat, which can be released or absorbed changing the phase of a material. The phase change usually occurs between solid and liquid phases, whilst vapours are not used. Its main drawbacks are reduced storage, chemical instability and high costs [18,19,21].
- **Thermochemical Energy Storage:** energy is stored within a reversible reaction. Heat is stored during the endothermic reaction step and released during the exothermic reaction step. Is still under development, but theoretically transportation and storage periods do not limit this storage method [18,19,21].

Chapter II

State of the art

Table of contents

2.1. POWER-TO-GAS	29
2.1.1. WATER ELECTROLYSIS	30
2.1.2. METHANATION	33
2.2. CARBON DIOXIDE METHANATION PROCESS	34
2.2.1. CATALYSTS FOR CARBON DIOXIDE METHANATION.....	36
2.2.1.1. <i>Active metals</i>	36
2.2.1.2. <i>Supports</i>	37
2.2.1.3. <i>Promoters</i>	37
2.2.1.4. <i>Preparation methods</i>	37
2.2.1.5. <i>Review of catalytic systems</i>	38
2.2.1.6. <i>Deactivation of catalytic systems</i>	40
2.2.2. REACTORS FOR CARBON DIOXIDE METHANATION	41
2.2.2.1. <i>Fixed bed reactors</i>	41
2.2.2.2. <i>Fluidized bed reactors</i>	42
2.2.2.3. <i>Other reactor configurations</i>	42
2.2.3. CARBON SOURCE FOR CARBON DIOXIDE METHANATION	43
2.2.4. PHOTOCATALYSIS FOR CARBON DIOXIDE METHANATION	44

In Chapter I of this PhD thesis the current energy scenario and future projections were described. The need of a renewable energy system was clearly presented, together with the need of implementing energy storage systems when an excess of electricity is produced from renewable sources. After describing the existing solutions for storing energy, Power-to-Gas (PtG) was selected as one of the most promising methods.

The current state of the art of Power-to-Gas will be extensively analysed in this chapter.

2.1. Power-to-Gas

Renewable energy sources, like wind and solar power, are intermittent and variable, thus, their production is not coupled with the demand [22]. PtG is a technology that overcomes the main disadvantage of renewable energy sources, their variability, as it stores the excess of electricity produced when the production is higher than the demand, or when it cannot be introduced into the electrical grid, in a chemical carrier (hydrogen and/or methane). As it has been mentioned, production of synthetic fuels represents one of the most convenient ways to store large amounts of surplus electricity for long periods [23].

PtG technology takes places in one step, if hydrogen is to be produced, or two steps if the objective is the production of methane [24]:

1. Hydrogen production via water electrolysis, using the excess of electricity produced from renewable energy sources.
2. Methanation process. The hydrogen produced in the first step reacts with carbon monoxide and/or carbon dioxide from an external source to produce methane.

A scheme of the PtG process is shown in Figure 2.1.

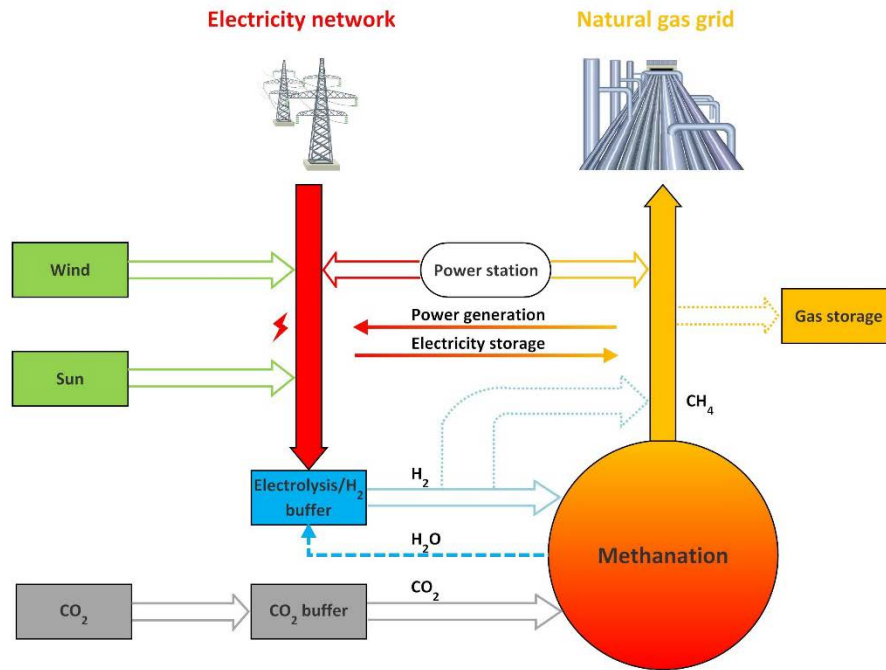
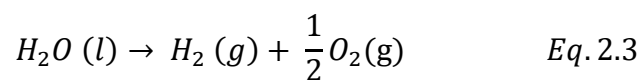
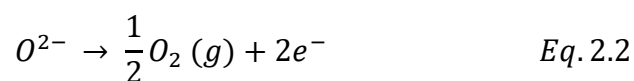
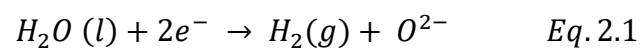


Figure 2.5. Scheme of the Power-to-Gas process

2.1.1. Water electrolysis

The first step, the only compulsory one, of PtG technology is the production of hydrogen by water electrolysis. Water electrolysis is an electrochemical reaction: reduction takes place at the cathode (**Eq. 2.1**) while oxidation takes place at the anode (**Eq. 2.2.**) giving the overall water electrolysis reaction (**Eq 2.3**), which is a highly endothermic reaction with a value of $\Delta H_r^0 = 285.8 \text{ kJ/mol}$ [24].



Depending on the technology employed for water electrolysis we can distinguish between alkaline electrolysis (AEL), polymer electrolyte membrane electrolysis (PEM) and solid oxide electrolysis (SOEC):

- AEL: it is the most mature technology, which has been available for decades. In this technique, an aqueous alkaline solution (KOH or NaOH) is used as the electrolyte. The main advantage of this technology is that it can work with fluctuating power supplies, as the ones expected from renewable energy sources, while its main disadvantage is that electrolytes are highly corrosive, leading to high maintenance costs [24]. This technology can reach efficiencies between 43-66 % [21].
- PEM: based on solid polymer membranes, these systems are more flexible than the ones based on AEL and can also work under intermittent power supplies, producing highly pure hydrogen. The main disadvantages of PEM, compared to AEL, are that it is more expensive and its life time is shorter [24]. This technology can reach efficiencies between 68-72 % [21].
- SOEC: still in the laboratory stage, ZrO₂ doped with 8 mol % Y₂O₃ is employed as electrolyte, allowing the conduction of oxygen ions at high temperatures. The main advantage of this system is its low electricity demand. The main challenges that need to be overcome before being a mature technology are the fast material degradation and the excessive steam production, which means post processing of the product and an increase in the costs [24]. This technology can reach efficiencies up to 98 % [21].

If electrolyzers are a well-established technology, even having room for improvement, and hydrogen can be produced with efficiencies above 50 %, how could the need of taking this process further, performing one step more, and producing methane be justified?

Hydrogen is not only considered one of the most promising energy vectors for electricity, mobility and heat, it is also an important raw material for the chemical

industry [25]. However, due to its high costs, most of the hydrogen employed in the chemical industry is not produced by water electrolysis but from fossil fuels instead [26].

Even if hydrogen has several uses, the main problems related to its use are both storage and transport. Hydrogen produced via PtG could be used locally without any problem but the main question is how it can be transported. Regular pipelines are not ready for its use with hydrogen and the amount that can be injected into the natural gas grid is limited. There is not actually an unified regulation for the amount of hydrogen that can be feed into the existing natural gas grid, even not all the countries measure the hydrogen content in their natural gas network [27]. As an example, Austria allows a hydrogen content up to 0.5 vol %, while this value is increased up to 5.0 vol % in Germany or Switzerland [28]. As the harmonisation of the European Natural Gas Network is still a to-do project, the Spanish case scenario will be considered in this PhD thesis, thus, the allowable amount of hydrogen to be injected in the natural gas grid will be considered of 5.0 vol % [29].

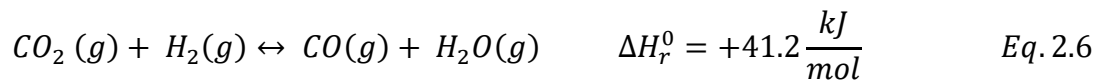
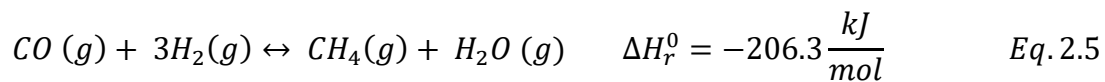
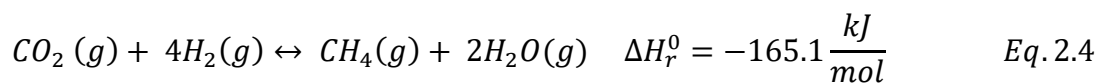
For large amounts of hydrogen, pipeline transport would be an efficient approach, however a dedicated pipeline needs to be designed and built [30].

Regarding to the storage, there are several options like high pressure gas storage, metal hydride storage, underground storage using caverns or cryogenic compressed liquid storage. Even though liquid hydrogen could be transported using ships, which is an established transportation method, this last option is the least feasible one as the costs related to compress and store hydrogen at cryogenic temperatures are really high. Among all the other options, either high pressure compression or metal hydrides seem to be the most promising ones, especially the first option as it is cheaper. The use of caverns can be discarded as it is only efficient for long term storage and hydrogen produced by PtG should be ready for its use at any time, as it should be employed to balance the electrical grid [24].

2.1.2. Methanation

Hydrogen produced from water electrolysis can react with carbon dioxide to produce methane, which is a well-known energy carrier with a widely established distribution system, mainly natural gas pipelines [21].

Several reactions take place in the methanation process: carbon dioxide hydrogenation (**Eq. 2.4**), carbon monoxide hydrogenation (**Eq. 2.5**), reverse water-gas shift (**Eq. 2.6**) and Boudouard reaction (**Eq. 2.7**). Moreover, carbon dioxide hydrogenation reaction can be seen as the combination of both carbon monoxide hydrogenation and reverse water-gas shift reactions, whilst Boudouard reaction is an important deactivation mechanism that results in the formation of solid carbon [24,31].



Apart from the reverse water-gas shift reaction, all the other reactions are highly exothermic [32,33], hence, controlling the temperature and ensuring good cooling is one of the most important parameters of the methanation process.

Being an exothermic process, high temperatures hinder the overall efficiency of the process. However, an eight-electron process is required to fully reduce the carbon to methane and there are serious kinetic limitations [34]. Apart from trying to develop more active and selective catalysts, and increase in the operating pressure of the methanation process also has a positive effect, increasing the yield to products according to Le Chatelier's principle [35].

The main problem associated to the methanation process is the overall loss of efficiency of the whole PtG process. Even if highly active catalysts were available and high hydrogen conversions were obtained, there would always be a decrease in the overall yield of the process comparing to just performing one step. According to this, why should we choose methane instead of hydrogen as the future energy carrier?

Methane has different advantages when compared to hydrogen: it can be applied in the short term, can be easily transformed again in electricity with current technologies and can be widely distributed and/or stored using the existing natural gas grid [36].

Moreover, it has higher volumetric density than hydrogen, is safer and it can also be used to produce different chemicals and fuels [37]. It also does have disadvantages being the main one that its conversion to electricity generates carbon dioxide, thus, contributes to the climate change [36] in opposition to hydrogen which is a carbon-free fuel [25]. However, as carbon dioxide is used in the methanation process, methane produced by this method can be considered a low-carbon or carbon-neutral fuel [38,39].

2.2. Carbon dioxide methanation process

Two carbon sources can be used for the second step of the PtG technology, namely, methanation process: carbon monoxide and carbon dioxide. Among these two sources, carbon dioxide is gaining attraction in the recent years as it is one of the main contributors to climate change and its producing chemicals and/or fuels could effectively mitigate climate change. Furthermore, carbon dioxide hydrogenation proceeds with a lower activation energy and at a higher rate than carbon monoxide hydrogenation [40].

Carbon dioxide methanation process is also known as Sabatier reaction [41] in honour to the French chemist Paul Sabatier who first discovered, together with Jean-Baptiste Senderens, the reaction in the early 20th century [42]. Carbon dioxide methanation is a topic that has gained interest within the scientific community in the last lustrum, especially as a tool for energy storage and balancing the electrical grid. The trend in the papers published related to carbon dioxide methanation can be observed in Figure 2.2.

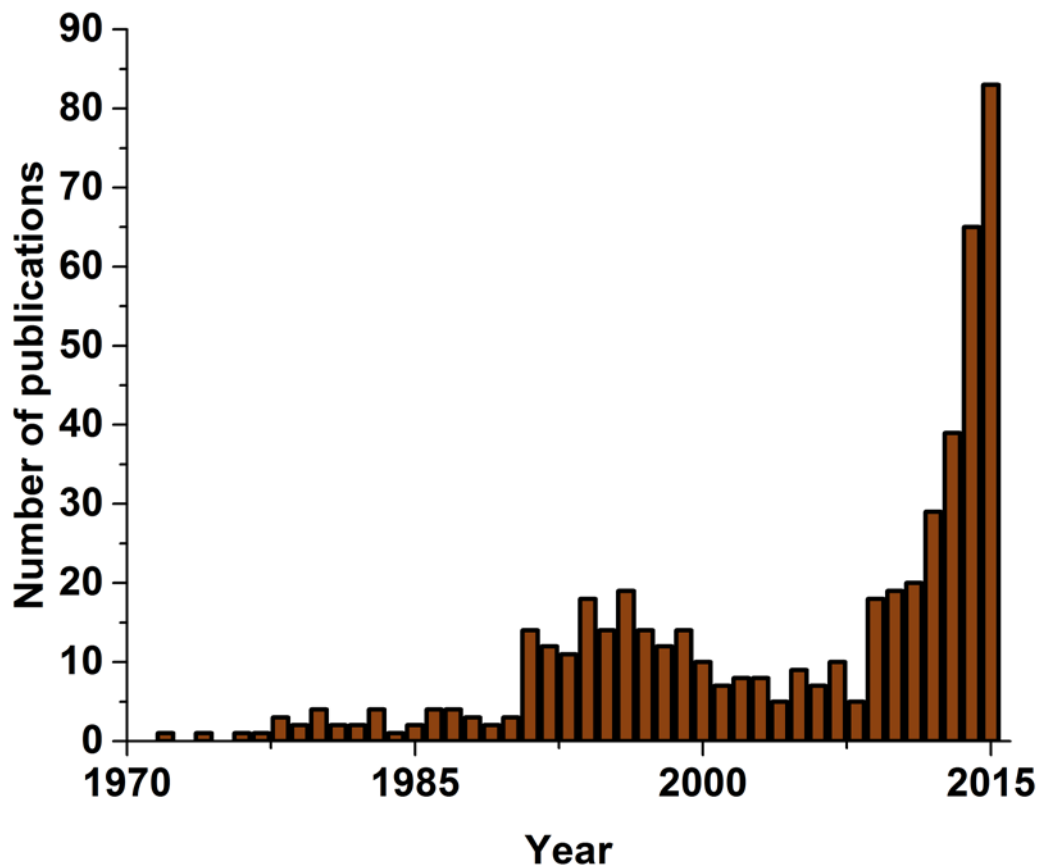


Figure 2.6. Trends in carbon dioxide methanation research

Besides its usefulness to produce a valuable energy carrier as a way to balance the electrical grid, carbon dioxide methanation is also part of innovative research projects as the one proposed by the National Aeronautic Space Administration (NASA), in their attempt to schedule a future manned expedition to Mars, they are thinking in using the carbon dioxide available in the atmosphere of Mars to generate fuel (methane) and water for astronauts life support systems (water) [41,43].

In spite of gaining a complete understanding of the current state of the art of carbon dioxide methanation three different parameters should be analysed as they determine the efficiency of the carbon dioxide methanation process: catalysts, reactors and carbon source.

2.2.1. Catalysts for carbon dioxide methanation

2.2.1.1. Active metals

Intensive research on carbon dioxide methanation has been carried out using catalytic systems based on group VIII B metals [33,34,43–59]. However, only some of those metals are relevant for the methanation reaction. The most suitable metals, taking into account activity and selectivity, for methanation process are [60]:

Activity: Ru > Fe > Ni > Co > Mo

Selectivity: Ni > Co > Fe > Ru

The active metals most commonly employed for carbon dioxide methanation can be further described [56]:

- Ruthenium: is the most active metal for methanation process, especially at low temperatures. However, its high price makes it not suitable for industrial applications.
- Iron: with high activity but low selectivity to methane, it is not suitable for methane production.
- Nickel: is the most selective to methane and has a high activity that it is combined with a low price, so it can be considered the most suitable metal for methane production. However, nickel based catalysts suffer from deactivation due to sintering [55] and coke deposition [41].
- Cobalt: similar to nickel based catalysts but more expensive, thus, it is not the best option for methanation process.
- Molybdenum: presents the lowest activity and C₂ formation is favoured. However, its sulphur tolerance makes it a suitable metal for methanation process under some particular conditions.

2.2.1.2. Supports

Even if unsupported metals have been tested for methanation reaction, the use of supported catalysts has different advantages. Supports improve the dispersion of the active phase, decrease the formation of inactive spinel phases and modify the reducibility of the catalysts due to the metal-support interaction [51].

The most relevant supports for methanation process are: Al_2O_3 (especially the γ -phase), SiO_2 , TiO_2 , ZrO_2 , zeolites and, more recently, foams (especially Ni-based monolithic foams) and biochar [50,56,61,62].

2.2.1.3. Promoters

The use of promoters and their effect depends both on the active metal and the support employed. The most commonly employed promoters for methanation process are alkaline-earth metal oxides like Mg, Ca, Sr and Ba which increase the dispersion of the active phase and stabilize the dispersed metal against sintering [55]. The use of alkali promoters can also be beneficial for some specific catalysts, creating new active sites in the interface between the active metal and the support [44]. Finally, one of the most common ways to improve a catalyst for methanation process is the combination of more than one transition metal oxides [63].

2.2.1.4. Preparation methods

Synthesis of catalysts can be carried out using different methods, depending on the metals, promoters and supports employed, but also taking into account the final use of the catalyst. Most common catalyst preparation methods are further described below [64].

- Impregnation: depends on the interaction between the support and the metallic species contained in a solution. We can distinguish two different approaches to this technique: i) when the volume of impregnation solution is equal to or less than the pore volume of the support, it is called incipient wetness impregnation

or dry impregnation and ii) when the volume of impregnation solution is used in excess, it is called wet impregnation. In both cases it is important to carry out a careful drying process.

- Coprecipitation: support and active metal cations are present together in the same solution. One of the greatest advantages of this method is its great reproducibility.
- Deposition-precipitation: involves using an aqueous solution of the salt of the metal to be deposited (usually nitrates) together with the support and urea. The solution is heated and urea hydrolyses giving OH⁻ ions. The metal then precipitates homogeneously on the surface of the support.

2.2.1.5. Review of catalytic systems

The combination of active metal-support-promoter and the preparation method is what gives its properties to a catalyst or catalytic system. Different reviews about the catalytic systems developed by researchers worldwide for methanation process have been performed. The catalytic systems developed in the recent years are summarized in Table 2.1 [65].

Table 2.1. Recently developed catalytic systems [65]

Catalytic system	Preparation method	Reaction temperature (K)	Pressure (bar)	CO ₂ conversion (%)	CH ₄ selectivity (%)
1Rh/ γ -Al ₂ O ₃	Wet impregnation	323-423	2	-	100
Ni/SiO ₂ -Al ₂ O ₃	Incipient wetness impregnation	773	1	35	30

Ni/RHA- Al ₂ O ₃	Impregnation	773	-	70	90
15Ni/TiO ₂	Deposition- precipitation	533	1	96	99
25Ni/Al ₂ O ₃	Impregnation- coprecipitation	598	15	67.3	87
12Ni/ γ - Al ₂ O ₃	Incipient wetness, impregnation	483	20	80	99.5
10Ni/La ₂ O ₃	Incipient wetness impregnation	623	15	97.1	100
Ni/MgAl ₂ O ₄	Incipient wetness impregnation	623	1	85.82	99
Ni/MgAl ₂ O ₄	Impregnation	-	-	-	98.4
0.5Ni/SiO ₂	Impregnation	623	1	10	60
10Ni/SiO ₂	-	-	-	-	87
Ni/ZrO ₂	Hydrogel	553-593	5	99	92
23Ni/Al ₂ O ₃	-	673	1	81	98

3Ni/MCM-41	-	573	1	16.8	96.1
------------	---	-----	---	------	------

Ni/CeAl-p	-	573	1	88	99
-----------	---	-----	---	----	----

2.2.1.6. Deactivation of catalytic systems

As a chemical reaction proceeds, catalysts suffer from deactivation. This means that the active sites of the catalyst are no longer active. There are different deactivation mechanisms [66]:

- **Coking:** it happens in reactions involving hydrocarbons. Coke formation occurs at the acid sites of the support. Coke is a high molecular entity that grows along the surface of the catalyst, covering not only the support but also the active sites. This is a chemical deactivation mechanism.
- **Poisoning:** a molecule interacts with the active sites of the catalysts causing their deactivation. Poison molecules are adsorbed on the active sites so they are not active for the reaction. However, poisoning can be reversible as the poison can be removed from the surface of the catalyst, for example by oxidation. One typical example is sulphur poisoning. This is a chemical deactivation mechanism.
- **Crushing:** when a catalyst cannot support its own weight, the catalyst at the bottom of the reactor suffers from crushing or attrition due to the weight of the catalyst at the top of the reactor. The forming of fine particles results in blocking the fluid flow through the reactor. Fluids flow at high velocity through the parts of the reactor that are not blocked, thus, at a short residence time that reduces catalysts productivity. This is a mechanical deactivation mechanism.
- **Sintering:** occurs at high temperatures, usually above 873 K. Metallic sites diffuse across the surface of the catalyst, until they encounter another active site and they form agglomerations which are inactive. This is a thermal deactivation mechanism.

2.2.2. Reactors for carbon dioxide methanation

Up to the date, different reactor concepts for carbon dioxide methanation process have been developed. There are two main approaches to the design of a reactor for carbon dioxide methanation: fixed bed reactor and fluidized bed reactor [22], but there are also other approaches.

2.2.2.1. Fixed bed reactors

Catalysts are introduced in pellet form inside the reactor, forming a homogeneous catalytic bed. Due to the high exothermicity of the reaction, usually a series of fixed bed reactors configured as a cascade are employed, with intermediate gas cooling, gas recycling and reaction heat recovery steps. Hot spots must be avoided in order to preserve the catalysts. Mass transfer limitations are one of the main drawbacks of this reactors [67]. Up to the date, different industrial methanation systems have been developed using fixed bed reactors [56].

- Air Liquide: developed in the 1970s, the system was based on two fixed bed reactors with intermediate gas cooling and gas recycling.
- British Gas and Conoco: developed in 1973, was based on three fixed bed reactors with intermediate gas cooling and gas recycling. This design is currently available by Johnson Matthey.
- Haldor Topsøe: similar to the one designed by Air Liquide, but with three-four fixed bed reactors instead of two. Developed in 1978 for high-temperature methanation (< 973 K). This design is still available.
- Ralph M. Parsons: a different approach, this design combined four-seven adiabatic fixed bed reactors to avoid cooling and recycling. However, it was never employed.
- Imperial Chemical Industries and Koppers: the system was based on the use of several fixed bed reactors in series with intermediate cooling. Steam was added between the reactors to limit catalyst temperature increase inside the reactors.

- Clariant and Foster Wheeler: the system was based on three fixed bed reactors with steam, as the design by Imperial Chemical Industries and Koppers, to gain control over the temperature.
- Linde: the system was based on a cooled reactor with an integrated heat exchanger and a second adiabatic reactor. This design was never employed, however it was useful for a further developing of reactors for methanol synthesis.

2.2.2.2. Fluidized bed reactors

Solid catalysts particles are fluidized, being the result a strong turbulence that creates an approximately isothermal temperature profile in the reactor. Fluidized bed reactors are characterised for a good heat release, combined with reduced mass transfer limitations so there is no need for a cascade set-up, making the design simpler. The main drawbacks of this reactors are that they are limited for unsteady operation and that the movement of the catalysts causes abrasion to both the catalyst and the reactor [67]. Up to the date, there are not industrial methanation systems using fluidized bed reactors, but different pilot-plants have been tested [56].

- Bituminous Coal Research Inc: the system was based on a reactor with two internal heat exchanger in the catalytic bed. The development started in 1963 and was tested at laboratory for several hours.
- Thyssengas: a similar concept, based on a reactor with internal heat exchanger, was operated from 1977.

2.2.2.3. Other reactor configurations

- Bubble columns: a 3-phase system. Introducing a liquid phase, this promotes the heat release, thus, reaching an isothermal profile in the reactor. Even if abrasion is avoided, the inclusion of a third phase results in a more complicated design and operation, plus increased mass transfer limitations [67].

- Biological processes: they are out of the scope of this PhD thesis. However, it is important to know that exists the possibility of substituting catalysts by enzymes. Biological methanation is particularly used for biogas processing [67].
- Process intensification: developed in recent years to overcome the main drawbacks of this process, as the formation of hot spots, monoliths and microreactors are an innovative concept for the methanation process. Structured reactors combine great heat transfer with small pressure drop, together with a more compact design. The main drawback of this reactors is that catalyst loading and replacing is more difficult [24].

2.2.3. Carbon source for carbon dioxide methanation

Carbon dioxide for the methanation process could be provided from different sources. The optimal carbon dioxide source should be cheap, with low energy requirements, with high purity and able to adapt to fluctuating demand due to the fact that hydrogen supply for the methanation would be intermittent, dependant in the excess of electricity from renewable energy sources.

We can distinguish different carbon dioxide sources as fossil fuel power plants, biogas, industrial processes and air.

- Fossil power plants: related to Carbon Capture and Sequestration (CCS) there are several technologies available for its separation from other compounds, being the total cost in the range of 20-60 €/tCO₂ and a loss of efficiency of the methanation process of 2-5 % due to the energy needed for its separation. The main disadvantage of this carbon source is that needs to be transported to the methanation plant [24,30].
- Biogas: gasification of biomass results in a carbon dioxide source approximately equal to the one obtained from fossil power plants. However, carbon dioxide from biomass fermentation is a free of charge source as it is provided by a waste without any need of energy. However, biogas produced from biomass fermentation has several components that need to be removed before the

methanation process [24]. Biogas from waste-water treatment could also be an interesting source, but again with the need to remove several compounds [23]

- Industrial process: as fossil power plants, providing carbon dioxide from industrial processes is based on CCS technology. The industrial processes that emit most carbon dioxide are cement and steel industries. These emissions cannot be avoided, so their use to produce methane is a good opportunity to valorise them. Once again, being stationary carbon dioxide sources it is a drawback as it implies transport costs [30].
- Air: it is a dynamic carbon source so transport is avoided but the costs of concentrating carbon dioxide from air are too high, being the cost of carbon dioxide of 1000 €/t. This price, together with the high amount of energy needed, makes it not a suitable carbon source [30].

At this moment, biogas is the most suitable source of carbon dioxide for carbon dioxide methanation process. The problem associated with the transport of carbon dioxide could be solved building the PtG plant close to a biogas treatment plant, as in currently available industrial projects like the one developed by Etogas [68].

In the future, with CCS fully developed and integrated in the industry almost pure carbon dioxide should be available from pipelines [23], as it is already in some specific industrial complexes [24].

2.2.4. Photocatalysis for carbon dioxide methanation

The catalysts and the reactor configurations reviewed in the previous sections can be considered the most established way to drive a reaction, namely, thermal catalysis. However, different approaches can also be taken into account. One of the most novel ways of driving a chemical reaction is photocatalysis which uses light of different wavelengths to drive a chemical reaction, thus, being photons of a correct wavelength the responsible of supplying energy to the reaction instead of the heat, as it happens in the thermal catalysis process. However, the influence of heat can also be present in photocatalytic reactions as localised heating induced by light irradiation.

Conventional photocatalysis takes advantage of the properties of semiconductor materials, specifically their electron-hole separation, to improve the rate of chemical reactions using light irradiation. Semiconductor based photocatalysts, when irradiated, suffer a charge separation that results in the formation of an electron-hole pair [69], being the generated electron responsible of the reduction step of a reaction and the hole where oxidation takes place [70]. One of the main drawbacks of using semiconductor based photocatalysts is their fast electron-hole recombination [71].

Recent advances in photocatalysis include the use of metallic nanostructures that enhance light absorption via localised surface plasmon resonance (LSPR) [72]. Some metals, especially noble ones like Au and Ag, present strong light absorption and scattering at specific wavelengths due to the LSPR effect that consists in the strong oscillation of metal's free electrons with the varying electric field of the incident light [73]. LSPR effect can be furtherly explained:

The free electrons confined in noble metal nanoparticles oscillate at a frequency. If irradiated with light of the same frequency they enter in resonance state, creating an intense and highly localised electromagnetic field [74]. A picture of the LSPR on metallic nanoparticles (NPs) can be seen in Figure 2.3 [75].

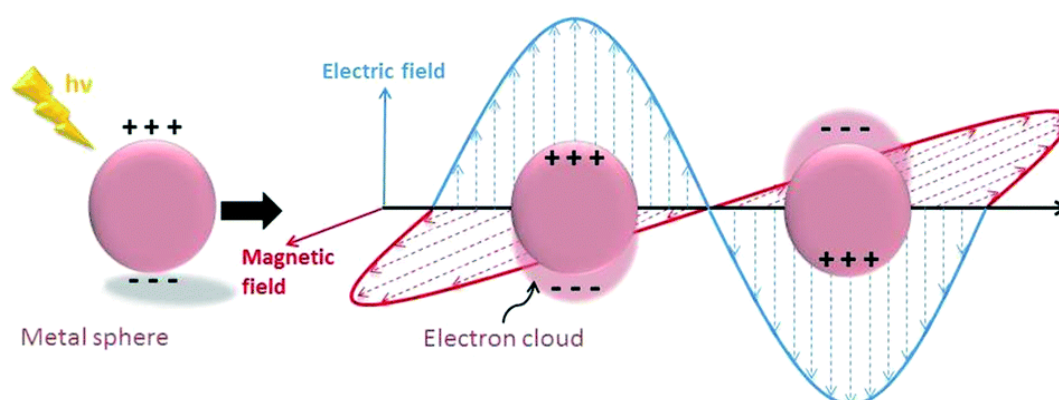


Figure 2.7. LSPR on metallic NPs [75]

The LSPR effect can be divided in two different mechanisms: i) indirect photocatalysis, where the excitation is transferred to a nearby semiconductor or other metal, and ii)

direct photocatalysis where the excited metal act as the catalytically active site [76]. The indirect effect takes place when the created hot electron, which is a free electron that has been promoted to a higher energy level, is transferred to nearby acceptors [77].

As it can be seen, LSPR assisted photocatalysis is a complex process where different mechanisms can take place. For a better understanding of this effect, all the mechanisms are summarised in Figure 2.4 [77].

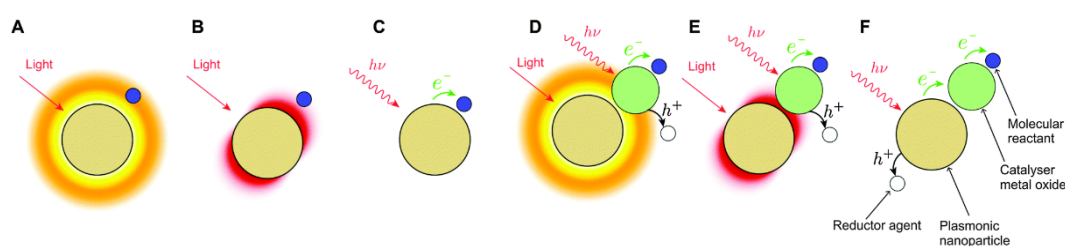


Figure 2.8. Possible mechanisms LSPR assisted photocatalysis [77]

The different mechanisms depicted in the picture can be described as follows:

- a) Localised heating.
- b) Enhancement of the optical near field at the vicinity of the NP, increasing the photon rate seen by the reactant.
- c) A hot electron being transferred to the adjacent reactant.
- d) Electron-hole generation rate is enhanced by the heat generated by the NP.
- e) Electron-hole generation rate is enhanced by the strong optical near field of the NP.
- f) The photocatalyst adjacent to the NP is activated by the hot electron transferred from the NP.

Up to the date most of the research that has been carried out in the field of LSPR for carbon dioxide methanation process is based in the use of semiconductors like TiO_2 as catalytic support, meaning that the mechanism that takes places is based in electron-

hole generation (either type d or type e mechanism), while the most used metal is gold due to its excellent plasmonic properties [32,69–71,78,79]. There are different alternatives to gold, like silver and copper, but they tend to oxidise [80] making them not suitable plasmonic materials for several reactions. However, the high sensitivity that presents the silver when irradiated [81] and taking into account that carbon dioxide methanation reactions occurs in hydrogen atmosphere so that oxidation should not be a problem, silver can be considered a promising metal for this reaction. Indeed, silver not only has strong LSPR properties but it is also considered an active metal for carbon dioxide methanation reaction, whilst gold and copper are not [56].

As it has been mentioned for the gold based photocatalysts, most of the research carried out in this field with silver based photocatalysts has been performed using a semiconductor, mostly TiO₂, as catalytic support [71]. Nevertheless, not much research has been carried out using silver NPs as LSPR material.

To our knowledge, the use of silver NPs over a non-semiconductor support for carbon dioxide methanation process has not been reported which makes this a novel research field.

Chapter III

Objective and scope

Table of contents

3.1. OBJECTIVE	53
-----------------------------	-----------

In the **Chapter I** of this PhD thesis an overview of world's actual energy system and projections for the future were presented. Moreover, the increasing population, therefore, increasing energy demand and the increasing awareness about the need to face the climate change were presented as the main reasons to rely on a sustainable energy system.

With the purpose of developing a sustainable energy system, Power-to-Gas was presented as a promising technology that allows the integration of renewable energy sources into the existing energy mix. It also decreases carbon dioxide emissions to the atmosphere, as it is used as raw material to produce methane, which can be used as fuel for transportation, for electricity generation or stored.

In the **Chapter II** of this PhD thesis, methane production step of Power-to-Gas was described, namely, methanation process performing an extensive literature review of the current state of the art in that research field.

3.1. Objective

The main objective of the current PhD thesis is the development of advanced catalytic systems for the carbon dioxide methanation reaction. This work aims to have an academic interest, being useful for the scientific community and serving as a contribution in the field of heterogeneous catalysis and sustainable engineering. Even more, it aims to have an industrial interest, proposing an effective way to produce methane via carbon dioxide methanation process.

For this research, nickel was selected as the main active metal as it has been proved that it shows great activity for carbon dioxide methanation process, likewise other metals from group VIII B. Although nickel is not as active as some noble metals, as ruthenium, its price way lower than the one of noble metals makes it a really interesting metal for this application.

In order to attain the objective of this thesis, some partial goals must be fulfilled:

- Selection of the optimal synthesis and operating conditions, including calcination temperature of the catalysts and operating pressure.
- Catalysts synthesis and activity tests in fixed bed reactors.
 - Use of novel materials for the synthesis of catalysts: industrial residues and natural supports.
- Testing in photocatalytic reactors, an innovative and sustainable approach to carbon dioxide methanation process and its comparison with fixed bed reactors. Gold and silver were selected, due to their surface plasmon properties, as the active metals for photocatalysts both alone or mixed with nickel.
- Study of the correlation among catalysts physicochemical properties and the activity results in driving the carbon dioxide methanation reaction. For this purpose, both fresh and used catalysts should be analysed using different characterisation techniques. This exhaust analysis should lead to the understanding of the different factors affecting the activity achieved by the catalysts.
- Process scale-up, design of an industrial plant to produce methane from carbon dioxide using all the knowledge gained in the previous steps to design the plant.

As it can be seen, the final objective of this PhD thesis is not only to design effective catalytic systems and reactors, but finally scale-up all the process and propose an industrial application of carbon dioxide methanation process.

Chapter IV

Experimental

Table of contents

4.1. CATALYST PREPARATION	59
4.1.1. CATALYSTS FOR FIXED BED REACTORS	59
4.1.2. CATALYSTS FOR PHOTOCATALYTIC REACTORS	61
4.2. CATALYST CHARACTERISATION	65
4.2.1. NH ₃ -TPD	65
4.2.2. CO ₂ -TPD.....	66
4.2.3. CO CHEMISORPTION	66
4.2.4. H ₂ -TPR	66
4.2.5. ICP-OES	67
4.2.6. N ₂ ADSORPTION-DESORPTION ISOTHERMS	67
4.2.7. TEM	67
4.2.8. UV-Vis.....	68
4.2.9. XRD	68
4.2.10. XPS	69
4.3. ACTIVITY TESTS	69
4.3.1. FIXED BED REACTORS	69
4.3.2. PHOTOCATALYTIC REACTORS	71

To ensure a better understanding of this thesis, without an unneeded repetition during the next chapters, all the experimental procedures carried out along the present PhD thesis are described in detail in this chapter. Furthermore, all the technical information is located in this chapter making it easier for the reader to find it. In the following chapters references are made to the corresponding sections of this *Chapter IV*.

4.1. Catalyst preparation

Three different catalyst preparation techniques were employed, corresponding to the final use of the catalysts in fixed bed reactors, microreactors or photocatalytic reactors.

4.1.1. Catalysts for fixed bed reactors

Catalysts prepared for being tested in fixed bed reactors were prepared by incipient wetness impregnation (IWI) method. The typical procedure carried out for catalysts preparation is detailed below.

The support, previously calcined at 673 K using a ramp of 5 K/min and maintaining the temperature during 4 hours except for two supports, calcined at 573 K and 773, with the same ramp and also during 4 hours, and metallic precursor were mixed in a calculated ratio in order to achieve the desired composition for each catalyst. The amount of water needed was determined taking into account the mass of support and the pore volume of the support, adding three times the amount of deionized water to completely fill all the pores of the support.

The pH of the mixture was adjusted according to the calculations made by Marek Kosmulski [82]. A homogeneous mixture of both compounds was obtained after mixing overnight the suspension containing the support and the metallic precursor. A rotary evaporator (model Heidolph Laborota 4000), equipped with a vacuum pump for reducing the boiling temperature of the solution, was employed to remove the excess of solvent in the prepared mixture. This evaporation was carried out at 338 K and 40-100 mbar.

Chapter IV

After the evaporation, the obtained solid was dried in an oven at 373 K during 1 hour, as to ensure a complete drying. Once dried, the catalysts were calcined in air atmosphere at 673 K, using a ramp of 5 K/min and then maintaining the temperature during 4 hours (except for some catalysts that were calcined at 573 K and 773 K using the same ramp and during the same time). Catalyst particles were later pressed and sieved to a particle size of $0.42 \text{ mm} < dp < 0.50 \text{ mm}$ in order to avoid bypassing near the wall of the reactor, as it was explained in a previous work [83].

Henceforth, the catalysts prepared by IWI are denoted as $13\text{Ni-}y\text{M}/\text{Support}$ where y denotes the theoretical amount in weight percent (wt %) of other metals (if applicable) and *Support* one of the supports employed.

The supports used for preparing the catalysts to be tested in fixed bed reactors are listed below:

- Al_2O_3 (γ) (Merck, ≥ 99.99 %)
- ASA (Sigma-Aldrich)
- Zeolite H-ZSM-5 (Zeolyst)
- SiO_2 (Sigma-Aldrich, 99.8 %)
- Zeolite H-Beta (Zeolyst)
- SBA-15 (Sigma-Aldrich, 99 %)
- FlyAsh- Al_2O_3 (γ) (1:1)
- Sepiolite (Sepiolsa)
- Stevensite
- Attapulgit (Sepiolsa)
- FeSiMg (Ilarduya)
- Lava Etna
- Waelz (Befesa)
- WDL (Waelz double leached) (Befesa)
- Paval (Befesa)
- PFS (fine and dried Paval) (Befesa)

The metallic precursors employed for preparing the catalyst to be tested in the fixed bed reactors are listed below:

- Nickel (III) nitrate hexahydrate (Sigma-Aldrich, 99.999 %)
- Zirconium (IV) oxynitrate hydrate (Sigma-Aldrich, 99.99 %)
- Chromium (III) nitrate nonahydrate (Sigma-Aldrich, ≥ 99.98 %)

Finally, the prepared catalysts using different combinations of supports and metallic precursors presented above, are listed below:

- 13Ni/Al₂O₃ (γ) (573 K)
- 13Ni/Al₂O₃ (γ) (673 K)
- 13Ni/Al₂O₃ (γ) (773 K)
- 13Ni/ASA
- 13Ni/H-ZSM-5
- 13Ni/SiO₂
- 13Ni/H-Beta
- 13Ni/SBA-15
- 13Ni/3Cr-4Zr-Al₂O₃ (γ)
- 13Ni/FlyAsh-Al₂O₃ (γ)
- 13Ni/Sepiolite
- 13Ni/Stevensite
- 13Ni/Attapulgite
- 13Ni/FeSiMg
- 13Ni/Lava Etna
- 13Ni/Waelz
- 13Ni/WDL
- 13Ni/Paval
- 13Ni/PFS

It is important to remind two key features of catalysts preparation:

1. All the catalytic systems were calcined at 673 K, unless a different temperature is stated among brackets. Catalysts calcined at different temperatures were part of a batch employed to determine the most suitable calcination temperature, which was determined as 673 K.
2. The metal loading appointed in the naming of the catalysts is a reference to the theoretical metal loading. Real metal loading was calculated by ICP-OES and will be depicted in future chapters.

4.1.2. Catalysts for photocatalytic reactors

In the case of the catalysts that were prepared for being tested in photocatalysis, not only the incorporation of the metal was carried out but also the supports were prepared in the laboratory.

The supports were prepared by flame spray pyrolysis (FSP) method. This method consists in the combustion of an appropriate organometallic precursor mixed with an organic solvent, in order to obtain a high energy of combustion, to create nanoparticles

of the desired material. FSP facilitates a self-sustaining flame, with proven scalability and the ability to tune the properties of the synthesised materials [84]. The supports were prepared using an experimental setup described extensively elsewhere [85] with a precursor feed rate of 5 mL/min. The SiO₂ support was prepared using this method, with a concentration of precursor of 1.0 M hexamethyl disiloxane (Sigma-Aldrich, ≥ 98.5 %) in xylenes (Sigma-Aldrich, reagent grade).

Metals were incorporated to the FSP prepared supports using deposition-precipitation or impregnation methods, depending on the metals employed. These catalysts were prepared with nickel (as active metal) and/or different noble metals like gold due to its proven plasmonic properties [32,70,78,79,86] or silver, due to its promising behaviour under light illumination [69,71]. The use of silver constitutes an interesting challenge due to the fact as, to our knowledge, it has not been widely studied due to different drawbacks as its easy oxidation. For the catalysts containing gold, deposition-precipitation was employed instead of the IWI method employed for preparing the catalysts tested in fixed bed reactors, as the impregnation of supported gold catalysts is difficult when small nanoparticles with a narrow size distribution are required [87]. The typical procedure carried out for catalysts preparation by deposition-precipitation method is detailed below:

A solution containing the support, an appropriate amount of the metallic precursor and 250 mL of deionized water was prepared. The pH of this solution was measured and if needed adjusted to 2.5. The solution containing the support and the metallic precursor was mixed with a solution containing approximately 0.5 g of urea and 5 mL of deionized water. This mixture was stirred at 1,200 RPM during 24 hours. After this time, the mixture was cooled down and centrifuged at 10,000 RPM during 15 min, obtaining a precipitated solid. This solid was washed with deionized water, and centrifuged again, repeating the centrifuge-washing procedure three times.

The obtained solid was introduced in an oven at 373 K during 17 hours to ensure its complete drying. After this, the catalyst was calcined in air atmosphere during 4 hours at 723 K with a heating ramp of 5 K/min.

The catalysts containing silver were prepared by the impregnation method described previously, although some modifications were made: the amount of water added was not dependent on the pore volume of the support, due to the fact that FSP prepared supports are non-porous material, but calculations were made to ensure a concentration of the metals in the solution of 1.0 M. For this catalysts pH was not adjusted during the preparation step. For the catalysts containing also nickel, impregnation method was also the employed one, but two different approaches can be distinguished: sequential impregnation and coimpregnation. In the case of the sequential impregnation first silver was added to the support by IWI and, after calcination, nickel was added by the same method followed by another calcination step. The coimpregnation method was analogue to the IWI method employed, however the prepared solution contained the two metals, namely, nickel and silver. In both cases, the solution was mixed during 3 hours and then dried in an oven at 373 K during 17 hours. After the drying step, the catalyst was calcined in air atmosphere during 4 hours at 723 K with a heating ramp of 5 K/min.

All the catalysts to be tested in photocatalytic reactors were manually milled after the calcination step.

The photocatalysts containing gold or used as a reference to analyse the influence of adding gold to the catalyst are listed below:

- 5Ni/SiO₂ (gold)
- 5Au/SiO₂
- 5Ni-5Au/SiO₂

The photocatalysts containing silver or used as a reference to analyse the influence of the addition of silver to the catalyst are listed below:

- 5Ni/SiO₂ (silver)
- 1Ag/SiO₂
- 5Ni-1Ag/SiO₂ coimpregnation (CI)

Chapter IV

- 5Ni-1Ag/SiO₂ sequential impregnation (SI)
- 1Ag-5Ni/SiO₂ SI

As it was stated for the catalysts prepared to be tested in fixed bed reactors, the metal loading in the naming of the catalysts is a reference to the theoretical metal amount (wt %) and not the real composition to be determined by a characterisation techniques.

In the case of the catalysts prepared by SI, the first metal in the naming is the one impregnated in the second step.

4.2. Catalyst characterisation

Different characterisation techniques were employed to gain information about the physicochemical properties of the catalysts, including: ammonia temperature programmed desorption (NH₃-TPD), carbon dioxide temperature programmed desorption (CO₂-TPD) carbon monoxide chemisorption (CO chemisorption), hydrogen temperature programmed reduction (H₂-TPR), inductively coupled plasma-optical emission spectroscopy (ICP-OES), nitrogen adsorption-desorption isotherms, transmission electronic microscopy (TEM), ultraviolet-visible spectroscopy (UV-Vis), X-ray diffraction (XRD) and X-ray photoelectron spectroscopy (XPS).

4.2.1. NH₃-TPD

NH₃-TPD technique was employed to determine the acidity of the fresh reduced catalysts. Measurements were performed in a Micromeritics Autochem 2920 II instrument. Prior to the analysis, samples were heated from room temperature up to 673 K with a heating ramp of 10 K/min and were reduced at 673 K during 4 hours under hydrogen atmosphere (equal to the reduction conditions carried out before the activity tests). After the reduction, samples were cooled down to 373 K and saturated with 10 % NH₃/He during 30 minutes. In order to remove the physically adsorbed NH₃, samples were heated up to 423 K while being flushed with He. Finally, samples were heated up to 723 K with a heating ramp of 10 K/min and the release of NH₃ was monitored by the TCD.

4.2.2. CO₂-TPD

CO₂-TPD technique was employed to determine the basicity of the fresh reduced photocatalysts. Measurements were performed in a Micromeritics Autochem 2920 II. Prior to the analysis, samples were heated from room temperature up to 723 K with a heating ramp of 5 K/min and were reduced at 723 K during 4 hours under hydrogen atmosphere (equal to the reduction conditions carried out before the activity tests). After the reduction, samples were cooled down to 323 K and saturated with 50 % CO₂/He during 30 minutes. In order to remove the physically adsorbed CO₂, samples were flushed with He. Finally, samples were heated up to 1173 K with a heating ramp of 10 K/min and the release of CO₂ was monitored by the TCD.

4.2.3. CO chemisorption

CO chemisorption technique was employed to determine the metallic dispersion of the fresh reduced catalysts. Measurements were performed in a Micromeritics Autochem 2920 II instrument. Prior to the analysis, samples were heated from room temperature up to 673 K with a heating ramp of 10 K/min and were reduced at 673 K during 4 hours under hydrogen atmosphere (equal to the reduction conditions carried out before the activity tests). Then, samples were cooled down to 308 K under helium atmosphere to remove impurities from the catalysts. After that, chemisorption measurements were performed using carbon monoxide as the probe molecule. CO chemisorption uptakes were measured by pulses of pure CO, the CO/nickel adsorption stoichiometry employed for the estimation of the metallic dispersion was 1.

4.2.4. H₂-TPR

Temperature programmed reduction technique was employed to determine the reducibility of the surface species of the calcined catalysts. Measurements were performed in a Micromeritics Autochem 2920 II instrument. Prior to the analysis, samples were heated under helium atmosphere from room temperature up to 523 K with a heating ramp of 10 K/min and maintaining the temperature 2 hours. This

procedure was carried out so as to remove water and other impurities from the surface of the catalysts. Hydrogen was selected as the reducing agent, thus, samples were heated under 5 % hydrogen in argon atmosphere from room temperature up to 1273 K with a heating ramp of 10 K/min. A thermal conductivity detector (TCD) downstream of the sample recorded the changes in the concentration of H₂.

4.2.5. ICP-OES

ICP-OES technique was employed to determine the chemical composition of the calcined catalysts. Measurements were performed in a Perkin-Elmer Optima 2000 instrument. Prior to the analysis, samples were disaggregated in an acid mixture (2 mL of HCl, 3 mL of HF and 3 mL of HNO₃). The solution containing the solid and the acid mixture was introduced in a microwave oven and heated from room temperature up to 453 K with a heating ramp of 7 K/min and maintaining the temperature 30 min. After this process the samples were totally decomposed, being the result a liquid that was diluted to 100 mL using deionized water. This solution was introduced in the instrument and as a result chemical composition was retrieved.

4.2.6. N₂ adsorption-desorption isotherms

N₂ adsorption-desorption isotherms technique was employed to determine the textural properties of the calcined catalysts (surface area, pore volume and average pore diameter). Measurements were performed in a Quantachrome Autosorb 1C-TCD instrument. Prior to the analysis, samples were degassed at 573 K during 3 hours. N₂ adsorption-desorption isotherms were measured at 77 K.

Surface area was calculated using the Brunauer, Emmett and Teller (BET) method while the average pore diameter was calculated with the Barrett, Joyner and Halenda (BJH) method applied to the desorption branch of the isotherms.

4.2.7. TEM

TEM technique was employed to determine the morphology of the fresh reduced catalyst and both the morphology and the presence of coke in the used catalysts.

Measurements were performed in a Philips SuperTwin CM200 instrument, operated at 200 kV and equipped with a LaB6 filament and EDAX EDS microanalysis sample. Prior to the analysis, fresh samples were heated from room temperature up to 673 K with a heating ramp of 10 K/min and were reduced at 673 K during 4 hours under hydrogen atmosphere (equal to the reduction conditions carried out before the activity tests) while used samples did not need any pre-treatment. All the samples were dispersed using ethanol as solvent and placed on a carbon-coated copper grid (300 mesh), then dried under vacuum.

4.2.8. UV-Vis

UV-Vis technique was employed to determine the plasmonic properties of the catalysts. Samples were measured in Shimadzu UV-Vis-NIR spectrophotometer in reflectance measuring mode, using BaSO₄ as reference material. The UV-Vis spectra was collected in a range of wavelength of 800-200 nm, with a sampling interval of 1 nm and in the slow mode. The slit width employed for the measurements was 2 nm. As the measurements were carried out in reflectance measuring mode, Kubelka-Munk transformation was performed to obtain the absorbance of the different samples [88].

4.2.9. XRD

XRD technique was employed to determine the crystalline species of the fresh reduced catalysts and their average crystal size. This technique can measure at about 1-2 μm depth of the sample. Measurements were performed in a PANalytical X'Pert Pro instrument. Prior to the analysis, samples were heated from room temperature up to 673 K with a heating ramp of 10 K/min and were reduced at 673 K during 4 hours under hydrogen atmosphere (equal to the reduction conditions carried out before the activity tests).

Average crystal size was calculated using Scherrer equation.

4.2.10. XPS

XPS technique was employed to determine the elemental composition at the surface of the fresh reduced and used catalysts. This technique can measure at about 10-20 nm depth of the sample so it can be considered, compared with XRD, a surface analysis. Measurements were performed in a SPECS instrument equipped with a Phoibos 150 1D-DLD analyser and an Al K α (1486.6 eV) monochromatic radiation source with electrons output angle of 90°. Prior to the analysis, fresh samples were heated from room temperature up to 673 K with a heating ramp of 10 K/min and were reduced at 673 K during 4 hours under hydrogen atmosphere (equal to the reduction conditions carried out before the activity tests) while used samples did not need any pre-treatment.

4.3. Activity tests

As with the catalysts synthesis techniques, we can also distinguish three different experimental setups.

4.3.1. Fixed bed reactors

Activity tests were performed in a bench-scale plant (PID Eng&Tech), using a stainless steel fixed bed reactor. The reactor (0.4 cm i.d. and 30 cm length) was electrically heated

in a furnace. A scheme of the bench-scale plant is shown in Figure 4.1.

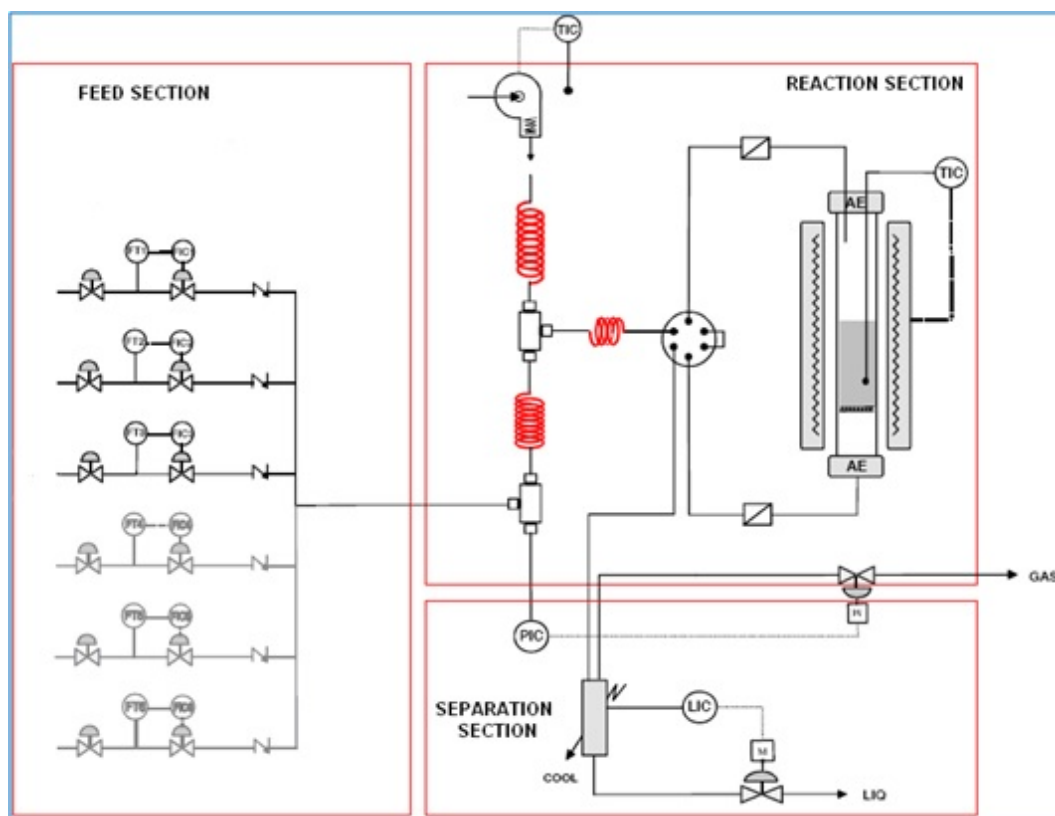


Figure 4.9. Scheme of the bench-scale plant

The catalysts were reduced in situ before the activity tests, at the same temperature used at the calcination step, during 4 hours using a mixture of N_2 and H_2 in a 3:1 ratio. During the reaction step H_2 and CO_2 were fed in a 4:1 ratio (with a total flow of 220 mL/min) with a weight hourly space velocity $33.5 \text{ g}_{\text{feed}}/(\text{g}_{\text{cat}} \text{ h})$.

Three different activity tests were performed:

1. Selection of the most suitable synthesis and operating conditions:
 - a. Temperature: a nickel/alumina (γ) catalyst calcined at three different temperatures was employed as a reference to determine the most suitable calcination temperature.
 - b. Pressure: once the most suitable calcination temperature was selected, that catalyst was tested at 1 bar, 10 bar and 15 bar to determine the most suitable operating pressure.

2. Regular activity tests: the activity of the prepared catalysts was tested at 10 bar pressure and at different temperatures between 523-773 K. Each temperature was maintained during 90 minutes. After this time, temperature was increased in 50 K.
3. Stability activity tests: the best catalysts from the regular activity tests were tested at 10 bar pressure and at 523 K during 25 hours and 120 hours in order to analyse the deactivation of the catalysts.

In all the cases, the catalyst was introduced in the reactor and diluted with inert SiC, in order to minimise thermal gradients in the catalytic bed ($\text{weight}_{\text{catalyst}}/\text{weight}_{\text{SiC}} = 1:4.5$). Condensed water and gas products were separated. The gas phase was on-line analysed using a Varian CP-4900 MicroGC equipped with a high sensitivity TCD and two columns (10 m Molecular Sieve 5, 10 m Poraplot Q). Produced water was collected, weighed and measured.

For a better understanding of the process behaviour, different parameters were calculated, which are defined below:

$$CO_2 \text{ conversion } (\%): X_{CO_2} = \frac{(\text{mol}_{CO_2}^{in} - \text{mol}_{CO_2}^{out})}{\text{mol}_{CO_2}^{in}} \times 100 \quad \text{Eq. 4.1}$$

$$H_2 \text{ conversion } (\%): X_{H_2} = \frac{(\text{mol}_{H_2}^{in} - \text{mol}_{H_2}^{out})}{\text{mol}_{H_2}^{in}} \times 100 \quad \text{Eq. 4.2}$$

$$CH_4 \text{ yield } (\%): \eta_{CH_4} = \frac{(\text{mol}_{CH_4}^{in} - \text{mol}_{CH_4}^{out})}{\text{mol}_{CH_4}^{out} \text{ stoichiometric}} \times 100 \quad \text{Eq. 4.3}$$

$$CH_4 \text{ selectivity } (\%): S_{CH_4} = \frac{\text{mol}_{CH_4}^{out}}{\text{mol}_C^{out}} \times 100 \quad \text{Eq. 4.4}$$

4.3.2. Photocatalytic reactors

Photocatalysis activity tests were carried out in a Raman high temperature reaction chamber consisting of three inlet/outlet ports for evacuating the cell and introducing

Chapter IV

gases, an 8 mm open aperture and removable 13 x 2 mm SiO₂ window to allow for laser light illumination. This reaction chamber was mounted on an optical breadboard and positioned below a laser diode mounted within an optical enclosure. A temperature bath supplied cooling water at 288 K through the reaction chamber at a flow rate of 5 L/min when in operation.

The catalysts containing gold were prereduced ex situ at 973 K during 1 hour and then passivated, to avoid further oxidation when contacting with the ambient, with O₂ highly diluted in He during 17 hours.

All the catalysts were reduced in situ during 3 hours at 673 K, using a mixture of N₂ and H₂ in a 1:1 ratio. During the reaction step H₂ and CO₂ were fed in a 4:1 ratio with a weigh hourly space $17.1 \text{ g}_{\text{feed}}/(\text{g}_{\text{cat}} \text{ h})$.

Different laser diodes were employed, being the one irradiating at 520 nm the main one for the gold catalysts and the one at 405 nm the main one for the silver catalysts. A laser diode of 660 nm was also employed to analyse the influence of different wavelengths. Both the reaction chamber and the laser diode were placed inside a black box, ensuring that laser light was not irradiated outside the box, which could be dangerous due to the intensity of the laser.

A scheme of the reaction chamber and the laser illumination system are presented in Figure 4.2.

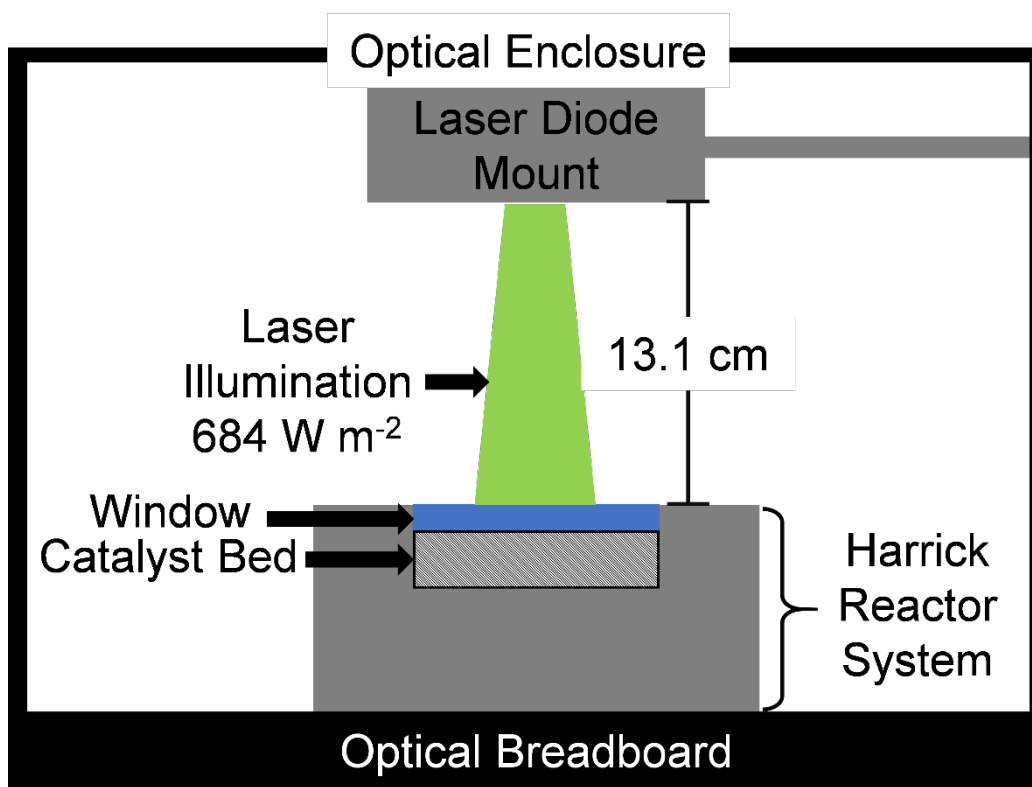


Figure 4.10. Reaction chamber and laser illumination system

Gas composition was determined using a Shimadzu 2010 Gas Chromatograph unit (30 m column), in which the FID was used to detect CO, CH₄ and CO₂ and the TCD was used to detect H₂ and N₂. A cold trap was placed upstream the GC in order to avoid injecting water into the GC which could damage the detectors.

A scheme of all the setup for the activity tests with photocatalysts can be observed in Figure 4.3, including all the mass-flow controllers for gas feeding and the gas composition analysis system.

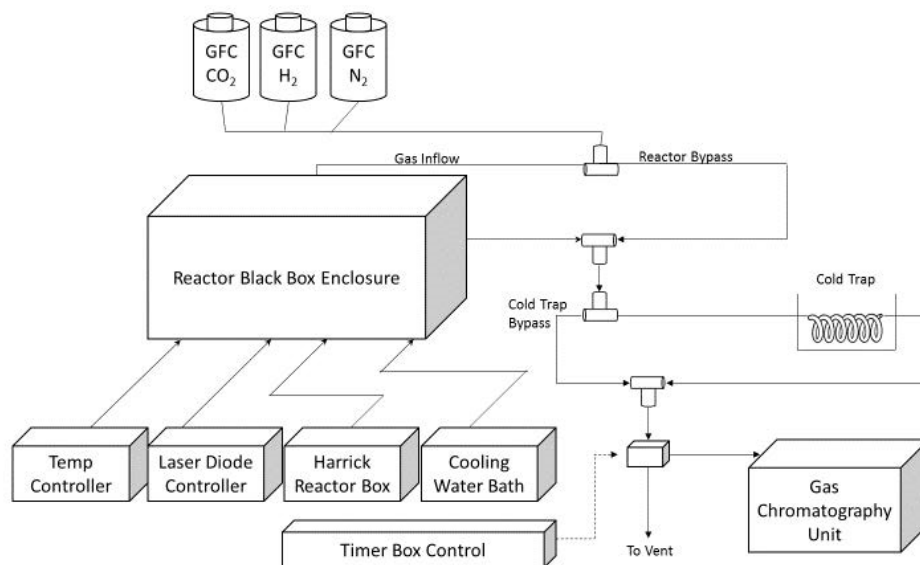


Figure 4.11. Scheme of the photoreactor system

Chapter V

Results

Table of contents

5.1. ANALYSIS OF THE MOST SUITABLE OPERATING CONDITIONS	81
5.1.1. EFFECT OF THE CALCINATION TEMPERATURE.....	81
5.1.1.1. <i>Chemical composition of the prepared catalysts.....</i>	<i>81</i>
5.1.1.2. <i>Reducibility of the catalysts calcined at different temperatures</i>	<i>82</i>
5.1.1.3. <i>XRD results of the catalysts calcined at different temperatures</i>	<i>83</i>
5.1.1.4. <i>Metallic dispersion of the catalysts calcined at different</i> <i>temperatures.....</i>	<i>85</i>
5.1.1.5. <i>TEM of the catalysts calcined at different temperatures.....</i>	<i>85</i>
5.1.1.6. <i>XPS of the catalysts calcined at different temperatures</i>	<i>87</i>
5.1.1.7. <i>Activity tests of the catalysts calcined at different</i> <i>temperatures.....</i>	<i>89</i>
5.1.1.8. <i>TEM of the spent catalysts calcined at different temperatures</i>	<i>90</i>
5.1.1.9. <i>XPS of the spent catalysts calcined at different temperatures</i>	<i>92</i>
5.1.1.10. <i>Discussion of the effect of the calcination temperature</i>	<i>93</i>
5.1.2. OPERATING PRESSURE	96
5.2. EFFECT OF THE CATALYTIC SUPPORT.....	97
5.2.1. ACIDIC SUPPORTS	97
5.2.1.1. <i>Chemical composition of the catalysts over acidic supports..</i>	<i>98</i>
5.2.1.2. <i>Structural properties of the catalysts over acidic supports....</i>	<i>99</i>
5.2.1.3. <i>Reducibility of the catalysts over acidic supports</i>	<i>100</i>

5.2.1.4. XRD results of the catalysts over acidic supports.....	104
5.2.1.5. Metallic dispersion of the catalysts over acidic supports.....	106
5.2.1.6. Acidity of the catalysts over acidic supports.....	107
5.2.1.7. TEM of the catalysts over acidic supports	109
5.2.1.8. XPS of the catalysts over acidic supports.....	112
5.2.1.9. Activity tests of the catalysts over acidic supports	114
5.2.1.10. TEM of the spent catalysts over acidic supports.....	115
5.2.1.11. XPS of the spent catalysts over acidic supports	117
5.2.1.12. Discussion of the catalysts over acidic supports	118
5.2.2. INDUSTRIAL RESIDUES AS SUPPORTS	122
5.2.2.1. Chemical composition of the catalysts over industrial residues as supports	122
5.2.2.2. Structural properties of the catalysts over industrial residues as supports	123
5.2.2.3. TPR of the catalysts over industrial residues as supports	124
5.2.2.4. XRD of the catalysts over industrial residues as supports....	127
5.2.2.5. Metallic dispersion of the catalysts over industrial residues as supports.....	129
5.2.2.6. Acidity of the catalysts over industrial residues as supports	129
5.2.2.7. TEM of the catalysts over industrial residues as supports ...	131
5.2.2.8. XPS of the catalysts over industrial residues as supports.....	133
5.2.2.9. Activity tests of the catalysts over industrial residues as supports.....	135
5.2.2.10. TEM of the spent catalysts over industrial residues as supports.....	136
5.2.2.11. XPS of the spent catalysts over industrial residues as supports	138

5.2.2.12. Discussion of the catalysts over industrial residues as supports.....	139
5.2.3. NATURAL SUPPORTS.....	142
5.2.3.1. Chemical composition of the catalysts over natural supports	142
5.2.3.2. Structural properties of the catalysts over natural supports	143
5.2.3.3. TPR of the catalysts over natural supports	144
5.2.3.4. XRD of the catalysts over natural supports	146
5.2.3.5. Metallic dispersion of the catalysts over natural supports ..	148
5.2.3.6. Acidity of the catalysts over natural supports	148
5.2.3.7. TEM of the catalysts over natural supports.....	150
5.2.3.8. XPS of the catalysts over natural supports	152
5.2.3.9. Activity tests of the catalysts over natural supports.....	153
5.2.3.10. TEM of the spent catalysts over natural supports	155
5.2.3.11. XPS of the spent catalysts over natural supports.....	156
5.2.3.12. Discussion of the catalysts over natural supports.....	157
5.3. STABILITY TESTS.....	160
5.4. CATALYSTS FOR PHOTOREACTORS.....	163
5.4.1. GOLD BASED PHOTOCATALYSTS	163
5.4.1.1. Chemical composition of the gold based photocatalysts.....	164
5.4.1.2. Structural properties of the gold based photocatalysts.....	164
5.4.1.3. TPR of the gold based photocatalysts	165
5.4.1.4. XRD of the gold based photocatalysts.....	167
5.4.1.5. CO ₂ -TPD of the gold based photocatalysts	168
5.4.1.6. TEM of the gold based photocatalysts	169
5.4.1.7. XPS of the gold based photocatalysts.....	170

5.4.1.8. UV-Vis of the gold based photocatalysts.....	175
5.4.1.9. Activity tests of the gold based photocatalysts	176
5.4.2. SILVER BASED PHOTOCATALYSTS	181
5.4.2.1. Chemical composition of the silver based photocatalysts ...	182
5.4.2.2. Structural properties of the silver based photocatalysts.....	182
5.4.2.3. TPR of the silver based photocatalysts	183
5.4.2.4. XRD of the silver based photocatalysts	186
5.4.2.5. CO ₂ -TPD of the silver based photocatalysts.....	187
5.4.2.6. TEM of the silver based photocatalysts.....	188
5.4.2.7. XPS of the silver based photocatalysts	191
5.4.2.8. UV-Vis of the silver based photocatalysts.....	196
5.4.2.9. Activity tests with silver based photocatalysts	197

In **Chapter III** of this current PhD thesis, different partial goals that should be fulfilled in order to attain the objective of the thesis were listed. As the experimental methodology was clearly described in **Chapter IV** of this PhD thesis, only the results will be presented in this chapter, specifically the results corresponding to the first two partial goals: analysis of the most suitable operating conditions and the activity tests carried out in fixed bed reactors and photocatalytic reactors.

5.1. Analysis of the most suitable operating conditions

Two different operating conditions were analysed to determine which the most suitable values were for both of them. These studied operating conditions were calcination temperature of the catalysts and operating pressure. These analyses were carried out in a fixed bed reactor.

5.1.1. Effect of the calcination temperature

A series of 13Ni/Al₂O₃ catalysts were prepared using the method described in **Chapter IV** of this PhD thesis and calcined at three different temperatures: 573 K, 673 K and 773 K. These catalysts were characterised by different techniques as to gain information about their chemical and structural properties.

5.1.1.1. Chemical composition of the prepared catalysts

According to the chemical composition determined by ICP-OES, all the catalysts presented an amount of nickel close to the desired one (13 wt %). This composition is presented in Table 5.1.

Table 5.2. ICP-OES of the prepared catalysts

Catalyst	Ni (wt %)
13Ni/Al ₂ O ₃ (γ) Calc: 573 K	9.7

$^{13}\text{Ni}/\text{Al}_2\text{O}_3$ (γ) Calc: 673 K 9.9

$^{13}\text{Ni}/\text{Al}_2\text{O}_3$ (γ) Calc: 773 K 10.8

5.1.1.2. Reducibility of the catalysts calcined at different temperatures

The reduction properties were determined by TPR measurements. The obtained TPR profiles are shown in Figure 5.1.

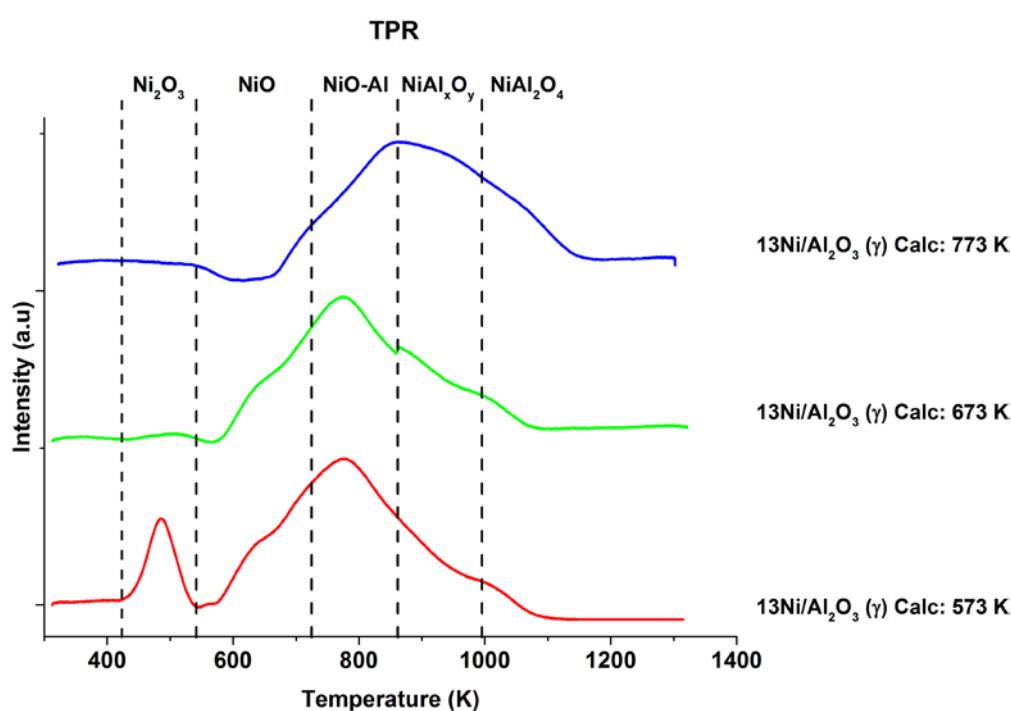


Figure 5.12. TPR profiles of the catalysts calcined at different temperatures

The catalyst calcined at the lowest temperature, 573 K, was the only one that presented a reduction peak at approximately 500 K. This peak can be attributed to Ni_2O_3 particles deposited onto the catalyst surface [89]. In addition, all the catalysts presented four reduction peaks that can be attributed in order of increasing temperature to: i) free nickel oxide, without interaction with the support, ii) nickel oxide, NiO-Al, with weak interaction with the support, iii) non-stoichiometric nickel aluminate specie, NiAl_xO_y with strong interaction with the support and iv) the most stable specie, stoichiometric

nickel aluminate (NiAl_2O_4) [90]. These four peaks combine their contributions to form a final peak, being the result of all of them, which is the one that can be seen in the final temperature programmed reduction profile. In order to analyse the contribution of each peak to the final profile peak deconvolution was carried out and results are shown in Table 5.2.

Table 5.3. TPR peak deconvolution of the catalysts calcined at different temperatures

Catalyst	Ni_2O_3	NiO	NiO-Al	NiAl_xO_y	NiAl_2O_4
13Ni/Al₂O₃ (γ) Calc: 573 K	485 K-11.0 %	636 K-5.8 %	764 K-62.7 %	905 K-17.1 %	1010 K-3.4 %
13Ni/Al₂O₃ (γ) - Calc: 673 K		646 K-7.3 %	770 K-67.8 %	896 K-13.0 %	983 K-11.9 %
13Ni/Al₂O₃ (γ) - Calc: 773 K		739 K-4.9 %	830 K-32.8 %	947 K-55.7 %	1067 K-6.6 %

As it can be seen, for the catalysts calcined at 573 K and 673 K nickel oxide with weak interaction with the support was the predominant nickel specie, while for the catalyst calcined at 773 K the most abundant nickel specie was the non-stoichiometric nickel aluminate. Also, for the catalyst calcined at 773 K, all the peaks were shifted towards higher temperatures as the result of a worse reducibility [34].

5.1.1.3. XRD results of the catalysts calcined at different temperatures

The main crystalline species present in the fresh-reduced catalysts were obtained by XRD. The catalysts were reduced at the same temperature employed for the calcination step. Results obtained are shown in Figure 5.2.

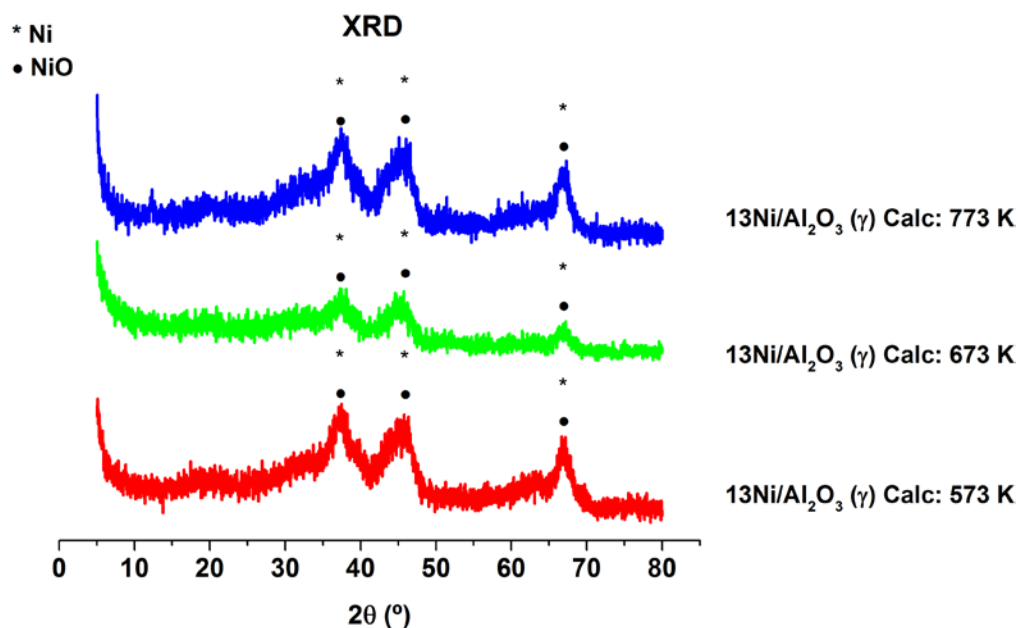


Figure 5.13. XRD profiles of the catalysts calcined at different temperatures

All the catalysts presented similar profiles with peaks located at the same angle. This is due to the fact that all the fresh-reduced catalysts contained alumina, which signal was detected in all the peaks, located at a value of 2θ of approximately 37°, 47° and 67° [90]. However, these peaks could also be related to different nickel species like NiO and metallic Ni, which signal is usually located at those angles and can overlap with the one corresponding to the alumina [91,92]. Due to the fact that the different species identified by XRD could not be properly distinguished, the average crystallite size was not calculated.

The results obtained by XRD are in accordance with those obtained by TPR. The presence of Ni₂O₃ in the catalyst calcined at 573 K made difficult the reduction of the other species as it consumed most of the hydrogen employed during the reduction step to NiO [93]. For the catalyst calcined at 773 K, the large amount of nickel aluminates was responsible for not being able to fully complete the reduction, as these nickel aluminates are highly stable species and difficult to be reduced [94–96].

5.1.1.4. Metallic dispersion of the catalysts calcined at different temperatures

Metallic dispersion was also measured by CO chemisorption technique over the fresh-reduced catalysts. The catalyst calcined at 573 K presented the highest metallic dispersion, probably due to the fact that a lowest calcination temperature resulted in minor structural changes in the support, thus, the metal could be incorporated in a structure with more pores and metal particles sintering is avoided in some extent. For the catalysts calcined at 673 K and 773 K. the first one presented the highest metallic dispersion. We can conclude that a higher calcination temperature results in a worse metallic dispersion for a given support. The results of CO chemisorption measurements are shown in Table 5.3.

Table 5.4. Metallic dispersion of the catalysts calcined at different temperatures

Catalyst	Metallic dispersion (%)
$^{13}\text{Ni}/\text{Al}_2\text{O}_3$ (γ) Calc: 573 K	1.1
$^{13}\text{Ni}/\text{Al}_2\text{O}_3$ (γ) Calc: 673 K	1.0
$^{13}\text{Ni}/\text{Al}_2\text{O}_3$ (γ) Calc: 773 K	0.8

These results can be supported with the data obtained by TPR. As it has been previously explained, the increase in the calcination temperature resulted in a shift of the reduction peak to higher temperatures as the result of a worse reducibility that can be attributed to a lower metallic dispersion [97] and less reducible metallic species.

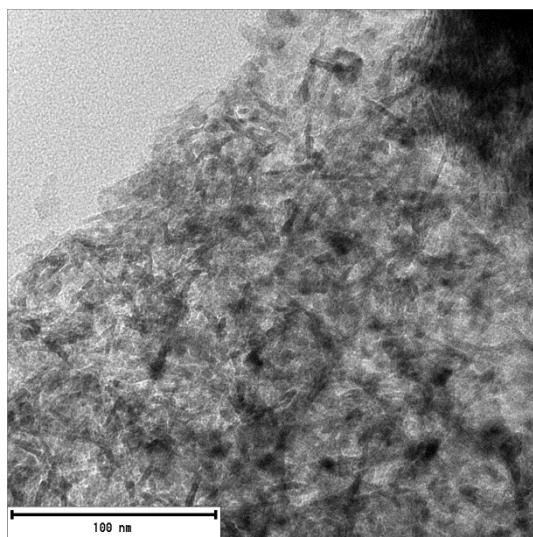
5.1.1.5. TEM of the catalysts calcined at different temperatures

TEM micrographs of the fresh-reduced catalysts were employed to observe the structure of the catalysts. These pictures can be observed in Figure 5.3. As it can be seen, for the catalyst calcined at 573 K it is difficult to distinguish the metal and the support,

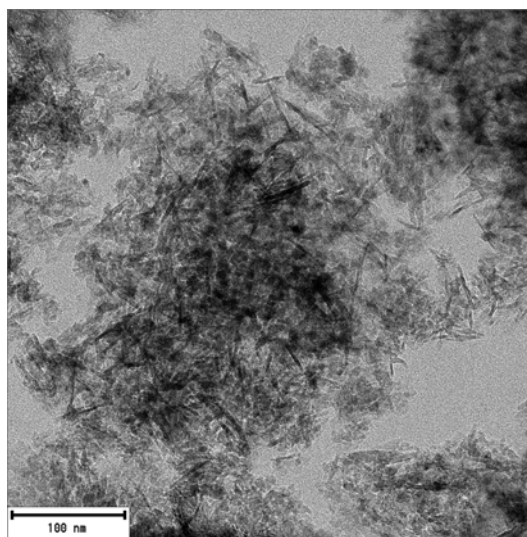
Chapter V

even though some big particles can be observed, the metal was well dispersed over the support. Increasing the calcination temperature up to 673 K resulted in a worse dispersion of the metallic particles, being easier to differentiate between metal and support. However, as it can be observed in the figure a homogeneous distribution of the particles was obtained. A further increase of the calcination temperature up to 773 K increased the sintering process of the metallic particles, as it can be seen in the picture different clusters formed by group of particles could be observed. However, it still presented a good metallic dispersion. Due to the low count of particles present in the picture a distribution of the particle size was not calculated by TEM. However, it was clearly appreciated that increasing the calcination temperature worsened the dispersion of the metal over the support, being easier to differentiate between metal and support.

a) 13Ni/Al₂O₃ (γ) Calc: 573 K



b) 13Ni/Al₂O₃ (γ) Calc: 673 K



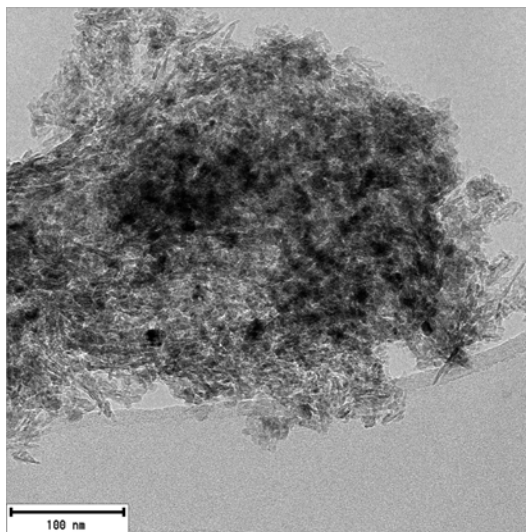
c) 13Ni/Al₂O₃ (γ) Calc: 773 K

Figure 5.14. TEM micrographs of the catalyst calcined at different temperatures

5.1.1.6. XPS of the catalysts calcined at different temperatures

The fresh-reduced catalysts were analysed by XPS in order to determine the species present on the surface of the catalyst. For all the catalysts, nickel was present in the surface as Ni²⁺ with four different contributions, main and satellite peak corresponding to two different core levels each: Ni2p_{3/2} and Ni2p_{1/2}. The fact that nickel was present as Ni²⁺ and not metallic nickel (Ni⁰) can be attributed to the exposure of the fresh-reduced samples to the atmosphere prior to the XPS analysis, resulting in a surface oxidation [98]. For the catalysts calcined at 573 K and 673 K the main peak corresponding to the Ni2p_{3/2} core level was measured at a binding energy of 853.0-855.0 eV while for the catalyst calcined at 773 K was measured at a binding energy higher than 855.0 eV. The peaks located at binding energies below 855.0 eV are usually attributed to nickel with none or weak interaction with the support, while the ones measured at higher binding energies are attributed to nickel with strong interaction with the support. The profiles obtained are presented in Figure 5.4.

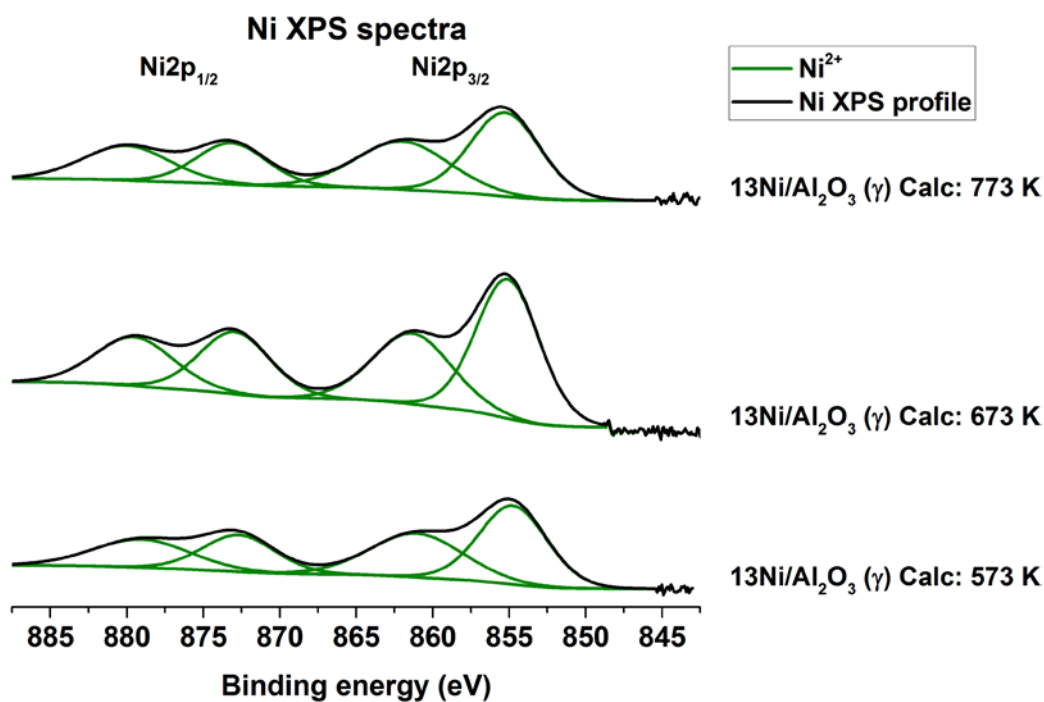


Figure 5.15. Ni XPS spectra of the catalysts calcined at different temperatures

For a better understanding of the results obtained by XPS, a summary of the measured binding energies is presented in Table 5.4.

Table 5.5. Binding energies (eV) XPS of the catalysts calcined at different temperatures

Catalyst	Ni ²⁺	Ni ²⁺	satellite	Ni ²⁺	Ni ²⁺	satellite
	(Ni2p _{3/2})	(Ni2p _{3/2})	(Ni2p _{3/2})	(Ni2p _{1/2})	(Ni2p _{1/2})	(Ni2p _{1/2})
13Ni/Al ₂ O ₃ (γ) Calc: 573 K	854.8	861.0		872.7	879.0	
13Ni/Al ₂ O ₃ (γ) Calc: 673 K	853.6	860.0		871.5	878.3	
13Ni/Al ₂ O ₃ (γ) Calc: 773 K	855.3	862.0		873.2	880.0	

Further information about the catalyst structure could be gained using the XPS technique to calculate the Ni/Al atomic ratio. These results are compared to the atomic ratios calculated by ICP-OES. The results obtained in for these catalysts are presented in Table 5.5.

Table 5.6. Ni/Al atomic ratio of the catalysts calcined at different temperatures

Catalyst	Ni/Al (at %) XPS	Ni/Al (at %) ICP-OES
13Ni/Al₂O₃ (γ) Calc: 573 K	0.07	0.10
13Ni/Al₂O₃ (γ) Calc: 673 K	0.07	0.10
13Ni/Al₂O₃ (γ) Calc: 773 K	0.11	0.11

For the catalysts calcined at the 573 K and 673 K, the value of the Ni/Al atomic ratio measured by XPS was approximately 30 % lower than the one obtained by ICP-OES. Being the bulk atomic ratio (obtained by ICP-OES) higher than the surface one (obtained by XPS) proved that most of the metal was located inside the pore structure of the support for these catalysts [99]. Increasing the calcination temperature of the catalyst resulted in increasing the Ni/Al atomic ratio calculated by XPS, thus, a larger amount of nickel was located on the outer surface of the support. For this catalyst, the Ni/Al atomic ratio obtained by XPS was equal to the one measured by ICP-OES, meaning that the nickel was homogeneously distributed on the support [100].

5.1.1.7. Activity tests of the catalysts calcined at different temperatures

The results obtained in the activity tests for these three catalysts can be seen in Figure 5.5. The results are compared with the values predicted by the thermodynamic equilibrium.

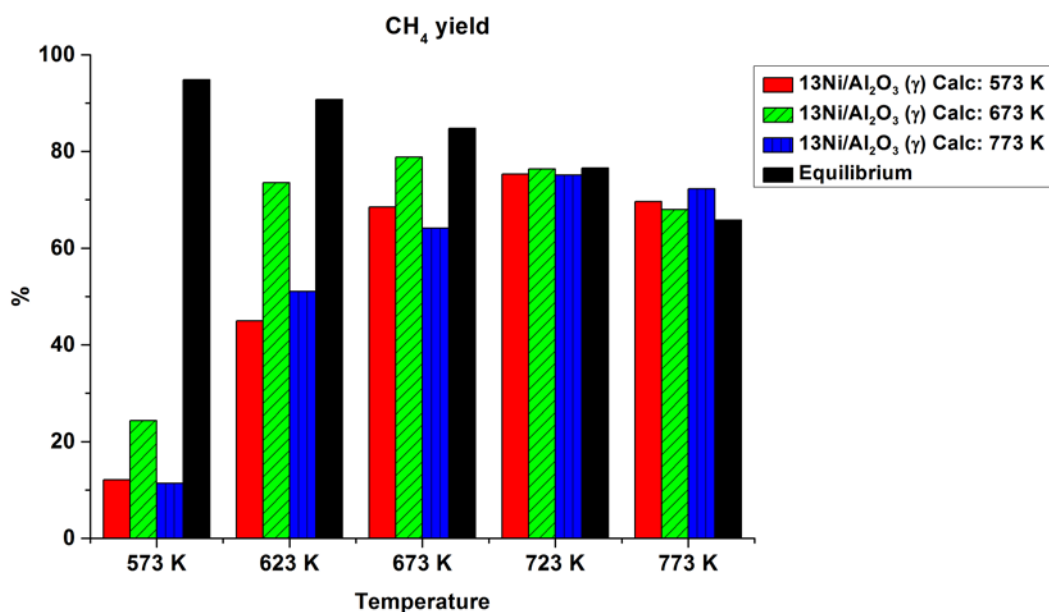


Figure 5.16. Activity results of the catalysts calcined at different temperatures

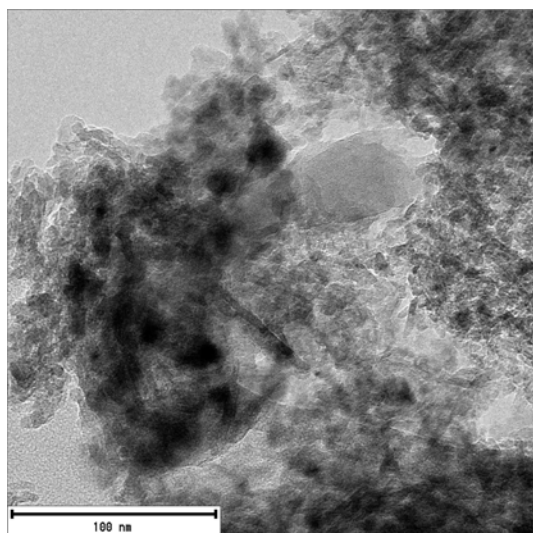
As it can be seen, at the lowest temperatures, all the catalysts presented very low value of methane yield, being the best of them the catalyst calcined at 673 K. When increasing the temperature at 623 K, all the catalysts increased their activity being the one calcined at 673 K the best one with a difference above 20 points in the methane yield. At 673 K, the catalyst calcined at the intermediate temperature was also the best catalysts among the ones tested. Above this temperature, all the catalysts were close to the thermodynamic equilibrium so it was not possible to establish comparisons among them. At the highest temperature tested the values of methane yield obtained were slightly higher to the ones predicted by the thermodynamic equilibrium, this can be justified with the experimental error as the difference between the values obtained and the thermodynamic fits inside the tolerable error. Moreover, the possible presence of temperature gradients in the reactor could result in these slight differences between the obtained results and the predicted thermodynamic equilibrium values.

5.1.1.8. TEM of the spent catalysts calcined at different temperatures

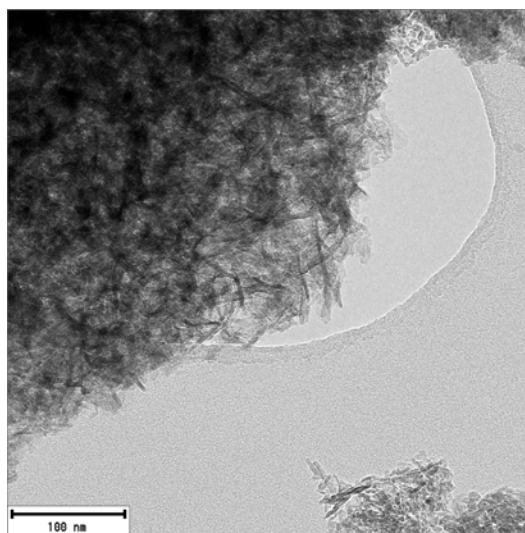
The catalysts calcined at different temperatures were analysed by TEM after carrying out the activity tests, in order to detect changes in the structure of the catalysts and also

the presence of coke. The results obtained can be observed in Figure 5.6. In the case of the catalyst calcined at 573 K, coke was not detected. However, when comparing with the fresh-reduced catalyst, a growth of the metallic particles could be observed. This can be due to the fact that the thermal stability of the catalysts can only be ensured at temperatures equal or below the calcination temperature, namely 573 K, and the activity tests were carried out at temperatures up to 773 K, thus a difference of 200 K could cause the sintering of the metallic particles. Same behaviour could be expected for the catalyst calcined at 673 K, however the difference of temperature between calcination and activity tests was not so high so the growth of the particles observed was not as significant. Also, for this catalyst, coke was not observed after the activity tests. Finally, when the catalyst was calcined at 773 K no clear differences in the structure of the catalysts after and before the activity tests were observed. As for the previous catalysts, coke was not detected for the catalyst calcined at 773 K after performing the activity tests.

a) 13Ni/Al₂O₃ (γ) Calc: 573 K spent



b) 13Ni/Al₂O₃ (γ) Calc: 673 K spent



c) 13Ni/Al₂O₃ (γ) Calc: 773 K spent

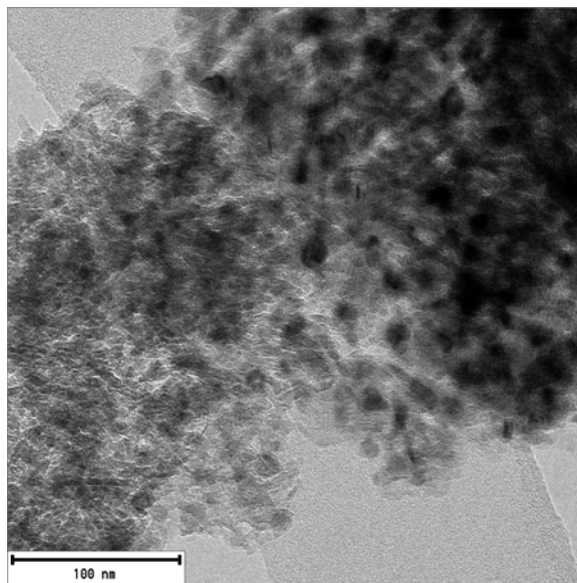


Figure 5.17. TEM micrographs of the spent catalysts calcined at different temperatures

5.1.1.9. XPS of the spent catalysts calcined at different temperatures

The spent γ -alumina catalysts were analysed by XPS. For the catalysts calcined at the lowest and the highest temperature, 573 K and 773 K, any contribution of carbon was detected. Graphitic carbon, located at a binding energy of 284.6 eV, was measured for the catalyst calcined at 673 K. The amount of this graphitic carbon, located at the surface of the catalyst, was approximately of 33 wt %. Results are presented in Figure 5.7.

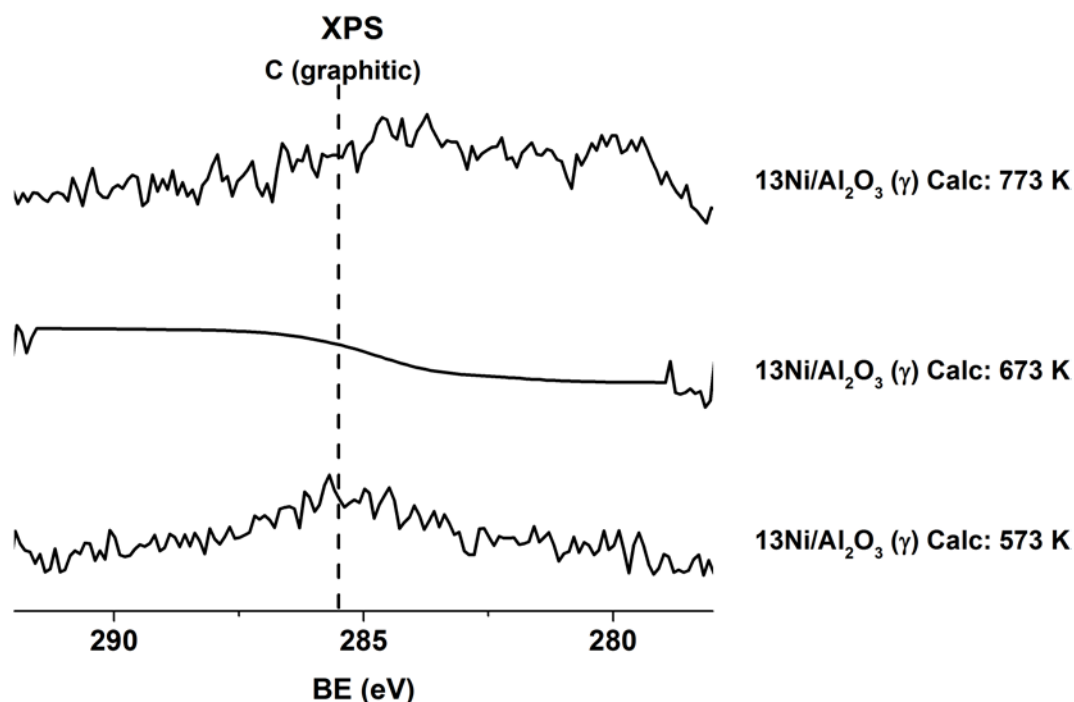


Figure 5.18. C XPS spectra of the spent catalysts calcined at different temperatures

Taking into account the results obtained by TEM, a growth in the particle size was observed for the catalyst calcined at the lowest temperature. For this catalyst, the low calcination temperature employed resulted in a lower resistance to the temperatures employed in the carbon dioxide methanation reaction. However, for the catalyst calcined at 673 K as this temperature was close to the highest temperature employed in the activity tests, not clear signs of sintering were observed. Finally for the catalyst calcined at the highest temperature, sintering was not observed by TEM. For all the catalysts TEM micrographs taken after the activity tests did not show the presence of coke.

5.1.1.10. Discussion of the effect of the calcination temperature

The different characterisation techniques let us establish a relationship between the physicochemical properties of the catalysts and their activity for carbon dioxide methanation reaction.

TPR results shed some light on the activity results. The distribution of the different reducible species present on the catalysts and their reduction temperature can be correlated to the catalytic activity. For the catalyst that presented the highest catalytic activity, the one calcined at 673 K, NiO weakly interacting with the support (NiO-Al) was the main reducible specie. This was also the main reducible specie for the catalyst calcined at 573 K, however in a lower amount than for the catalyst calcined at 673 K. Moreover, the catalyst calcined at 573 K also presented a remarkable amount of Ni₂O₃ without any interaction with the support. Finally, for the catalyst calcined at 773 K the presence of a large amount of nickel aluminates which are highly stable and difficult to be reduced species [94–96] is attributed as one of the causes of the lower activity of this catalyst. An incomplete reduction of the catalysts resulted in the absence of metallic nickel particles, thus, the absence of active sites for the carbon dioxide methanation reaction [48]. Results obtained by XRD proved the possible presence of both metallic nickel and NiO but due to the signals overlapping at the same angle it was not possible to further correlate this results with the ones obtained by TPR.

Regarding to the results obtained by CO chemisorption, even if metallic dispersion has proved to enhance catalytic activity [63] it is not the only important parameter and a combination of the physicochemical properties of the catalysts are the responsible for the catalytic activity.

The micrographs obtained by TEM proved the good dispersion achieved for all the catalysts, being larger for the catalyst calcined at the lowest temperature. Even though due to the low particle count available in the pictures it was not possible to calculate a particle size distribution, the structure observed on the pictures was clear enough to appreciate difference between the catalysts.

The surface results obtained by XPS proved that nickel oxide was the only nickel specie present, as it has been explained due to the oxidation of the samples in contact with the atmosphere prior to the analysis. In all the cases, but for the catalyst calcined at 773 K, the measured Ni/Al atomic ratio was lower than the one measured by ICP-OES, thus, for all these catalysts most of the metal was located inside the porous structure of the

support being this affirmation in agreement with the structure that was observed by TEM. Regarding to the Ni/Al atomic ratios measured by XPS, the catalysts calcined at 573 K and 673 K presented approximately the same value while the one calcined at the highest temperature, 773 K, presented a higher value indicating that this catalyst presented a larger amount of metal on the outer surface than the other catalysts, as it was previously concluded by TEM.

The catalysts were also characterised after performing the activity tests, in order to understand how the carbon dioxide methanation reaction could affect to the structure of the catalysts but also to determine if any deactivation mechanisms could decrease the activity of the catalysts.

Even if coke was not measured by TEM, XPS measurements proved the presence of coke for the catalyst calcined at 673 K. The amount of coke measured was quite high, approximately 33 %, being only graphitic coke the measured one. The difference between both techniques, TEM and XPS, can be attributed to the fact that the detected coke could be deposited surrounding the nickel particle, thus, being difficult to be distinguished from the support [101].

Even if some hints of sintering and coking were observed for the different catalysts tested, deactivation was not clearly observed during the activity tests. For all the catalysts, the results obtained at the highest temperatures tested were close to the ones predicted by the thermodynamic equilibrium. For all of them, the decrease in the activity at the highest temperatures tested can be attributed to the fact that carbon dioxide methanation is an exothermic reaction, thus, its yield is hindered as the operating temperature is increased. However, the null effect of the sintering and/or coking on the results of the activity tests can be attributed to the fact that the activity tests were only run for 450 minutes. Further running the activity tests could result in the sintering and/or the coking reducing the active sites of the catalysts and this would be reflected in the activity test results as a decrease in the catalytic activity.

To summarise, the results obtained in the activity tests and the characterisation techniques employed made us conclude that 673 K is the most suitable calcination temperature for these catalysts.

5.1.2. Operating pressure

After choosing the best calcination temperature for the nickel based catalysts, 673 K, this catalyst was tested at three different pressures: 1 bar, 10 bar and 15 bar, and compared with the thermodynamic equilibrium. Results for these activity tests are shown in Figure 5.8.

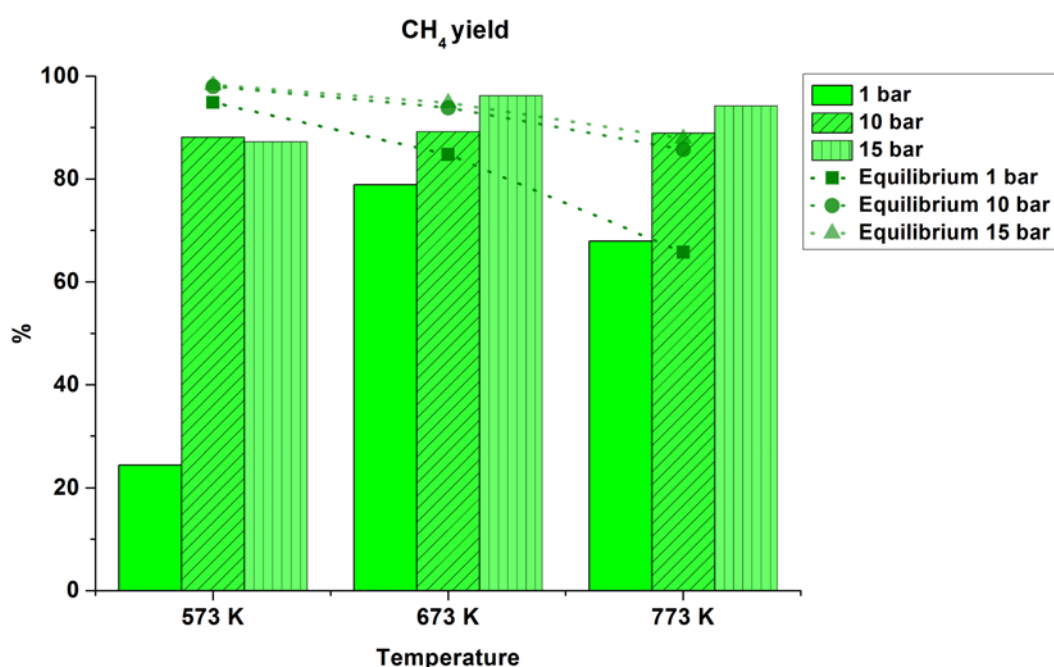


Figure 5.19. Activity results of the catalyst operating at different pressures

As it can be seen, the effect of the pressure on the thermodynamic equilibrium is only remarkable at temperatures above 673 K, shifting the limits set by thermodynamics to higher values. According to the obtained results, an increase in the pressure from 1 bar to 10 bar resulted in an outstanding increase in the catalytic activity at 573 K, from slightly above 20 % of methane yield at 1 bar to almost 90 % at 10 bar. At the intermediate temperature, thermodynamic equilibrium is almost reached at both pressures, being the effect of the pressure less remarkable but still beneficial. At the

highest temperature thermodynamic equilibrium is reached at both pressures resulting in a difference of methane yield of about 20 points higher when operating at 10 bar.

Further increase in the pressure from 10 bar to 15 bar does not have a remarkable impact on the thermodynamic equilibrium, neither in the results obtained in the activity tests. It can be appreciated that, at the highest temperature tested, values obtained operating at 15 bar are above the ones predicted by the thermodynamic equilibrium. However, the difference between them is negligible and it can be attributed to the experimental error.

Taking into account the results, 10 bar was selected as the most suitable operating pressure. The difference between 10 bar and 15 bar, both at intermediate and high temperatures, was not large enough to justify the risks and the costs associated with operation at higher pressures.

5.2. Effect of the catalytic support

Catalytic systems based on nickel and prepared over different supports were tested in fixed bed reactors. These catalysts can be grouped, in order to ease the comparison and better understand the process, in three different groups: acidic supports, industrial supports and natural supports.

5.2.1. Acidic supports

As CO₂ is a weak Lewis acid, basic supports are normally used to enhance its adsorption [58]. However, the use of an acidic support has proved to enhance the influence of the active metal, as the bonds between the CO (one of the probable intermediates for CO₂ methanation process) and metal are weaker than those formed on basic supports. As CO and H₂ compete for the same adsorption site, weaker metal-CO bond leads to less CO coverage and more sites available for H₂, thus, an increase in the methanation rate. This is the consequence of a higher positive polarization of the active metal, as a result of the ionic exchange between the metal and the protons of the support [102].

A series of catalysts with a theoretical content of nickel of 13 wt % were prepared over different supports with acidic properties. These supports were ASA (amorphous silico-aluminate), zeolite H-ZSM-5, SiO₂, zeolite H-Beta, SBA-15 (mesostructured silica) and chromium-zirconium modified alumina (γ). The results can be compared with the ones obtained for the 13Ni/Al₂O₃ (γ) catalyst that can be found in section 5.1.1. Some of the results obtained for this catalyst are included in this section in order to ease the understanding of the results.

5.2.1.1. Chemical composition of the catalysts over acidic supports

The chemical composition of all these catalysts was determined by ICP-OES. According to the results, all the catalysts presented a content of metals (nickel and, when applicable, chromium and zirconium) close to the desired ones. These results are shown in Table 5.6.

Table 5.7. ICP-OES of the catalysts over acidic supports

Catalyst	Ni (wt %)	Cr (wt %)	Zr (wt %)
13Ni/ASA	11.7	-	-
13Ni/H-ZSM-5	13.2	-	-
13Ni/SiO ₂	13.9	-	-
13Ni/H-Beta	12.4	-	-
13Ni/SBA-15	12.9	-	-
13Ni/3Cr-4Zr-Al ₂ O ₃ (γ)	12.8	2.3	3.4

5.2.1.2. Structural properties of the catalysts over acidic supports

Structural properties (BET surface area, pore volume and pore size) were determined by N₂ adsorption-desorption isotherms. Results are summarized in Table 5.7.

Table 5.8. Structural properties of the catalysts over acidic supports

Catalyst	BET surface area (m ² /g)	Pore volume (cm ³ /g)	Average pore size (nm)
Al ₂ O ₃ (γ)	232	0.80	13.2
13Ni/Al ₂ O ₃ (γ)	182	0.25	5.5
ASA	323	0.64	7.6
13Ni/ASA	224	0.26	4.8
H-ZSM-5	388	0.19	3.0
13Ni/H-ZSM-5	241	0.25	5.4
SiO ₂	191	0.81	17.2
13Ni/SiO ₂	140	0.41	11.5
H-Beta	414	0.38	4.7
13Ni/H-Beta	287	0.20	3.9
SBA-15	662	1.60	9.5

13Ni/SBA-15	357	0.63	6.8
3Cr-4Zr-Al₂O₃ (γ)	228	0.77	12.9
13Ni/3Cr-4Zr-Al₂O₃ (γ)	149	0.13	4.2

As it can be seen, all the catalysts presented high surface area between 140 and 360 m²/g. In all the cases, the surface area of the catalysts was lower than the one presented by the support prior to carrying out the impregnation procedure. This decrease in the surface area of the supports can be attributed to metal particles blocking the mesopores of the support [103]. This behaviour can further be observed in the changes of the pore volume and the average pore size, which also decreased after the impregnation of the different metals. Only one exception was observed, for the catalyst supported on zeolite H-ZSM-5 although the surface area decreased when nickel was incorporated, both the pore volume and the average pore size increased. This behaviour could be attributed to the presence of small pores in the zeolite, being blocked first, while the biggest pores did not suffer from this blockage [104].

5.2.1.3. Reducibility of the catalysts over acidic supports

The reducibility of the catalysts and the reduced species were measured by TPR. In order to compare these results with the 13Ni/Al₂O₃ (γ) catalyst a dashed line has been added to the figure to represent the temperature at which the main reduction peak of this catalyst appeared. These results are shown in Figure 5.9.

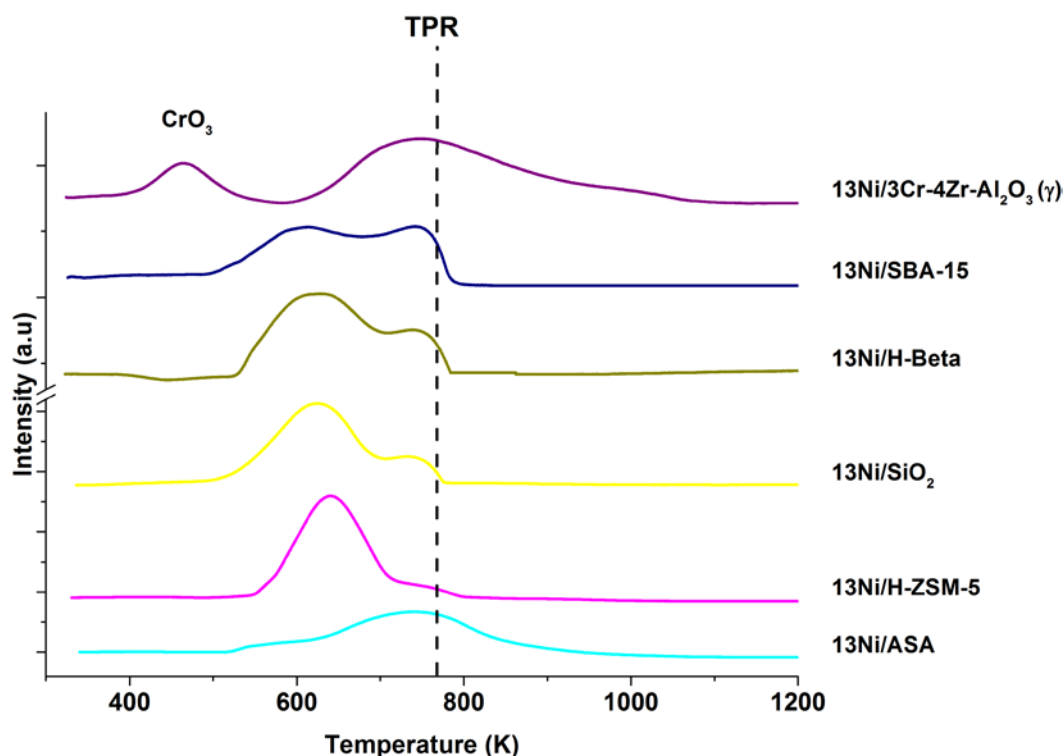


Figure 5.20. TPR profiles of the catalysts over acidic supports

Comparing the main reduction peaks of all the catalysts prepared over acidic supports with the catalyst supported on γ -alumina, only the catalyst supported on ASA and on chromium-zirconium modified alumina presented the main reduction peak at approximately the same temperature as the reference catalyst. For all the other catalysts, the main reduction peak was shifted down to lower temperatures, this means a weaker interaction between the metal and the support, thus, an improved reducibility of the catalyst [50]. In the case of the catalyst containing chromium and zirconium, apart from the main reduction peak also a reduction peak was presented at approximately 450 K which can be attributed to the reduction of Cr^{6+} to Cr^{3+} . Regarding to the main reduction peak presented by all the catalysts, this was the result of the contribution of different nickel species with different degree of interaction with the support. In order to analyse the contribution of each peak to the final profile peak deconvolution was carried out and results are shown in Table 5.8.

Table 5.9. TPR peak deconvolution of the catalysts over acidic supports

Catalyst	Specie-Temperature (K)-Relative amount (%)
13Ni/ASA	NiO-572 K-5.2 %
	NiO crystallites-737 K-91.8%
	Nickel hydrosilicate-909 K-3.0 %
13Ni/H-ZSM-5	NiO-640K-92.8 %
	Ni phyllosilicate-752 K-7.2 %
13Ni/SiO₂	NiO-599 K-13.9 %
	NiO weak interaction-623 K-75.8 %
	NiO strong interaction-739 K-10.3 %
13Ni/H-Beta	NiO-625 K-77.4 %
	NiO interaction with the support-741 K-22.6 %
13Ni/SBA-15	NiO weak interaction -622 K-72.7 %
	NiO strong interaction-738 K-21.3 %
13Ni/3Cr-4Zr-Al₂O₃ (γ)	CrO ₃ -464 K-17.4 %
	NiO-684 K-10.2 %
	NiO-Al-742 K-27.6 %

NiAl_xO_y -827 K-35.1 %

NiAl_2O_4 -977 K-9.7 %

The catalyst supported on ASA presented three different nickel species, in an increasing order of temperature: NiO, NiO crystallites formed due to nucleation and NiO hydrosilicate [105], being the NiO crystallites the most abundant specie (> 90 %). Regarding to the use of zeolite H-ZSM-5 as support for the catalyst, the nickel species determined by TPR were, in order of an increasing temperature, NiO and NiO phylisilicates [106] being NiO the main specie (> 90 %). For the catalyst supported on SiO_2 , bulk NiO, NiO with weak interaction with the support and NiO with strong interaction with the support were identified as the reducible species [107] with NiO with weak interaction with the support being the most abundant (> 75 %) nickel specie. For the catalyst supported on H-Beta large NiO particles, being the most abundant specie (> 75 %) and NiO interacting with the support were identified [108,109] as the reducible nickel species. The catalyst supported on SBA-15 only presented two nickel species; NiO with weak interaction with the support and NiO with strong interaction with the support being the first one the most abundant (> 70 %) nickel specie. Finally, for the chromium-zirconium modified alumina (γ) catalyst the reduction peak at the lowest temperature was attributed to the reduction of Cr^{6+} to Cr^{3+} , while the other main peak was the final result of the contribution of different nickel species: bulk NiO, NiO weakly interacting with the support (NiO-Al), non-stoichiometric nickel aluminate (NiAl_xO_y) and stoichiometric nickel aluminate (NiAl_2O_4), being non-stoichiometric nickel aluminate the most abundant one (> 35 %). All these species were shifted to lower temperatures comparing with the non-modified alumina (γ) catalyst due to the effect of adding zirconium that improved the reducibility of the catalyst [51]. However, the effect of adding zirconium was weakened due to the influence of chromium, which has the opposite effect of the zirconium and increases the metal-support interaction, thus, shifts the peaks towards higher temperatures [110].

5.2.1.4. XRD results of the catalysts over acidic supports

XRD measurements were also carried out for these catalysts in order to determine the main crystalline species. The results obtained for the fresh-reduced catalysts are shown in Figure 5.10.

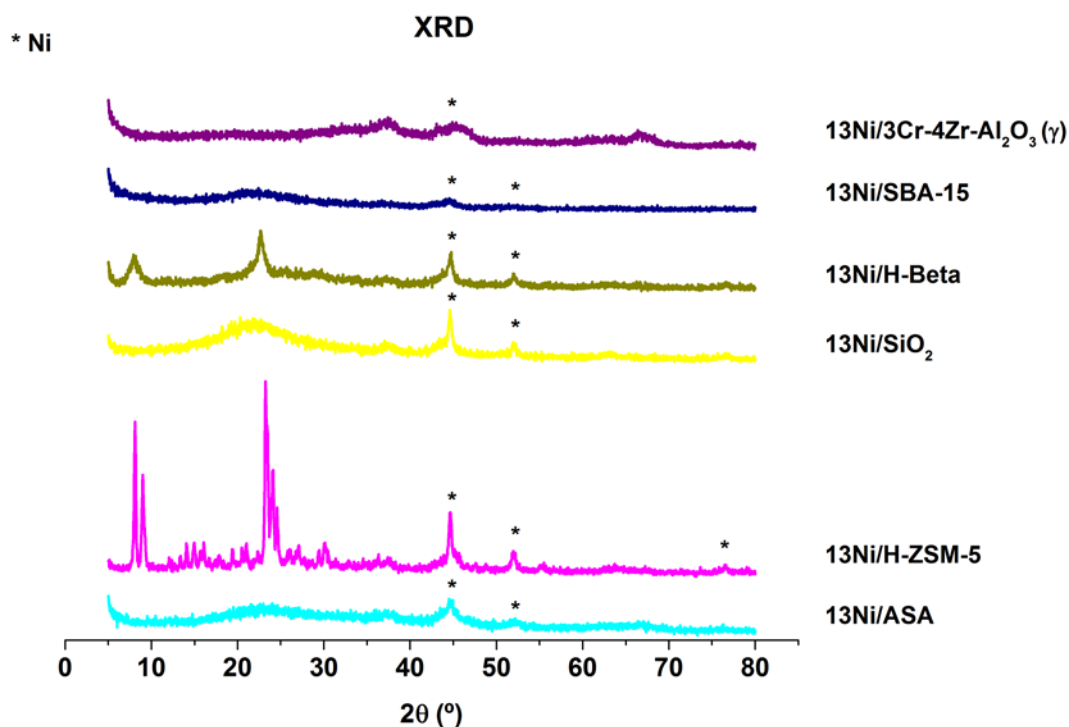


Figure 5.21. XRD profiles of the catalysts over acidic supports

All the catalysts presented diffraction peaks that could be attributed to metallic nickel, so complete reduction of the catalysts was achieved. These results are in good agreement with those obtained by TPR, as none of the catalysts presented a large amount of nickel species with strong interaction with the support, thus more difficult to be reduced, and it was possible to achieve a complete reduction of the catalysts. It is also noticeable that both zeolites, especially H-ZSM-5, presented various sharp peaks at angles below 30° due to the highly crystalline structure of the zeolites. Not chromium neither zirconium were detected for the catalyst containing them, although their presence was confirmed by ICP-OES as it has been shown in Table 5.6. This can be due

to the fact that they were present in a low concentration and probably formed crystallites too small to be detected by XRD.

Average crystallite size of nickel was calculated employing the most intense nickel peak from XRD profiles and the Scherrer equation. Results are shown in Table 5.9.

Table 5.10. Average nickel crystallite size of the catalysts over acidic supports

Catalyst	Average nickel crystallite size (nm)
13Ni/ASA	31
13Ni/H-ZSM-5	21
13Ni/SiO₂	29
13Ni/H-Beta	29
13Ni/SBA-15	22
13Ni/3Cr-4Zr-Al₂O₃ (γ)	18

The catalyst supported on ASA presented the largest average nickel crystallite size, this can be correlated to the data obtained by TPR as NiO crystallites formed by nucleation, and thus, larger crystallites were determined as the main nickel specie for the catalyst supported on ASA. Employing H-ZSM-5 as support resulted in one of the smallest average nickel crystallite sizes, probably due to the cage-like crystalline structure of the zeolite that inhibits nickel particle agglomeration [111] which can be correlated with TPR results, being reducible NiO the main nickel specie for this catalyst. The catalyst supported on SiO₂ presented one of the largest average crystallite size, this can be explained with the results obtained by TPR that proved a weak metal-support interaction for this catalyst, which results in a worse metallic dispersion [112]. This

behaviour was also observed for the catalyst supported on H-Beta, both by XRD and by TPR. The small average nickel crystallite size observed for the catalyst supported on SBA-15, even if the main nickel specie observed by TPR was NiO with weak interaction with the support, can be attributed to the ordered pore channels and narrow pore size distribution [113] of the support, resulting in a good dispersion of the metal over the support. Regarding to the catalyst supported on chromium-modified alumina, it presented the smallest average nickel crystallite size among all the catalysts supported on acidic supports.

5.2.1.5. Metallic dispersion of the catalysts over acidic supports

Metallic dispersion was also measured for these catalysts using CO chemisorption technique. These results are shown in Table 5.10.

Table 5.11. Metallic dispersion of the catalysts over acidic supports

Catalyst	Metallic dispersion (%)
13Ni/ASA	0.2
13Ni/H-ZSM-5	0.7
13Ni/SiO ₂	0.5
13Ni/SBA-15	0.7
13Ni/H-Beta	0.5
13Ni/3Cr-4Zr-Al ₂ O ₃ (γ)	0.9

According to these results, the catalyst supported on chromium-zirconium modified alumina (γ) presented the highest metallic dispersion, however it was slightly lower than

the one presented by the catalyst supported on non-modified alumina (γ) probably due to the presence of chromium and/or zirconium blocking the pores of the support that leads to a smaller amount of pores available for the active metal to be deposited. The results obtained by CO chemisorption are in accordance with the average crystallite size obtained by XRD, as the catalysts that presented the smallest average crystallite size presented the highest dispersion and it is known that dispersion is inversely proportional to crystallite size [114].

5.2.1.6. Acidity of the catalysts over acidic supports

As it has been previously explained, acidic supports were chosen for catalysts synthesis in order to enhance the properties of the active metal. Measurements of the acidity of the catalysts were carried out by NH_3 -TPD. The acidity of the catalyst supported on alumina (γ) and calcined at 673 K was also measured to be used as a reference. Results obtained are presented in Figure 5.11.

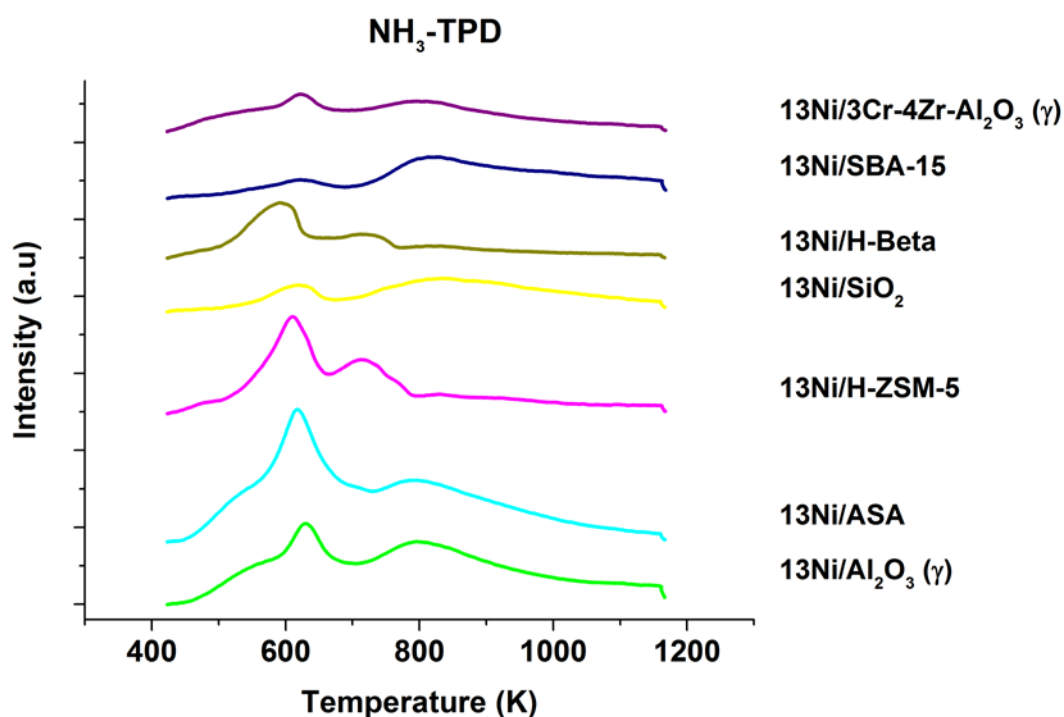


Figure 5.22. NH_3 -TPD profiles of the catalysts over acidic supports

As it can be seen in the figure, all the catalysts presented two different desorption peaks: the first one located at approximately 600 K for most of them, while the high temperature peak was measured at approximately 800 K. As the use of NH₃ as probe molecule presents different drawbacks, like the possibility of being adsorbed on non-acidic part of the surface, the peak temperature cannot be directly correlated to the acid strength [115] so deconvolution of the peaks was not carried out. However, 723K was selected as the temperature to distinguish between low and high temperature acid sites [116]. The results obtained for both the total amount of NH₃ adsorbed and the percentage corresponding to the low/high acid sites are presented in Table 5.11.

Table 5.12. Distribution of the acid sites of the catalysts over acidic supports

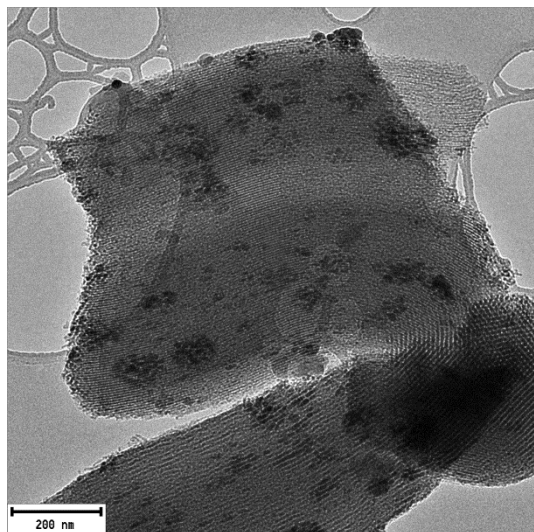
Catalyst	Low temperature acid sites (%)	High temperature acid sites (%)	Adsorbed NH ₃ amount (mmol/g _{cat})
13Ni/Al₂O₃ (γ)	36.5	63.5	1.5
13Ni/ASA	50.0	50.0	1.5
13Ni/H-ZSM-5	56.8	43.2	1.0
13Ni/SiO₂	23.1	76.9	0.6
13Ni/H-Beta	60.6	39.4	1.4
13Ni/SBA-15	17.0	83.0	0.8
13Ni/3Cr-4Zr-Al₂O₃ (γ)	42.2	57.8	1.4

The catalyst supported on Al_2O_3 (γ) presented a higher amount of high temperature acid sites and one of the highest acidities. The $^{13}\text{Ni}/\text{ASA}$ catalyst presented the highest acid character with an even distribution between low and high temperature acid sites. The catalyst supported on zeolite H-ZSM-5 was mainly composed by low temperature acid sites, with an overall average acid character. For the $^{13}\text{Ni}/\text{SiO}_2$ catalyst the lowest acidity was measured, however this acid character was mainly due to high temperature acid sites. The catalyst supported on zeolite H-Beta presented a behaviour close to the one presented by the catalyst supported on zeolite H-ZSM-5, being the acid character attributable to low temperature acid sites, but it presented a higher total acidity. Using SBA-15 as catalytic support resulted in a catalyst with low acidity, related mainly to high temperature acid sites. Finally, the modification of alumina (γ) with chromium-zirconium slightly decreased the acid character, when compared with the bare alumina (γ) catalyst, and changed the distribution of acid sites, increasing the low temperature ones, however the high temperature acid sites were still the most abundant ones.

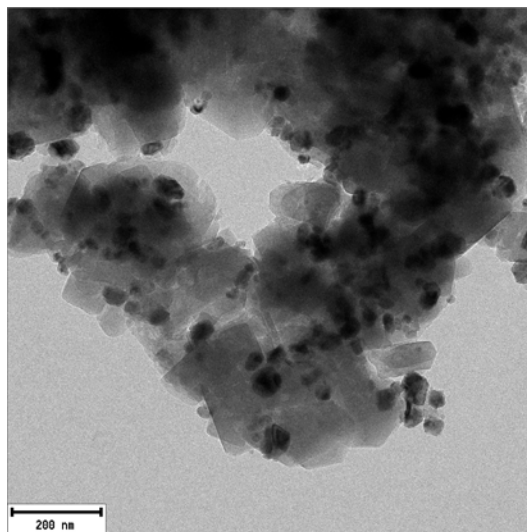
5.2.1.7. TEM of the catalysts over acidic supports

Catalysts over acidic supports were analysed by TEM to gain information about their physical structure, especially the metallic dispersion over the support and the size of the metallic particles. Results obtained are presented in Figure 5.12.

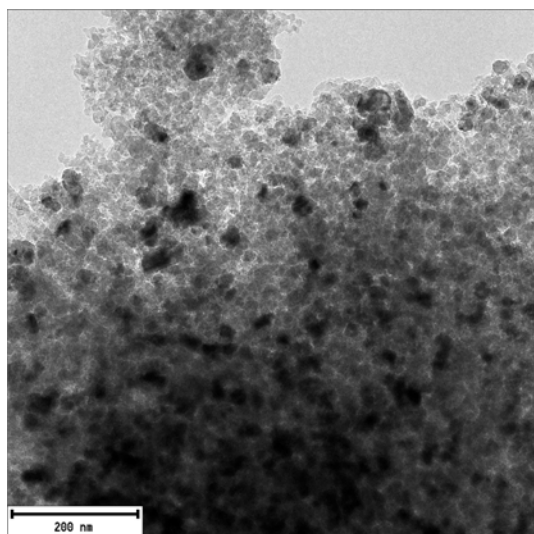
a) $^{13}\text{Ni}/\text{ASA}$



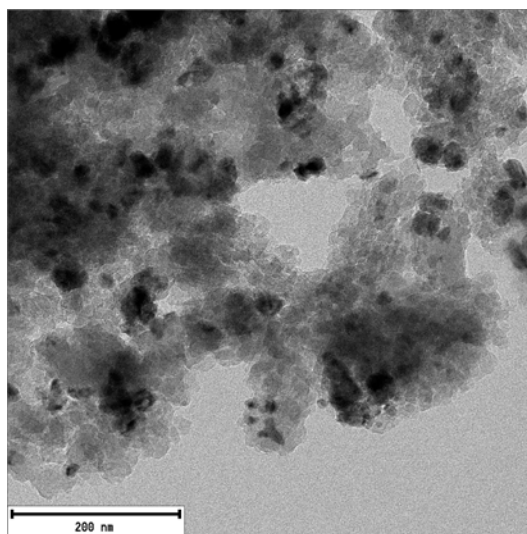
b) $^{13}\text{Ni}/\text{H-ZSM-5}$



c) $^{13}\text{Ni}/\text{SiO}_2$



d) $^{13}\text{Ni}/\text{H-Beta}$



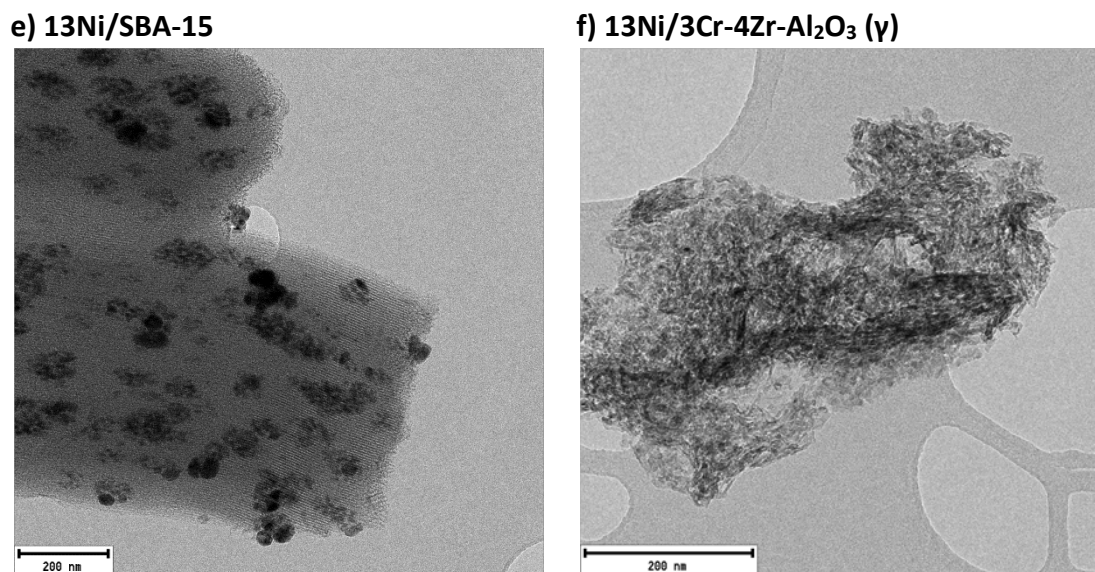


Figure 5.23. TEM micrographs of the catalysts over acidic supports

The catalyst supported on ASA presented big particles, poorly dispersed over the support. The 13Ni/H-ZSM-5 catalyst presented well dispersed particles with a homogeneous particle size distribution. Both the catalyst supported on SiO₂ and the one supported on H-Beta presented a similar structure with particles quite well dispersed, although not as well as the catalyst supported on zeolite H-ZSM-5, with a homogeneous particle size distribution. When using SBA-15 as support, nickel particles were mainly located inside the well-defined mesoporous structure of the support [113], as it can be seen in the figure, however some big particles located outside this structure were also observed. Finally, for the catalyst supported on chromium-zirconium modified alumina (γ) it was really difficult to distinguish the nickel particles from the support, probably due to its higher metallic dispersion.

Even though particle size could not be measured by this technique, due to a small count that would induce a large error in the particle size distribution [117], the particle size distribution observed in the micrographs obtained by TEM is in good agreement with both the average nickel crystallite size measured by XRD and the metallic dispersion measured by CO chemisorption.

5.2.1.8. XPS of the catalysts over acidic supports

Fresh-reduced catalysts were also analysed by XPS to detect metallic species on the surface of the catalyst. Nickel was present as Ni^{2+} for the catalyst supported on ASA, at a binding energy of 855.6 eV [118], with a satellite peak at a binding energy of 862.0 eV corresponding both to the $\text{Ni}2p_{3/2}$ core level, while the peaks corresponding to the $\text{Ni}2p_{1/2}$ core level were measured at a binding energy of 873.6 eV for the main peak and 880.2 eV for the satellite peak. The same nickel specie, Ni^{2+} , was the only nickel specie detected for all the catalysts probably due to the exposure of the fresh-reduced samples to the atmosphere prior to the analysis, resulting in a surface oxidation of the catalysts as it has been previously explained. In all the cases this specie was present at two different core levels, $\text{Ni}2p_{3/2}$ and $\text{Ni}2p_{1/2}$, and it presented a main and a satellite peak at each core level.

A summary of the binding energies of the different electrons measured is presented in Table 5.12.

Table 5.13. Binding energies (eV) XPS of the catalysts over acidic supports

Catalyst	Ni^{2+} ($\text{Ni}2p_{3/2}$)	Ni^{2+} satellite ($\text{Ni}2p_{3/2}$)	Ni^{2+} ($\text{Ni}2p_{1/2}$)	Ni^{2+} satellite ($\text{Ni}2p_{1/2}$)
13Ni/ASA	855.6	862.0	873.6	880.2
13Ni/H-ZSM-5	853.9	860.2	871.5	878.2
13Ni/SiO₂	853.5	859.7	871.0	877.9
13Ni/H-Beta	854.8	861.3	872.6	879.4
13Ni/SBA-15	853.6	860.0	871.5	878.3

$^{13}\text{Ni}/^{3}\text{Cr-4Zr-Al}_2\text{O}_3$ 854.6 860.7 872.4 878.8

(γ)

The differences on the binding energies for the different catalysts can be associated to Ni^{2+} species with a different degree of interaction with the support. Usually, the species located, for the $\text{Ni}2p_{3/2}$ core level, at binding energies of 853.0-854.0 are attributed to none or weak interactions with the support while the ones located at 855.0-856.0 are due to nickel interacting with the support [119], thus the upshift in the binding energy can be attributed to a stronger interaction with the support [120]. Neither metallic nickel (Ni^0), which common peaks for the $\text{Ni}2p_{3/2}$ core level is usually located at 853.2 eV [121], nor complex nickel-support species with $\text{Ni}2p_{3/2}$ core level peaks located at binding energies above 856.0 eV [122] were detected.

The profiles measured by XPS can be observed in Figure 5.13.

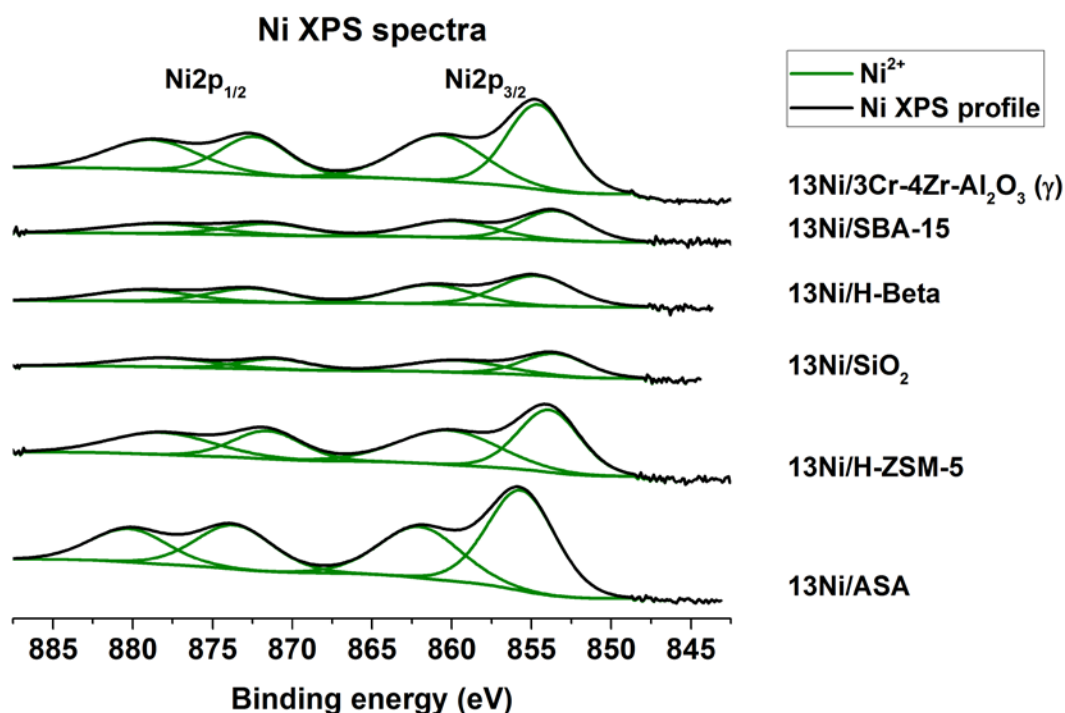


Figure 5.24. Ni XPS spectra of the catalysts over acidic supports

5.2.1.9. Activity tests of the catalysts over acidic supports

The results obtained in the activity tests are shown in Figure 5.14. The results are compared with the values predicted by the thermodynamic equilibrium.

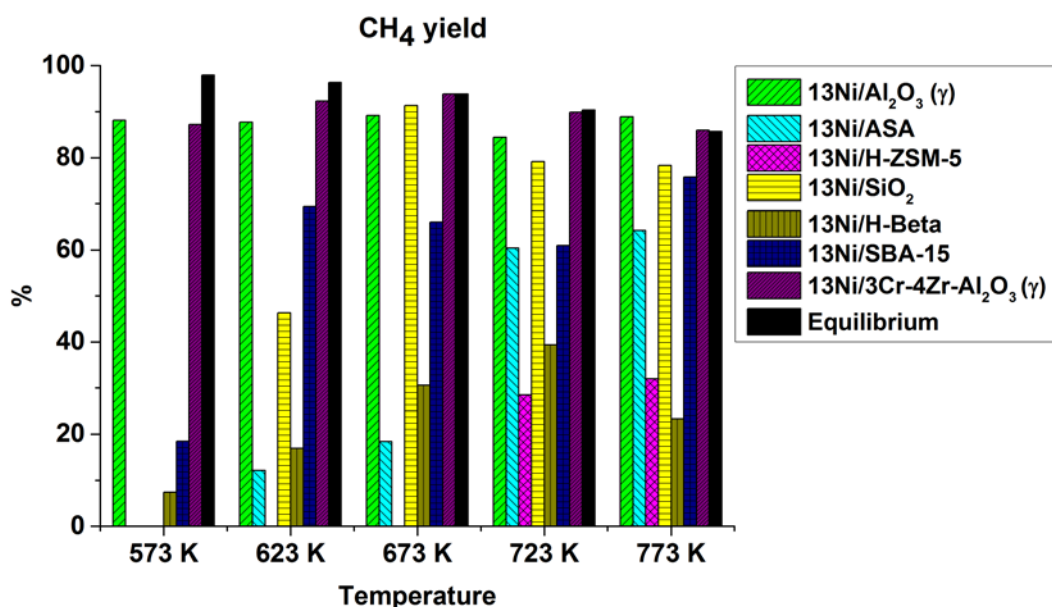


Figure 5.25. Activity results of the catalysts over acidic supports

The catalyst supported on ASA did not present catalytic activity at the lowest temperature tested. Increasing the temperature of the reaction resulted in an increase of the catalytic activity, however far from the thermodynamic equilibrium at all the temperatures tested. For the catalyst supported on zeolite H-ZSM-5, catalytic activity was not observed until the temperature of the reaction was set at 723 K. A further increase in the temperature up to 773 K slightly increased the activity of this catalyst, however it was still far from the values predicted by the thermodynamic equilibrium. While the catalyst supported on SiO₂ did not present catalytic activity at the lowest temperature tested, increasing the temperature had a beneficial effect and the catalyst reached its maximum activity, and the thermodynamic equilibrium, at 673 K. Increasing the temperature above this temperature resulted in a decrease of the catalytic activity more pronounced than the one that also experiences the thermodynamic equilibrium when increasing the temperature. The catalyst supported on zeolite H-Beta presented

catalytic activity at all the temperatures tested, reaching its maximum at 723 K but being always far from the thermodynamic equilibrium. Employing SBA-15 as support resulted in the presence of catalytic activity at all the temperatures tested reaching a maximum CH₄ yield, after a sudden increase, at 773, close to the thermodynamic equilibrium. The catalyst supported on chromium-zirconium modified alumina (γ) presented the best results among all the catalysts supported on acidic supports, being close to the thermodynamic equilibrium at all the temperatures tested and presenting a maximum in its activity at 623 K.

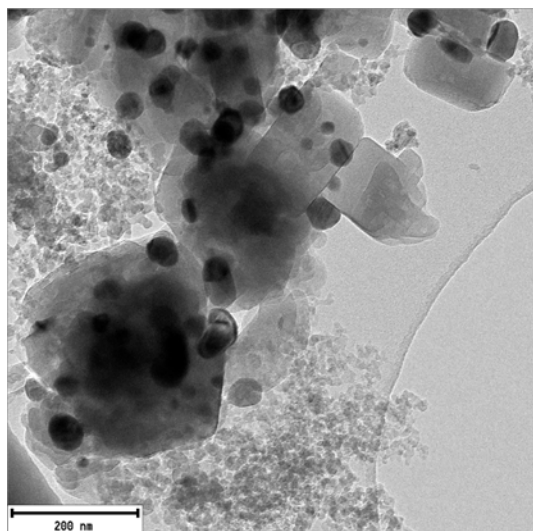
As it has been previously stated, all these catalysts were compared with the 13Ni/Al₂O₃ (γ) catalyst employed previously to determine the best calcination temperature and operating pressure, in order to establish a reference to choose the best catalytic system. Among all the acidic supports only silica, at temperatures above 673 K, and chromium-zirconium modified alumina (γ), at all the temperatures tested, can be considered as effective as alumina (γ) for carbon dioxide methanation process. In fact, the modifying of the alumina (γ) with chromium-zirconium resulted in an improvement of the activity when compared with the bare alumina support, being even more effective at all the temperatures tested and always close to the values predicted by the thermodynamic equilibrium.

5.2.1.10. TEM of the spent catalysts over acidic supports

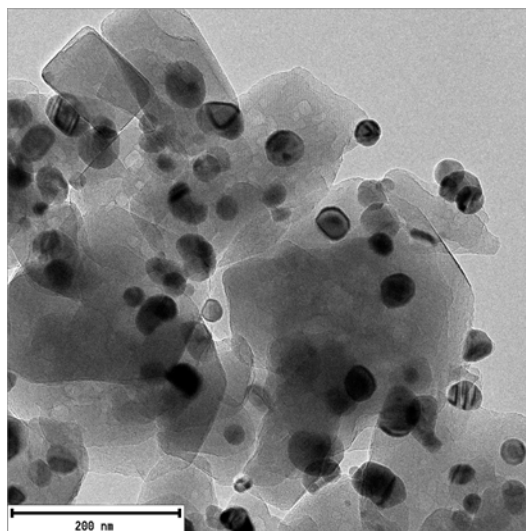
In order to analyse the influence of the activity tests on the structure of the catalysts, and also to detect the presence of coke, TEM analysis were performed to the catalysts after carrying out the activity tests. The TEM micrographs taken are presented in Figure 5.15. The 13Ni/ASA catalyst did not present any coke specie, while particle growth and agglomeration was observed when comparing with the fresh-reduced catalyst. For the catalyst supported on zeolite H-ZSM-5, coke was observed encapsulating the metallic particles, which also presented a growth after the activity tests. For the catalyst synthesised over SiO₂, coke was not observed in the TEM images, however clear differences in the particle size could be observed after performing the activity tests. Thus, for this catalyst the growth of particles and formation of particle clusters was

observed. The catalyst supported on zeolite H-Beta presented, as the one supported on the other zeolite, coke encapsulating the metallic particles. Regarding to the particle size after the activity tests, a growth in the particles and the formation of particle clusters as a consequence of this growth was observed. Neither coke, nor a clear growth in the particle size was observed for the 13Ni/SBA-15 catalyst even if some bigger particles could be observed. Finally, the catalyst supported on chromium-zirconium modified alumina (γ) maintained its structure after the activity tests, with small particles well dispersed on the support (the scale for this catalyst is 100 nm and not 200 nm like for the other catalysts). For this latter catalyst any specie of coke was not observed.

a) 13Ni/ASA spent

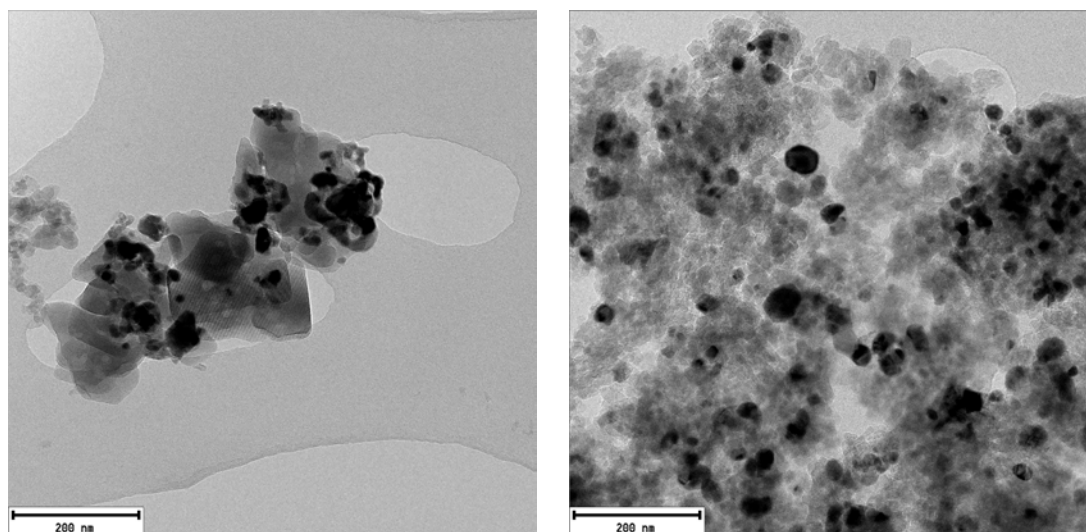


b) 13Ni/H-ZSM-5 spent



c) 13Ni/SiO₂ spent

d) 13Ni/H-Beta spent



e) 13Ni/SBA-15 spent

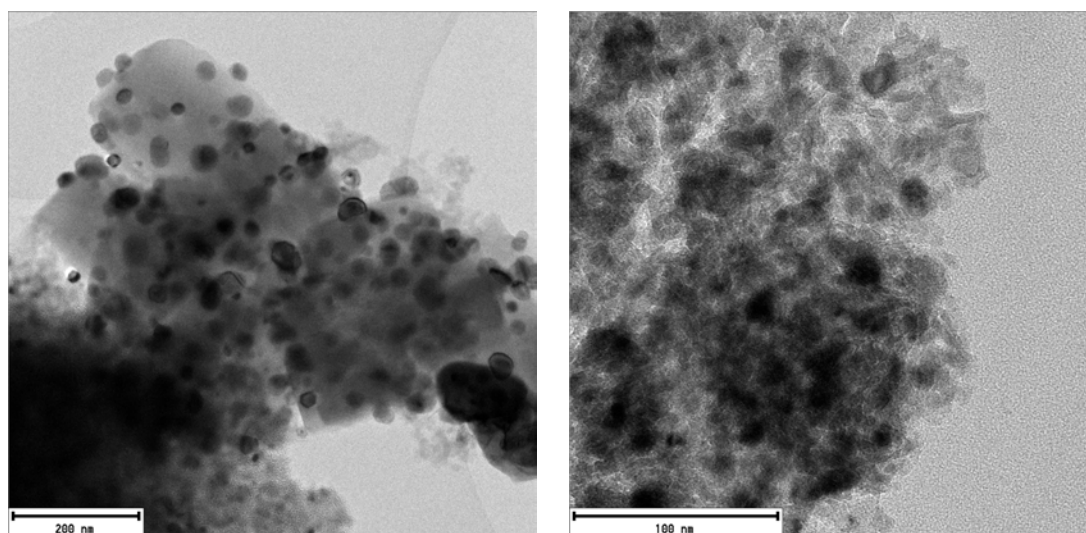
f) 13Ni/3Cr-4Zr-Al₂O₃ (γ) spent

Figure 5.26. TEM micrographs of the spent catalysts over acidic supports

5.2.1.11. XPS of the spent catalysts over acidic supports

The catalysts were analysed by XPS after the activity tests in order to measure any carbon derived specie formed on the surface of the catalysts. For the catalysts supported on ASA, SiO₂, SBA-15 and chromium-zirconium modified alumina (γ) carbon species were not detected. For the catalyst supported on zeolite H-ZSM-5 two different carbon species were detect; the main one (> 90 %) at a binding energy of 284.6 eV and the second one at a binding energy of 288.5 which can be attributed to graphitic C and C=O

respectively [123]. Regarding to the catalyst supported on zeolite H-Beta, only graphitic carbon located at a binding energy of 284.6 eV was measured. In the case of the catalyst supported on H-ZSM-5 the amount of carbon on the surface was approximately 23 wt % while for the catalyst supported on H-Beta it was only of approximately 10 wt %. The results obtained can be observed in Figure 5.16.

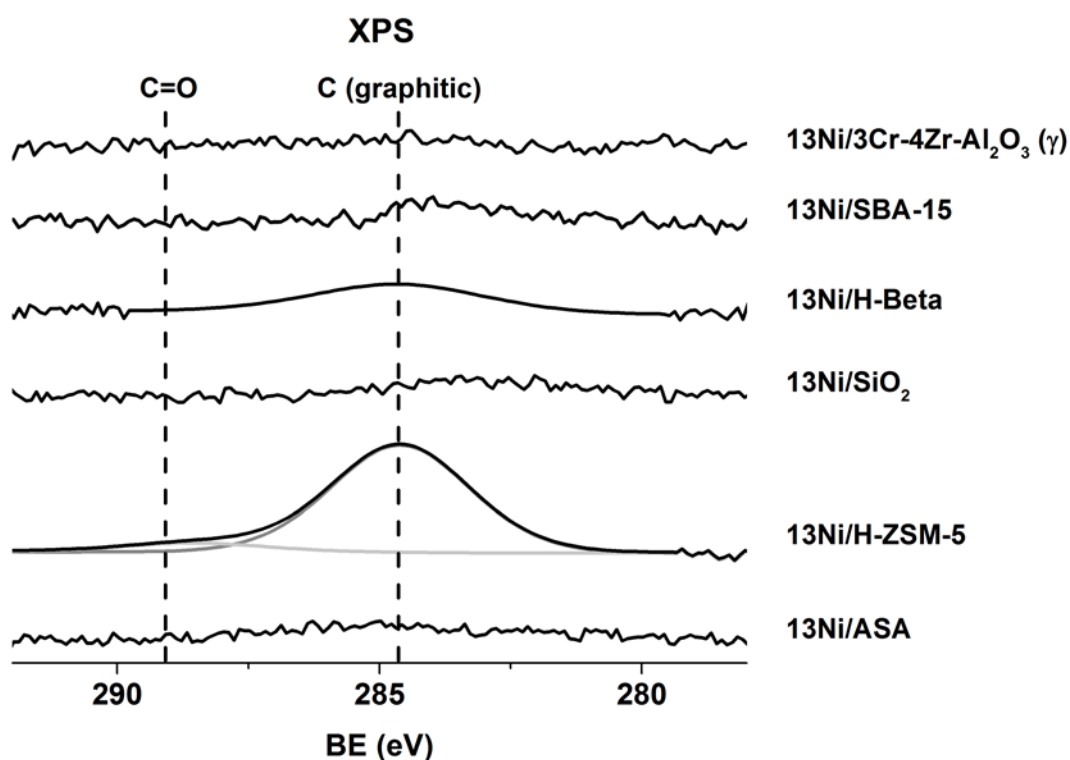


Figure 5.27. C XPS spectra of the spent catalysts over acidic supports

5.2.1.12. Discussion of the catalysts over acidic supports

The results obtained with the different characterisation techniques were employed to establish a relationship between the physicochemical properties of the catalysts and their catalytic activity.

According to the results obtained by the BET all the catalysts presented a high surface area, even though the impregnation of the metals resulted in a decrease of the initial surface area of the support. In all the cases, the decrease of the pore volume and the average pore size proved that the metal was incorporated, although to a different

extent, inside the porous structure of the supports. For the catalyst supported on H-ZSM-5, this effect was observed as an increase of the pore volume and the average of the pore size, due to the fact that micropores were impregnated first. The presence of the active metal inside the micropores can also be responsible of the low catalytic activity of this catalyst, due to the slower diffusion inside the micropores when comparing with mesopores [96].

As it has been previously mentioned during the comparison of the different calcination temperatures, the reducibility of the catalysts plays a crucial role in the catalytic activity. A larger amount of nickel species with weak interaction with the support resulted beneficial for the catalytic activity, while a large amount of nickel species without interaction with the support or with strong interaction with the support had the opposite effect. In the case of the catalyst supported on ASA, the increase in the catalytic activity together with an increase in the operating temperature can be attributed to the presence of NiO crystallites, hardly to reduce, as the main nickel specie. As the activity tests were carried out under hydrogen atmosphere, further reduction was probably carried out during the activity tests that resulted in active sites being formed from the nickel crystallites. For the $^{13}\text{Ni}/\text{H-ZSM-5}$ catalyst, its low catalytic activity can be related to the low amount of nickel species interacting with the support and the presence of the active sites inside micropores, resulting in diffusion issues. The use of SiO_2 as support resulted in a catalyst with predominantly weak interaction between metal and support, thus, a good catalytic activity. For the catalyst supported on zeolite H-Beta the low catalytic activity presented can be attributed to the large amount of NiO not interacting with the support. The high catalytic activity observed for the $^{13}\text{Ni}/\text{SBA-15}$ catalyst can be attributed to the high presence of NiO with weak interaction with the support. Finally, for the catalyst supported on chromium-zirconium modified alumina (γ) the high presence of both NiO-Al and NiAl_xO_y with weak and medium interaction with the support resulted in a high catalytic activity. The better performance of this catalyst when compared with the one supported on non-modified alumina (γ) could be due to the improvement of the thermal stability of the catalyst as a result of adding both support modifiers [124].

Further relationship between the catalytic activity and the physicochemical properties of the catalysts can be established with the results obtained by XRD and CO chemisorption. The first technique demonstrated that all the catalysts were completely reduced, thus, active sites were formed after the reduction under hydrogen atmosphere. The average crystallite size measured for all the catalysts constituted an estimation of the metallic dispersion, while the results obtained by CO chemisorption proved that the estimation was correct. The metallic dispersion is an important parameter as a higher metallic dispersion can enhance the catalytic activity. However, for the catalyst supported on ASA the catalytic activity was high even if it presented the lowest metallic dispersion among all the catalysts over acidic supports. It has been explained that this catalyst was mostly formed by big NiO crystallites, which caused the low metallic dispersion measured by CO chemisorption. Nevertheless, during the activity tests the hydrogen atmosphere was able to further reduce these big particles and the catalytic activity increased while temperature was increased.

To analyse the influence of the acidic character of the supports in the catalytic activity, measurements were carried out by NH₃-TPD. A high acid character did not seem to influence the activity of the catalyst, as the catalyst that presented the lowest acid character (13Ni/SiO₂) was more active than, for example, the catalyst supported on zeolite H-Beta which almost doubled the amount of NH₃ adsorbed by the catalyst supported on SiO₂. However, the ratio low:high temperature acid sites played an important role on the catalytic activity. This can be explained taking into account that low temperature acid sites take part in the reaction, which is performed at temperatures below 773 K, and as it has been explained acid sites inhibit the adsorption of CO₂ and hinder the activity of the catalyst. When the amount of high temperature acid sites increased the activity decreased, as it can be seen comparing SiO₂ and SBA-15 supported catalysts presenting the latter one more high temperature acid sites and being its activity slightly lower. The most appropriate low:high temperature acid sites ratio was determined as 1:1.5, taking into account that the catalyst that presented approximately 60 % of high temperature acid sites were the ones that also presented the highest

catalytic activity. A larger amount of low temperature acid sites than high temperature ones, like in the case of both zeolites, hindered the catalytic activity.

Even though a distribution of the particle size could not be calculated by TEM, due to the low count of particles measurable in the pictures, the results obtained were useful to further understand the results obtained by XRD and CO chemisorption and correlate the structure of the catalysts with the catalytic activity achieved in the activity tests. As it has been explained, TEM micrographs proved the results obtained by XRD and CO chemisorption, being the metallic dispersion of the catalysts an important parameter for the final catalytic activity. Although a high metallic dispersion does not ensure a high catalytic activity, it enhances the performance of the catalysts.

The results obtained by XPS proved the presence of Ni^{2+} as the unique nickel specie on the surface of the catalyst as a result of surface oxidation due to the exposure of the samples prior to the analysis.

To understand how the carbon dioxide methanation reaction could modify the structure of the catalysts and determine if any deactivation mechanism could result in a decrease of the yield presented by these catalysts different characterisation techniques were carried out on the spent catalysts.

Even if TEM micrographs proved that sintering happened for some of the catalysts, this particle growth did not seem to have any effect on the activity of some of the catalysts. For the catalyst supported on ASA, not only a decrease in the catalytic activity was not observed during the activity tests but its activity improved as the activity test was being performed and the temperature was increased. As it has been previously explained, this behaviour can be attributed to the fact that this catalyst was mainly composed by nickel crystallites that were reduced, thus being activated, when the temperature was increased. The $^{13}\text{Ni}/\text{H-ZSM-5}$ did not present a decrease in the activity even if not only sintering but also coking, as proved both by TEM and XPS, happened for this catalyst during the reaction. This can be attributed to the fact that the tests were only run for 450 minutes. For the catalyst supported on SiO_2 , which strongly suffered from sintering

according to the TEM results, a decrease in the catalytic activity was clearly observed and can be attributed to this change in the structure of the catalyst. This decrease in the catalytic activity was also observed for the $^{13}\text{Ni}/\text{H-Beta}$ that suffered from sintering, as proved by TEM, but also by coking as it was demonstrated by TEM and XPS.

Nor the catalyst supported on SBA-15 neither the $^{13}\text{Ni}/3\text{Cr-4Zr-Al}_2\text{O}_3$ (γ) catalyst suffered from sintering or coking, as clear differences were not observed between the micrographs of the fresh and the spent catalysts and coke was not detected by XPS. The absence of any deactivation mechanism affecting to these catalyst was observed in the activity tests as none of them decreased the methane yield when the reaction temperature was increased.

5.2.2. Industrial residues as supports

The use of industrial residues as supports for synthesizing catalytic systems is a really interesting approach: it cannot only lower down the price of a catalyst, as industrial residues are cheaper than conventional supports, but also would be an efficient manner of valorising residues.

A series of catalysts with a theoretical content of nickel of 13 wt % were prepared over different industrial residues employed as supports. These supports were FeSiMg, Waelz oxide, WDL (double leached Waelz oxide), Paval and PFS (fine and dried Paval). The results were compared with the $^{13}\text{Ni}/\text{Al}_2\text{O}_3$ (γ) catalysts employed previously for determining the most suitable catalyst calcination temperature.

5.2.2.1. Chemical composition of the catalysts over industrial residues as supports

ICP-OES was carried out to determine the chemical composition of these catalysts. According to the results, all the catalysts presented a real content of nickel (wt %) close to the desired one. The obtained results are presented in Table 5.14.

Table 5.14. ICP-OES of the catalysts over industrial residues as supports

Catalyst	Ni (wt %)
13Ni/FeSiMg	13.3
13Ni/Waelz	13.2
13Ni/WDL	12.7
13Ni/Paval	13.8
13Ni/PFS	12.4

5.2.2.2. Structural properties of the catalysts over industrial residues as supports

BET surface area, pore volume and pore size were measured by N₂ adsorption-desorption isotherms. Results are presented in Table 5.15.

Table 5.15. Structural properties of the catalysts over industrial residues as supports

Catalyst	BET surface area (m ² /g)	Pore volume (cm ³ /g)	Average pore size (nm)
FeSiMg	< 1	< 0.01	13.1
13Ni/FeSiMg	4	0.01	13.5
Waelz	< 1	< 0.01	26.8
13Ni/Waelz	2	0.01	24.3

WDL	3	0.02	26.1
¹³Ni/WDL	4	0.01	13.1
Paval	35	0.06	6.9
¹³Ni/Paval	24	0.04	7.2
PFS	95	0.17	7.3
¹³Ni/PFS	81	0.14	7.3

Two different behaviours were observed for the structural properties of the catalysts over industrial residues as supports. In the case of the supports with low surface area (FeSiMg, Waelz and WDL) an increase in the surface area was observed after nickel impregnation. The increase in the surface area for these catalysts can be attributed to the nickel being impregnated in the outer surface, generating a new surface [83]. For the WDL a decrease in the pore size was observed, thus, part of the nickel was impregnated inside the pores of the support. For the catalysts supported on Paval and PFS a decrease in the surface area was observed after the impregnation, being attributed to the blockage of the pores of the support by the nickel observed as a slight decrease in the pore volume.

5.2.2.3. TPR of the catalysts over industrial residues as supports

The reducibility of the catalysts and the reduced species were measured by TPR. In order to compare these results with the $^{13}\text{Ni}/\text{Al}_2\text{O}_3(\gamma)$ catalyst, a dashed line has been added to the figure to represent the temperature at which the main reduction peak (NiO interacting with the support) of this catalyst appeared. These results are shown in Figure 5.17.

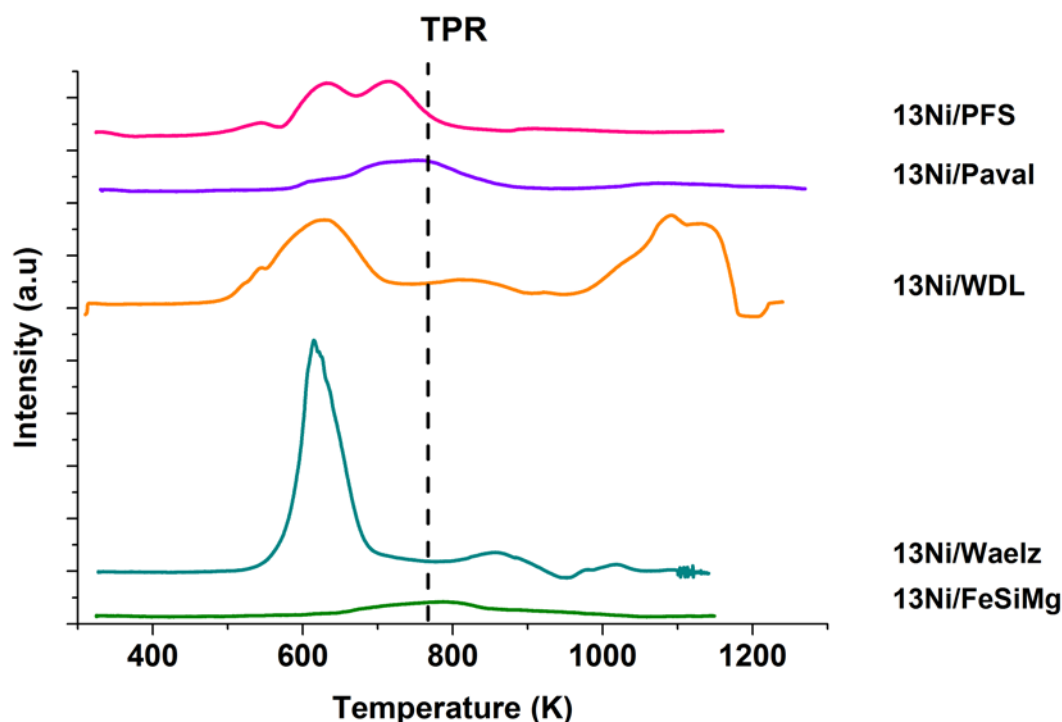


Figure 5.28. TPR profiles of the catalysts over industrial residues as supports

As it can be seen except the catalysts supported on FeSiMg and Paval, which presented their main reduction peak at approximately the same temperature that the 13Ni/Al₂O₃ (γ) catalyst, for the other catalysts it was shifted to lower temperatures. As it has been previously explained this is the effect of a weaker interaction between metal and support and an improved reducibility of the catalysts. For the catalyst supported on WDL a peak at high temperatures (> 1000 K) was also observed. This peak cannot be attributed to any nickel specie but to the reduction of ZnO which is reduced at temperatures above 1000 K [125]. The reduction profile is the result of the combination of different reduction peaks attributed to different species that combine into the final peaks observed in the profile. Deconvolution of these peaks was carried out in order to determine the contribution of each reducible specie to the final reduction peak. Due to the complexity of the supports the reducible species were not determined but previous experience with nickel based catalysts on conventional supports indicates that the species are, in order of increasing temperature: Ni₂O₃, free NiO, NiO with weak interaction with the support and NiO with strong interaction with the support. The obtained results are presented in Table 5.16.

Table 5.16. TPR peak deconvolution of the catalysts over industrial residues as supports

Catalyst	Ni ₂ O ₃	NiO	NiO interaction	weak NiO interaction	strong interaction
13Ni/FeSiMg	-	666 K-14.2 %	774 K-70.9 %	941 K-14.9 %	
13Ni/Waelz	-	623 K-70.0 %	785 K-30.0 %	-	
13Ni/WDL	543 K-7.7 %	624 K-75.1 %	802 K-17.2 %		
13Ni/Paval	-	615 K-2.5 %	740 K-73.6 %	1109 K-23.9 %	
13Ni/PFS	536 K-5.9 %	626 K-39.5 %	714 K-54.6 %	-	

The catalyst supported on FeSiMg has as its main specie NiO weakly interacting with the support (> 70 %), but it also presented NiO without interaction with the support and NiO strongly interacting with the support. For the catalyst supported on Waelz, NiO without interaction with the support (> 70 %) was the main specie and it also presented NiO weakly interacting with the support. When WDL was employed as support the resulting catalyst presented NiO without interaction with the support as the main specie (> 70 %). NiO weakly interacting with the support was the main specie for the catalyst supported on Paval (> 70 %) followed by NiO with strong interaction with the support. Finally, the catalyst supported on PFS presented NiO weakly interacting with the support as the main specie (> 50 %).

5.2.2.4. XRD of the catalysts over industrial residues as supports

The main crystalline species in the fresh-reduced catalysts were determined by XRD. The results are presented in Figure 5.18.

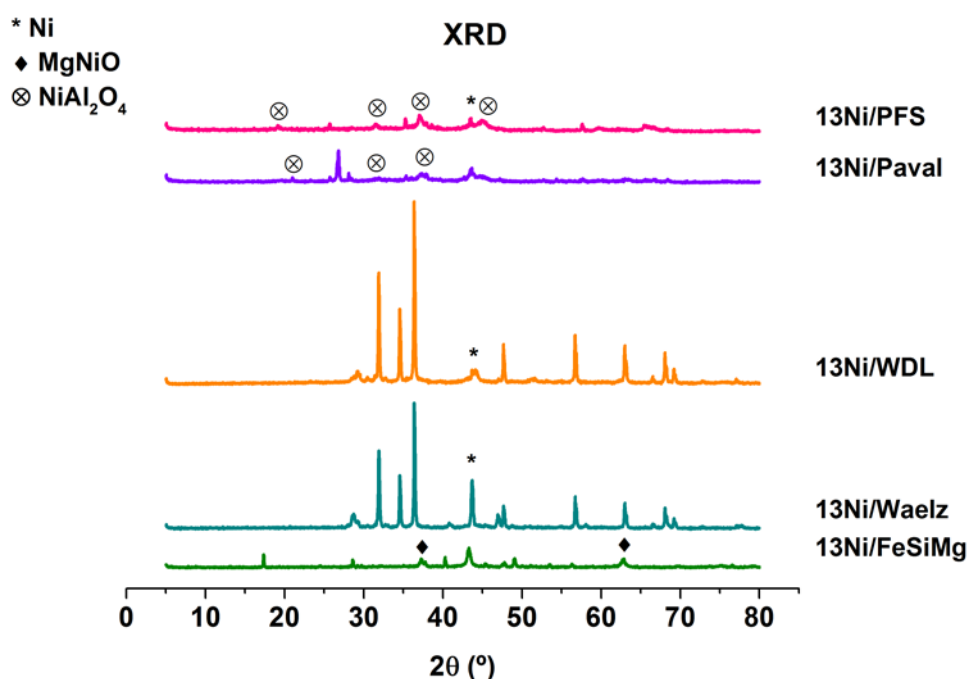


Figure 5.29. XRD profiles of the catalysts over industrial residues as supports

Only the catalysts supported on Waelz, WDL and PFS presented the peaks corresponding to metallic nickel. For the two first catalysts this means a complete reduction of the present nickel, as no other nickel specie was observed. In the case of PFS, NiAl_2O_4 peaks were also identified so this catalyst was not completely reduced. The catalyst supported on FeSiMg presented two peaks corresponding to a complex MgNiO specie while metallic nickel was not observed, which means that reduction was not properly accomplished. Finally, the catalyst supported on Paval only presented peaks corresponding to NiAl_2O_4 , a complex Ni-support specie, which is very difficult to reduce. All the peaks that can be observed and have not been depicted in the figure correspond to different species attributed to the supports, like different iron or zinc crystalline oxides.

XRD results are in good agreement with the results obtained by TPR, as all the catalysts that presented metallic nickel had a remarkable amount of easily reducible species. In the case of the catalyst supported on PFS the presence of another nickel specie can be attributed to the high reduction temperature of the NiO weakly interacting with the support. Moreover, in the case of the catalysts supported on FeSiMg and Paval even if NiO weakly interacting with the support was the main specie its reduction temperature was higher than the one employed for the reduction (673 K) resulting in an incomplete reduction of these catalysts.

Average crystallite size of nickel was calculated, if applicable, employing the most intense nickel peak from XRD profiles and the Scherrer equation. Results are shown in Table 5.17.

Table 5.17. Average nickel crystallite size of the catalysts over industrial residues as supports

Catalyst	Average nickel crystallite size (nm)
13Ni/FeSiMg	-
13Ni/Waelz	51
13Ni/WDL	41
13Ni/Paval	-
13Ni/PFS	23

The catalyst supported on PFS presented the lowest average nickel crystallite size among the catalysts supported on industrial residues. The catalysts supported on Waelz and WDL presented the largest average nickel crystallite size. This measurement was not

carried out for the catalysts supported on FeSiMg and Paval due to the fact that metallic nickel was not detected.

5.2.2.5. Metallic dispersion of the catalysts over industrial residues as supports

Pulse CO chemisorption technique was carried out to measure metallic dispersion of the catalysts. The only catalyst that presented the ability to adsorb CO was the 13Ni/PFS, giving as a result a value of the metallic dispersion of 0.54 %.

Due to the fact that only one catalyst presented metallic dispersion we cannot correlate the results obtained by this characterisation technique with the ones obtained employing other techniques. However, we can consider that the fact that the other catalyst did not present any metallic dispersion, even if metallic nickel was measured by TPR, can be attributed to value of the metallic dispersion below the limits of the measurement equipment employed.

5.2.2.6. Acidity of the catalysts over industrial residues as supports

Measurements of the acidity of the catalysts were carried out by NH₃-TPD. Results obtained are presented in Figure 5.19.

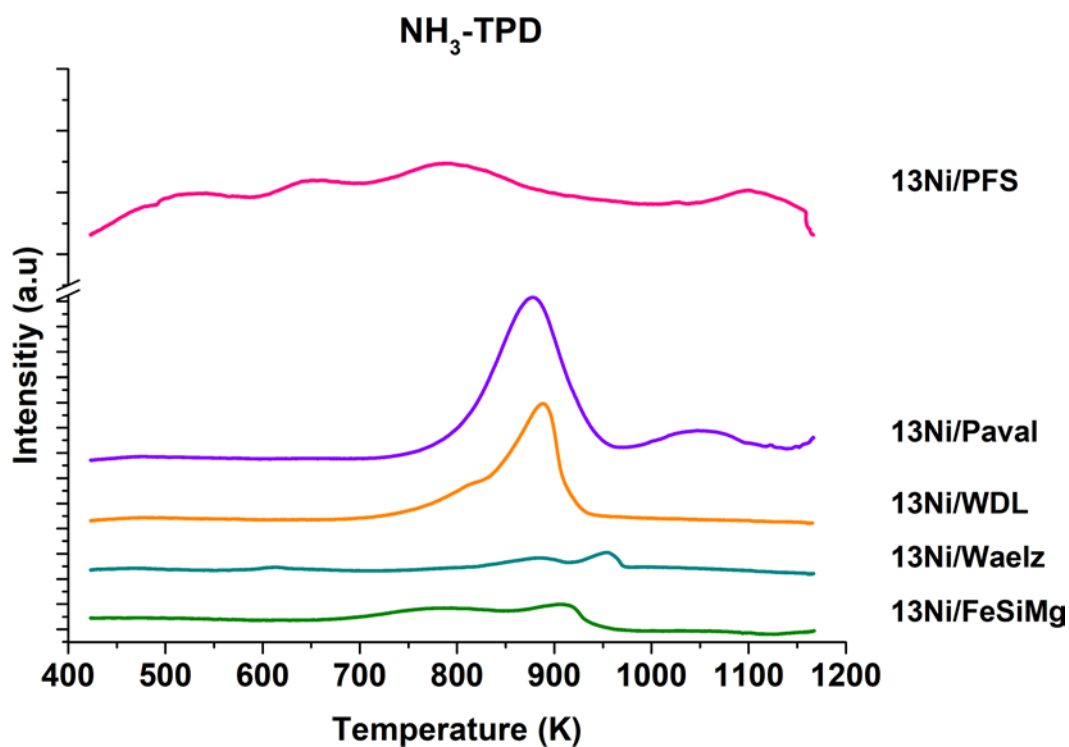


Figure 5.30. NH₃-TPD profiles of the catalysts over industrial residues as supports

The catalysts supported on FeSiMg and Waelz oxide presented almost flat desorption profiles. The peaks observed were too close to the noise region to perform the deconvolution of the profile and they could not be attributed to an acidic character. Both the catalysts supported on WDL and Paval presented an intense desorption peak at about 880 K. The catalysts supported on WDL and Paval presented the same low acidity, both being composed almost only by high temperature acid sites. Finally, the catalyst supported on PFS presented a wide acidity peak corresponding to a low acidity with a composition of approximately 1/3 low temperature acid sites and 2/3 high temperature ones.

Both the amount of NH₃ adsorbed for each catalyst and the amount of low and high temperature are presented, if available, in Table 5.18.

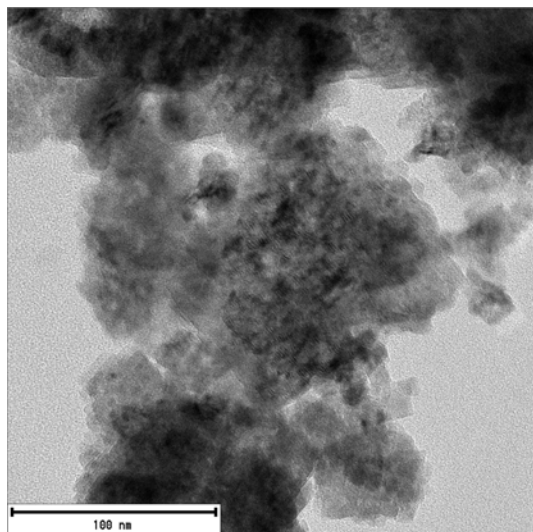
Table 5.18. Distribution of the acid sites of the catalysts over industrial residues as supports

Catalyst	Low temperature acid sites (%)	High temperature acid sites (%)	Adsorbed NH ₃ amount (mmol/g _{cat})
13Ni/FeSiMg	-	-	0.3
13Ni/Waelz	-	-	0.1
13Ni/WDL	5.1	94.9	0.6
13Ni/Paval	-	100	0.6
13Ni/PFS	33.8	66.2	0.7

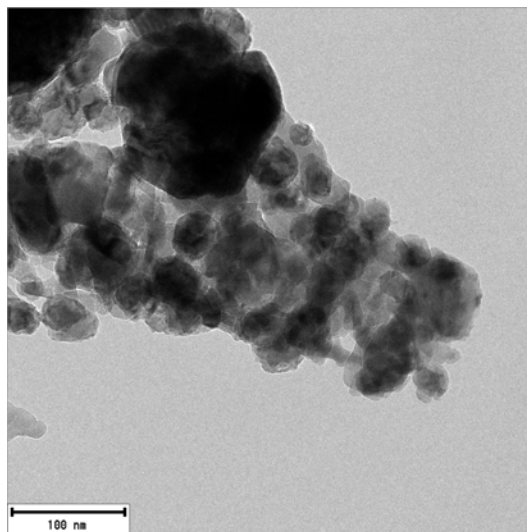
5.2.2.7. TEM of the catalysts over industrial residues as supports

The catalysts supported on industrial residues were also characterised by TEM in order to gain more information about their physical structure, the size of the metallic particles and their dispersion over the surface of the support. These results are presented in Figure 5.20.

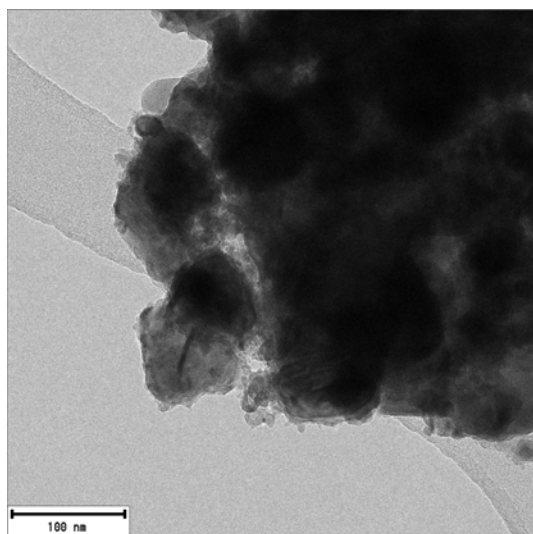
a) $^{13}\text{Ni}/\text{FeSiMg}$



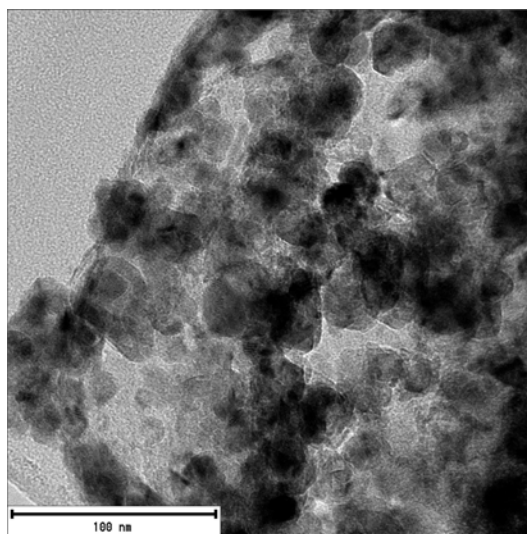
b) $^{13}\text{Ni}/\text{Waelz}$



c) $^{13}\text{Ni}/\text{WDL}$



e) $^{13}\text{Ni}/\text{Paval}$



e) 13Ni/PFS

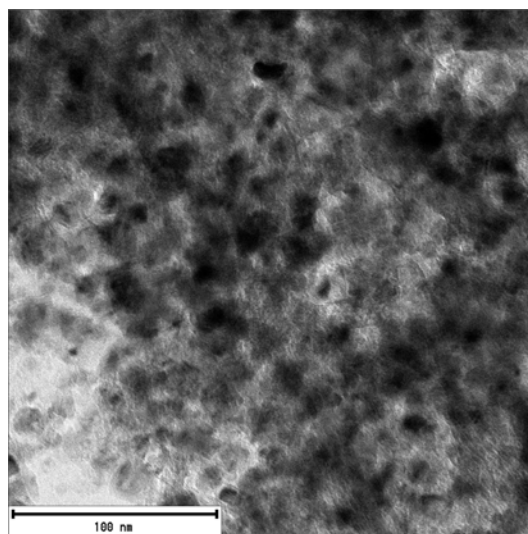


Figure 5.31. TEM micrographs of the catalysts over industrial residues as supports

Metallic particles could not be observed for the catalyst supported on FeSiMg, probably due to the poor contrast between nickel and one of the main components of the support, iron. For the catalysts supported on Waelz, WDL and Paval big clusters of nickel particles were observed. For the catalyst supported on PFS particles of different size could be observed, these particles were quite well dispersed even though some aggregated particles could also be observed. Particles could not be measured due to the fact that, as it has been previously mentioned, the number of observed particles was not enough to calculate a proper particle size distribution. However, the results obtained by TEM are in agreement with the ones obtained by other techniques and they confirm the previous statement about the average nickel crystallite size of the different catalysts.

5.2.2.8. XPS of the catalysts over industrial residues as supports

The species present in the surface of the fresh reduced catalysts were identified using XPS. For all the catalyst supported on industrial residues, nickel was measured as Ni^{2+} at two different core levels, $\text{Ni}2p_{3/2}$ and $\text{Ni}2p_{1/2}$, with two different contributions at each core level: a main peak and its satellite peak. The absence of metallic nickel (Ni^0) can be attributed, as it has been previously explained, to the oxidation of the fresh-reduced

samples due to the exposure to the atmosphere prior to the analysis. The main peak for the Ni2p_{3/2} core level was measured at a binding energy of approximately 855.0 eV while the satellite peak was measured at a binding energy of approximately 861.0 eV. The peaks corresponding to the Ni2p_{1/2} core level were measured at a binding energy of approximately 873.0 eV, the main one, and 880.0 eV the satellite peak. The slight differences in the binding energies of the different catalysts can be attributed to a different nickel-support interaction. As it has been previously explained, if the main peak of the Ni2p_{3/2} core level is located at binding energies lower than 855.0 eV, it means a weaker interaction between metal and support. The measured profiles are presented in Figure 5.21 while a summary of the binding energies is presented in Table 5.20.

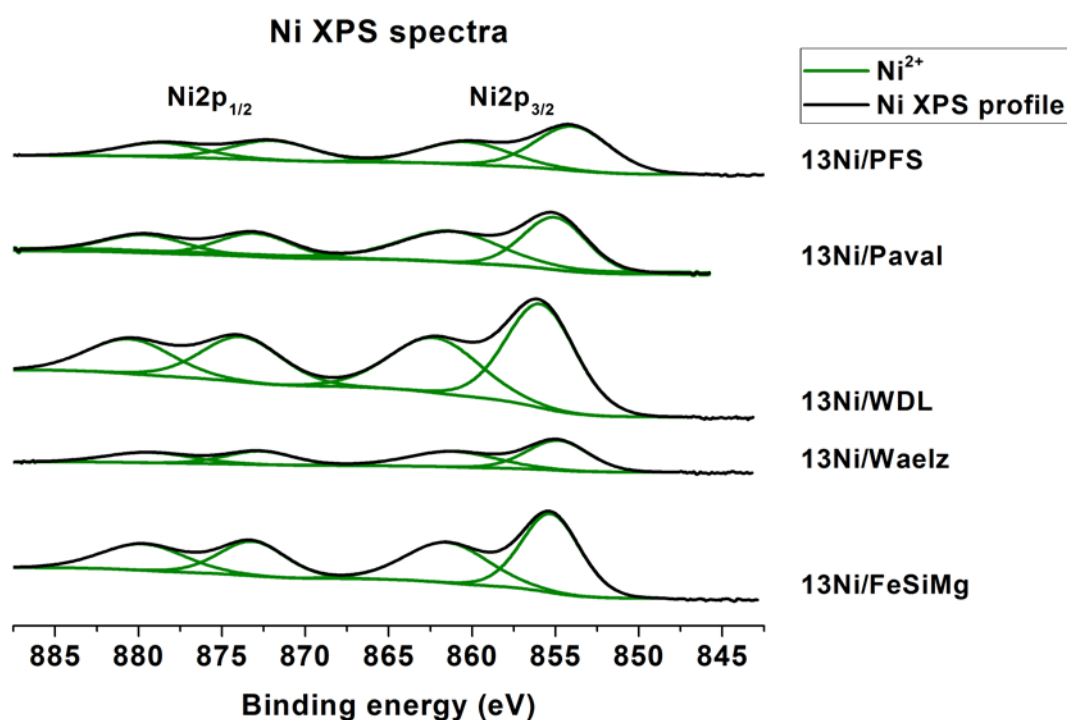


Figure 5.32. Ni XPS spectra of the catalysts over industrial residues as supports

Table 5.19. Binding energies (eV) XPS of the catalysts over industrial residues as supports

Catalyst	Ni ²⁺ (Ni2p _{3/2})	Ni ²⁺ (Ni2p _{3/2})	satellite	Ni ²⁺ (Ni2p _{1/2})	Ni ²⁺ (Ni2p _{1/2})	satellite
----------	--	--	-----------	--	--	-----------

13Ni/FeSiMg	855.3	861.5	873.2	879.7
13Ni/Waelz	854.9	861.2	872.7	879.4
13Ni/WDL	855.0	861.3	873.0	879.7
13Ni/Paval	855.9	862.2	873.8	880.5
13Ni/PFS	854.0	860.4	872.0	878.6

5.2.2.9. Activity tests of the catalysts over industrial residues as supports

The results obtained in the activity tests are shown in Figure 5.22. The results are compared with the values predicted by the thermodynamic equilibrium.

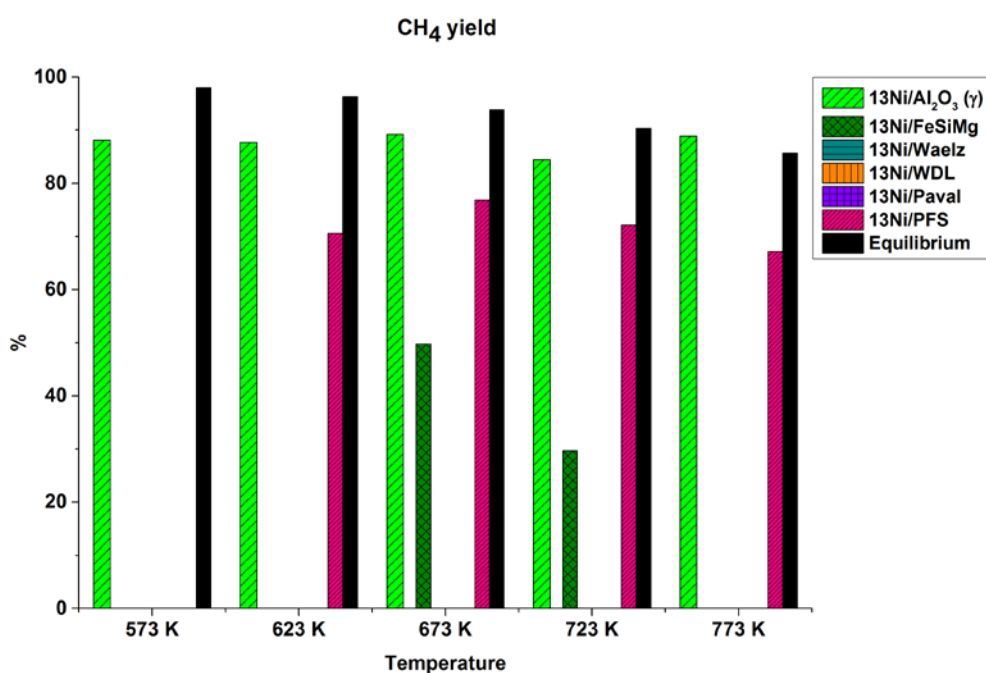


Figure 5.33. Activity results of the catalysts over industrial residues as supports

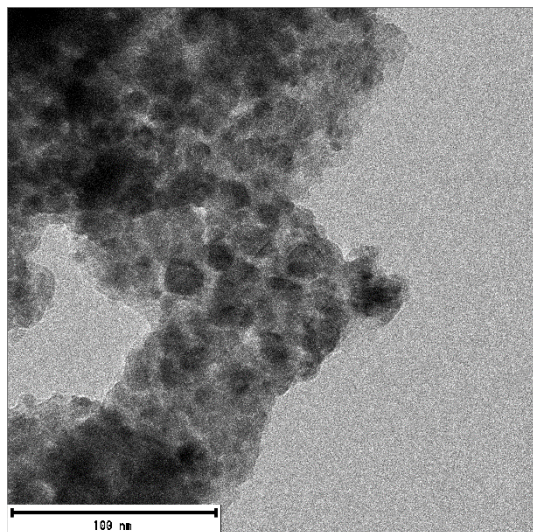
The catalyst supported on FeSiMg did not present catalytic activity until the reaction temperature was increased up to 673 K. At this temperature the obtained methane yield

was close to 50 %, far from the thermodynamic equilibrium though. A further increase of the temperature decreased the catalytic activity and at 773 K this was not observed. The catalysts supported on Waelz oxide, WDL and Paval did not present any catalytic activity at all the temperatures tested, thus they cannot be considered suitable supports for the synthesis of catalysts to be employed in CO₂ methanation process. Finally, the catalysts supported on PFS did not present catalytic activity at the lowest temperature tested but once the temperature was increased up to 623 K methane production could be observed, reaching its maximum at 673 K and decreasing when temperature was further increased. Even if the catalyst supported on PFS did not reach the thermodynamic equilibrium, it was not so far. Moreover, an additional advantage of this catalyst has to be considered: the use of an industrial residue for the synthesis of the catalyst, resulting in a cheaper catalyst and the valorisation of a residue.

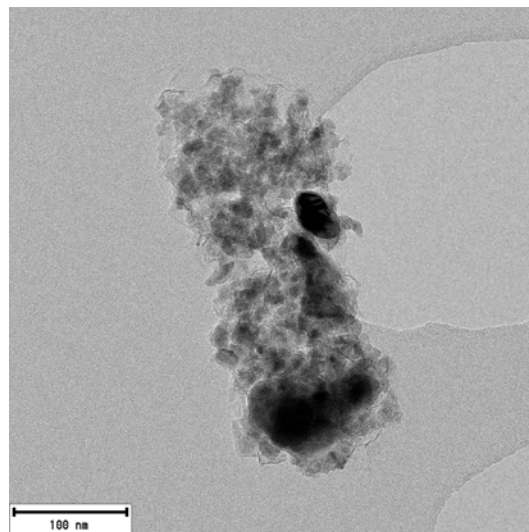
5.2.2.10. TEM of the spent catalysts over industrial residues as supports

The presence of coke and the changes in the structure after the activity tests were analysed by TEM. The obtained results are presented in Figure 5.23. For the catalyst supported on FeSiMg, as it happened for the fresh reduced catalyst, metallic particles could not be clearly distinguished due to the poor contrast between metal and support. The catalysts supported on Waelz, WDL and Paval presented big metallic particles, as it was observed previously for the same fresh reduced samples. All these samples also presented coke encapsulating the metallic particles. The ¹³Ni/PFS catalyst did not present any coke species after being employed in the activity tests, however the temperatures employed in the reaction had as a consequence the growing of the metallic particles and the formation of particle clusters.

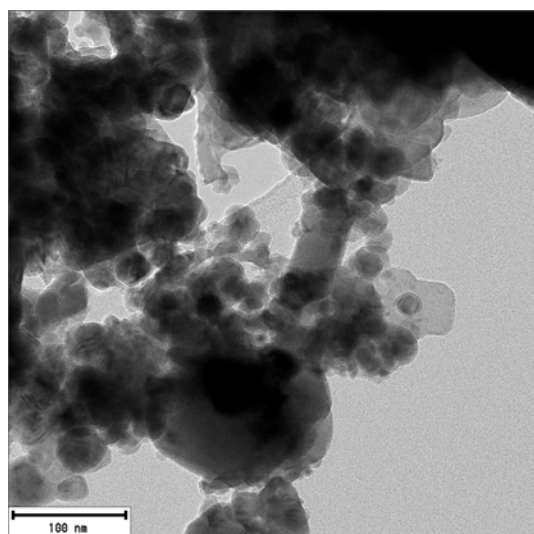
a) 13Ni/FeSiMg spent



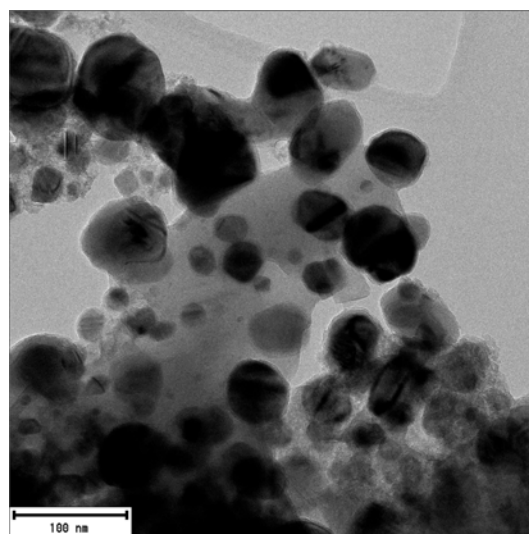
b) 13Ni/Waelz spent



c) 13Ni/WDL spent



d) 13Ni/Paval spent



f) $^{13}\text{Ni}/\text{PFS}$ spent

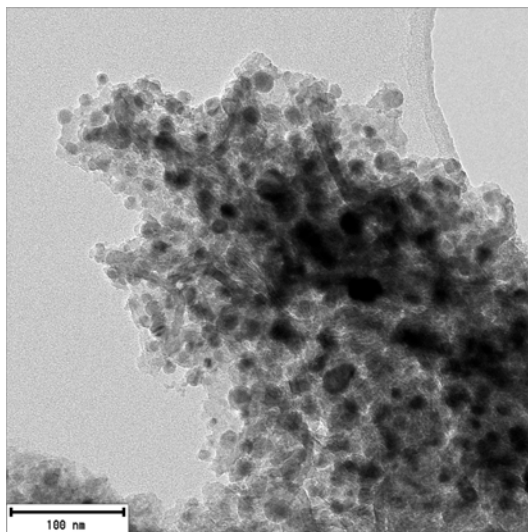


Figure 5.34. TEM micrographs of the spent catalysts over industrial residues as supports

5.2.2.11. XPS of the spent catalysts over industrial residues as supports

Spent catalysts over industrial residues as supports were analysed by XPS in order to detect carbon species on the surface. For the catalysts supported on FeSiMg, and Paval only one carbon specie was detected, graphitic carbon at a binding energy of approximately 284.6 eV. For the catalysts supported on Waelz and WDL, not only graphitic carbon at a binding energy of approximately 284.6 eV but also C=O at a binding energy of approximately 288.5 eV was measured, but the graphitic carbon was the main specie. All the catalysts presented a large amount of carbon on the surface; 37 wt % for the catalyst supported on FeSiMg, 66 wt % for the catalyst supported on Waelz, 55 wt % for the catalyst supported and 35 wt % for the catalyst supported on Paval. Surface carbon was not detected for the catalyst supported on PFS. The results obtained are presented in Figure 5.24.

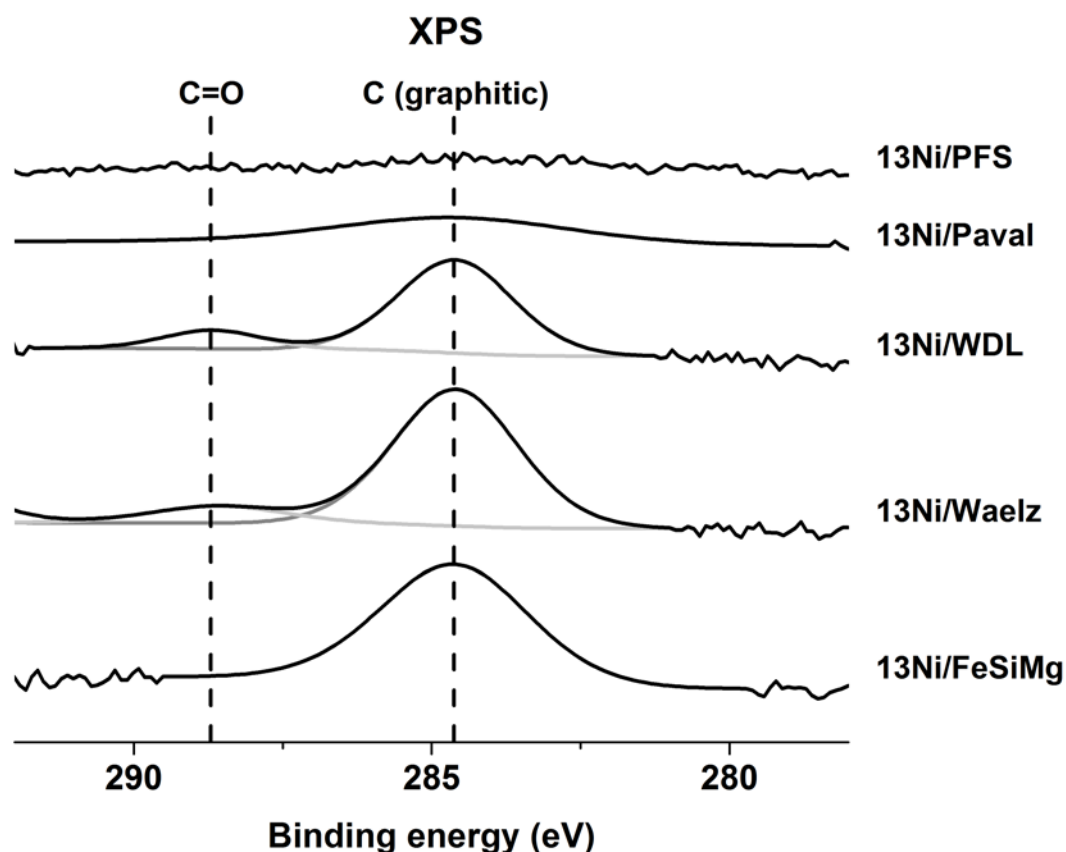


Figure 5.35. CXPS spectra of the spent catalysts over industrial residues as supports

5.2.2.12. Discussion of the catalysts over industrial residues as supports

It has been suggested that reducibility of the catalysts plays a crucial role in the catalytic activity, namely, the presence of nickel species with weak to medium interaction with the support. The sudden increase in the activity of the 13Ni/FeSiMg can be correlated to the presence of a large amount of NiO weakly interacting with the support with a high reduction temperature, which could be further reduced during the activity tests. Moreover, the composition of the support can provide some information about the results obtained: the support contained Mg, which is known to be a promoter of the carbon dioxide methanation reaction [53]. For the catalyst supported on Waelz the presence of a large amount of NiO without interaction with the support resulted in the null catalytic activity. Both the catalyst supported on WDL and Paval did not present any catalytic activity. For the one supported on WDL can be attributed to the abundant presence of NiO without interaction with the support. For the catalyst supported on

Paval, the high reduction temperature of the NiO weakly interacting with the support specie and the remarkable amount of NiO strongly interacting with the support resulted in the null catalytic activity. Lastly, the use of PFS as support resulted in a catalyst mainly formed by NiO weakly interacting with the support that together with other physicochemical properties of the catalyst gave as a result a catalyst with quite high activity.

The results obtained by XRD allow us to deepen in the correlations between the properties of the catalysts and their activity. In the case of the catalyst supported on FeSiMg it was due to the high reduction temperature of the main reducible specie. While both Waelz and WDL presented metallic nickel, according to the XRD measurements the lack of catalytic activity can be attributed to the big average nickel crystallite size. The catalyst supported on Paval did not present any metallic nickel, as expected by the high reduction temperature of the NiO weakly interacting with the support specie observed by TPR, ergo no active sites were accessible for carbon dioxide methanation reaction and catalytic activity was not observed. For the catalyst supported on PFS all the reducible species measured by TPR were easily reducible that resulted in the presence of metallic nickel with a small average crystallite size that led to the quite high catalytic activity observed.

Metallic dispersion was only measured for the catalyst supported on PFS. For all the other catalysts, not obtaining a value of the metallic dispersion by this technique can be attributed to a low metallic dispersion.

Results obtained by NH₃-TPD for the catalysts over industrial residues as supports proved that the catalyst supported on FeSiMg presented low acidity and an amount of high temperature acid sites higher than the optimum one, which according to the data obtained with the acidic supports was defined as approximately 60 %. However this catalyst presented activity at different temperatures, probably due to the presence of Mg that enhances the carbon dioxide methanation reaction [126]. The absence of acid character of the catalyst supported on Waelz, combined with its other physicochemical properties, resulted in a catalyst without any catalytic activity. Both the catalyst

supported on WDL and Paval presented approximately the same acidity, which was low, and were mainly composed by high temperature acid sites that resulted in the null catalytic activity. Finally, the catalyst supported on PFS presented a low acidity but the distribution of low/high temperature acid sites was close to the optimal one (low:high temperature acid sites 1:1.5) being this beneficial for the catalytic activity, explaining why this catalyst presented the highest catalytic activity at temperatures above 623 K when compared to all the catalysts over industrial residues as supports.

TEM micrographs further demonstrated the metallic dispersion of the catalysts, even if it was not measured by CO chemisorption. The influence of this parameter, metallic dispersion, on the performance of the catalysts was high as the catalyst that did not present metallic dispersion, neither presented catalytic activity.

The only nickel specie measured in the surface of the catalysts by XPS was Ni²⁺ for all the catalysts synthesised over industrial residues as supports.

The changes in the structure of the catalysts due to performing the carbon dioxide methanation reaction and the possible formation of coke on the catalysts, due to the presence of hydrocarbons in the reaction, were determined by characterising the spent catalysts by TEM and XPS.

The only catalyst that clearly suffered from sintering was 13Ni/PFS and this deactivation mechanism could be responsible of the lower catalytic activity of this catalyst once the reaction temperature was increased above 673 K, the temperature at which the maximum catalytic activity was observed. The fact that sintering was not observed for the other catalysts does not mean that they were resistant to this deactivation mechanism, but that the metallic particles of the fresh catalysts were so big that even if they grew after the activity tests this could not be observed.

To sum up with, both TEM and XPS over the spent catalysts proved the presence of a large amount of coke for the catalysts supported on FeSiMg, Waelz, WDL and Paval; as graphitic carbon for the 13Ni/FeSiMg and 13Ni/Paval catalysts and as both graphitic

carbon and C=O for the 13Ni/Waelz and 13Ni/WDL catalysts. In the case of the 13Ni/FeSiMg catalyst the decrease in the catalytic activity observed in the activity tests could be related to this presence of graphitic carbon on the surface of the catalyst. For all the other catalysts, none of them presented any catalytic activity so coking cannot be considered a deactivation mechanism, but it proves that instead of the carbon dioxide methanation reaction one of the possible side reactions, namely Boudouard reaction, was catalysed.

5.2.3. Natural supports

The use of natural supports for synthesising catalysts is a good alternative to the use of conventional supports, as natural ones are widely available and they are also cheaper.

A series of catalysts with a theoretical content of nickel of 13 wt % were prepared over different natural supports. These supports were: sepiolite, stevensite, attapulgite and Lava (from Mount Etna). As it has been done in the previous sections, the results obtained with the 13Ni/Al₂O₃ (γ) catalyst are included as a reference for comparison.

5.2.3.1. Chemical composition of the catalysts over natural supports

The real metallic content of the catalysts was determined by ICP-OES. The results are presented in Table 5.22. According to these, all the catalysts presented a metallic content close to the desired one (13 wt %), being the catalyst supported on sepiolite the one that presented the lowest nickel content among all the catalysts prepared with natural supports.

Table 5.20. ICP-OES of the catalysts over natural supports

Catalyst	Ni (wt %)
13Ni/Sepiolite	10.8

13Ni/Stevensite 11.4

13Ni/Attapulgite 11.9

13Ni/Lava 12.3

5.2.3.2. Structural properties of the catalysts over natural supports

The structural properties (BET surface area, pore volume and pore size) measured for these catalysts by N₂ adsorption-desorption isotherms are presented in Table 5.23.

Table 5.21. Structural properties of the catalysts over natural supports

Catalyst	BET surface area (m ² /g)	Pore volume (cm ³ /g)	Average pore size (nm)
Sepiolite	129	0.29	9.1
13Ni/Sepiolite	122	0.21	7.5
Stevensite	213	0.15	3.3
13Ni/Stevensite	140	0.19	5.8
Attapulgite	90	0.22	10.0
13Ni/Attapulgite	76	0.25	13.6
Lava	< 1	0.01	92.0
13Ni/Lava	3	0.01	15.1

For the catalysts supported on sepiolite, stevensite and attapulgite a decrease in the surface area was observed after the impregnation of the nickel, due to the metal blocking mesopores of the support. For the catalyst supported on sepiolite both the pore volume and the pore size decreased, while for the ones supported on stevensite and attapulgite these values were larger probably to being the smallest pores the ones blocked [127]. For the $^{13}\text{Ni}/\text{Lava}$ catalyst an increase in the surface area was observed after the impregnation procedure. This can be attributed to the nickel being impregnated in the outer surface of the support and creating new area.

5.2.3.3. TPR of the catalysts over natural supports

The reducible species and their reducibility were measured by TPR. So as to compare these results with the $^{13}\text{Ni}/\text{Al}_2\text{O}_3(\gamma)$ catalyst a dash line has been added to the figure to represent the temperature at which the main reduction peak of this catalyst was observed. These results are shown in Figure 5.25.

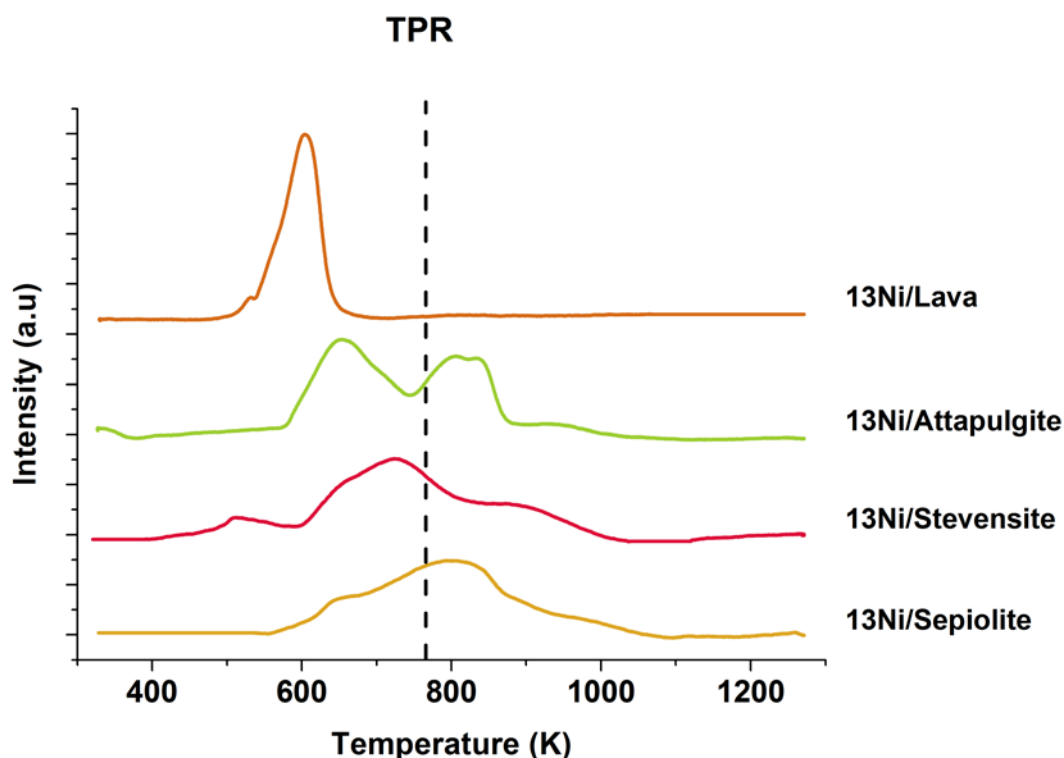


Figure 5.36. TPR profiles of the catalysts over natural supports

As it can be seen in the figure, the temperature of the main reduction peak for the 13Ni/Sepiolite catalyst was slightly shifted to higher temperature comparing with the catalyst supported on alumina (γ), thus, as it has been explained it was more difficult to reduce. The opposite behaviour was observed for the catalysts supported on stevensite and attapulgite, with the main reduction peak being shifted to lower temperatures. Finally, for the catalyst supported on lava this behaviour was more pronounced, presenting a sharp peak at approximately 600 K. All the reduction peaks presented were the result of the combination of different peaks. In order to analyse the influence of each peak, which correspond to different species, in the reduction profile deconvolution was carried out. Results are presented in Table 5.24.

Table 5.22. TPR peak deconvolution of the catalysts over natural supports

Catalyst	NiO	NiO interaction	weak NiO interaction	strong NiO interaction	Ni-support complex specie
13Ni/Sepiolite	649 K- 10.4 %	787 K-81.4 %		831 K-2.4 %	957 K-5.8 %
13Ni/Stevensite	647 K- 7.5 %	719 K-39.4 %		851 K-50.1 %	903 K-3.0 %
13Ni/Attapulgite	660 K- 53.4 %	804 K-38.1 %		843 K-3.9 %	938 K-4.6 %
13Ni/Lava	603 K- 100 %	-		-	-

The main nickel specie present in the catalyst supported on sepiolite was NiO weakly interacting with the support (> 81 %), while both NiO interacting strongly with the support and complex Ni-support specie were the less abundant ones. For the catalyst

supported on stevensite the main reducible specie was NiO strongly interacting with the support (> 50 %) together with NiO weakly interacting with the support (> 39 %) so the most abundant specie was one difficult to be reduced. When attapulgite was employed as catalytic support, NiO without interaction with the support was the main reducible specie (> 53 %) together with NiO with weak interaction with the support (> 38 %) whilst the hardest reducible species were the less abundant ones. Employing lava as support resulted in a catalyst with NiO without interaction with the support as the main, and only, reducible specie.

5.2.3.4. XRD of the catalysts over natural supports

XRD measurements were carried out to determine the main crystalline species in the fresh-reduced catalysts. The results are presented in Figure 5.26. As it can be observed all the catalyst presented a characteristic peak related to metallic nickel at approximately 45° so it can be confirmed the complete reduction of these catalysts. Another remarkable feature that can be clearly observed is the intensity of the peak corresponding to the catalyst supported on lava. This higher intensity, when compared with the other catalysts, is associated to bigger crystallites [128].

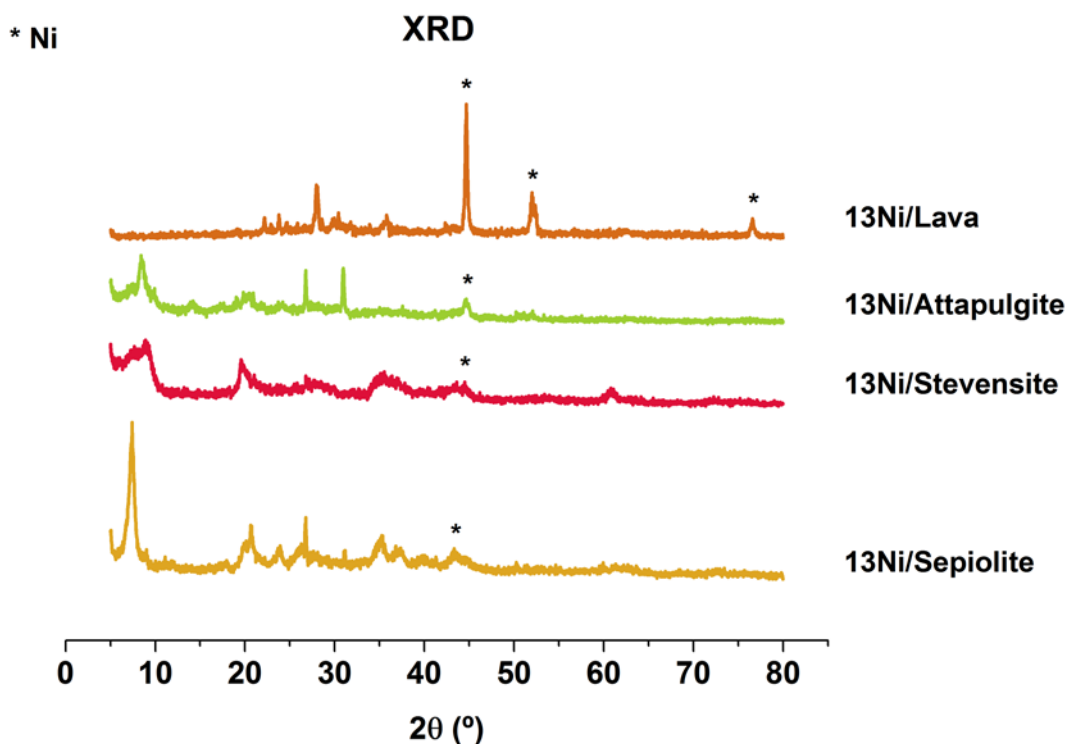


Figure 5.37. XRD profiles of the catalysts over natural supports

Results obtained by TPR are in good agreement with the ones obtained by XRD. The catalyst supported on sepiolite, that contained easily reducible species was completely reduced. For the catalyst that contained hardly reducible nickel species as the most abundant ones, namely 13Ni/Stevensite catalyst, nickel was detected by XRD meaning that reduction was achieved probably due to the fact that even though it was composed by hardly reducible species it also presented a remarkable amount of NiO weakly interacting with the support. The 13Ni/Attapulgite catalyst presented the same behaviour as the one supported on sepiolite because, even if at a different proportion, it was also composed by nickel species that were easy to reduce. Finally, the catalyst supported on lava only presented a nickel specie according to TPR results: NiO not interacting with the support, thus, the nickel specie that is most easily reduced which is in agreement with XRD results as different peaks related to metallic nickel could be observed.

Scherrer equation was applied to the most intense nickel peak obtained by XRD for each catalyst in order to calculate the average crystallite size. These results can be observed in Table 5.25.

Table 5.23. Average nickel crystallite size of the catalysts over natural supports

Catalyst	Average nickel crystallite size (nm)
13Ni/Sepiolite	28
13Ni/Stevensite	32
13Ni/Attapulgite	31
13Ni/Lava	49

The catalyst supported on sepiolite presented the smallest average nickel crystallite size, while the catalyst supported on stevensite and attapulgite presented higher average nickel crystallite size. As expected by the sharp peak observed in the XRD profile, the 13Ni/Lava catalyst presented the largest average nickel crystallite size.

5.2.3.5. Metallic dispersion of the catalysts over natural supports

Metallic dispersion was measured using CO pulse chemisorption technique. Results are presented in Table 5.26.

Table 5.24. Metallic dispersion of the catalysts over natural supports

Catalyst	Metallic dispersion (%)
13Ni/Sepiolite	0.5
13Ni/Stevensite	0.2
13Ni/Attapulgite	0.3
13Ni/Lava	-

The catalyst supported on sepiolite presented the highest metallic dispersion. The catalyst supported on stevensite and the one supported on attapulgite presented approximately the same metallic dispersion. Regarding to the catalyst supported on lava, the metallic dispersion obtained can be considered null. These results are in agreement with the results obtained by XRD, as the catalyst that presented the smallest average crystallite size presented the highest metallic dispersion.

5.2.3.6. Acidity of the catalysts over natural supports

NH₃-TPD was the technique employed to measure the acidity of the catalysts supported on natural supports. The results obtained are presented in Figure 5.27.

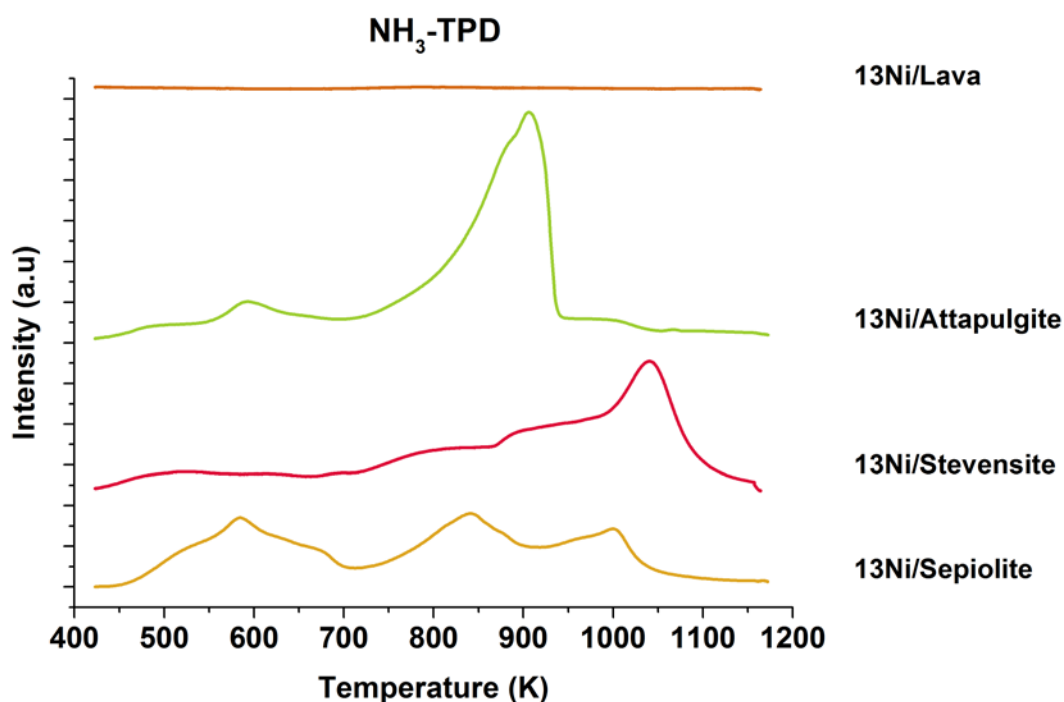


Figure 5.38. NH₃-TPD profiles of the catalysts over natural supports

The catalyst supported on sepiolite presented a heterogeneous desorption profile with three different peaks located at approximately 600 K, 850 K and 1000 K. The 13Ni/Stevensite catalyst presented a wide peak in the range 700-1100K with the maximum located at approximately 1050 K. For the catalyst supported on attapulgite a small peak was measured at approximately 600 K and a more intense peak was measured at approximately 900 K. Finally, using lava as support resulted in a catalyst without acid character as it can be seen in the flat profile depicted in the figure. The comparison between the acid characters of the different catalysts was carried out with the methodology explained previously: attributing the peaks at temperatures lower than 723 K to low temperature acid sites and correlating the peaks at temperatures above this to high temperature acid sites. The distribution of the different acid sites and the NH₃ amount adsorbed by each catalyst are presented in Table 5.27.

Table 5.25. Distribution of the acid sites of the catalysts over natural supports

Catalyst	Low temperature acid sites (%)	High temperature acid sites (%)	Adsorbed NH ₃ amount (mmol/g _{cat})
13Ni/Sepiolite	37.6	62.4	2.7
13Ni/Stevensite	13.4	86.6	6.5
13Ni/Attapulgite	16.1	83.9	3.3
13Ni/Lava	-	-	-

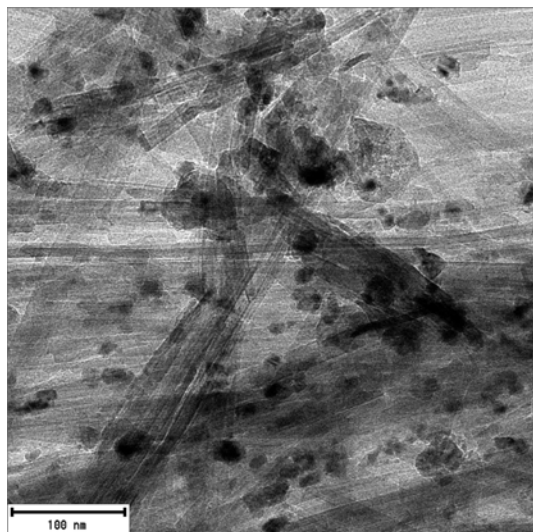
It can be seen that, except for lava that did not present any acidic property, all the other catalysts presented a strong acid character even stronger than the supports previously classified as “acidic supports”. However, due to the natural procedure of these ones and the conventional commercial nature of the others they were separated in two different categories in order to establish a better comparison during this PhD thesis.

Having said that, the catalyst supported on sepiolite presented the weakest acid character of them, however it presented the optimal distribution of acid sites (low:high temperature 1:1.5) as concluded for the catalysts prepared over acidic supports. The 13Ni/Stevensite catalyst presented the strongest acid character, being most of the acid sites measured at high temperatures. This kind of acid sites were also the dominant ones for the catalyst support on attapulgite, however its acid character was weaker.

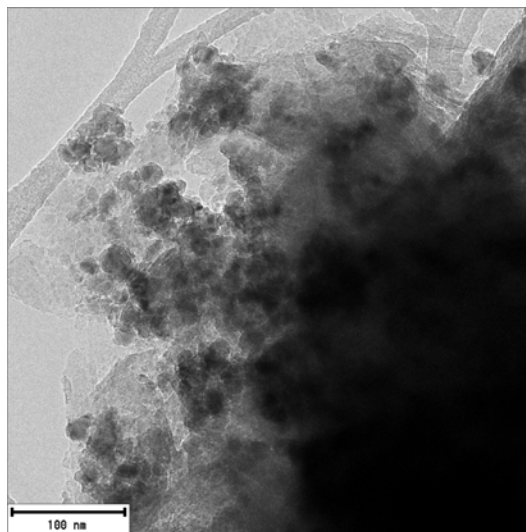
5.2.3.7. TEM of the catalysts over natural supports

Micrographs of the catalysts prepared over natural supports were taken by TEM technique in order to gain a better understanding about the structure of the catalyst and the metal-support interactions. Results obtained are presented in Figure 5.28.

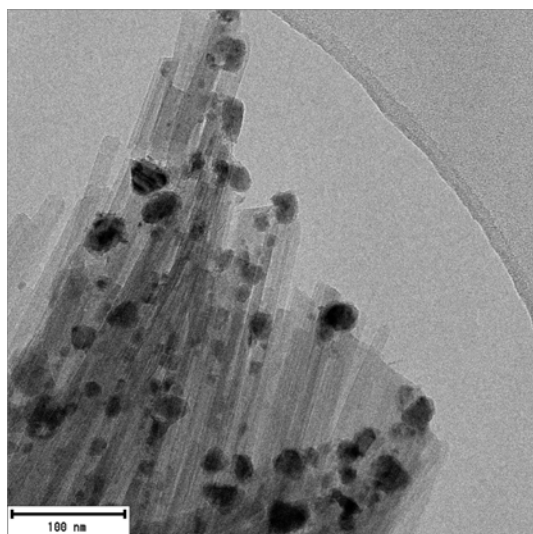
a) 13Ni/Sepiolite



b) 13Ni/Stevensite



c) 13Ni/Attapulgite



d) 13Ni/Lava

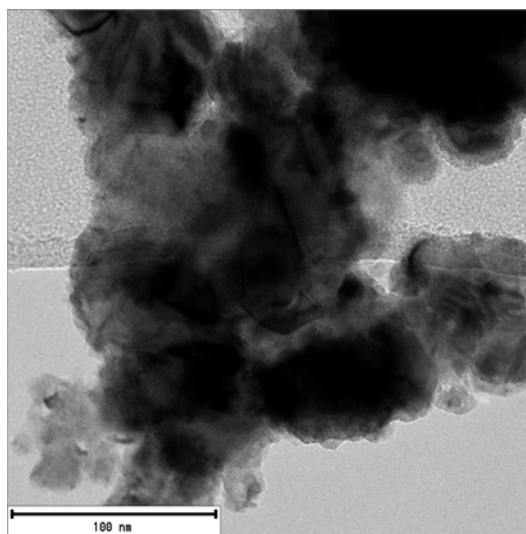


Figure 5.39. TEM micrographs of the catalysts over natural supports

As it can be seen, a homogeneous particle distribution with small particles well dispersed was obtained for the catalyst supported on sepiolite. The one supported on stevensite, on the contrary, presented big metallic particles that can be associated with a poor dispersion. The behaviour of the catalyst supported on attapulgite was close to the one supported on sepiolite, with small metallic particles well dispersed, nevertheless they

were bigger than the ones observed for the former. Using lava as a support resulted in the formation of big chunks of nickel, being the dispersion for this catalyst low.

As it has been previously explained, the small amount of particles to be measured would result in a huge error so that particles were not measured as the particle size distribution would not be representative. However, the differences observed in the micrographs are in agreement with the statements made with the results obtained for the average nickel crystallite size, measured by XRD, and the metallic dispersion measured by CO chemisorption.

5.2.3.8. XPS of the catalysts over natural supports

Fresh-reduced catalysts over natural supports were analysed by XPS in order to detect the species presents on the surface of the catalysts. In all the cases nickel was detected as Ni^{2+} with a main peak and a satellite peak for two different core levels: $\text{Ni}2p_{3/2}$ and $\text{Ni}2p_{1/2}$. In all the cases the main peaks were measured at a binding energy of approximately 855.0 eV, for the $\text{Ni}2p_{3/2}$ core level, and 873.0 eV for the $\text{Ni}2p_{1/2}$ core level while the satellite peaks were measured at a binding energy of approximately 860.0-862.0 eV and 880.0 eV for the different core levels. The measured profiles are presented in Figure 5.29 while a summary of the binding energies measured can be observed in Table 5.28.

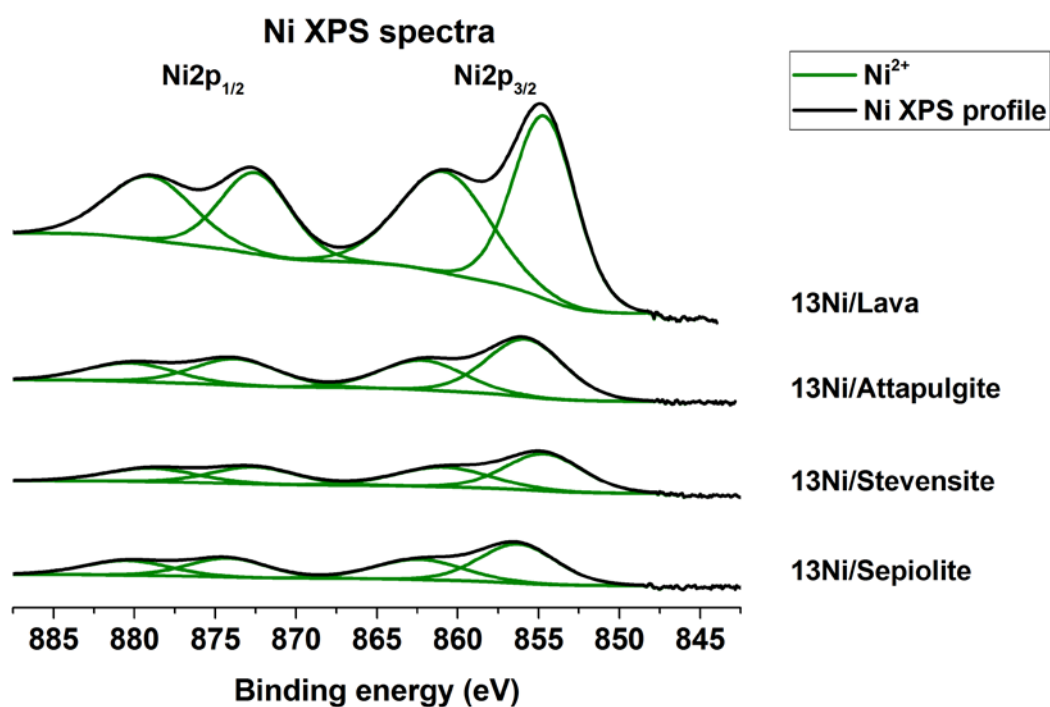


Figure 5.40. Ni XPS spectra of the catalysts over natural supports

Table 5.26. Binding energies (eV) XPS of the catalysts over natural supports

Catalyst	Ni ²⁺ (Ni2p _{3/2})	Ni ²⁺ (Ni2p _{3/2}) satellite	Ni ²⁺ (Ni2p _{1/2})	Ni ²⁺ (Ni2p _{1/2}) satellite
13Ni/Sepiolite	856.3	862.4	874.2	880.4
13Ni/Stevensite	854.7	860.9	872.6	879.0
13Ni/Attapulgite	855.8	862.2	873.7	880.2
13Ni/Lava	854.6	860.8	872.5	879.0

5.2.3.9. Activity tests of the catalysts over natural supports

The results obtained in the activity tests are presented in Figure 5.30. The results are compared with the values predicted by the thermodynamic equilibrium.

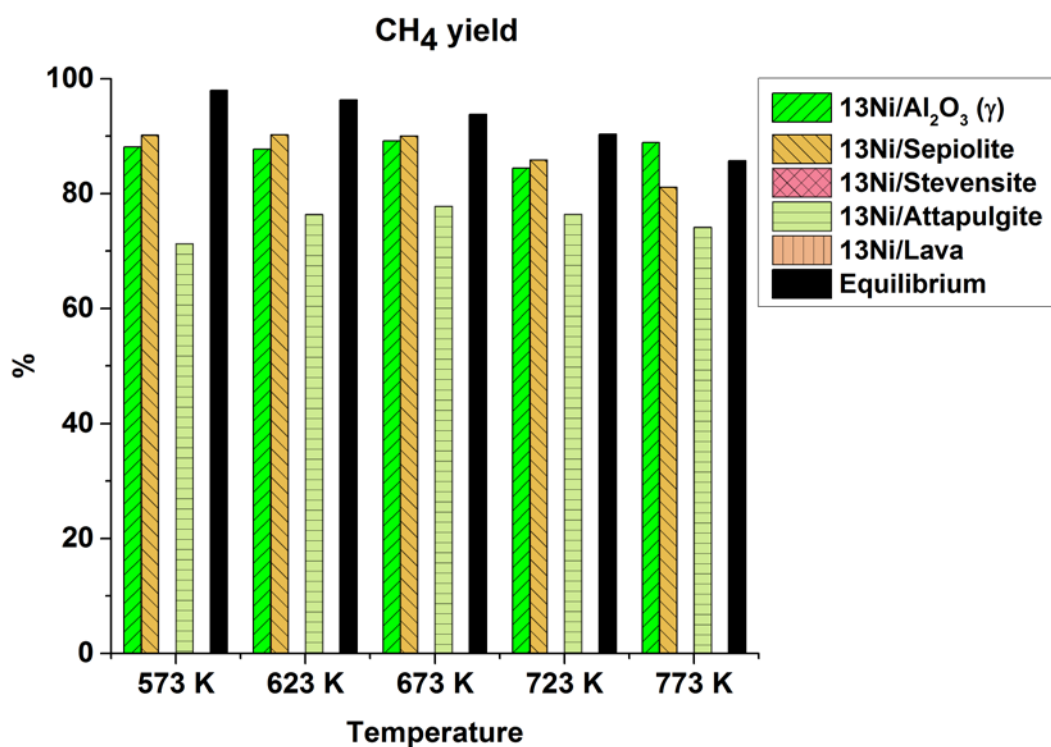


Figure 5.41. Activity results of the catalysts over natural supports

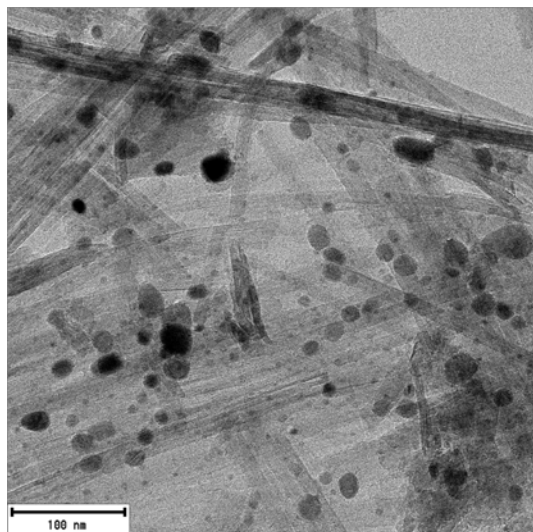
The catalyst supported on sepiolite presented high catalytic activity at all the temperatures tested, being close to the thermodynamic equilibrium at all these temperatures. Comparing with the catalyst supported on alumina (γ) the catalyst supported on sepiolite presented slightly higher catalytic activity at all the temperatures tested apart from the highest one, however being both catalysts close to the thermodynamic equilibrium was not possible to establish comparisons between them. Regarding to the catalyst supported on stevensite, catalytic activity was not observed at any of the temperatures tested. Catalytic activity was observed at all the temperatures tested for the 13Ni/Attapulgite catalyst but the values obtained were not close to the thermodynamic equilibrium, thus, its performance was worse than the presented by the catalysts supported on alumina (γ) and sepiolite. However, it could be considered a promising alternative support to the conventional ones, as it presented average catalytic activity at a low price. Finally, the catalyst supported on lava did not present any catalytic activity at all the temperature tested, so it cannot be considered a useful support for carbon dioxide methanation process.

5.2.3.10. TEM of the spent catalysts over natural supports

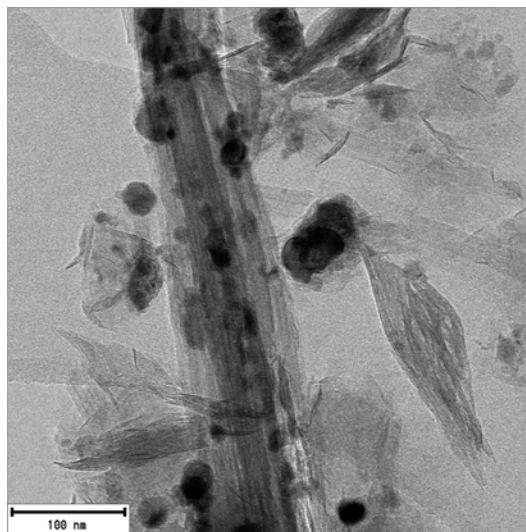
The possible presence of coke and the changes in the structure of the catalysts after performing the activity tests were measured by TEM, being these results presented in Figure 5.31. These micrographs were taken to analyse the changes in the structure of the catalysts after the activity tests but also to determine if coke was formed due to the presence of hydrocarbons in the reaction. As it can be observed, the catalyst supported on sepiolite suffered both from coke deposition, in form of coke encapsulating the metallic nickel, and growth of the metallic particles due to sintering. However, none of the deactivation mechanisms were so important and both small particles, well dispersed, and particles not being encapsulated by nickel were mostly observed in the micrograph.

For the ^{13}Ni /Stevensite catalyst mostly big and poorly dispersed particles were observed, as expected due to the structure of the catalyst prior to the activity tests. Coke was also observed for this catalyst, encapsulating the metallic particles too. The catalyst supported on attapulgite also presented growth of the particles, being some of them encapsulated by coke. Finally, growth of the particles could not be appreciated for the catalyst supported on lava as it already presented big, not dispersed, particles before performing the activity tests. However, carrying out the activity tests with this ^{13}Ni /Lava catalyst had as a consequence a great formation of coke, which can be observed in the picture encapsulating most of the particles present in the image.

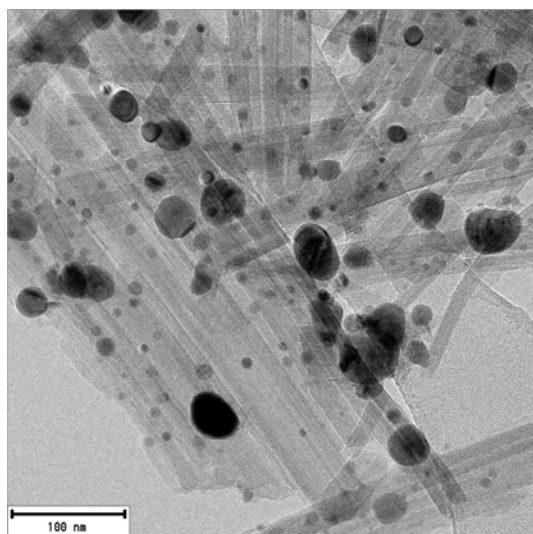
a) ^{13}Ni /Sepiolite spent



b) ^{13}Ni /Stevensite spent



c) ^{13}Ni /Attapulgite spent



d) ^{13}Ni /Lava spent

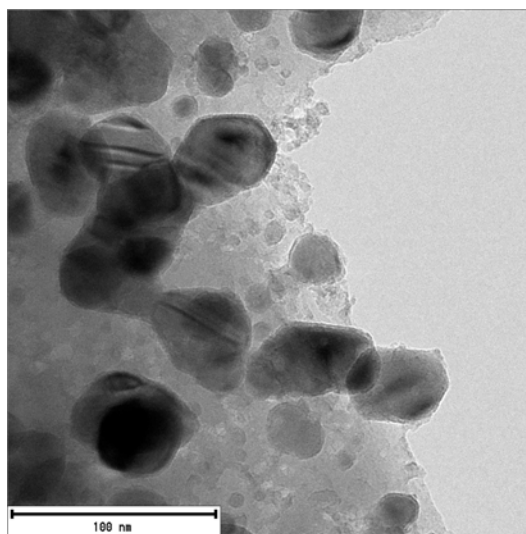


Figure 5.42. TEM micrographs of the spent catalysts over natural supports

5.2.3.11. XPS of the spent catalysts over natural supports

The amount of carbon on the surface of the catalysts over natural supports was measured by XPS. For all the catalysts unique carbon specie was detected, graphitic carbon at a binding energy of 284.6 eV. While for the catalysts supported on sepiolite, stevensite and attapulgite the amount detected was of approximately 9 wt %, the

catalyst supported on lava presented a great amount of graphitic carbon, approximately 47 wt %. The results are presented in Figure 5.32.

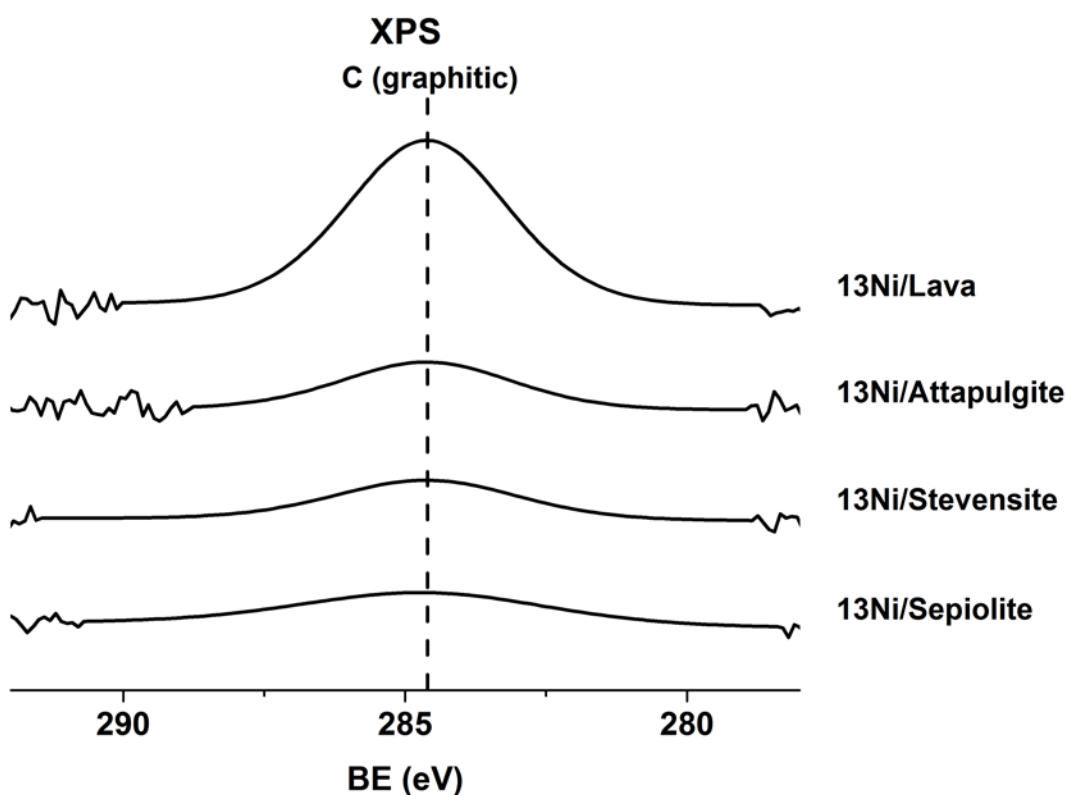


Figure 5.43. C XPS spectra of the spent catalysts over natural supports

Sintering was observed for all the catalysts by TEM, however it did not have much influence on the activity of the catalysts as both the catalyst supported on sepiolite and attapulgite did not present a noticeable decrease in their catalytic activity when the reaction temperature was increased while performing the activity tests. As the 13Ni/Stevensite and 13Ni/Lava catalysts did not present any catalytic activity, the sintering observed by TEM was not considered in the activity tests as a deactivation mechanism.

5.2.3.12. Discussion of the catalysts over natural supports

The results obtained for the structural properties of the catalysts proved that in all of them, but the one supported on lava, the nickel was impregnated inside the porous structure of the support, resulting in a catalyst with a lower surface area than the bare

support. For the catalyst supported on sepiolite, the decrease in the pore volume and the average pore size can be attributed to the fact of the biggest pores being blocked while the opposite trend was observed for the catalysts supported on stevensite and attapulgite. For the latter, the increase in the values of the pore volume and the average pore size are attributed to the smallest pores being blocked by the nickel. The presence of the nickel in smaller pores results in a slower diffusion than the one that can be achieved in larger mesopores, thus, a worse catalytic activity [96].

The measurements of the reducibility of the different catalysts proved again, as it happened for all the catalysts previously explained, the great influence of the NiO with weak interaction with the support on the catalytic activity. The catalyst supported on sepiolite, which was the one that presented the highest catalytic activity among all the catalysts over natural supports, presented a great amount of this NiO specie. For the 13Ni/Stevensite catalyst the lack of catalytic activity can be attributed to the large amount of NiO with strong interaction with the support. Being NiO without interaction with the support the main specie measured for the catalyst supported on attapulgite hindered its catalytic activity, however it presented a large amount of NiO with weak interaction with the support that performed as the active site for the CO₂ methanation process. Finally, the catalyst supported on Lava only presented NiO without interaction with the support, resulting in a catalyst without any activity.

Results obtained by XRD proved that all the catalysts were reduced, as metallic nickel was detected for all of them. Whilst the ability to achieve the reduction can be explained for the catalysts supported on sepiolite, attapulgite and lava, due to being composed mainly by easy to reduce nickel species, a different approach is needed for the catalyst supported on stevensite. In this case, although the main nickel species detected for the catalyst were the ones with strong interaction with the support, they were measured at low temperatures so they could still be reduced. The average nickel crystallite size calculated with the Scherrer equation showed that the catalyst supported on sepiolite, the one that presented the best catalytic activity, presented the smallest average nickel crystallite size. The catalysts supported on stevensite and attapulgite roughly presented

differences on their average nickel crystallite size, while the largest one was measured for the catalyst supported on lava.

Although average nickel crystallite size can be used to estimate the metallic dispersion, this was measured by CO chemisorption. The results obtained with this technique sustained the estimations that were previously made. The catalyst supported on sepiolite presented the highest metallic dispersion, with the catalyst supported on stevensite and attapulgite showing approximately the same value and the one supported on lava presenting a value of the metallic dispersion that can be considered low. The obtained results are in accordance with the assumption that a higher metallic dispersion is beneficial for the performance of the catalyst in the studied reaction.

When using the acidity data retrieved to understand the catalytic activity of the catalysts, the results obtained by the catalyst supported on sepiolite are useful to confirm that there is an optimal low:high temperature acid sites ratio, being this close to 1:1.5, together with an overall moderate acidity. As it was observed for the catalysts over acidic supports and the catalysts using industrial residues as supports, an increase in the amount of high temperature acid sites is detrimental for the catalytic activity, as it was observed both for the catalyst supported on stevensite and attapulgite. This effect was more pronounced for the catalyst supported on stevensite, which did not present any catalytic activity. This cannot only be attributed to the really strong acid character measured, that could inhibit the adsorption of CO₂, but also to the sum of all the other measured physicochemical properties.

The different metallic dispersion, approximately calculated by XRD and quantitatively measured by CO chemisorption, were further proved by TEM. With the micrographs obtained by this technique the dispersion of the metal over the surface of the support was clearly observed. It has been previously concluded, the higher the metallic dispersion, the better the performance of the catalyst on the carbon dioxide methanation reaction. However, other parameters must also be taken into account and even if it does enhance the catalytic activity, it cannot ensure a high catalytic activity if other physicochemical parameters hinder the performance of the catalyst.

The catalysts over natural supports only presented Ni^{2+} in the surface, as it was concluded by XPS.

TEM and XPS measurements were also performed for the spent catalysts in order to observe changes in their structure after the activity tests or determine if coke was formed after performing the carbon dioxide methanation reaction.

The presence of coke, observed by TEM, was further proved by XPS. The catalysts supported on sepiolite, stevensite and attapulgite presented a low amount of graphitic coke on the surface ($\approx 10\%$) that in any of the cases resulted in a decreased of the catalytic activity. However, for the catalyst supported on stevensite could be correlated to this catalyst favouring the Boudouard reaction instead of the desired carbon dioxide methanation reaction. This behaviour was more explicit for the $^{13}\text{Ni}/\text{Lava}$ that presented approximately a 50 % of graphitic carbon on the surface.

Even though, neither sintering nor coking seemed to decrease the catalytic activity of the $^{13}\text{Ni}/\text{Sepiolite}$ and $^{13}\text{Ni}/\text{Attapulgite}$ catalyst, it has to be taken into account that the activity tests were carried out only during 450 minutes. The presence of both deactivation mechanisms suggests that the stability of the catalysts could be compromised if the reaction time was increased.

5.3. Stability tests

Stability tests were carried out with the catalysts that presented the best results during the activity tests in fixed bed reactors, namely, $^{13}\text{Ni}/3\text{Cr-4Zr-Al}_2\text{O}_3$ (γ) and $^{13}\text{Ni}/\text{Sepiolite}$. The stability tests were carried out during 25 hours at 573 K, results are presented in Figure 5.33. A black line representing the thermodynamic equilibrium at 573 K is added for comparison.

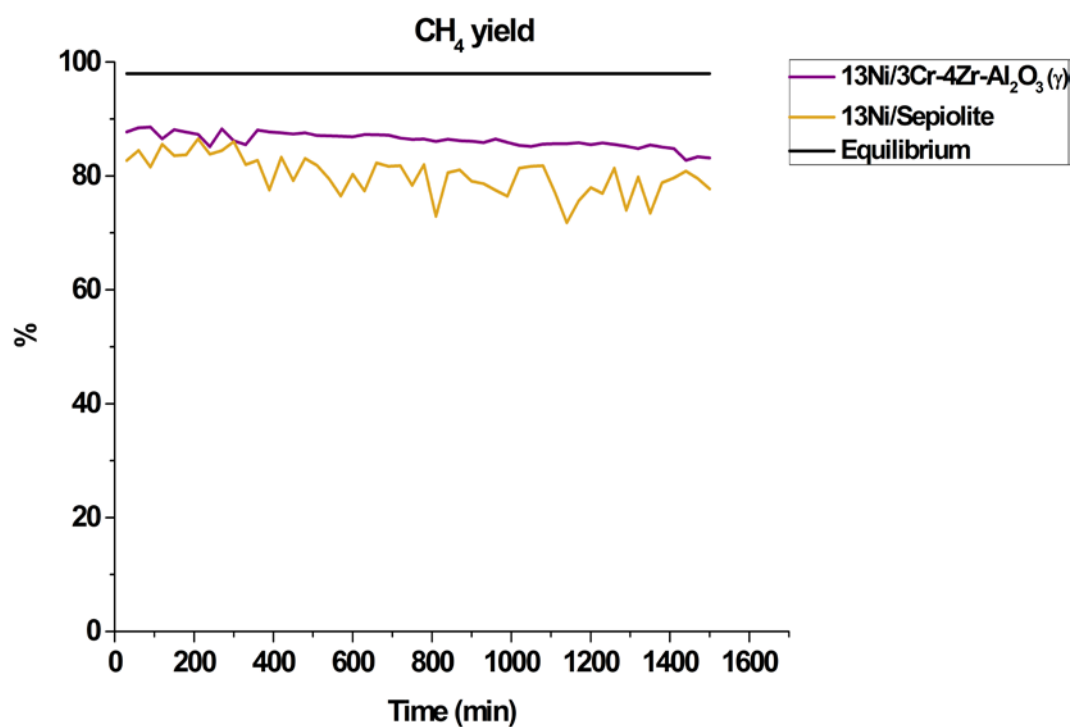


Figure 5.44. 25 h activity test

The catalyst supported on chromium-zirconium modified alumina (γ) was stable during 25 hours, and it approximately maintained its initial activity after 25 hours. Regarding to the catalyst supported on sepiolite, its performance was more unstable as its activity fluctuated during 25 hours. In order to obtain a better comparison, these catalysts were tested during 120 hours and the WHSV was doubled in order to accelerate the deactivation of the catalysts. The results are presented in Figure 5.34, the thermodynamic equilibrium is included as reference.

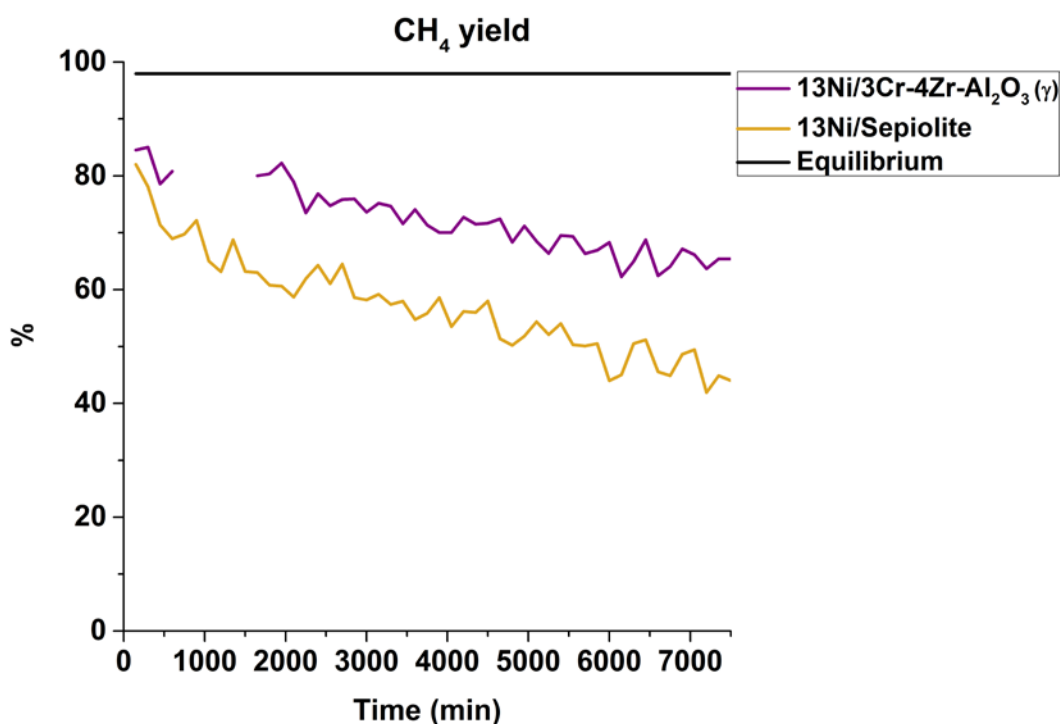


Figure 5.45. 120 h activity test

As it can be seen, 120 hours on stream resulted in fluctuating activity for both catalysts. Both catalysts presented approximately the same initial activity, however the final one was lower for the catalyst supported on sepiolite. This proves that the catalyst supported on chromium-zirconium modified alumina (γ) performs better than the catalyst supported on sepiolite for longer activity test runs. Regarding to the blank range for the catalyst supported on chromium-zirconium modified alumina (γ) is attributable to an experimental error that did not allow recording the results.

Now that the loss of activity after 25 hours and 120 hours runs has been presented, another interesting feature of these catalysts is the average CH₄ yield during those activity tests. These results are shown in Table 5.30.

Table 5.27. Average CH₄ yield stability tests

Catalyst	Average CH ₄ yield 25 h (%)	Average CH ₄ yield 120 h (%)
13Ni/3Cr-4Zr-Al ₂ O ₃ (γ)	86.3	71.9
13Ni/Sepiolite	80.1	57.1

As it has been previously mentioned, during the 25 hours stability test both catalysts presented close performances even though the one supported on chromium-zirconium modified alumina (γ) was the best. After 120 hours on stream and at double WHSV activity test, both catalysts presented a decrease in their catalytic activity being it more pronounced for the catalyst supported on sepiolite.

5.4. Catalysts for photoreactors

The photocatalysts tested can be divided in two different groups: gold and silver based photocatalysts. Due to the fact that the experimental setup for the photocatalytic methanation reactor was different to the one carried out both in fixed bed and microreactors, comparisons cannot be established between the results previously presented and the ones that will be presented in the following sections.

5.4.1. Gold based photocatalysts

Two different catalysts with a theoretical content of gold of 5 wt % were prepared by deposition-precipitation method, using flame spray pyrolysis (FSP) SiO₂ as catalytic support. One of the prepared catalysts also had a theoretical loading of nickel of 5 wt %. To analyse the interaction between gold and nickel, another catalyst containing only a theoretical amount of nickel of 5 wt % was prepared by the same method as reference.

5.4.1.1. Chemical composition of the gold based photocatalysts

ICP-OES technique was employed to determine the chemical composition of the photocatalysts. According to the results obtained all the catalysts presented a loading of the different metals, nickel and/or gold, close to the desired one. These results can be observed in Table 5.31.

Table 5.28. ICP-OES of the gold based photocatalysts

Catalyst	Ni (wt %)	Au (wt %)
5Ni/SiO ₂	4.4	-
5Au/SiO ₂	-	4.2
5Ni-5Au/SiO ₂	5.4	5.0

5.4.1.2. Structural properties of the gold based photocatalysts

The only structural property measured by N₂ adsorption-desorption isotherms for the gold photocatalysts was BET surface area, regarding to the fact that the supports prepared by FSP are non-porous so parameters like the pore volume and the average pore size were not measured. The results obtained are presented in Table 5.32.

Table 5.29. Structural properties of the gold based photocatalysts

Catalyst	Surface area (m ² /g)
SiO ₂	344
5Ni/SiO ₂	257

5Au/SiO ₂	262
----------------------	-----

5Ni-5Au/SiO ₂	285
--------------------------	-----

The SiO₂ support prepared by FSP presented a high surface area, this surface area decreased after the loading of the different metals. The monometallic catalysts presented approximately the same surface area while the value was higher for the bimetallic catalyst, however the difference was not significant. The decrease in the surface area after the loading of the metals could be attributed to interparticle blocking, providing that FSP supports do not present pores to be blocked.

5.4.1.3. TPR of the gold based photocatalysts

Information about the reducibility and the reducible species of these catalysts was obtained by TPR. The results obtained for these catalysts are presented in Figure 5.35.

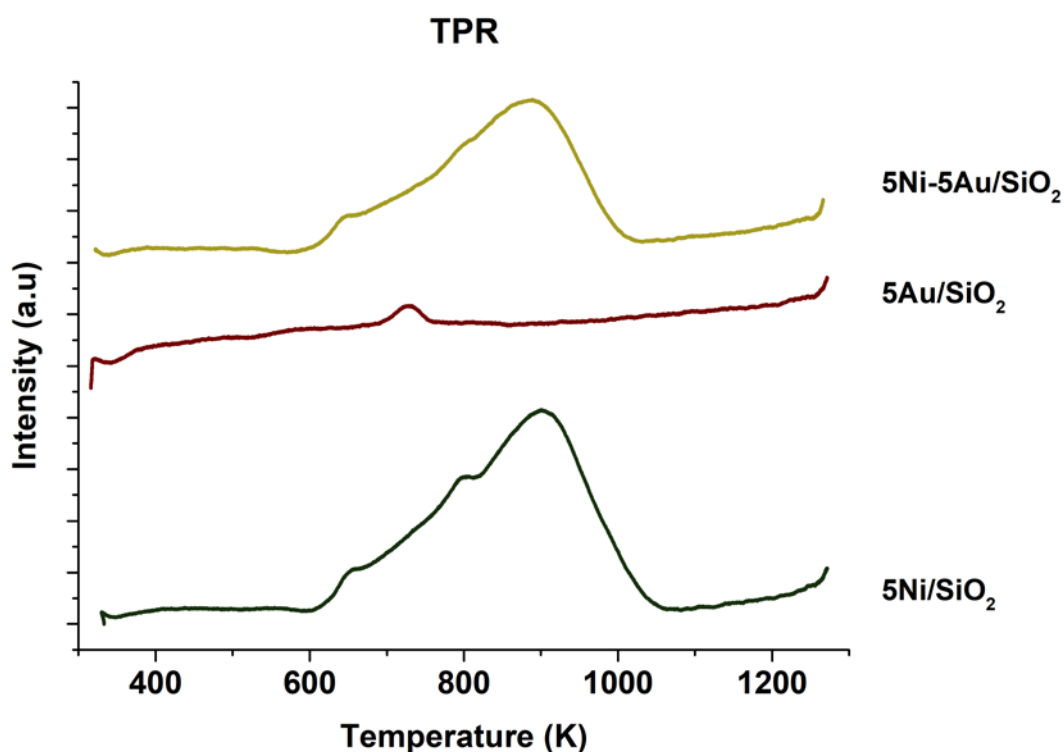


Figure 5.46. TPR profiles of the gold based photocatalysts

As it can be seen, the main reduction peak for the monometallic nickel catalyst was located at approximately 900 K. The monometallic gold presented a small reduction peak at approximately 700 K, however this peak cannot be attributed to the reduction of gold, which is usually located at approximately 423 K [129], but to a possible excess of urea after the synthesis of the catalyst. The reduction profile of the bimetallic nickel-gold catalyst implies the interaction between nickel and gold, as the reduction peak is slightly shifted to lower temperatures when comparing with the monometallic nickel catalyst. All the reduction peaks presented were the result of the combination of different peaks. In order to analyse the influence of each peak, which correspond to different species, in the final reduction profile deconvolution was carried out. Results are presented in Table 5.33.

Table 5.30. TPR peak deconvolution of the gold based photocatalysts

Catalyst	NiO	NiO	weak interaction	NiO interaction	strong interaction	Ni-support complex specie
5Ni/SiO₂	653 K-2.8 %	707 K-8.6 %		784 K-19.6 %		902 K-69.0 %
5Ni-5Au/SiO₂	646 K-2.6 %	698 K-8.1 %		804 K-39.0 %		903 K-50.3 %

The monometallic nickel catalyst presented a Ni-support complex specie as the main one (> 68 %) followed by NiO with strong interaction with the support (> 19 %). For the bimetallic nickel-gold catalyst, the Ni-support complex specie was the main one too (> 50 %), however the addition of gold change the interaction of the different species with the support and it presented a higher amount of NiO with strong interaction with the support (> 39 %).

5.4.1.4. XRD of the gold based photocatalysts

XRD measurements were carried out to determine the main crystalline species in the fresh-reduced catalysts. The results are presented in Figure 5.36. Metallic nickel was not observed for any of the catalyst, but NiO was. As it can be observed all the gold containing catalyst presented several peaks related to metallic gold, being the main one located at approximately 37°. The hump observed at approximately 20° is attributed to the amorphous silica support [130].

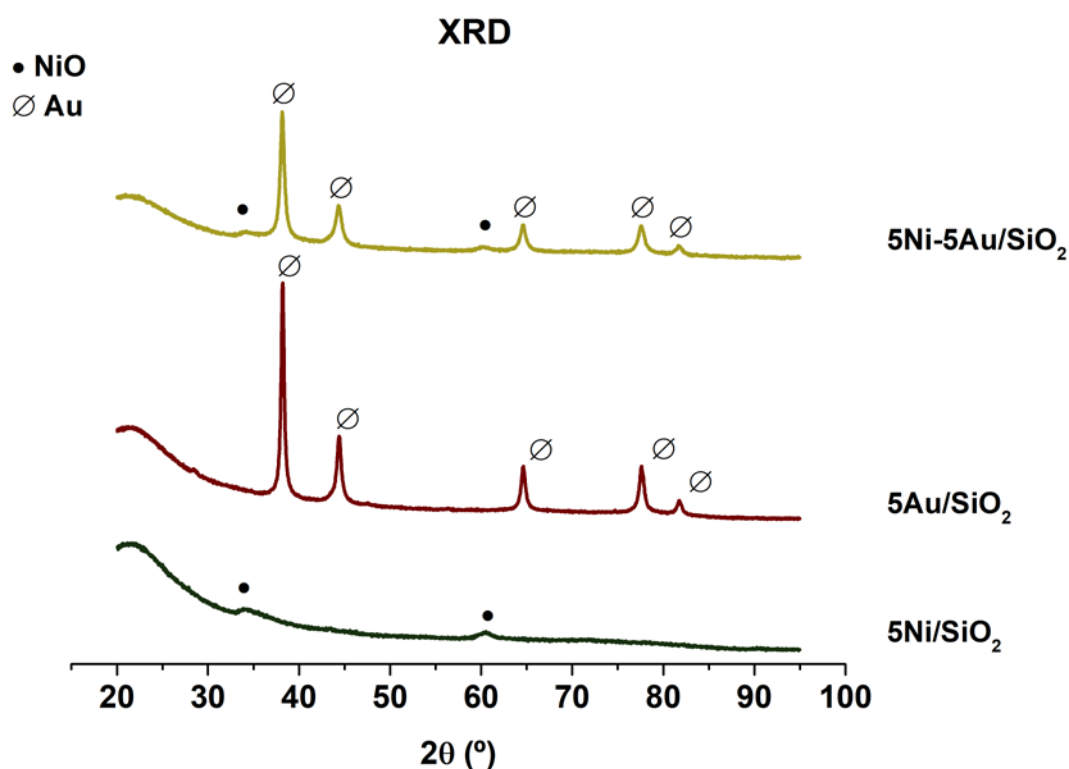


Figure 5.47. XRD profiles of the gold based photocatalysts

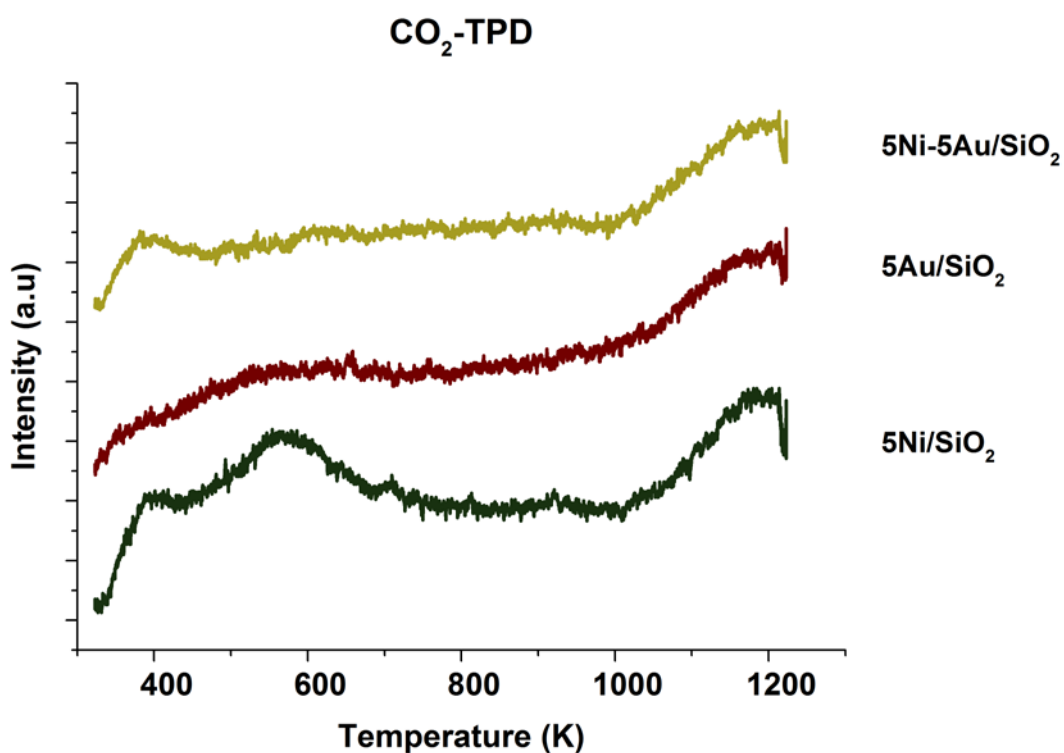
Scherrer equation was applied to the most intense gold peak obtained by XRD for each catalyst in order to calculate the average crystallite size. These results can be observed in Table 5.34. Both catalysts presented small gold crystallite size, being it smaller for the bimetallic nickel-gold catalyst.

Table 5.31. Average gold crystallite size of the gold based photocatalysts

Catalyst	Average gold crystallite size (nm)
5Au/SiO ₂	25
5Ni-5Au/SiO ₂	18

5.4.1.5. CO₂-TPD of the gold based photocatalysts

The basicity of the gold based photocatalysts was measured by CO₂-TPD. The results obtained are presented in Figure 5.37.

*Figure 5.48. CO₂-TPD profiles of the gold based photocatalysts*

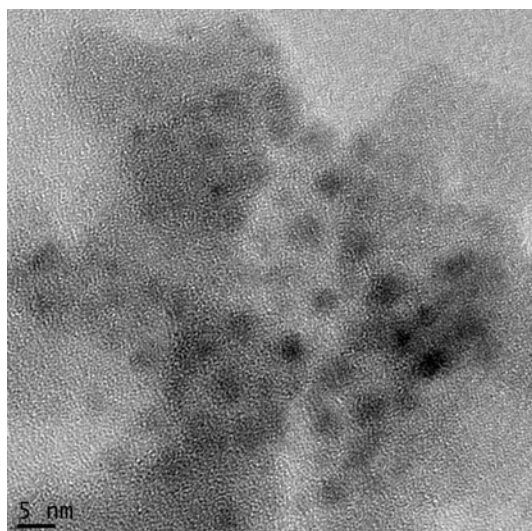
As it can be seen, the monometallic nickel catalyst presented two desorption peaks, one located at approximately 573 K and another one located at 1178 K. The first peak can be attributed to a medium basic sites and the second one to strong basic sites [49]. Both

the monometallic gold and bimetallic nickel-gold catalysts only presented the peak associated to strong basic sites at approximately 1178 K. For the monometallic nickel and the bimetallic nickel-gold catalysts a small peak was observed at approximately 373 K but can be related to water desorption.

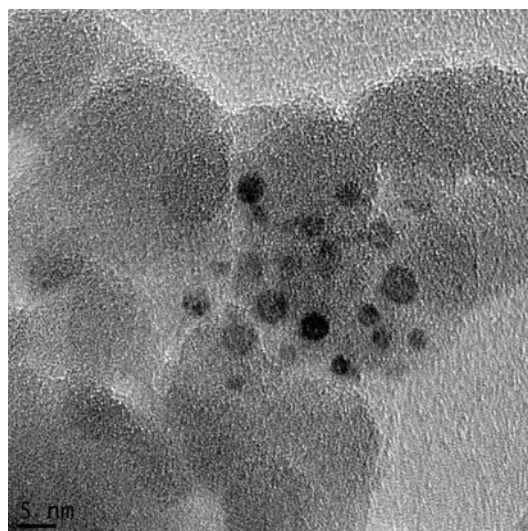
5.4.1.6. TEM of the gold based photocatalysts

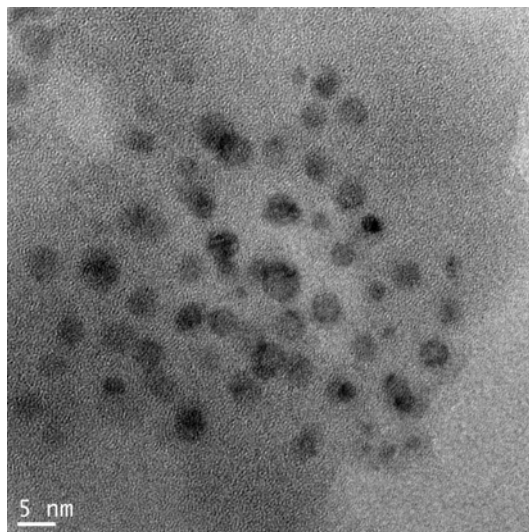
Information about the structure of the gold photocatalysts and the metal-support interactions was gained taking micrographs by TEM technique. The results obtained are presented in Figure 5.38.

a) 5Ni/SiO₂



b) 5Au/SiO₂



c) 5Ni-5Au/SiO₂*Figure 5.49. TEM micrographs of the gold based photocatalysts*

All the catalysts presented a homogeneous particle distribution, with small particles of approximately 5 nm well dispersed on the support. The difference between the particle size measured by TEM and the average crystallite size calculated by XRD can be attributed to the small size of the particles, being close to the detection limit of the XRD so only the bigger ones were taken into account by this technique, thus, giving as a result a higher average crystallite size. This could also explain why metallic nickel was not detected by XRD, due to the small particle size below the detection limit of the technique.

5.4.1.7. XPS of the gold based photocatalysts

Fresh-reduced catalysts were analysed by XPS to detect metallic species on the surface of the catalyst. For the monometallic nickel catalyst, two nickel species were detected: metallic nickel (Ni⁰) and NiO (Ni²⁺). For the metallic nickel, the main peak for the Ni2p_{3/2} core level and the satellite peak were detected at a binding energy of 853.8 eV and 860.9 eV respectively. The peaks corresponding to Ni²⁺ were measured at a binding energy of 856.7 eV for the main peak and 863.6 eV for the satellite peak. Regarding the Ni2p_{1/2} core level, metallic nickel was measured at a binding energy of 871.1 eV for the main

peak and 879.4 eV for the satellite peak. Main Ni^{2+} peak for this core level was measured at a binding energy of 874.8 eV, while the satellite peak was detected at a binding energy of 881.7 eV.

The monometallic gold catalyst presented metallic gold (Au^0) at two different core levels: $\text{Au}4f_{7/2}$ and $\text{Au}4f_{5/2}$. For the $\text{Au}4f_{7/2}$ core level, the peak was detected at a binding energy of 84.2 eV and for the $\text{Au}4f_{5/2}$ core level at 88.0 eV. The spin energy separation between both core levels of approximately 3.8 eV confirmed the identification of the specie as metallic gold [131].

Regarding to the bimetallic catalyst, both nickel and gold contributions must be analysed. Two species, Ni^0 and Ni^{2+} were detected for this catalyst, at two different core levels. For $\text{Ni}2p_{3/2}$ core level metallic nickel was detected at 853.6 eV (main) and 860.1 eV (satellite) binding energies, while Ni^{2+} peaks were observed at 856.4 eV (main) and 862.6 eV (satellite) binding energies. The metallic nickel peaks for the $\text{Ni}2p_{1/2}$ core level were measured at a binding energy of 871.1 eV, the main peak, and 878.4 eV for the satellite peak. Ni^{2+} at this core level presented the main peak at a binding energy of 874.4 eV and the satellite peak at a binding energy of 881.0 eV. Two different gold species were detected for this catalyst, metallic gold and cationic gold (Au^{3+}). The metallic gold was detected at a binding energy of 84.3 eV for the $\text{Au}4f_{7/2}$ core level, while the Au^{3+} was measured at a binding energy 86.3 eV for this core level. Regarding to the $\text{Au}4f_{5/2}$ core level, Au^0 was detected at a binding energy 88.1 eV and the Au^{3+} at a binding energy of 90.0 eV. The difference on the binding energies between the metallic gold and the specie that was measured at higher binding energies, 2.0 eV, confirms the identification of the latter as Au^{3+} [132].

Comparing the monometallic nickel catalyst with the bimetallic one, a shift to lower binding energies can be appreciated for the bimetallic catalyst which can be attributable to a highest electron density [133] in the latter sample, as a result of the interaction between nickel and gold. When comparing this bimetallic catalyst with the monometallic gold catalyst, a small binding energies shift (0.1 eV) towards higher binding energies was detected, being indicative of surface alloy formation [134]. This

shift in the binding energies, together with the presence of the Au³⁺ and the change in the electron density of the nickel suggest an interaction between Ni and Au.

A summary of the nickel XPS spectra is presented in Table 5.35 while the gold XPS spectra is presented in Table 5.36.

Table 5.32. Ni binding energies (eV) XPS of the gold based photocatalysts

Catalyst	Ni ⁰	Ni ⁰	Ni ⁰	Ni ⁰	Ni ²⁺	Ni ²⁺	Ni ²⁺	Ni ²⁺
	(Ni2p _{3/2})	satellite (Ni2p _{3/2})	(Ni2p _{1/2})	satellite (Ni2p _{1/2})	(Ni2p _{3/2})	satellite (Ni2p _{3/2})	(Ni2p _{1/2})	satellite (Ni2p _{1/2})
5Ni/SiO₂	853.8	860.9	871.1	879.4	856.7	863.6	874.8	881.7
5Ni- 5Au/SiO₂	853.6	860.1	871.1	878.4	856.4	862.6	874.4	881.0

Table 5.33. Au binding energies (eV) XPS of the gold based photocatalysts

Catalyst	Au ⁰	Au ⁰	Au ³⁺	Au ³⁺
	(Au4f _{7/2})	(Au4f _{5/2})	(Au4f _{7/2})	(Au4f _{5/2})
5Au/SiO₂	84.2	88.0	-	-
5Ni- 5Au/SiO₂	84.3	88.1	86.3	90.0

The measured profiles can be observed in Figure 5.39 and Figure 5.40 for the Ni and Au spectra respectively.

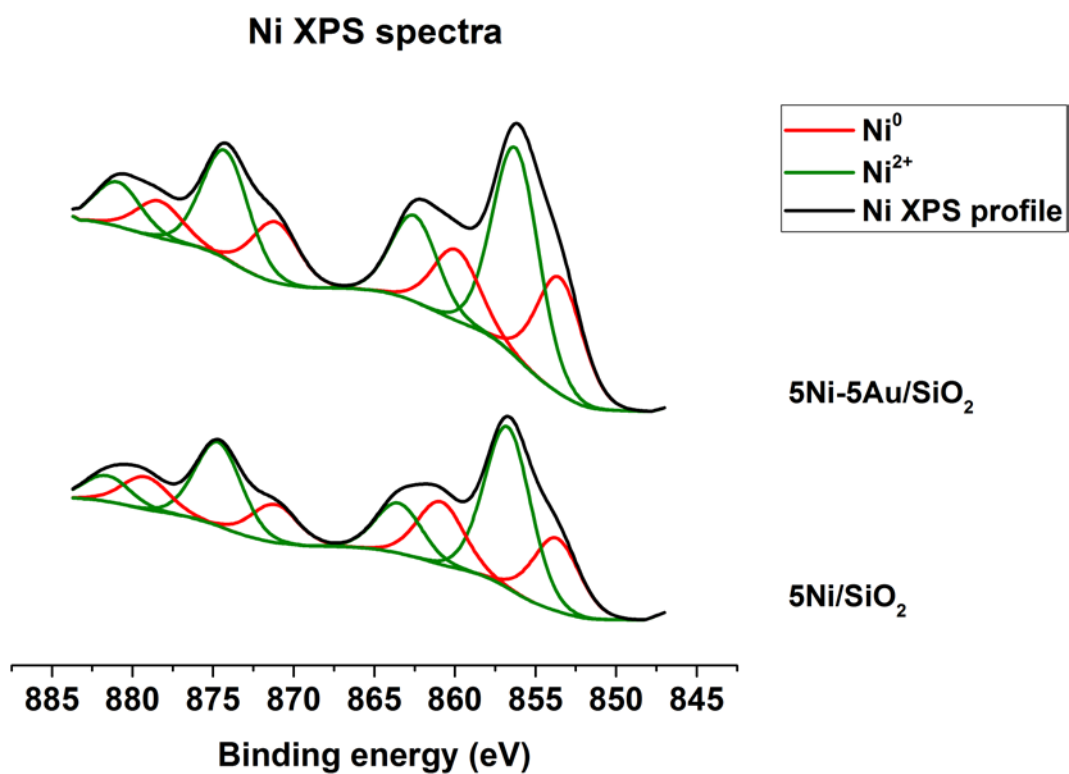


Figure 5.50. Ni XPS spectra of the gold based photocatalysts

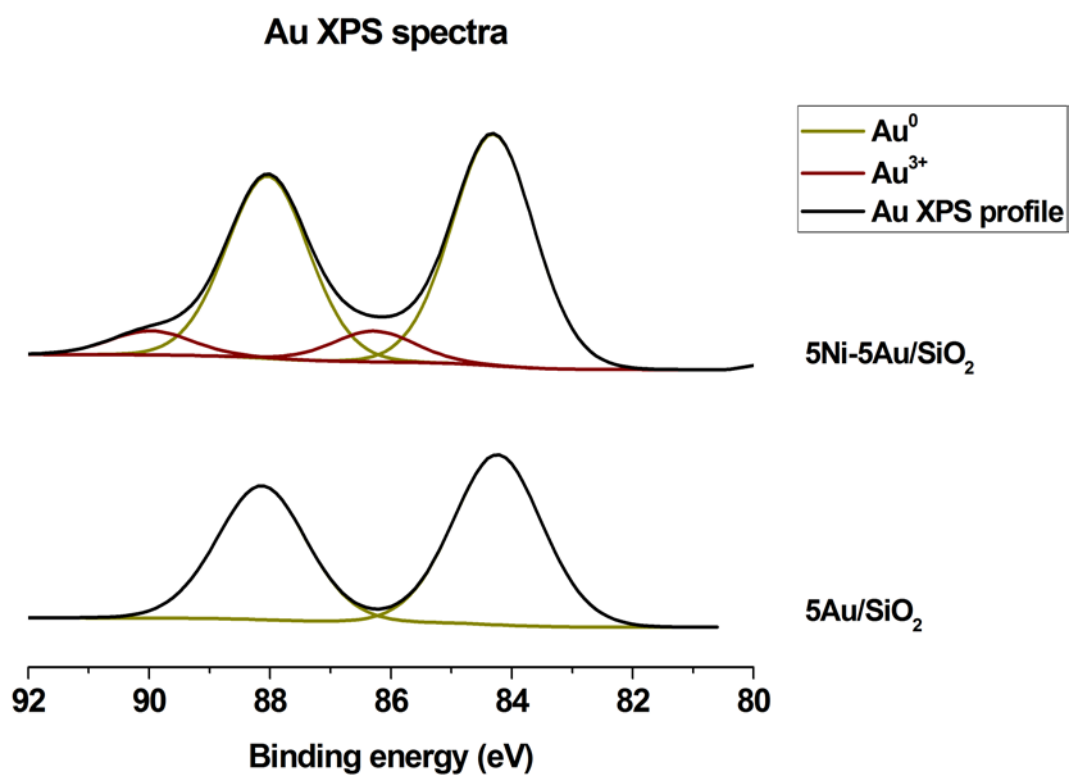


Figure 5.51. Au XPS spectra of the gold based photocatalysts

As it has been explained, for all the catalysts containing nickel two different species were detected, metallic nickel (Ni^0) and Ni^{2+} . The amount of these species was quantified and presented in Table 5.37.

Table 5.34. Ni species distribution XPS of the gold based photocatalysts

Catalyst	Ni^0 (%)	Ni^{2+} (%)
5Ni/SiO₂	39.0	61.0
5Ni- 5Au/SiO₂	38.5	61.5

As it can be seen, both for the monometallic and the bimetallic catalyst, Ni^{2+} was the main specie, accounting for approximately 2/3 of the total nickel measured by XPS. Same measurements were carried out for the catalysts containing gold, being the results present in Table 5.38. For the monometallic gold catalyst only the metallic gold (Au^0) was measured, as it has been explained previously, while for the bimetallic catalyst 90 % of the measured gold was metallic gold with a 10 % corresponding to Au^{3+} .

Table 5.35. Au species distribution XPS of the gold based photocatalysts

Catalyst	Au^0 (%)	Au^{3+} (%)
5Au/SiO₂	100.0	
5Ni- 5Au/SiO₂	90.0	10.0

Further information about the catalysts was obtained comparing the metal/support atomic ratios with the ones measured by ICP-OES. These results are presented in Table 5.39.

Table 5.36. Metal/support atomic ratios of the gold based photocatalysts

Catalyst	Ni/Si (at %) XPS	Ni/Si (at %) ICP-OES	Au/Si (at %) XPS	Au/Si (at %) ICP-OES
5Ni/SiO ₂	0.02	0.10	-	-
5Au/SiO ₂	-	-	0.002	0.10
5Ni-5Au/SiO ₂	0.03	0.14	0.003	0.13

It can be observed that in all the cases the ratios measured by ICP-OES were higher than those measured by XPS, thus, for all the catalysts most of the metal was located in the bulk of the catalyst instead of on the outer surface. As the support employed, SiO₂ prepared by FSP, was non-porous the difference in the surface atomic ratios measured by XPS and the bulk atomic ratios measured by ICP-OES cannot be attributed to the metal being located mainly in the pores of the support. For these catalysts the difference in the values of the atomic ratios can be attributed to phase segregation, a phenomena observed in catalysts prepared over FSP supports as it has been previously reported [135].

5.4.1.8. UV-Vis of the gold based photocatalysts

As these catalysts were to be tested in photocatalytic methanation their plasmonic properties were measured by UV-Vis. The results obtained are presented in Figure 5.41.

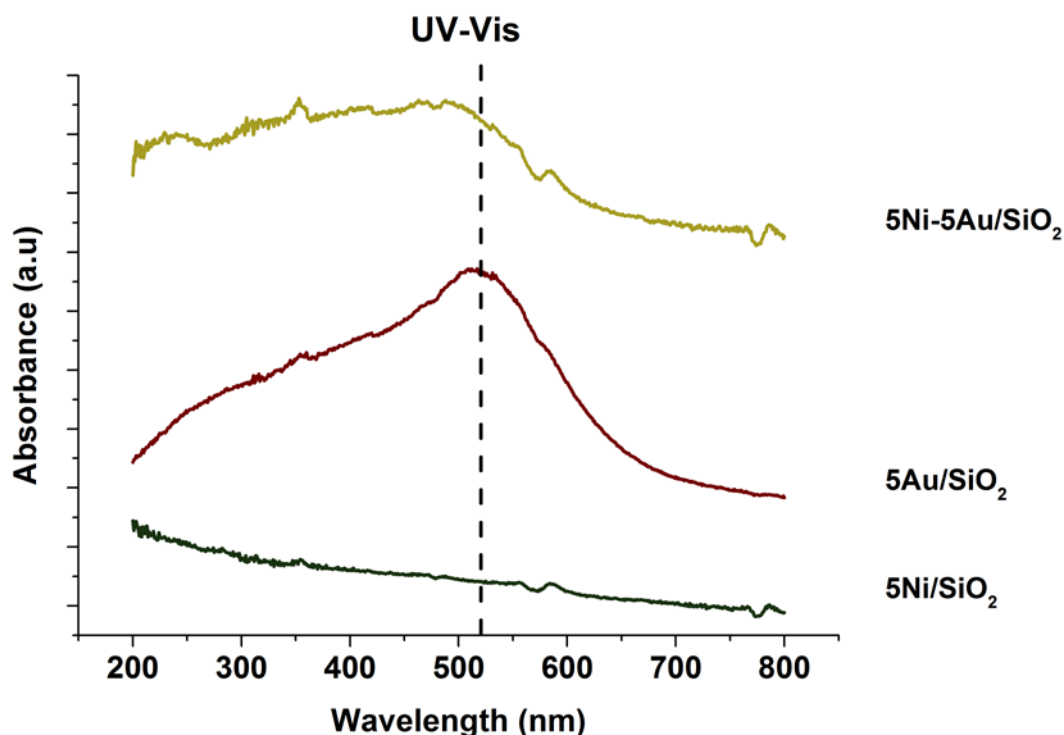


Figure 5.52. UV-Vis profiles of the gold based photocatalysts

No distinct absorption peak was observed for the monometallic nickel catalyst, probably due to the fact that Ni deposits absorb in the visible region where the absorption is broad [136,137]. The monometallic catalyst containing gold presented the maximum absorbance at about 520 nm, corresponding to the localised surface plasmon resonance (LSPR) of Au nanoparticles (NPs) which is usually located at 520-530 nm for particles with sizes between 5-50 nm [75]. The bimetallic Ni-Au/SiO₂ catalyst presented the maximum absorbance at approximately 500 nm, which is in agreement with the behaviour previously reported in the literature [138].

5.4.1.9. Activity tests of the gold based photocatalysts

For all the catalysts discussed previously, the ones tested in the fixed bed reactors, selectivity was 100 % towards methane. This means that methanation was the only reaction taking part and, as the molar ratio CO₂:CH₄ in the methanation reaction is 1, with a 100 % selectivity CH₄ yield should be equal (with an allowable error of ± 15 %, due to the possibility of carbon being deposited on the surface of the catalyst) to CO₂

conversion. Thus, CH₄ yield was employed as the main parameter to compare the activity of the catalysts. However, for gold photocatalysts not only CH₄ but also CO was produced during the activity tests. Hence, two parameters are needed to properly compare the behaviour of the different gold photocatalysts: CO₂ conversion and CH₄ selectivity. The results obtained for CO₂ conversion are presented in Figure 5.42.

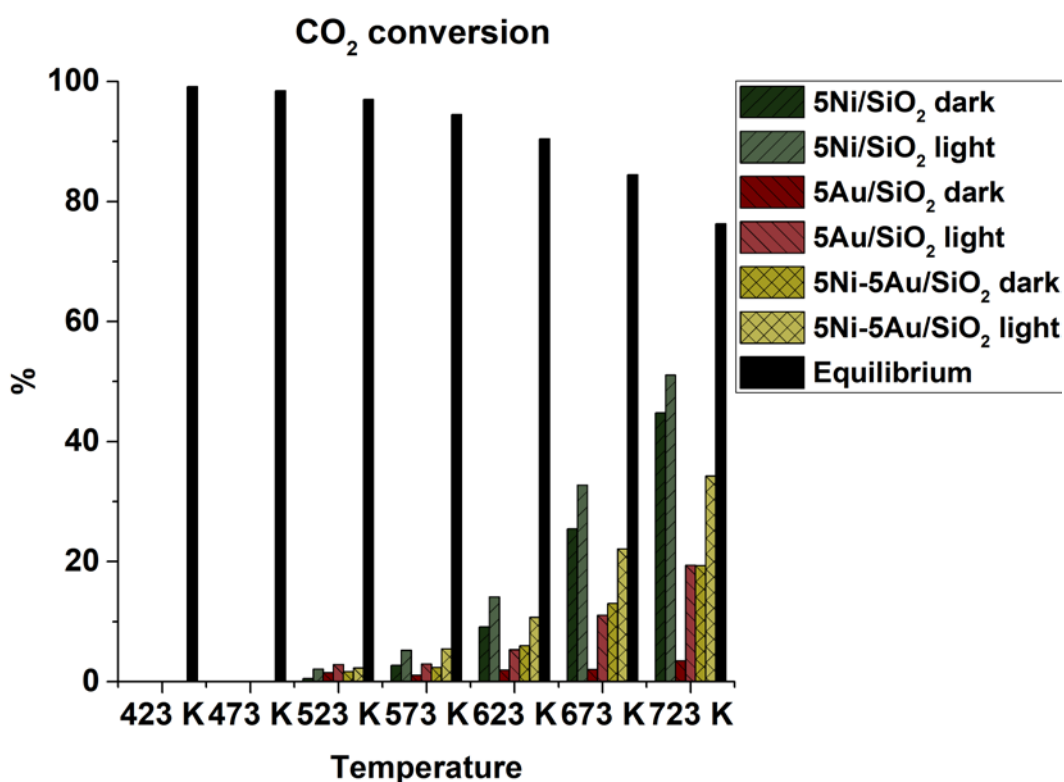


Figure 5.53. Activity results of the gold based photocatalysts I: conversion

The monometallic nickel catalyst did not present any CO₂ conversion at the lower temperatures tested. At temperatures above 523 K it presented an increasing CO₂ conversion while the temperature was increased. For all the temperatures tested, CO₂ conversion increased under light illumination; however this increase was low and cannot be attributed to the light illumination but to the experimental error margin between different activity tests. The monometallic gold catalyst presented CO₂ conversion at temperatures above 523 K, however the values obtained were lower than 5 % so it could not be dissociated from the intrinsic error associated to any measurement. Under light illumination it presented a noticeable CO₂ conversion at temperatures above 623 K, it

higher being while temperature was also higher. The bimetallic catalyst also presented an increasing CO₂ conversion for temperatures above 523 K under dark conditions. The same trend was observed under light illumination, with the values obtained being higher at all the temperatures tested. All the catalysts were far from the values predicted by the thermodynamic equilibrium.

For all the catalysts CO was also produced together with CH₄. The results obtained for CH₄ selectivity are presented in Figure 5.43.

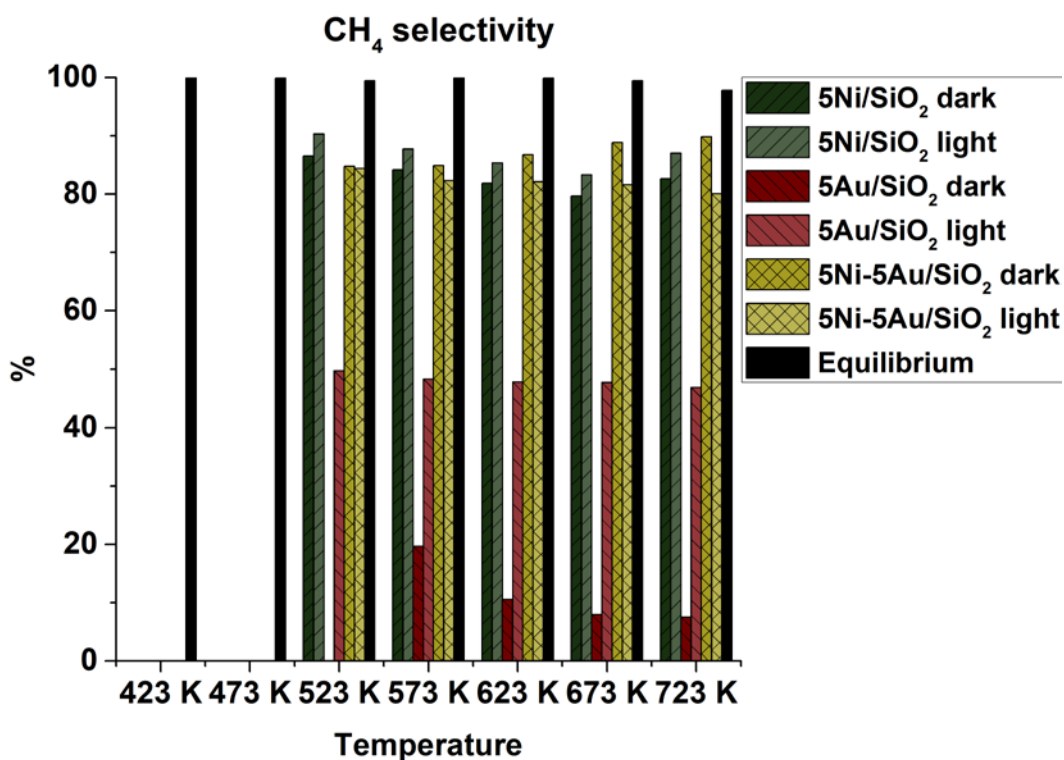


Figure 5.54. Activity results of the gold based photocatalysts II: selectivity

For the monometallic nickel catalyst there was a slight increase in the selectivity under light illumination at all the temperatures tested, but this increase was lower than 10 % so the selectivity can be considered approximately constant. The monometallic gold catalyst presented a substantial increase in the methane selectivity when comparing light illumination with dark conditions. However, the low values of the conversion measured under dark conditions, that could be considered null, make the values of the selectivity measured under dark conditions not appropriated for any comparison. As it

has been discussed for the monometallic nickel catalyst, selectivity towards methane also remained approximately constant for the monometallic gold catalyst under light illumination. The bimetallic nickel-gold catalyst presented a slight decrease of the methane selectivity when illuminated, but this decrease was not high enough to be considered and the selectivity can be considered constant. Summarising, selectivity remained approximately constant for all the catalyst no matter the operating conditions, as light illumination did not have any effect and neither had the operating temperature.

Even though selectivity was not affected by the illumination, for the catalysts containing gold an increase in the conversion was measured under light illumination. At the highest temperature tested, the conversion for the 5Au/SiO₂ was enhanced from 3.5 % under dark conditions to 19.3 % under light illumination. For the bimetallic nickel gold catalyst the measured improvement was from 19.3 % to 34.3 %. It is clear that light had a beneficial effect in the activity of these catalysts; however they were outperformed by the monometallic nickel, non-photo, catalyst. This finding suggest that although plasmonic effect can enhance the activity of a catalyst for carbon dioxide methanation reaction, other physicochemical parameters play a more important role in this reaction.

In order to explain why the activity of the monometallic nickel catalyst, a catalyst without any plasmonic properties that was synthesised as a reference, was higher than the one obtained by the catalysts that presented an increase in their performance due to light illumination, it is necessary to take into account the results obtained for all of them with the different characterisation techniques.

The measurements of the reducibility proved the addition of gold improved the reducibility of the catalyst. However, due to the high temperature employed for the prereduction of the catalyst (973 K) metallic nickel was obtained both for the monometallic nickel and the bimetallic nickel-gold catalyst, thus, for both catalysts the presence of active sites was ensured after the prereduction.

Results obtained by XRD proved the full reduction of gold. Regarding to the average gold crystallite size it was approximately the same (20 nm) for both monometallic gold and bimetallic nickel-gold catalysts.

The basicity measured by CO₂-TPD was useful to identify differences in the physicochemical properties of the gold photocatalysts, leading to the different catalytic activity observed for them. While all the catalysts presented a desorption peak at approximately 1178 K, this could be related to strong basic sites not taking part in the reaction as it was performed at lower temperatures. However, the monometallic nickel catalyst also presented a peak at about 573 K, attributed to weak-medium basic sites that were able to take part in the reaction as it was performed in a range of temperatures of 423-723 K. These basic sites could adsorb the carbon dioxide enhancing the conversion obtained for the methanation reaction.

The structural pictures obtained by TEM demonstrated the presence of NPs smaller than 5 nm. These particles were well dispersed for all the catalysts, being for the monometallic nickel catalyst an important characteristic that influenced the final catalytic activity. Even if the gold particles were also well dispersed, this had no influence on the activity of the monometallic gold catalyst as gold it is known for being an inactive metal for carbon dioxide methanation [56]. For the bimetallic nickel-gold catalyst the particles were well dispersed, but instead of distinguishing between nickel and gold particles, a Ni-Au alloy was formed. This new structure resulted in a decrease of the catalytic activity, when compared to bare nickel, due to the ineffectiveness of gold towards carbon dioxide methanation.

The results obtained by XPS demonstrated the presence metallic nickel, in the monometallic nickel and the bimetallic catalyst, and metallic gold for the gold containing catalysts. Also small amount of non-metallic nickel was detected for the nickel containing catalysts. For the bimetallic catalyst, when comparing with the results obtained for the monometallic catalysts, an interaction between nickel and gold could be observed. These results are in agreement with the ones obtained by TPR, where an improvement in the reducibility of the bimetallic catalyst was observed due to the

presence of gold. The results obtained by XPS also served to further prove the presence of metallic nickel, even if not detected by XRD, in the catalysts. This technique also supported the results obtained by TEM, demonstrating the formation of a Ni-Au alloy for the bimetallic catalyst.

Due to the catalysts being tested under light conditions, the results obtained by UV-Vis are of great importance to understand the behaviour of the catalysts under light illumination. No distinct peak was observed for the monometallic nickel catalyst, as it has been explained due to the broad absorption in the visible region. According to the results, obtained in the activity tests, this broad absorption does not promote carbon dioxide reduction. The monometallic nickel catalyst did not present any absorbance peak, thus, light illumination did not have any effect on the performance of this catalyst. For the monometallic gold catalyst an absorbance peak was observed at a wavelength of approximately 520 nm, which was the main wavelength employed for light illumination during the activity tests. These results explained the high increase in the conversion for the monometallic gold catalyst under light illumination, as it was able to absorb the incident light and this had a positive effect in the catalytic activity. Finally, the bimetallic nickel-gold catalyst also presented an absorbance peak. In this case it was not located at 520 nm but shifted to a slightly lower wavelength due to the fact that the metallic particles present in the catalyst were, as it has been previously explained, a Ni-Au alloy. However, this catalyst still presented absorbance at a wavelength close to 520 nm so it was able to absorb the incident light, which had a positive effect in this catalyst increasing its catalytic activity, when compared with the performance of the same catalyst under dark conditions.

5.4.2. Silver based photocatalysts

Different catalysts containing silver were prepared to be tested in photocatalytic reactors, all of them with nickel as main active metal and using FSP SiO₂ as catalytic support. Two different monometallic catalysts were also prepared to analyse the effect of the interaction between nickel and silver: 5Ni/SiO₂ and 1Ag/SiO₂. The bimetallic catalysts are listed below: 5Ni-1Ag/SiO₂ coimpregnation (CI), 5Ni-1Ag/SiO₂ sequential

impregnation (SI), 1Ag-5Ni/SiO₂ SI. The differences between the synthesis methods were further explained in **Chapter IV** of the present PhD thesis. The digit in the naming of the catalysts is a reference to the theoretical metal loading (wt %), with the real metal loading calculated by ICP-OES and given in the next section.

5.4.2.1. Chemical composition of the silver based photocatalysts

The real metal loading, calculated by ICP-OES is presented in Table 5.40. As it can be seen, in most of the cases nickel and silver loading were lower than expected.

Table 5.37. ICP-OES of the silver photocatalysts

Catalyst	Ni (wt %)	Ag (wt %)
5Ni/SiO ₂	4.0	-
1Ag/SiO ₂	-	0.9
5Ni-1Ag/SiO ₂ Cl	3.9	0.9
5Ni-1Ag/SiO ₂ SI	4.0	0.6
1Ag-5Ni/SiO ₂ SI	4.7	1.0

5.4.2.2. Structural properties of the silver based photocatalysts

Taking into account that the support employed for silver photocatalysts was FSP prepared SiO₂, which was also employed for gold photocatalysts, the only property measured by N₂ adsorption-desorption isotherms for these catalysts was also the BET surface area. Other properties, like pore volume or average pore size, are not applicable for these catalysts due to the absence of pores in the employed supports. Results obtained are presented in Table 5.41. Differences could be observed in all the catalysts;

however these differences were approximately $\pm 15\%$, so they were not large enough to be significant. According to the results obtained all the catalysts presented high surface area of approximately 250-300 m^2/g .

Table 5.38. Structural properties of the silver based photocatalysts

Catalyst	BET surface area (m^2/g)
SiO₂	309
5Ni/SiO₂	302
1Ag/SiO₂	357
5Ni-1Ag/SiO₂ Cl	246
5Ni-1Ag/SiO₂ SI	250
1Ag-5Ni/SiO₂ SI	313

5.4.2.3. TPR of the silver based photocatalysts

The reducibility of the catalysts and the present reducible species were measured by TPR. The reduction profiles obtained are presented in Figure 5.44.

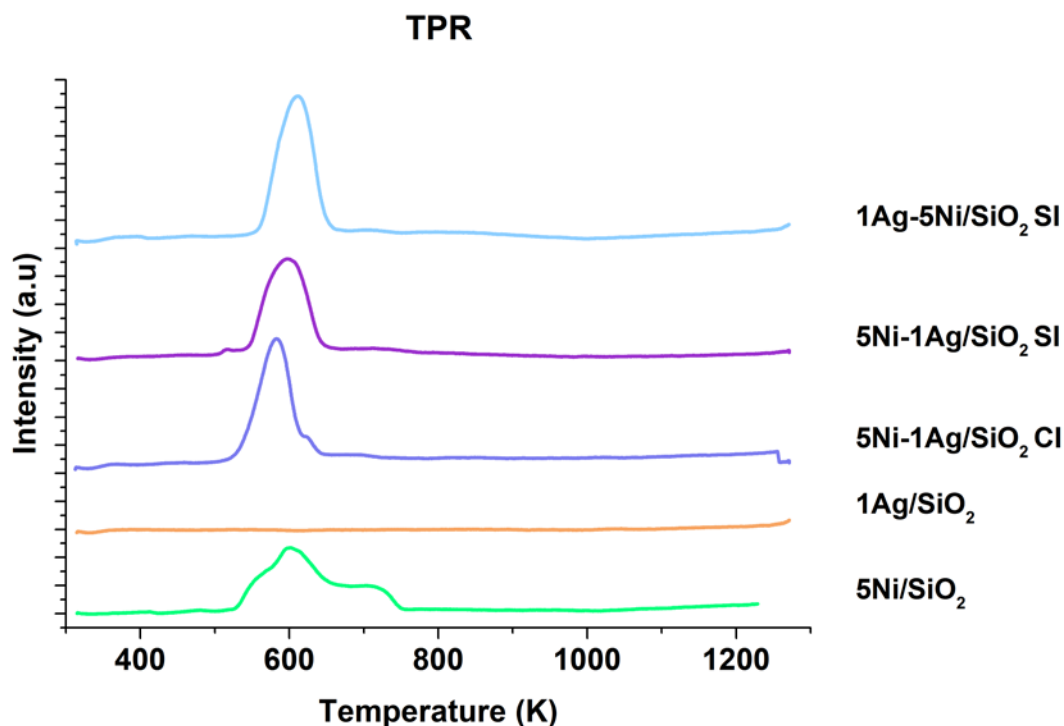


Figure 5.55. TPR profiles of the silver based photocatalysts

As it can be seen in the figure all the nickel containing catalysts presented a main reduction peak at temperatures between 500-600 K. No reduction peak was observed for the monometallic silver catalyst. However, the catalyst containing both nickel and silver presented a shift in their main peak to lower temperatures, due to the influence of silver [139]. The influence of adding silver, for catalysts with the same loading, was as follows: 5Ni-1Ag/SiO₂ CI > 5Ni-1Ag/SiO₂ SI > 1Ag-5Ni/SiO₂ SI. Thus, coimpregnation method resulted in a stronger Ni-Ag interaction. For the sequential impregnation method, being silver the metal impregnated in the first place also resulted in a stronger Ni-Ag interaction when compared with carrying out the impregnation of nickel in the first place.

The reduction profiles observed are the result of the combination of different reduction peaks attributable to different species. These main reduction peaks were deconvoluted so as to determine the contribution of each specie to the final reduction peak. The results obtained are presented in Table 5.42.

Table 5.39. TPR peak deconvolution of the silver based photocatalysts

Catalyst	NiO weak interaction	NiO strong interaction
5Ni/SiO₂	602 K-77.9 %	704 K-22.1 %
5Ni-1Ag/SiO₂ CI	580 K-86.4 %	658 K-13.6 %
5Ni-1Ag/SiO₂ SI	595 K-90.7 %	719 K-9.3 %
1Ag-5Ni/SiO₂ SI	608 K-97.0 %	711 K-3.0 %

As it can be observed, all the catalysts presented two nickel species: NiO weakly interacting with the support and NiO strongly interacting with the support, being in all the cases the specie with a weak interaction with the support the most abundant one. The addition of silver and the use of different synthesis methods not only altered the temperatures of the reduction peaks but also the amount of each of the measured NiO species. Addition of 1 wt % Ag resulted in an increase of the NiO specie with weak interaction with the support for all the bimetallic catalysts, when compared with the monometallic one, being the largest increase observed for the 1Ag-5Ni/SiO₂ SI catalyst. When CI was impregnated as the synthesis method the influence of the silver loading in the reduction temperature was stronger than if prepared by SI, however the effect on the amount of the different species was slightly lower than for the catalyst prepared by SI.

5.4.2.4. XRD of the silver based photocatalysts

The reduced crystalline species present in the catalyst were determined by XRD. Results are presented in Figure 5.45.

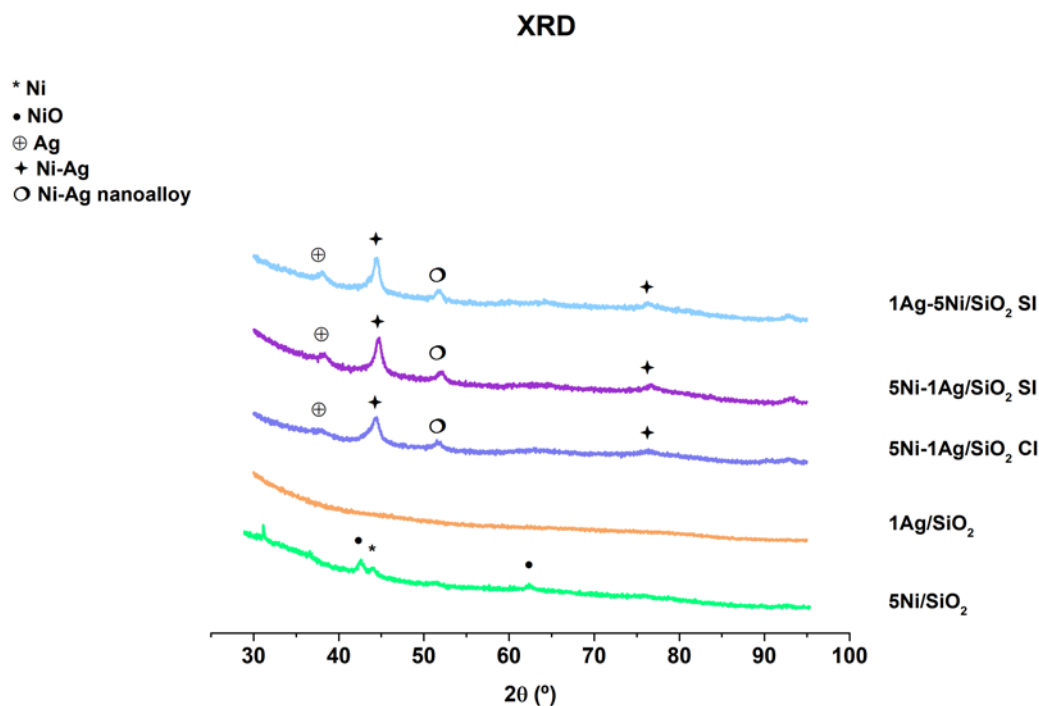


Figure 5.56. XRD profiles of the silver based photocatalysts

For the monometallic nickel catalyst two different nickel species were measured, metallic nickel (Ni) at a 2θ of approximately 44.6° [140,141] while NiO was also measured at 2θ 43 and 63 [140–143]. No diffraction peaks were observed for the monometallic silver catalyst, probably due to the fact of the silver particles being so small that they were below the detection limit of the technique, of approximately 3 nm [144]. All the bimetallic nickel-silver catalysts presented the same crystalline species: metallic silver (Ag), with a diffraction peak located at 2θ of approximately 38° , overlapping Ni-Ag located at 2θ of approximately 44° and 76° [145] that can be attributed to Ni-Ag in mixed state [146] or core-shell structure [147,148] and a diffraction peak located at 2θ 51.7° that can be attributed to the Ni-Ag nanoalloy [146].

5.4.2.5. CO₂-TPD of the silver based photocatalysts

Basic properties of the silver photocatalysts were measured by CO₂-TPD. The obtained desorption profiles are presented in Figure 5.45.

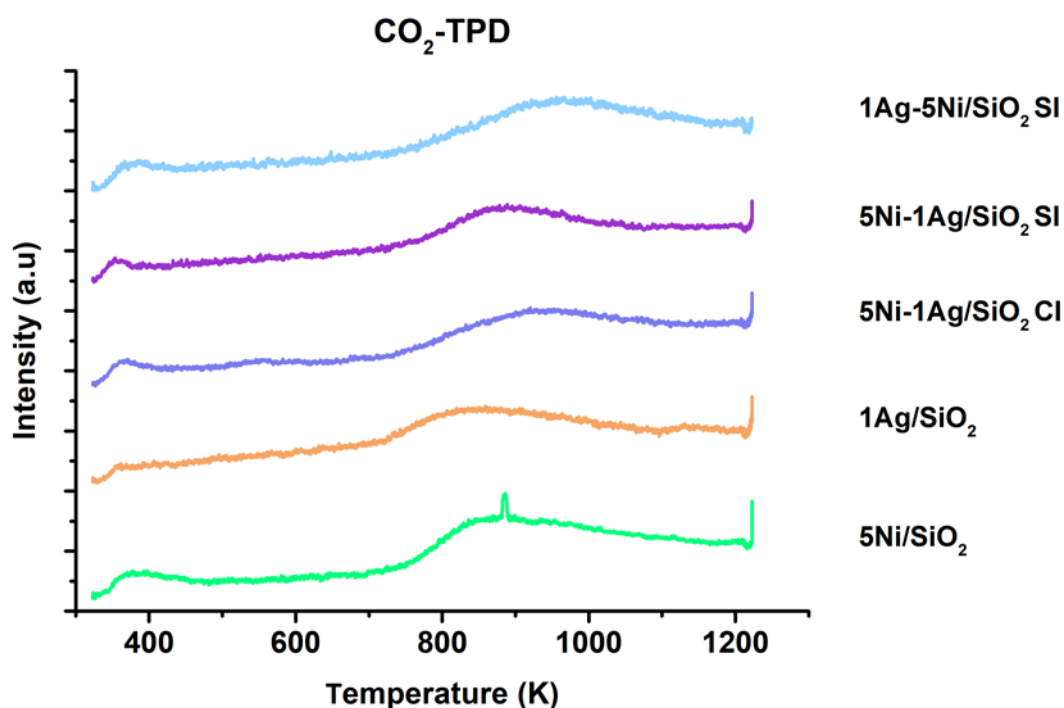


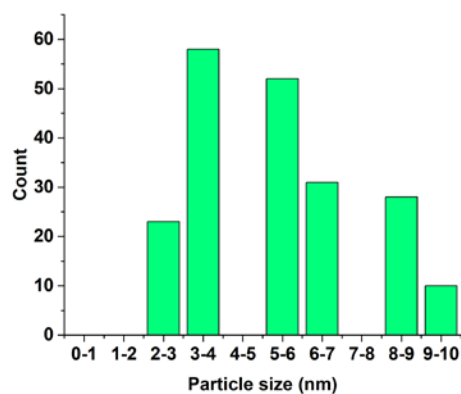
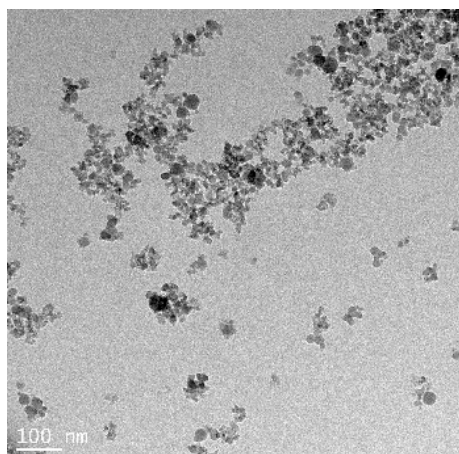
Figure 5.57. CO₂-TPD profiles of the silver based photocatalysts

As it can be seen, all the catalyst presented a similar desorption profile with a main peak located at temperatures above 800 K. Regarding to the intensity of the peak, the monometallic nickel catalyst presented the most intense peak among all the compared catalysts. The peak for the 1Ag/SiO₂ catalyst was shifted to lower temperature, when compared with the monometallic nickel catalyst, and it was also less intense. The basic character of the monometallic catalysts is useful to understand the behaviour of the bimetallic catalysts. For the Cl catalyst the intensity of the peak was lower than for the monometallic one, due to the effect of the addition of silver. The same behaviour was observed for the SI catalyst. However, for the 1Ag-5Ni/SiO₂ catalyst this shift was not observed, due to the fact that nickel was impregnated in the first place.

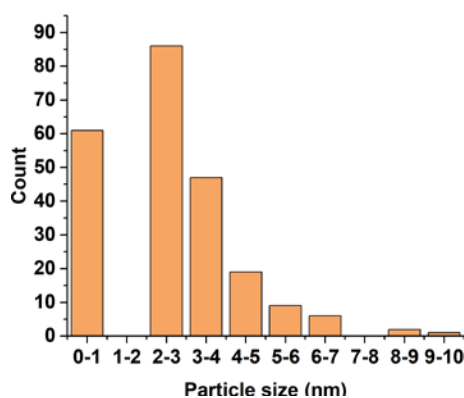
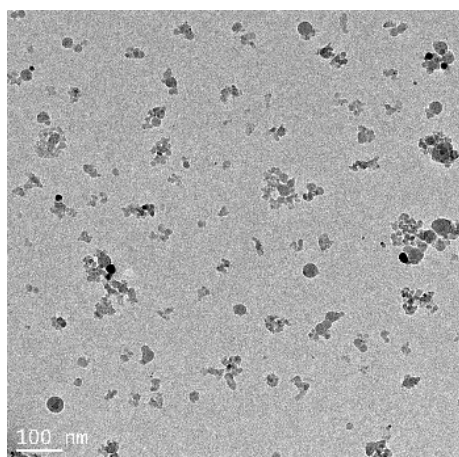
5.4.2.6. TEM of the silver based photocatalysts

Information about the structure of the silver based photocatalysts was gained by TEM micrographs. The micrographs taken together with the calculated particle size distribution, with a minimum count of 200 particles, are presented in Figure 5.47.

a) 5Ni/SiO₂



b) 1Ag/SiO₂



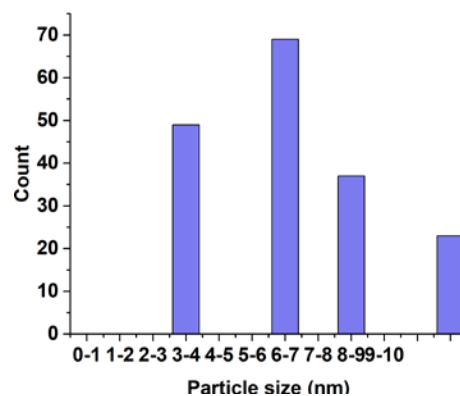
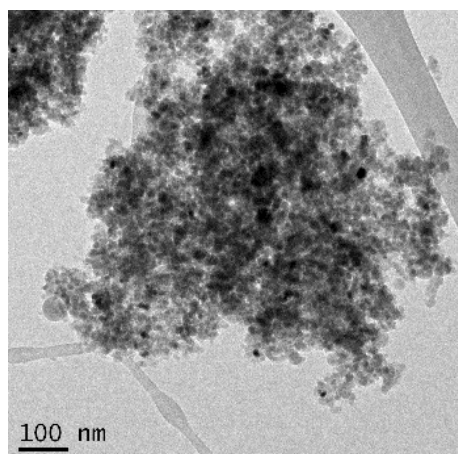
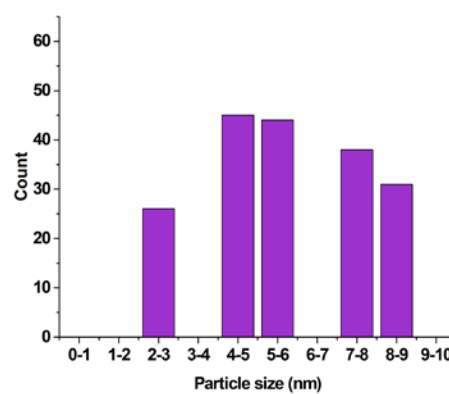
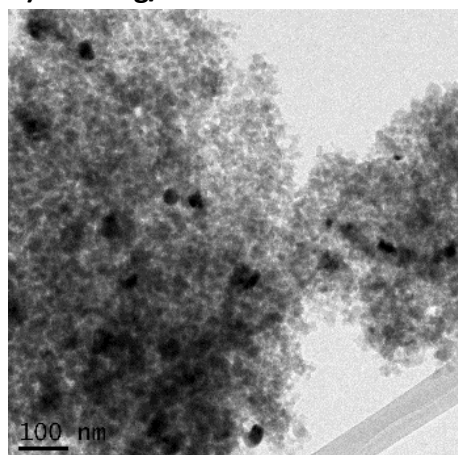
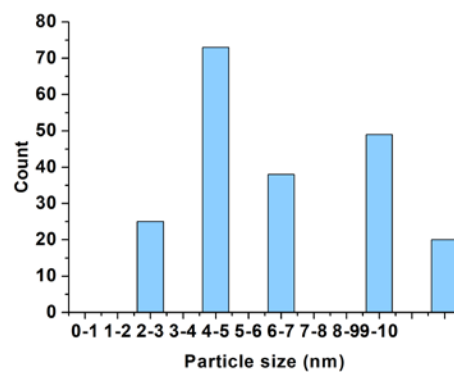
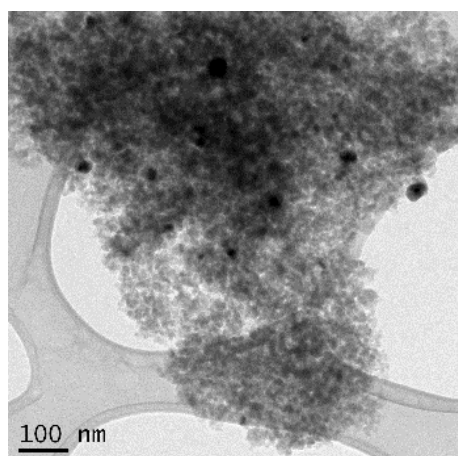
c) 5Ni-1Ag/SiO₂ CId) 5Ni-1Ag/SiO₂ SIe) 1Ag-5Ni/SiO₂ SI

Figure 5.58. TEM micrographs and particle size distribution of silver based photocatalysts

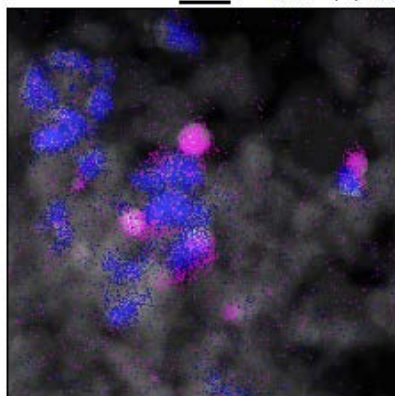
For the monometallic nickel catalyst, an average particle size of 6.4 ± 0.2 nm. The 1Ag/SiO₂ catalyst presented an average particle size of 3.2 ± 0.1 nm. For the bimetallic catalyst synthesized by CI an average particle size of 10.2 ± 0.4 nm was measured. Regarding to the bimetallic catalysts synthesized by SI, the 5Ni-1Ag/SiO₂ presented an average particle size of 6.8 ± 0.2 nm, while these particles were bigger when nickel was impregnated during the first step of the SI procedure; 1Ag-5Ni/SiO₂ SI catalyst, presented an average particle size of 8.6 ± 0.2 nm.

Further information about the structure of the catalysts was obtained by performing energy-dispersive x-ray spectroscopy (EDX) elemental mapping to the samples characterized by high-resolution (HR) TEM. These measurements were only carried out for the bimetallic catalysts, in order to determine the possible structures formed by the nickel and the silver. Results are presented in Figure 6. For the catalysts prepared by CI, nickel and silver particles could be easily distinguished, in the form of linked nanoparticles or subcluster. However, some particles in the form of Ni-Ag mixed alloy were also observed. The 5Ni-1Ag/SiO₂ SI catalyst presented both some silver particles without any interaction with the nickel particles and Ni-Ag mixed alloy. When nickel was impregnated in the first step of the SI procedure, both Ni-Ag mixed alloy and Ni-Ag cluster, with different silver particles in contact with a unique nickel particle were detected [149].

a) 5Ni-1Ag/SiO₂ SI

17030318 maps of 17

25 nm 15560 25695



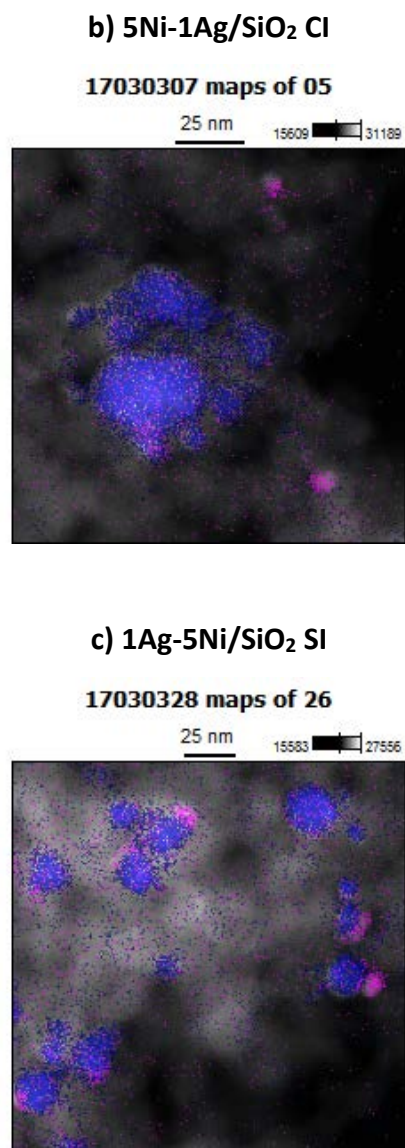


Figure 5.59. EDX pictures of the silver based photocatalysts

5.4.2.7. XPS of the silver based photocatalysts

The species present on the surface of the silver photocatalysts were measured by XPS. For the catalysts containing nickel, two different species were detected: metallic Ni (Ni⁰) and Ni²⁺, being this last one the main specie. Both species were detected only at one core level, the Ni2p_{3/2}. The monometallic nickel catalyst presented the main peak for metallic nickel at a binding energy of 854.1 eV and the satellite peak at 861.7 eV, while the peaks corresponding to Ni²⁺ were measured at a binding energy of 857.1 eV (main)

and 864.5 eV (satellite). Metallic nickel was measured at a binding energy of 853.8 eV (main) and 860.8 eV (satellite) for the bimetallic nickel-silver catalyst synthesised by coimpregnation, and the peaks corresponding to Ni²⁺ were measured at 856.7 eV (main) and 863.0 eV (satellite). When the catalyst was prepared by sequential impregnation, the main peaks corresponding to Ni⁰ and Ni²⁺ were measured at a binding energy of 853.2 eV and 856.5 eV respectively, with the satellite peaks located at a binding energy of 860.4 eV and 863.0 eV. The 1Ag-5Ni/SiO₂ SI presented a slight shift in the peaks when compared with the catalyst synthesised also by SI, being the main peak corresponding to Ni⁰ measured at 853.5 eV and the satellite peak at 860.2 eV. The peaks attributed to Ni²⁺ were measured at a binding energy of 856.3 eV, the main one, and 862.7 eV the satellite peak. For a better understanding of the results obtained by XPS for the Ni spectra, all the binding energies measured are presented in Table 5.43.

Table 5.40. Ni binding energies (eV) of the silver based photocatalysts

Catalyst	Ni ⁰ (Ni2p _{3/2})	Ni ⁰ (Ni2p _{3/2}) satellite	Ni ²⁺ (Ni2p _{3/2})	Ni ²⁺ (Ni2p _{3/2}) satellite
5Ni/SiO ₂	854.1	861.7	857.1	864.5
5Ni-1Ag/SiO ₂ CI	853.8	860.8	856.7	863.0
5Ni-1Ag/SiO ₂ SI	853.2	860.4	856.5	863.0
1Ag-5Ni/SiO ₂ SI	853.5	860.2	856.3	862.7

The measured XPS spectra profile is presented in Figure 5.46.

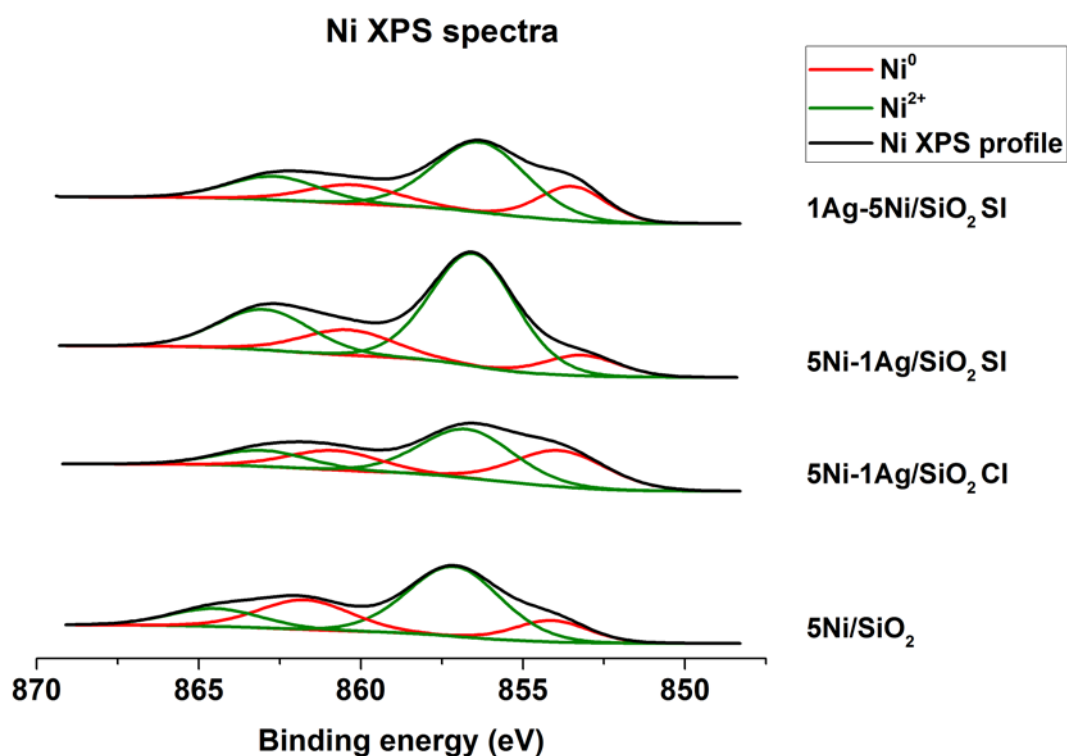


Figure 5.60. Ni XPS spectra of the silver based photocatalysts

For all the catalysts containing silver, it was measured as metallic silver (Ag⁰) at two different core levels: Ag3d_{5/2} and Ag3d_{3/2}. The monometallic silver catalyst presented the peak corresponding to the Ag3d_{5/2} core level was measured at a binding energy of 368.7 eV and the one corresponding to the Ag3d_{3/2} core level at a binding energy of 374.7 eV. For the bimetallic nickel-silver catalyst prepared by coimpregnation the peaks were measured at a binding energy of 368.6 eV and 374.5 eV for the Ag3d_{5/2} and Ag3d_{3/2} core level, respectively. When the catalyst was prepared by sequential impregnation, the peak at the Ag3d_{5/2} core level was measured at a binding energy of 368.4 eV and the peak corresponding to the Ag3d_{3/2} core level at 374.5 eV. Finally, for the 1Ag-5Ni/SiO₂ catalyst the peak corresponding to the Ag3d_{5/2} core level was measured at a binding energy of 368.4 eV and the one attributed to the Ag3d_{3/2} core level at a binding energy of 374.5 eV. For a better understanding of the results obtained by XPS for the Ag spectra, all the binding energies measured are presented in Table 5.44.

Table 5.41. Ag binding energies (eV) of the silver based photocatalysts

Catalyst	Ag ⁰ (Ag3d _{5/2})	Ag ⁰ (Ag3d _{3/2})
5Ag/SiO ₂	368.7	374.7
5Ni-1Ag/SiO ₂ Cl	368.6	374.5
5Ni-1Ag/SiO ₂ SI	368.4	374.5
1Ag-5Ni/SiO ₂ SI	368.4	374.5

The measured profiles are presented in Figure 5.47.

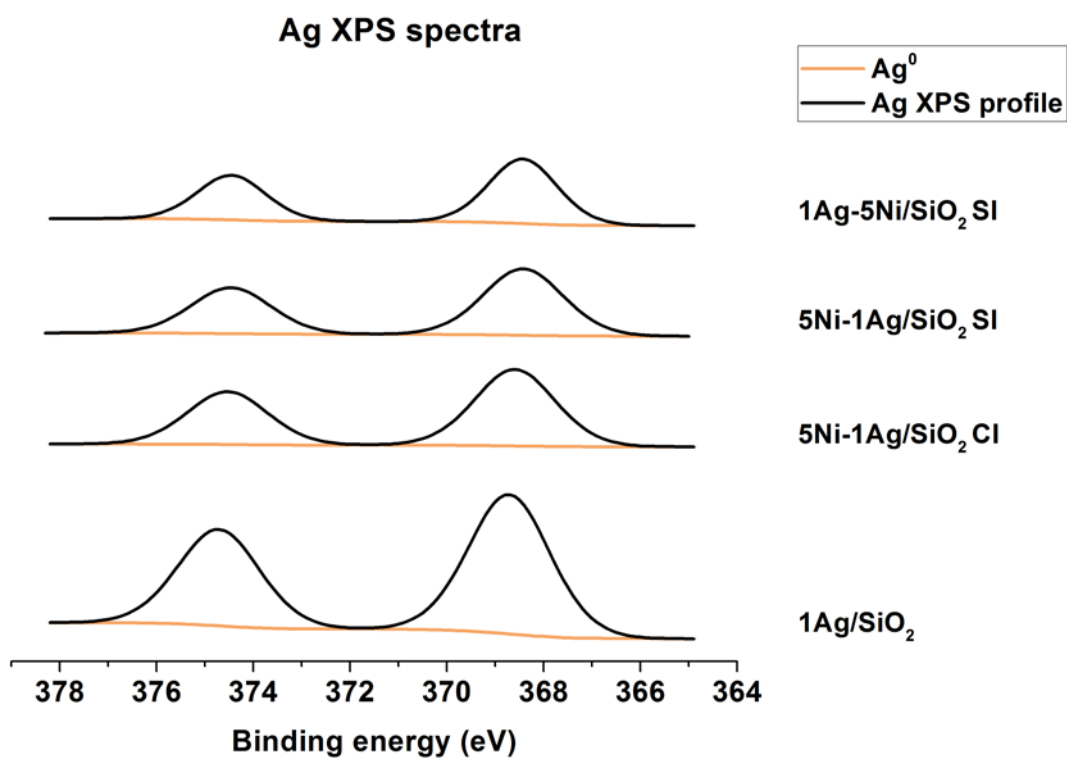


Figure 5.61. Ag XPS spectra of the silver based photocatalysts

As it has been explained, two different nickel species were measured for all the nickel containing catalysts. The relative amount of each of the species was quantified and presented in Table 5.45.

Table 5.42. Ni species distribution XPS of the silver based photocatalysts

Catalyst	Ni ⁰ (%)	Ni ²⁺ (%)
5Ni/SiO ₂	35.6	64.4
5Ni-1Ag/SiO ₂ CI	46.1	53.9
5Ni-1Ag/SiO ₂ SI	31.9	68.1
1Ag-5Ni/SiO ₂ SI	21.3	78.7

Ni²⁺ was the main nickel specie detected by XPS for all the silver photocatalysts. However, a different distribution was present by each of the catalyst analysed. Using the monometallic nickel catalyst as reference, when silver was added and the catalyst was prepared by coimpregnation the amount of Ni²⁺ was reduced and the ratio between the two nickel species on the surface of the catalyst was almost equal to 1. Synthesising the catalyst by SI reduced the amount of metallic nickel on the surface while the amount of Ni²⁺ was increased. If silver was impregnated first, differences between this catalyst and the monometallic nickel one were not highly remarkable. However, when the impregnation of nickel was carried out in the first place, the amount of Ni⁰ was highly reduced.

More information could be gained by XPS, comparing the metal/support atomic ratios measured by this technique with the same atomic ratios calculated with the results obtained by ICP-OES. The results obtained are presented in Table 5.46.

Table 5.43. Metal/support atomic ratios of the silver based photocatalysts

Catalyst	Ni/Si (at %) XPS	Ni/Si (at %) ICP-OES	Ag/Si (at %) XPS	Ag/Si (at %) ICP-OES
5Ni/SiO ₂	0.014	0.09	-	-
5Ag/SiO ₂	-	-	0.010	0.02
5Ni-1Ag/SiO ₂ Cl	0.012	0.09	0.004	0.02
5Ni-1Ag/SiO ₂ SI	0.014	0.09	0.003	0.01
1Ag-5Ni/SiO ₂ SI	0.019	0.012	0.003	0.02

All the catalysts presented, either for Ni and/or Ag, a metal/support atomic ratio higher when measured by ICP-OES than when measured by XPS. This feature of the catalysts, even though employing a non-porous support can be explained the same way it was previously done for the gold photocatalysts: attributing the differences in the XPS and ICP-OES atomic ratios to phase segregation.

5.4.2.8. UV-Vis of the silver based photocatalysts

The plasmonic properties of the silver based photocatalysts were measured by UV-Vis. The obtained results are presented in Figure 5.49.

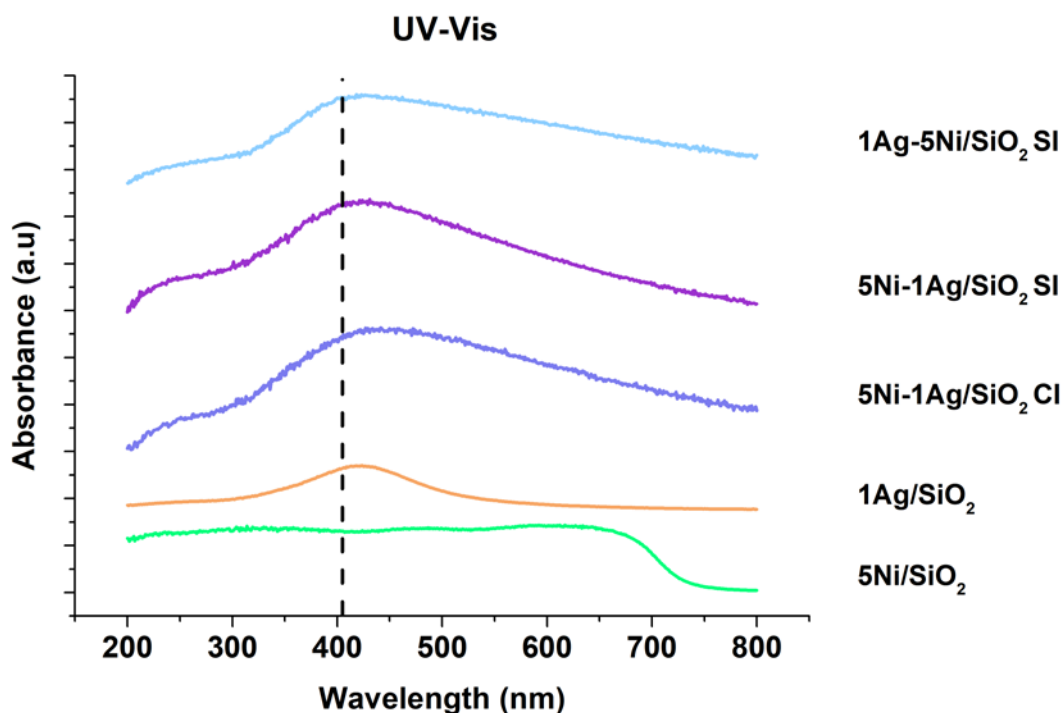


Figure 5.62. UV-Vis profiles of the silver based photocatalysts

As it has been previously explained for the gold based photocatalyst, nickel presents broad light absorption in the visible region. Due to the broadness of the absorption, no distinct peak was observed by UV-Vis for the monometallic nickel catalyst. For the monometallic silver catalyst an absorption peak was observed in a wavelength ranging from 350 nm to 500 nm, with a maximum at 424 nm that can be attributed to the presence of spherical silver nanoparticles [150]. The same absorption peak was observed for all the bimetallic catalysts. For all these catalysts a broadening of the absorption peak and a shift of the maximum to higher wavelengths was observed, being these characteristic features of larger particles [151] or due to the chemical interaction between Ni and Ag [139].

5.4.2.9. Activity tests with silver based photocatalysts

As it has been previously commented for the gold based photocatalysts, due to the fact that not only CH₄ but also CO was produced during the activity tests with the silver based photocatalysts. Thus, instead of comparing the performance of the catalysts in terms of CH₄ yield they will be compared using CO₂ conversion and selectivity to CH₄ as the

parameters to rate the performance of the different silver based photocatalysts. Moreover, due to the fact that the most interesting parameter to be analysed is the behaviour of the catalysts when illuminated with light of the proper wavelength, firstly the results of the catalysts will be commented individually before comparing all of them.

The monometallic nickel catalyst was tested both under dark conditions and laser light illumination as a reference to study the activity of the bimetallic catalysts with LSPR properties. Under dark conditions a maximum value of CO₂ conversion of 31% was achieved at the highest temperature tested, 723 K, with a CH₄ selectivity of 66%, being CH₄ the main product of the reduction of the CO₂. Slight differences were observed when laser light illumination at 405 nm was applied to the catalyst, being both the conversion and the selectivity lower than the ones obtained under dark conditions. However, all the values fitted inside a margin of $\pm 20\%$ so the activity of the catalyst under both conditions can be considered approximately the same. Moreover, the monometallic nickel catalyst yielded CH₄ as the main product under dark conditions or under laser light illumination. Results are shown in Figure 5.52.

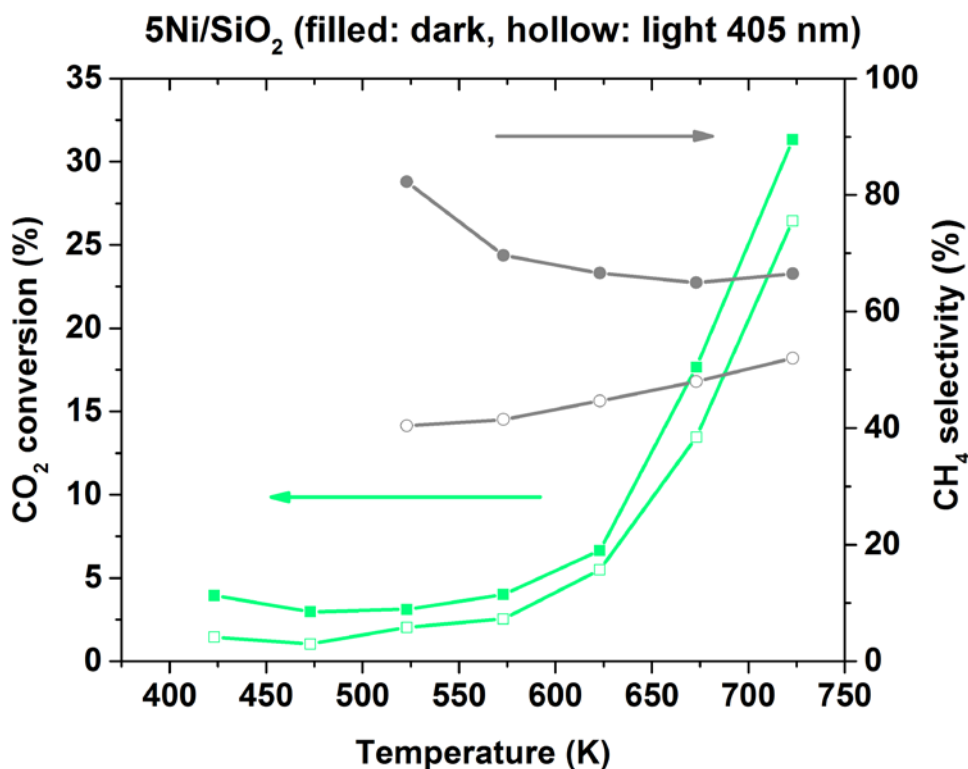


Figure 5.63. 5Ni/SiO₂ activity results

In order to study the influence of silver as a plasmonic metal, the monometallic silver catalyst was tested under dark conditions and laser light illumination. No CO₂ conversion was obtained (< 5%) for this catalyst under dark conditions or laser light illumination at 405 nm at any of the temperatures tested. Being the conversion considered null, hence selectivity cannot be properly discussed.

As it has been previously explained, the bimetallic catalysts with a nominal content of 5 wt.% Ni and 1 wt.% Ag were synthesized by two different wetness impregnation methods: i) coimpregnation (CI), both metals impregnated in one step and ii) sequential impregnation (SI), impregnating the metals in two steps with an intermediate calcination step between both impregnations. Moreover, the SI technique was further studied with the synthesis of two different catalysts changing the order in which the metals were consecutively impregnated.

Under dark conditions a maximum of CO₂ conversion of 27% was obtained for the catalyst prepared by CI at the highest temperature tested. The selectivity of this catalyst towards CH₄ was approximately 43%, being CO the main product obtained for the reduction of CO₂. When laser light illumination at 405 nm was employed, the maximum CO₂ conversion achieved was 23% with the CH₄ selectivity being approximately 47%. As it can be seen, minimum differences were observed for this catalyst under dark conditions or laser light illumination at 405 nm, making us conclude that this catalyst did not present any LSPR properties, as its behaviour was the same for any of the reaction conditions tested. Results are presented in Figure 5.53.

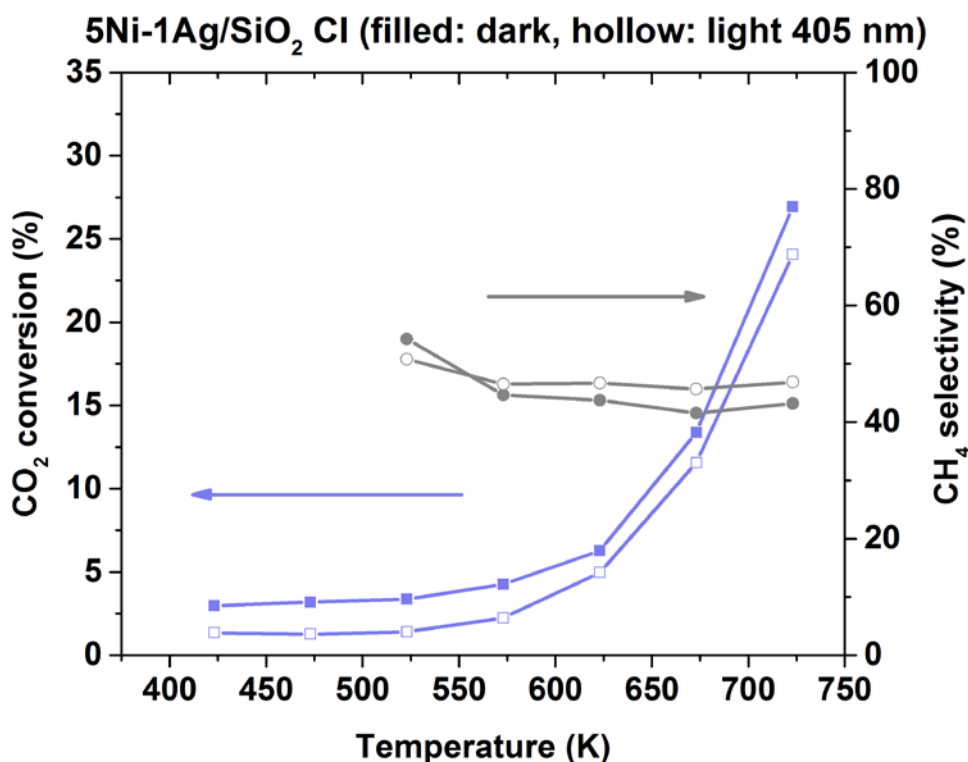


Figure 5.64. 5Ni-1Ag/SiO₂ CI activity results

The catalytic activity observed under dark conditions for the catalyst prepared by SI was lower than the one obtained by the catalyst prepared by CI. The maximum value of CO₂ conversion, achieved at 723 K, for the catalyst prepared by SI was approximately 15%, being the selectivity towards CH₄ of approximately 44%. However, when laser light illumination at 405 nm was employed, the CO₂ conversion was greatly increased, being

the maximum obtained of approximately 27%. However, this increase in the catalytic activity resulted in a decrease in the CH₄ selectivity to approximately 38%. The results can be observed in Figure 5.54.

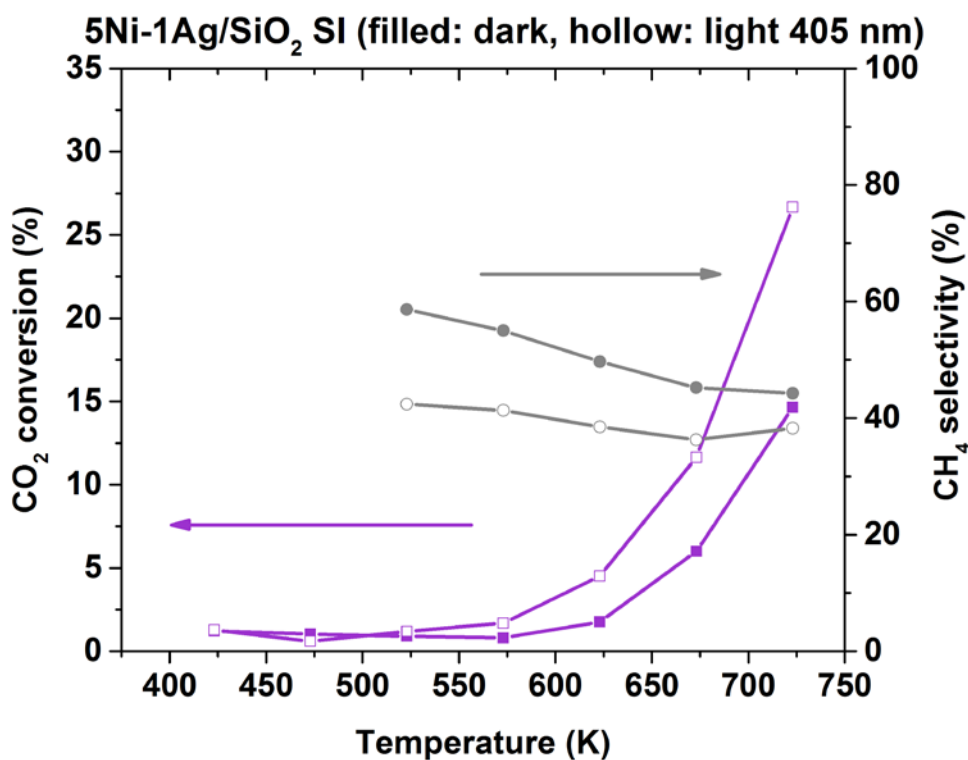


Figure 5.65. 5Ni-1Ag/SiO₂ SI activity results

A second catalyst was prepared by SI, being nickel instead of silver the metal impregnated in the first step. The maximum CO₂ conversion observed for this catalyst was approximately 16% at 723 K and the CH₄ selectivity of 55% under dark conditions. The use of laser light illumination at 450 nm resulted in an increase of the CO₂ conversion up to 23% while the CH₄ selectivity decreased down to 42%. The results are presented in Figure 5.55.

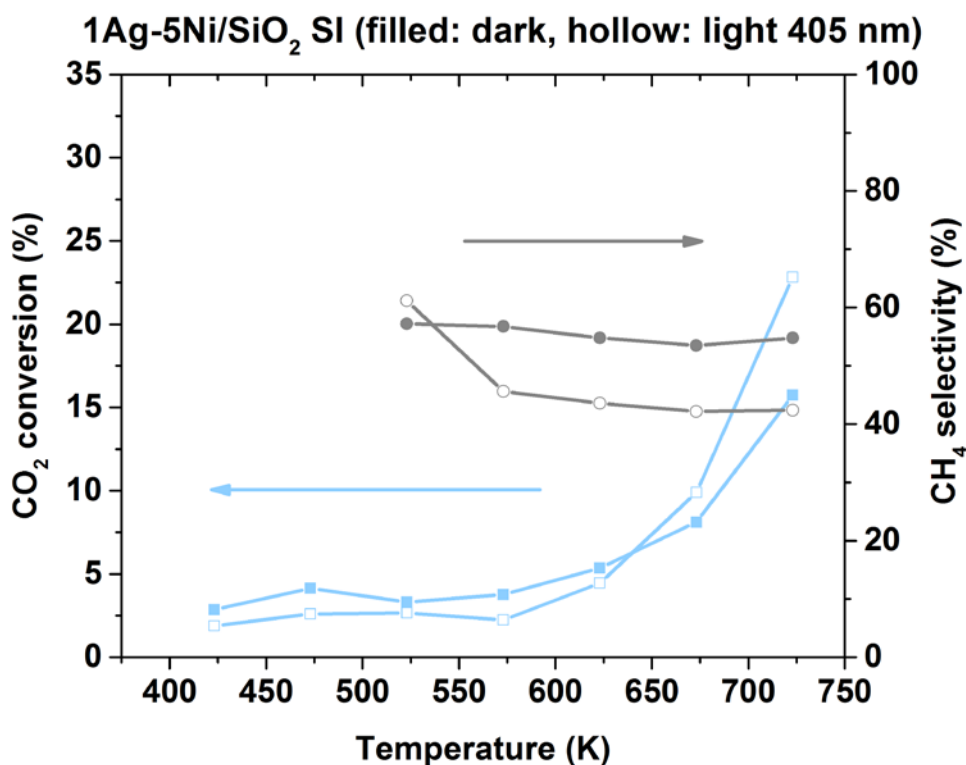


Figure 5.66. 1Ag-5Ni/SiO₂ SI activity results

All the catalysts presented the maximum CO₂ conversion at the highest temperature tested, 723 K. So as to better understand the behaviour of the catalysts, the maximum conversion achieved and the CH₄ selectivity associated to that maximum are presented in Table 5.47, both under dark conditions and laser light illumination at 405 nm.

Table 5.44. Activity results of the silver based photocatalysts

Sample	CO ₂ conversion (%) Dark conditions	CO ₂ conversion (%) Laser light illumination 405 nm	CH ₄ selectivity (%) Dark conditions	CH ₄ selectivity (%) Laser light illumination 405 nm
5Ni/SiO ₂	31.3	26.4	66.5	52.0

1Ag/SiO₂	3.6	3.5	7.1	8.4
5Ni- 1Ag/SiO₂ CI	26.9	24.1	43.2	46.8
5Ni- 1Ag/SiO₂ SI	14.7	26.7	44.3	38.3
1Ag- 5Ni/SiO₂ SI	15.7	22.8	54.8	42.4

As it can be observed, the maximum CO₂ conversion was achieved for the monometallic nickel catalyst. Moreover, this catalyst also presented the highest selectivity towards CH₄ being this the main product of the CO₂ reduction under any of the conditions tested. The monometallic silver catalyst proved that Ag cannot be considered an active metal for CO₂ reduction. The use of laser light illumination at 405 nm did not have any remarkable effect on the behaviour of the monometallic silver catalyst. The bimetallic nickel-silver catalysts synthesized by CI presented a lower value of both CO₂ conversion and CH₄ selectivity than the monometallic nickel catalyst. Therefore, the addition of silver resulted in a decrease of the catalytic activity. No effect of light illumination was observed for this catalyst. However, a different behaviour was observed when the bimetallic catalyst was synthesized by SI. In this case, the addition of silver had a more noticeable effect in the form of a larger decrease of the CO₂ conversion, whilst the selectivity towards CH₄ was approximately the same under dark conditions. For this catalyst, the use of laser light illumination at 405 nm resulted in a substantial increase of CO₂ conversion of more than 80%. This increase in the conversion was associated with a decrease in the selectivity towards CH₄; however this decrease was less remarkable being of approximately only 13%. When nickel was impregnated in the first step of the SI procedure, no significant changes in the CO₂ conversion were observed, however the selectivity was favoured towards CH₄ (55%). Nevertheless, the effect of laser light

illumination for this catalyst was lower than the one obtained when silver was impregnated first, being the increase in the CO₂ conversion of the 45%.

The results obtained in the activity tests clearly indicate the presence of the LSPR effect in the bimetallic catalysts prepared by SI, being this beneficial for the CO₂ reduction reaction. However, the addition of Ag results in a catalyst with a lower basicity than the monometallic nickel catalyst, thus, a decrease in the catalytic activity. This decreased basicity means that the beneficial plasmonic effect is offset. In order to further analyse this feature of the catalysts activity tests were carried out using two different laser light illumination wavelengths: 520 and 660 nm. The variation in the CO₂ conversion for the different catalysts at different wavelengths, using dark conditions as reference, is presented in Figure 5.56. Due to the null catalytic activity of the monometallic silver catalyst; it is not depicted in the figure.

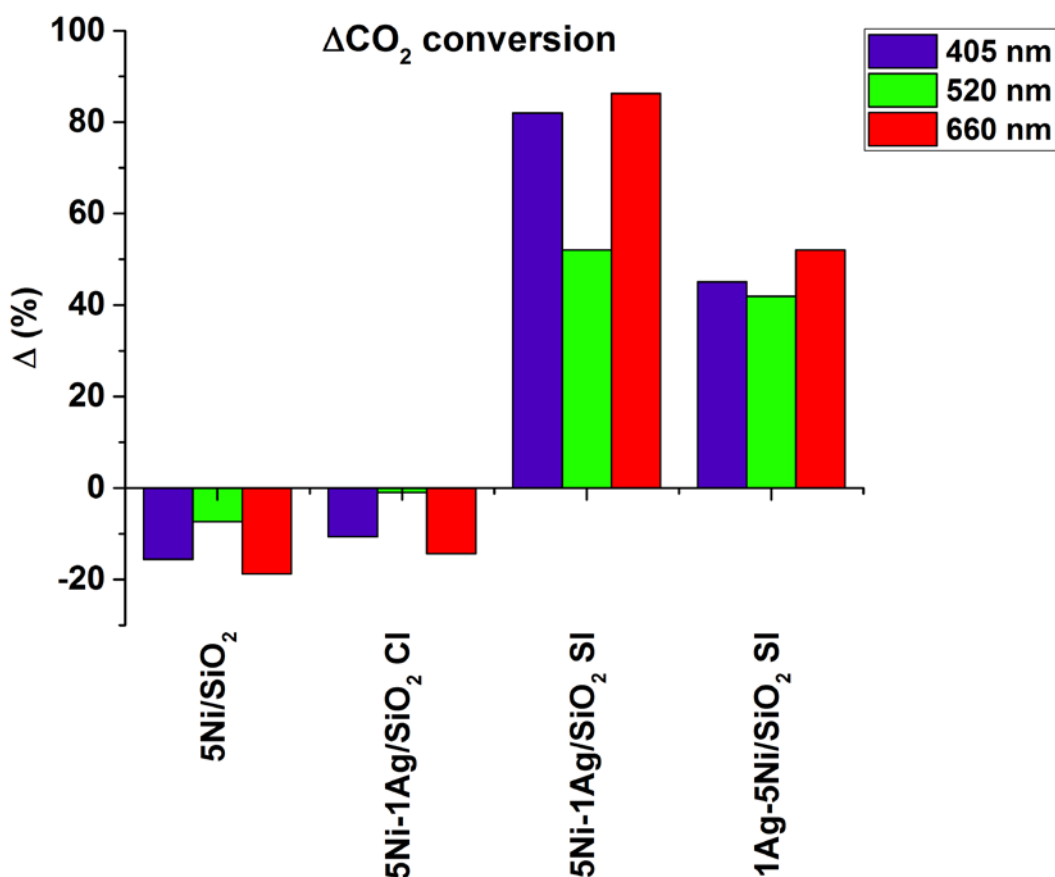


Figure 5.67. CO₂ conversion changes at different wavelengths of the silver based photocatalysts

As it can be seen, neither the monometallic nickel catalyst nor the bimetallic catalyst synthesized by CI presented remarkable changes in their catalytic activity when irradiated with laser at different wavelengths. For the monometallic nickel catalyst this is the expected behaviour due to the absence of any distinct plasmonic absorption peak in the UV-Vis spectra, probably due to the broad absorption of the nickel not being able to promote carbon dioxide reduction reaction. For the bimetallic CI catalyst no light effect was observed, even though an absorption peak was observed with a maximum close to the 405 nm wavelength that was employed to irradiate the sample during the activity tests.

For the catalysts prepared by SI, the use of laser light of any wavelength resulted in an increase in the CO₂ conversion, when compared with the results obtained for the same catalysts under dark conditions. For both catalysts, using 405 nm or 660 nm as the irradiation wavelengths resulted in a higher increase in the conversion than the use of 520 nm.

The use of laser light illumination resulted in slight changes in the selectivity to CH₄ of the catalysts. These changes were dependant on the irradiated wavelength. However, all the changes fitted inside the $\pm 20\%$ so it cannot be attributed to the light irradiation the ability of tuning the selectivity of the catalysts. The variation of the CH₄ selectivity for the different laser light wavelengths, compared with the tests carried out under dark conditions, is presented in Figure 5.57.

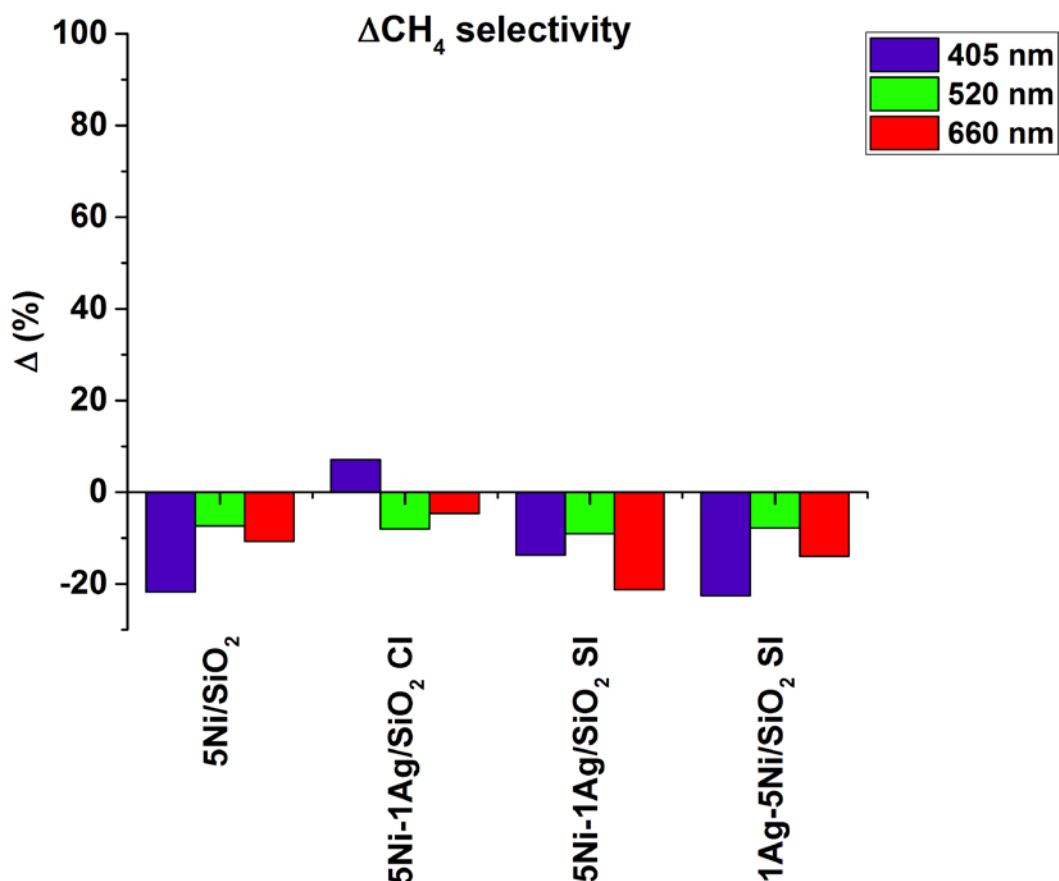


Figure 5.68. CH_4 conversion changes at different wavelengths of the silver based photocatalysts

According to the results obtained, the monometallic nickel catalyst presented the highest catalytic activity under any of the reaction conditions tested. This catalyst was mainly composed by NiO weakly interacting with the support, which could be reduced at the temperature employed. The highest activity of this catalyst can be attributed to its higher basic character, as observed in the results obtained by CO_2 -TPD. The higher intensity of the peak can be attributed to a higher amount of CO_2 being adsorbed, thus, available for its reduction with H_2 [47]. The main difference between this catalyst and all the other catalysts is the presence of a more intense peak at low temperatures (300-500 K), thus, basic sites that take part in the reaction [49]. The results obtained by XRD confirmed those obtained by TPR, with the presence of metallic nickel but also NiO due to the NiO strongly interacting with the support that could only be reduced at temperatures higher than the one employed for the reduction of the catalyst. The average size of the particles was measured by TEM and confirmed the presence of small

particles (6.4 ± 0.1 nm). The data obtained by XPS also confirmed the existence of both NiO (Ni^{2+}) and metallic nickel (Ni^0) with the former being the main one present on the surface of the catalyst. This can be explained due to the nickel being prone to oxidation even at room temperature [152]. Finally, not observing an increase in the activity of this catalyst under laser light illumination can be explained with the results obtained by UV-Vis with the absence of a distinct absorption peak attributable to the broad absorption of the nickel in the visible region.

The monometallic silver catalyst did not present any catalytic activity, due to the fact that it did not have the main active metal, nickel. Even though silver can also be considered an active metal for CO_2 reduction [56] its activity is the lower among all the active metals. Moreover this catalyst presented a low content of silver (≤ 1 wt.%). However, it needs to be taken into account that the synthesis of this monometallic catalyst was performed as a reference to compare the activity of the bimetallic catalysts with LSPR property and to further understand their behavior, when it was added as a LSPR metal and not the main active metal. No reducible species were detected by TPR. The CO_2 -TPD proved the basic character of the catalyst. Results obtained by TEM confirmed the presence of small silver particles (3.2 ± 0.1 nm). The presence of metallic silver was confirmed by XPS, being the only silver specie measured on the surface of the catalyst. UV-Vis technique was useful to determine the presence of an absorption peak with a maximum located at a wavelength of 424 nm that was attributed to silver NPs, whose presence was confirmed by TEM.

The synthesis of the bimetallic nickel-silver catalyst by CI resulted in an increase in the amount of NiO weakly interacting with the support and a decrease in the reduction temperature, thus, making this catalyst easier to reduce than the monometallic nickel catalyst. This catalyst also presented a basic character, as proved by the CO_2 -TPD analysis, however the intensity of the desorption peak was lower than the one presented by the monometallic nickel catalyst which can be correlated to the lower activity presented by the bimetallic catalyst. The results obtained by XRD confirmed the existence Ni-Ag in a mixed state but also the presence of Ni-Ag nanoalloy. A diffraction

peak attributed to silver was identified too, although the intensity of this diffraction peak was lower than the one presented by the other bimetallic catalysts. The average particle size, measured by TEM, was 10.2 ± 0.4 nm. This average particle size was approximately the sum of the average size presented by the monometallic nickel and silver catalysts, suggesting the presence of linked nanoparticles or subclusters. The larger particle size, when comparing to the monometallic nickel catalyst, can also be responsible of the lower activity of the bimetallic CI catalyst. The use of EDX confirmed the existence of the nanoalloy, however the main structure identified was a Ni-Ag subcluster, confirming the assumption made with the data obtained after measuring the average particle size by TEM. The XPS measurements proved the existence of metallic nickel, being identified as the main specie, in the surface of the catalyst but also Ni^{2+} . All the peaks attributed to nickel were shifted to lower binding energies, when compared to the ones measured for the monometallic nickel catalyst., that can be attributed to a higher electron density [133]. Moreover, the peaks attributed to metallic silver were also shifted to lower binding energies, probably due to surface oxidation of this silver or an environment change [153], like an increase in the outer electron cloud density [154]. The fact that the binding energies of both nickel and silver were shifted to lower values than the ones obtained for the respective monometallic catalysts can be attributed to a strong bonding formation between Ni-Ag. [155] or interaction between the metals and the support [156]. Regarding the plasmonic properties of the catalyst, the addition of silver conferred the LSPR property to the catalyst. When comparing the absorption maximum to the one presented by the monometallic silver catalyst, the CI catalyst presented a shift to higher wavelength as a result of the presence of larger particles [157].

The 5Ni-1Ag/SiO₂ SI catalyst presented a higher amount of NiO weakly interacting with the support than the monometallic nickel catalyst, and with a slightly lower reduction temperature. This feature made this catalyst easier to reduce. It presented a similar CO₂-TPD profile than the monometallic catalyst; however it presented a weaker basic character. This could be responsible of the lower catalytic activity of the catalyst synthesized by SI. The presence of metallic silver, Ni-Ag in mixed state and as alloy was confirmed by XRD. According to the results obtained by TEM, this catalyst presented an

average particle size of 6.8 ± 0.2 nm. This average particle size was slightly higher than the one observed for the monometallic nickel catalyst, suggesting that the silver was mixed with the nickel forming a new structure, like an alloy, instead of being only connected particles. The results obtained by EDX corroborated the ones obtained by XRD, as nickel interacting with silver as alloy and metallic silver were both detected. Metallic nickel and Ni^{2+} , the latter being the main one, were detected as the nickel species on the surface of the catalyst while silver was detected as metallic silver. Both the peaks attributable to nickel and the ones attributed to silver were shifted to lower binding energies than the ones detected for the respective monometallic catalysts. The shift to lower binding energies is the result, as it has been previously discussed, of a change in the electron density due to the strong bonding formation between both metals. The results obtained by UV-Vis probed the presence of a strong light absorption attributed to the LSPR at a wavelength close to the one observed for the monometallic silver catalyst. However, the absorption band for this bimetallic catalyst was broader and the maximum was shifted to higher wavelengths (red shift) being both characteristics attributed to an increase in the size of the particles, as previously discussed, but also to a heterogeneous distribution of size and shape of the particles [158].

When nickel was impregnated in the first step of the SI procedure, the amount of NiO weakly interacting with the support was highly increased up to more than 97 %.. However, the reduction temperature of this catalyst was slightly increased, probably due to increase in the interaction nickel-support as the result of calcinating the impregnated nickel twice [159]. The basic character of the catalyst was confirmed by CO_2 -TPD but as it has been previously stated its strength was lower than the one presented by the monometallic nickel catalyst. Different species; metallic silver, Ni-Ag mixed state and nanoalloy were detected by XRD. Further characterization by EDX proved the presence of Ni-Ag as a cluster and in alloyed form. The average particle size measured by TEM was 8.5 ± 0.2 nm. This catalyst presented a higher average particle size when comparing with the bimetallic SI catalyst with silver impregnated in the first step. This increase in the average particle size suggests the formation of a different

structure between Ni-Ag rather than the alloy. The results obtained by EDX proved both the presence of alloy and the cluster, being this one the most abundant Ni-Ag structure. The main nickel specie detected by XPS was Ni^{2+} , however a small amount of metallic nickel was also detected. As it has been previously discussed, nickel is prone to oxidation, it is not surprising to find NiO on the surface of the catalyst. However, the higher amount for this catalyst when compared to the other bimetallic ones can be attributed to the different Ni-support interaction due to the double calcination steps of the impregnated nickel. The plasmonic nature of this material was measured by UV-Vis, presenting an absorption peak close to the one presented by Ag NPs, with a red shift characteristic of larger particles.

According to all the results obtained and the discussion presented above it can be stated which physicochemical properties of the catalysts played an important role both in the catalytic activity and the plasmonic properties of the materials. The catalyst that presented the highest catalytic activity under dark conditions, 5Ni/SiO₂, presented a combination of basic sites at low temperature [49], strong basic sites [65] and small particle size [41] which are physicochemical properties with a proven ability to enhance carbon dioxide reduction process. The absence of light absorption at any wavelength, as observed by UV-Vis, meant this catalyst presented the same catalytic activity under dark conditions and any of the laser light illumination wavelengths employed.

The small metallic loading of silver in the monometallic catalyst was responsible for the null catalytic activity at any of the conditions tested. Nevertheless, the synthesis of this catalyst was helpful to study the plasmonic properties of the bimetallic catalysts.

For the bimetallic catalysts the synthesis method played an important role in their physicochemical properties. When synthesized by CI, the catalyst suffered from an increase in the average particle size that together with the decrease in the strength of the basic sites hindered its catalytic activity. Although this catalyst presented absorption due to the presence of silver NPs, the structure formed with the nickel (mainly cluster) did not increase the activity when laser light illumination was irradiated. The 5Ni-1Ag/SiO₂ SI catalyst presented lower catalytic activity under dark conditions due to the

weaker basic character and the fact that the particles, even if being of a size approximately equal to the one presented by the monometallic nickel catalyst, were a mixed Ni-Ag structure (alloy) and not only nickel which is more active for carbon dioxide reduction. The presence of Ni-Ag alloy resulted in the plasmonic effect of silver increasing the activity of this catalyst when the reaction was carried out under laser light illumination of any wavelength. Alternatively, the 1Ag-5Ni/SiO₂ SI catalyst presented approximately the same behavior that its counterpart synthesized by SI under dark conditions. The different Ni-Ag structures formed, not only alloyed but also as cluster, resulted in a different behavior under laser light illumination. Even if these conditions resulted in an increase in the catalytic activity this enhancement was lower than when the silver was impregnated in the first step.

Summarizing, the addition of Ag by SI promotes the LSPR of the catalysts at expense of the activity. Even though this catalyst presents a substantial increase in the carbon dioxide conversion when illuminated at different wavelengths, the addition of Ag results in a decrease of the basicity, when compared with the monometallic nickel catalyst, that hinders the overall activity of this catalyst. Moreover, the LSPR effect results in an increase of the CO selectivity in detriment of the production of CH₄.

Chapter VI

Design of an industrial process

Table of contents

6.1. DESIGN OF THE INDUSTRIAL PLANT	217
6.1.1. INITIAL ASSUMPTIONS	217
6.1.2. EQUIPMENT	219
6.1.2.1. <i>Water electrolysis</i>	219
6.1.2.2. <i>Carbon dioxide methanation</i>	219
6.1.2.3. <i>Condensation and injection to the gas grid</i>	225
6.1.3. CATALYST	227
6.1.4. UTILITIES	227
6.1.5. COST SUMMARY.....	228
6.1.5.1. <i>Streams cost and product sales revenue</i>	228
6.1.5.2. <i>Equipment cost</i>	230
6.1.5.3. <i>Electrolyser cell stack cost</i>	231
6.1.5.4. <i>Catalyst cost</i>	231
6.1.5.5. <i>Utilities cost</i>	231
6.1.5.6. <i>Labour cost</i>	232
6.1.5.7. <i>Total capital investment</i>	233
6.1.6. PROFITABILITY CRITERIA	234
6.1.6.1. <i>Time criterion</i>	234
6.1.6.2. <i>Cash criterion</i>	236
6.1.6.3. <i>Interest criterion</i>	237
6.2. ANNEX: FULL SIZE DESIGN.....	238

One of the main objectives of any research should be gaining enough knowledge about the studied process to be able to develop an industrial process. In this chapter a first approach to the design of an industrial plant that integrates both carbon dioxide methanation process and water electrolysis, so as to generate the hydrogen needed for the methanation step, is proposed.

6.1. Design of the industrial plant

Aspen Plus V8.8 (Aspentech) software was employed for the simulation of the process and the sizing of the different equipments.

The industrial plan design should be separated in three different areas: i) water electrolysis process, ii) carbon dioxide methanation process and iii) condensation of the produced gas stream, with the gas product being injected into the natural gas grid and the liquid product, mainly water, being recycled in the electrolysis process. In this later step a membrane was added in order to purify the product stream to meet the desired composition requirements. The design also should present different heat exchangers in order to improve the overall energy efficiency of the process. At the end of this chapter a full size design is presented.

6.1.1. Initial assumptions

In order to perform the capital costs it is necessary to size the different equipment employed. Being a first approach to the design of an industrial plant different assumptions are made.

First of all, the lifetime of the plant was defined as 20 years, however both the catalyst and the electrolysis cell stack should be replaced several times during the average lifetime of the project [160].

One of the first decisions that needs to be made before starting the design of the industrial plant is the production volume. In this case, the maximum electricity consumption of the designed plant was set to 20 MW based the average power of a

wind power plant in Spain [161]. This way, the proposed design would be able to absorb the excess of electricity of a wind power plant at maximum load, while not requiring an extra electricity input that would result in a higher operating cost.

Pure carbon dioxide was selected as the feed for the methanation reaction. Other components, as H_2S , were not taken into account. If needed, a gas conditioning step should be performed as this compound would poison the catalyst. The selection of pure carbon dioxide as feed results in the most expensive feed case scenario.

As products, we can take into account four different outlet streams: synthetic natural gas that is the main product, oxygen as a byproduct produced during the electrolysis step, water as a byproduct of the methanation step that is recycled to the electrolysis step and non-reacted hydrogen. The molar flows of the products were calculated by the software using a kinetic model obtained from the literature [35] that is in agreement with the data obtained in the activity results, previously presented in the **Chapter V** of this PhD thesis, so it can be considered an achievable value of the conversion. A summary of the molar flow (kmol/h) of the different streams is presented in Table 6.1.

Table 6.45. Feed and product streams flows

Stream	Molar flow (kmol/h)
Feed	
Carbon dioxide	35.5
Hydrogen	7.75
Product	
Water	71

Synthetic natural gas	34.10
-----------------------	-------

Oxygen	67.81
--------	-------

6.1.2. Equipment

As it has been previously stated the industrial plant can be divided in three different sections. 304L stainless steel was selected as the material of construction (MOC) for all the equipment, but the heat exchangers, due to the fact that it presents excellent stability against all the substances involved in the process at the operating conditions. The MOC selected for the heat exchangers was carbon steel, being this the most commonly employed material for this type of equipment [162].

6.1.2.1. Water electrolysis

The software employed did not include a model for a water electrolyser. Thus, a reactor and a separator were used to simulate a real electrolyser stack.

To be able to process the water stream, a stack of 14 electrolysers of 1.25 MW/electrolyser capable of processing 3,150 m³/h are needed. PEM was the technology selected for the electrolyser stack, as PEM electrolysers are able to operate at variable rates [30] and the electricity obtained from renewable energy sources is variable. The cost of this technology is expected to be 576 \$/kW by 2020 [163].

The mixer needed before the electrolyser stack in order to mix the three different water streams: feed water, water recycled from electrolysis and water recycled from methanation were automatically sized and thus its cost was automatically calculated.

6.1.2.2. Carbon dioxide methanation

The software was not able to automatically size the reactor, thus it was designed using a kinetic model, specifically a LHHW rate equation proposed in the literature.

$$r = \frac{k p_{\text{H}_2}^{0.5} p_{\text{CO}_2}^{0.5} \left(1 - \frac{p_{\text{CH}_4} p_{\text{H}_2\text{O}}^2}{p_{\text{CO}_2} p_{\text{H}_2}^4 K_{\text{eq}}}\right)}{\left(1 + K_{\text{OH}} \frac{p_{\text{H}_2\text{O}}}{p_{\text{H}_2}^{0.5}} + K_{\text{H}_2} p_{\text{H}_2}^{0.5} + K_{\text{mix}} p_{\text{CO}_2}^{0.5}\right)^2} \quad \text{Eq. 6.1}$$

With this equation, the molar flow rate of CO₂ fed to the reactor and the maximum carbon dioxide conversion achievable at 573 K being set to 0.9798 according to the thermodynamic equilibrium, a calculation of the weight of catalyst was made.

$$W = 35500 \int_0^{0.9798} \frac{dX}{\frac{600.56 \frac{(1-x)}{(1-0.4x)}}{1 + 2540 \frac{(1-x)}{(1-0.4x)}}} \quad \text{Eq. 6.2}$$

The result was an amount of catalyst of 332 kg. The carbon dioxide conversion as a function of the catalyst weight is presented in Figure 6.1.

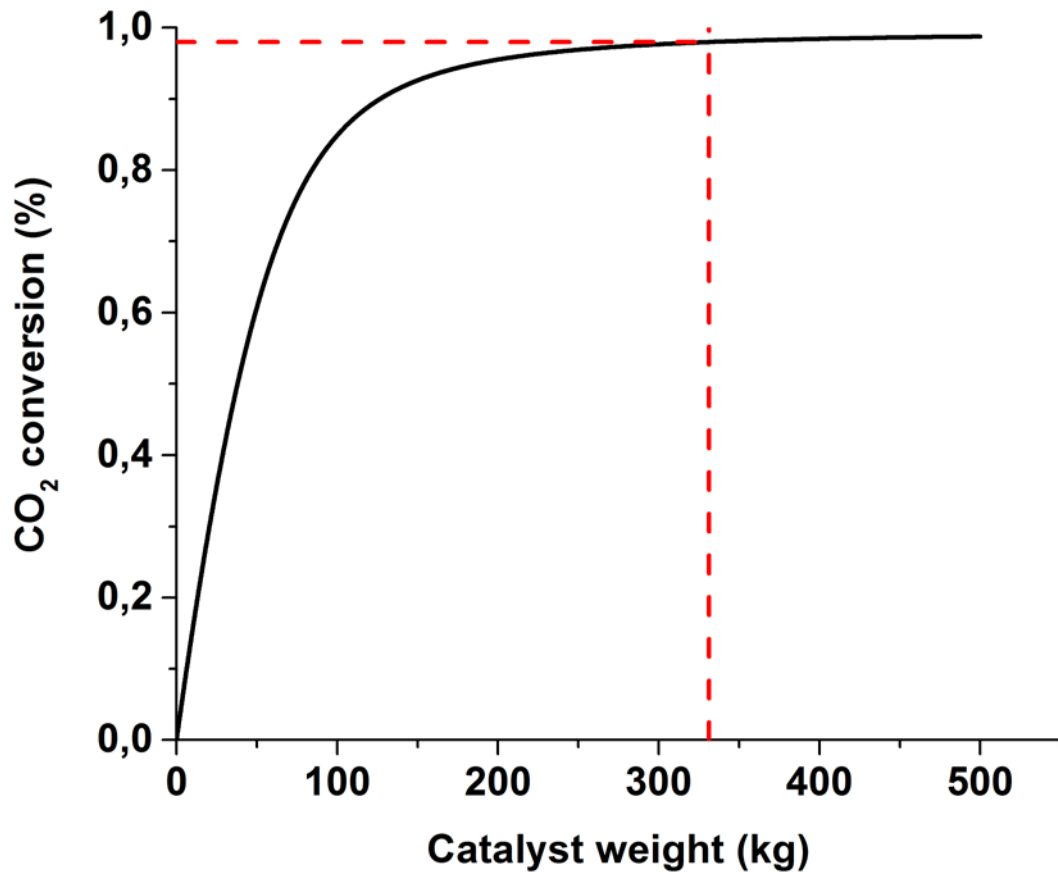


Figure 6.69. Carbon dioxide conversion as a function of the catalyst weight

So as to avoid temperature gradients in the reactor due to the high exothermic nature of the carbon dioxide reaction, the proposed reactor is formed by a series of tubes that are cooled with a thermal fluid. With a fixed length (L) of 2 m, the diameter of the tubes was determined taking into account different parameters. First of all, the ratio between the internal diameter of the reactor (ID) and the diameter of the catalyst particles (d_p) should be higher than 10 in order to avoid bypassing near the reactor wall [83]. Taking into account that the d_p was fixed to an arbitrary value of 0.0054 m, the reactor ID should be at least of 0.054 m. For the sake of obtaining a good heat transfer, the ratio of the reactor L/ID should be maximized. Knowing the total volume of the catalyst we also calculated the number of reactor tubes needed. The proposed reactor configurations are presented in Table 6.2.

Table 6.46. Proposed reactor configurations

Length (m)	ID (m) (DN)	Number of tubes
2	0.05868 (50)	56
2	0.07092 (65)	39
2	0.08679 (80)	26
2	0.09949 (90)	20
2	0.11219 (100)	16

In order to avoid any transfer limitations in the reactor, modified Reynolds number (Eq. 6.3) was calculated for different reactor internal diameters. This number is defined as:

$$Re = \frac{V \rho \phi}{\mu (1 - \varepsilon)} \quad Eq. 6.3$$

Being:

V (m/s): flow velocity.

ρ (kg/m³): fluid density.

ϕ (m): catalyst diameter.

μ (Pa.s): dynamic viscosity.

ε : bed voidage (representative value: 0.45).

Design of an industrial process

Mass transfer limitations are avoided with turbulent flow, thus modified Reynolds number > 100 . These values of Reynolds number are obtained for all the reactor internal diameters proposed.

Pressure drop along the reactor, as a function of the reactor length, was calculated using Ergun equation (Eq. 6.4):

$$\Delta P = \frac{150 \mu V}{\emptyset^2} \frac{(1 - \varepsilon)^2}{\varepsilon^3} + \frac{1.75 \rho V}{\emptyset} \frac{(1 - \varepsilon)}{\varepsilon^3} \quad \text{Eq. 6.4}$$

Being:

ΔP (Pa/m): pressure drop as a function of the reactor length.

While the rest of parameters have been previously defined as part of the *Eq. 6.1*. The calculated pressure drops for the different proposed reactors are presented in Table 6.4.

Table 6.47. Calculated pressure drop for different reactor configurations

ID (m) (DN)	Pressure drop (%)
0.05868 (50)	2.16
0.07092 (65)	2.09
0.08679 (80)	2.09
0.09949 (90)	2.05
0.11219 (100)	1.99

Chapter VI

The reasonable pressure drop should be at least equal to the highest of one of these values [164].

- 10 % of the inlet pressure.
- 35 cm of height of a column of water (0.0035 bar).
- 100 times the pressure drop through the empty reactor.

The highest allowable pressure drop was defined as 10 % of the inlet pressure, thus, all the proposed reactor configurations could be employed.

With all this data, the reactor that presented the lowest pressure drop was chosen for the design of the industrial plant. Moreover, the absence of external mass transfer limitations was also ensured.

The wall thickness was calculated taking into account the nominal size of the piping. For the chose tubes of DN 100 with a Sch of 5/5S the wall thickness is 0.00211 m.

The gases were fed to the reactor at a temperature of 613 K so as to avoid the need of electrically heating the reactor. Finally, the reactor was cooled using Dowtherm-A in concurrent mode as thermal fluid. A liquid fluid was employed due to the fact that gas-liquid heat exchangers require lower surface than liquid-liquid heat exchangers.

To summarize, all the specifications for the reactor are presented in Table 6.4.

Table 6.48. Methanation reactor specifications

Parameter	Value
Tube external diameter (m)	0.1143
Tube length (m)	2

Number of tubes	16
Total volume (m ³)	0.30
Operating temperature (K)	613
Operating pressure (bar)	10
Pressure drop (bar)	0.20
Material	304L stainless steel
Thermal fluid	Dowtherm-A (co-current)

6.1.2.3. Condensation and injection to the gas grid

The design of the industrial plant included a condensation step to separate the gas product, to be pressurized and injected into the natural gas grid, and the liquid product to be recycled to the electrolysis step.

Condensation of the product obtained during the methanation step was carried out at 276 K and 10 bar. The condenser was automatically sized, and its cost calculated, by the software using the flow of the streams to perform the calculations.

The injection of natural gas in the gas grid is regulated in order to ensure the quality of the distributed final product and avoid potential risks due to the injection of different compounds. As the harmonisation of the natural gas grid specifications is still in the to-do list of the European Union, the specifications required to inject natural gas into the natural gas grid in Spain [29] are presented in Table 6.5. So as to meet these specifications a membrane was added after the condensation step so as to increase the concentration of methane in the product stream.

Table 6.49. Natural gas grid specifications in Spain

Parameter	Required value
CH ₄ (mol %)	> 95
CO (mol %)	< 2
CO ₂ (mol %)	< 2.5
H ₂ (mol %)	< 5
O ₂ (mol %)	0.01
Pressure (bar) [165]	4
Temperature (K) [166]	273-293

Different membrane configurations were simulated [167], studying two main alternatives: one membrane module and two membrane modules in series with the permeate of the second volume being recirculated. In both cases, a compressor was added before the membrane in order to increase the pressure of the feed stream to 16 bar, so as to meet the requirements to inject the gas in the grid. For the case with the two modules, another compressor is needed in order to increase the pressure of the recirculated permeate from atmospheric pressure to 16 bar. The chosen configuration was the one with one membrane, so there was no need to add another compressor as it would increase the electricity usage of the design above the allowable 20 MW limit defined for the project.

6.1.3. Catalyst

Catalyst loading was calculated during the sizing of the reactor, resulting in 332 kg. The catalyst can be considered to present an average lifetime of 20,000-25,000 h [160] and a cost of 60 \$/kg [168] based on literature.

6.1.4. Utilities

Electricity is the utility needed for the plant to operate. Assuming that the plant operates 8760 h per year the annual electricity usage can be calculated. Results are presented in Table 6.6.

Table 6.50. Electricity usage

Equipment	Electricity usage (MWh)
Electrolyser stack (R101-S101)	153,300
Reactor (R102)	-
Condenser (F101)	526
Membrane (V101)	-
Heater (H101)	-
Heat Exchanger 1 (HX101)	-

Heat Exchanger 2 -
(HX102)

Heat Exchanger 3 -
(HX103)

Fin Fan Cooler (F101) 19,447

Pump (P101) 0.3

Plant 173,273

As it can be seen the electricity usage of the plant annually was calculated as, approximately, 173,273 MWh. As the plant operates 8,760 h it results in a mean power of 19.8 MW.

6.1.5. Cost summary

6.1.5.1. Streams cost and product sales revenue

The cost of both feed streams water and carbon dioxide, was set as 1 \$/tonne [169] and 61 \$/tonne respectively [160]. The cost of the Dowtherm-A was set as 4.4 \$/tonne with a circle time of 0.5 h. [168]. Being a closed loop it is only necessary to pay for the Dowtherm-A once, so this cost can be considered as a part of the fixed capital cost.

Regarding to the benefits that can be obtained due to the operation of the plant, synthetic natural gas is the most interesting product. The price considered for the produced synthetic natural gas is 0.2 \$/m³ being this the lowest price set by Gazprom [170]. However, not only synthetic natural gas can be sold but also the oxygen produced during water electrolysis. For this byproduct a price of 84 \$/tonne was considered, taking into account that the oxygen produced can be considered pure. For not pure oxygen a price of 12 \$/tonne can be considered, decreasing the revenue obtained [24].

Design of an industrial process

Moreover, the excess of hydrogen that does not react can also be sold, at a price of 1.8 \$/kg [171].

The cost of the different feed streams (\$/yr) can be observed in Table 6.7.

Table 6.51. Feed streams cost

Stream	Cost (\$/yr)
Carbon dioxide	834,856
Water	11,204
Total	846,060

While the profit obtained with the products is presented in Table 6.8.

Table 6.52. Product sales revenue

Product	Sales revenue (\$/yr)
Synthetic natural gas	82,705
Oxygen	1,596,965
Hydrogen	1,945,158
Total	3,624,828

6.1.5.2. Equipment cost

As it has been stated, the cost of all the equipment but the electrolyser stack and the membrane was calculated by the software after a proper sizing. In the case of the electrolyser stack, literature was used [30]. The cost of the membrane was also calculated using the literature [172].

The cost of all the equipment can be observed in Table 6.9.

Table 6.53. Equipment cost

Equipment	Installed cost (\$)
Electrolyser stack (R101-S101)	10,080,000
Reactor (R102)	135,900
Condenser (F101)	86,700
Membrane (V101)	23,600
Heater (H101)	12,680
Heat Exchanger 1 (HX101)	68,600
Heat Exchanger 2 (HX102)	42,000

Heat Exchanger (HX103)	3	201,300
---------------------------	---	---------

Fin Fan Cooler (F101)		113,600
-----------------------	--	---------

Pump (P101)		51,400
-------------	--	--------

Plant		10,815,780
-------	--	------------

6.1.5.3. Electrolyser cell stack cost

As it has been explained, the cell stack has a shorter lifetime than the 20 years period defined for the proposed design. According to the literature, the cell stack should be replaced every 40,000 h with a cost of approximately 50 % of the full electrolyser cost [160], thus, 5,040,000 \$.

6.1.5.4. Catalyst cost

With an estimated lifetime for the proposed design of 20 years and taking into account that the plant operates 8,760 h/year the catalyst should be replaced every 3 years.

Taking into account the amount catalyst loaded into the reactor and the price of the catalyst previously reported, it results in a cost of 1404 \$/replacement.

6.1.5.5. Utilities cost

Regarding to the cost of the electricity it can be assumed as free electricity as the plant proposed has a power of 19.8 MW and it has been designed to absorb the excess of electricity, thus, free electricity of an average wind power plant which presents a power of 20 MW.

6.1.5.6. Labour cost

Labour costs were calculated using the equation provided by Turton et al. [173].

$$N_{OL} = (6.29 + 31.7P^2 + 0.23N_{np})^{0.5} \quad Eq. 6.5$$

Being:

N_{OL} : number of operators per shift.

P : number of processes involving handling of particulate solids.

N_{np} : number of nonparticulate processing steps.

As the number of particulate solids handlings processes is null and the number of nonparticulate processing steps is 10 (electrolyser stack, reactor, condenser, membrane, heat exchanger (x3), heater, fin fan cooler, pump) the number of operators per shift is 2.93.

An operator works 49 weeks/yr and 5 shifts/week, resulting in 245 shifts/yr. A chemical plants operates 365 days/yr and 3 shifts/day this results in 1095 shifts/yr. If an operator works 245 shifts/yr this results in 4.5 operators need to be hired for each operator needed for the plant. As it has been mentioned, 2.68 operators are needed in the plant so approximately 13 operators need to be hired.

The average wages from the collective bargaining agreement (CBA) for the chemical industry in Spain [174] have been employed in order to calculate the labour costs. The average wage for an operator is 20,082 \$/year, thus labour costs were calculated as 261,066 \$/year. However, this only includes the operators and no other staff.

Usually a supervisor:operator ratio of 1:4 is considered as valid. Assuming that all the supervisors are chemical engineers, according to the CBA for the chemical industry in Spain the average wages for this position are 25,448 \$/year, thus another 101,793 \$/year have to be added to the cost calculation.

Finally we have to take into account a chief executive with an average wage of 45,877 \$/year.

A summary of the labour costs is presented in Table 6.10.

Table 6.54. Labour costs

Position	Salary (\$/yr)
Operators	261,066
Supervisors	101,793
Executive chief	45,877
Total	408,736

6.1.5.7. Total capital investment

Total capital investment can be calculated as the sum of fixed capital, presented in Table 6.9, the working capital, defined as the sum of salaries (see Table 6.10) and material inventories (see Table 6.7) plus catalyst cost; and contingencies [173]. For the contingencies a value of 15 % of the fixed capital was considered [175].

Total capital investment is summarized in Table 6.11.

Table 6.55. Total capital investment

Concept	Cost (\$)
Fixed capital cost	10,815,780

Working capital	1,254,796
Contingencies	1,622,367
Total capital investment	13,692,943

6.1.6. Profitability criteria

There are two main different criteria to study the profitability of a project, non-discounted and discounted profitability criteria. The main difference between them is that the latter considers the time-value of the money [173]. This is the most realistic criteria and was the one employed to evaluate the profitability of the designed industrial plant.

To evaluate the profitability of a project according to the discounted profitability criteria time, cash or interest rates have to be taken into account. All these criteria are further defined in the upcoming sections according to the definitions by Turton et al.[173].

6.1.6.1. Time criterion

The discounted payback period (DPBP) is defined as the time required to recover the initial fixed capital investment or total capital investment. In this case total capital investment was chosen due to being a more realistic value.

To calculate the DPBP it is necessary to calculate the discounted cumulative cash flow. The present value of the cash flows is calculated dividing the cash flow by $(1+i)^n$ being i a discount factor (considered 0.1 for a 20 year project) and n the year. Taking into account the initial investment, namely, total capital investment results obtained are presented in Table 6.12.

Table 6.56. Discounted cumulative cash flow

Year	Discounted cumulative cash flow
1	-9,152,832
2	-7,194,128
3	-5,413,488
4	-3,795,683
5	-2,324,079
6	-3,831,207
7	-2,615,726
8	-1,510,089
9	-504,964
10	408,245
11	-527,563
12	227,603
13	913,710
14	1,537,813

15	2,105,180
----	-----------

16	1,523,812
----	-----------

17	1,992,710
----	-----------

18	2,418,981
----	-----------

19	2,806,271
----	-----------

20	3,158,561
----	-----------

The DPBP is calculated as the latest period with a negative cumulative cash flow plus the result of dividing the absolute value of that negative cash flow by the total cash flow after that period.

In this case a DPBP of 11.03 years was obtained.

6.1.6.2. Cash criterion

The present value ratio (PVR) is the more realistic way to evaluate the profitability of a project according to the discounted cash criterion. It is defined as the present value of all positive cash flows divided by the present value of all negative cash flows. A project can be considered profitable if this value is greater than the unity.

The present value of the cash flows was calculated as explained above for the calculations of the DPBP.

The result obtained was a PVR of 1.14, thus, a profitable project.

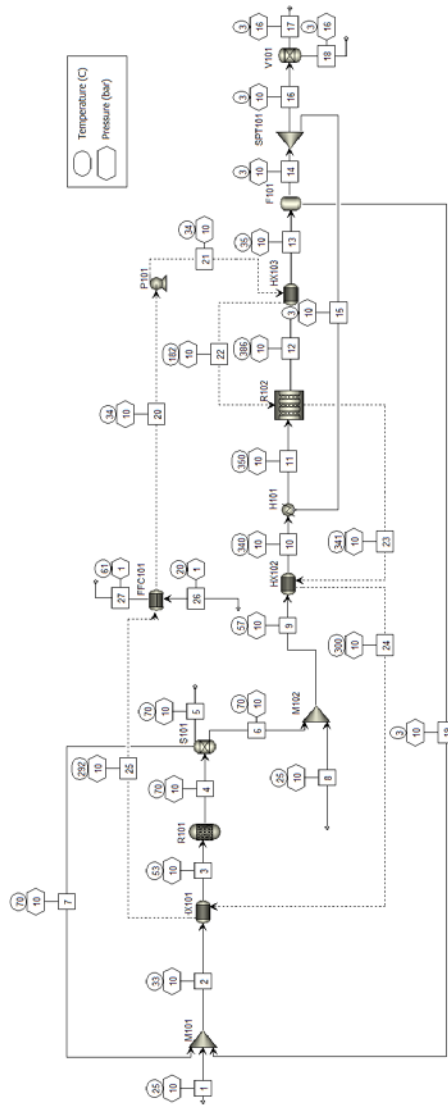
6.1.6.3. Interest criterion

The discounted cash flow rate of return (DCFROR) is the interest rate at which the cash flow values must be discounted in order for the net present value (NPV) of the project to be equal to zero. The following equation was solved to calculate the DCFROR:

$$\sum_{n=1}^{20} \text{net cash flow}/(1 + \text{DCFROR})^n - \text{total capital investment} \quad \text{Eq. 6.6}$$

Being the net cash flow the sum of the profit obtained selling the products minus the feed stream cost and the operating labour cost; n the year and the total capital investment the value calculated previously and presented in Table 6.11. Solving the real part of this equation gives as a result a DCFROR of 0.16, thus, 16 %.

6.2. Annex: full size design



Chapter VII

Conclusions

In the current PhD thesis an exhaustive study of different catalytic systems for the carbon dioxide methanation has been carried out. Moreover, a novel approach to this reaction based on catalysts with localised surface plasmon resonance was also studied. Finally, the feasibility of building an industrial plant was also analysed presenting a design together with an economic analysis.

First of all an analysis of the most suitable calcination temperature of the catalysts and the operating pressure was carried out with a nickel/alumina catalyst. The conclusions obtained are summarized below:

1. 673 K was selected as the most suitable calcination temperature for nickel based catalysts. This temperature was determined taking into account the activity presented by the catalysts and correlating it with the physicochemical properties of the catalysts. Calcinating the catalysts at 673 K increased the amount of the most active nickel species.
2. 10 bar was selected as the most suitable operating pressure. Although a slightly higher activity was observed at 15 bar, there was not much difference and operating at higher pressures results in higher costs and higher risks.

All the catalytic systems were prepared with nickel as the main active metal. The information obtained from the activity tests and the different characterisation techniques carried out over the fresh-reduced and the used catalysts led to the identification of the optimal physicochemical properties for a catalyst to be active in the carbon dioxide methanation reaction:

3. A high surface area of the support resulted beneficial for the synthesis of the catalysts, favouring a high metallic dispersion.
4. Among all the different reducible species identified, a large amount of nickel oxide weakly interacting with the support enhanced the catalytic activity whilst free nickel oxide or strongly interacting with the support resulted detrimental for the catalytic activity.

5. A small nickel crystallite size, measured by XRD correlated, well with a high metallic dispersion, measured by CO chemisorption, and resulted in a benefit for the catalytic activity.
6. A proportion of low:high temperature acids sites of 1:1.5 was identified as the most suitable acid sites ratio. Even though basic catalysts are the most usually employed catalysts for carbon dioxide methanation, a proper ratio of low:high temperature acid sites proved to be beneficial for this reaction.

An important achievement of this PhD thesis is the successful use of non-conventional catalytic supports, both natural supports and industrial residues. The use of this kind of supports resulted in a double benefit: i) valorisation of residues obtained from different industrial processes and ii) reducing the cost of the catalysts employed for the carbon dioxide methanation reaction. The study of this conventional supports resulted in a main conclusion:

7. Sepiolite demonstrated being a promising support for carbon dioxide methanation reaction as it presented a high methane yield at all the temperatures tested and it presents a cost several times lower than a conventional support such as alumina (γ).

During the PhD thesis a research fellowship was carried out at the University of New South Wales (UNSW) in Sydney, Australia. The aim of this research fellowship was to study feasibility of employing localised surface plasmon resonance catalysts, a kind of photocatalysts, for the studied reaction. The main advantage of this catalysts are that they are activated under light irradiation. The studied catalysts with localised surface plasmon resonance properties also contained nickel as the main active metal, thus, being the conclusions previously listed also applicable. However, due to the presence of plasmonic nanoparticles (NPs) of gold or silver further conclusions were obtained:

8. A basic character resulted beneficial for the catalytic activity, as it has been usually proved for carbon dioxide methanation reaction. The catalysts that presented a stronger basic character also presented higher catalytic activity.

9. Both gold and silver promoted the conversion of carbon dioxide to carbon monoxide in a higher extent than to methane.
10. Bimetallic catalysts presented an enhancement in their carbon dioxide conversion when irradiated with light of the appropriate wavelength.

Finally, the design of an industrial process for the carbon dioxide methanation reaction was proposed. The main feature of this design was the use of a multitube reactor. This reactor was employed to overcome the main drawback of the reaction, its high exothermic character. The multitubular design allows a more efficient heat exchange, improving the reaction but also allowing to use the excess of heat in several parts of the process. Regarding to the design of an industrial plant we can conclude that:

11. Cooling the reactor is critical to ensure a proper operation with a methane yield close to the desired one.
12. The heat produced in the reaction can be efficiently employed to preheat the feed of the reactor.
13. The proposed industrial design proved to be profitable taking into account different criterions such as:
 - a. Time criterion: the design presented a discounted payback period (DPBP) of 11 years for a 20 years lifetime.
 - b. Cash criterion: the design presented a present value ratio (PVR) of 1.13.
 - c. Interest criterion: the design presented a discounted cash flow rate of return (DCFROR) of 16 %.

References

-
- [1] International Energy Agency. Energy Statistics. Statistics (Ber) 2016.
- [2] Doman LE, Arora V. International Energy Outlook 2016 Liquid fuels. vol. 484. 2016. doi:DOE/EIA-0484(2014).
- [3] Breeze P. The Natural Gas Resource. Gas-Turbine Power Gener 2016;9–19. doi:10.1016/B978-0-12-804005-8.00002-1.
- [4] Dincer I, Zamfirescu C. Chapter 3: Fossil Fuels and Alternatives. Adv Power Gener Syst 2014;95–141. doi:http://dx.doi.org/10.1016/B978-0-12-383860-5.00003-1.
- [5] Taylor P, Kostic MM. Energy : Global and Historical Background Energy : Global and Historical Background. Encycl Energy Eng 2008;1–15. doi:10.1081/E-EEE-120042341.
- [6] Zou C, Zhao Q, Zhang G, Xiong B. Energy revolution: From a fossil energy era to a new energy era. Nat Gas Ind B 2016;3:1–11. doi:10.1016/j.ngib.2016.02.001.
- [7] Zhu H, Guo P. Are shocks to nuclear energy consumption per capita permanent or temporary? A global perspective. Prog Nucl Energy 2016;88:156–64. doi:10.1016/j.pnucene.2015.12.013.
- [8] Sovacool BK, Andersen R, Sorensen S, Sorensen K, Tienda V, Vainorius A, et al. Balancing safety with sustainability: Assessing the risk of accidents for modern low-carbon energy systems. J Clean Prod 2016;112:3952–65. doi:10.1016/j.jclepro.2015.07.059.
- [9] McCombie C, Jefferson M. Renewable and nuclear electricity: Comparison of environmental impacts. Energy Policy 2016;96:758–69. doi:10.1016/j.enpol.2016.03.022.
- [10] Panwar NL, Kaushik SC, Kothari S. Role of renewable energy sources in environmental protection: A review. Renew Sustain Energy Rev 2011;15:1513–24. doi:10.1016/j.rser.2010.11.037.
- [11] Trevor M. Letcher. Chapter 1 – Introduction with a Focus on Atmospheric Carbon Dioxide and Climate Change. Elsevier; 2014. doi:10.1016/B978-0-08-099424-6.00001-6.
- [12] Misra AK, Verma M. A mathematical model to study the dynamics of carbon dioxide gas in the atmosphere. Appl Math Comput 2013;219:8595–609. doi:10.1016/j.amc.2013.02.058.
- [13] Correljé A, van der Linde C. Energy supply security and geopolitics: A European perspective. Energy Policy 2006;34:532–43. doi:10.1016/j.enpol.2005.11.008.

References

- [14] Westphal K. Energy Policy between Multilateral Governance and Geopolitics: Whither Europe? *Ipg* 2006;44–62.
- [15] Holz F, Brauers H, Richter PM, Roobeek T. Shaking Dutch grounds won't shatter the European gas market. *Energy Econ* 2016. doi:10.1016/j.eneco.2016.03.028.
- [16] Wood DA. Natural gas imports to Europe: The frontline of competition between LNG and pipeline supplies. *J Nat Gas Sci Eng* 2016;36:A1–4. doi:10.1016/j.jngse.2016.09.065.
- [17] Rodríguez-Gómez N, Zaccarelli N, Bolado-Lavín R. European ability to cope with a gas crisis. Comparison between 2009 and 2014. *Energy Policy* 2016;97:461–74. doi:10.1016/j.enpol.2016.07.016.
- [18] Aneke M, Wang M. Energy storage technologies and real life applications – A state of the art review. *Appl Energy* 2016;179:350–77. doi:10.1016/j.apenergy.2016.06.097.
- [19] Lefebvre D, Tezel FH. A review of energy storage technologies with a focus on adsorption thermal energy storage processes for heating applications. *Renew Sustain Energy Rev* 2017;67:116–25. doi:10.1016/j.rser.2016.08.019.
- [20] Li T, Wang S, Gao D, Wang S. Effect of support calcination temperature on the catalytic properties of Ru/Ce_{0.8}Zr_{0.2}O₂ for methanation of carbon dioxide. *J Fuel Chem Technol* 2014;42:1440–6. doi:10.1016/S1872-5813(15)60001-9.
- [21] Gallo AB, Simões-Moreira JR, Costa HKM, Santos MM, Moutinho dos Santos E. Energy storage in the energy transition context: A technology review. *Renew Sustain Energy Rev* 2016;65:800–22. doi:10.1016/j.rser.2016.07.028.
- [22] Schaaf T, Grünig J, Schuster M, Rothenfluh T, Orth A. Methanation of CO₂ - storage of renewable energy in a gas distribution system. *Energy Sustain Soc* 2014;4:1–14. doi:10.1186/s13705-014-0029-1.
- [23] Giglio E, Lanzini A, Santarelli M, Leone P. Synthetic natural gas via integrated high-temperature electrolysis and methanation: Part I—Energy performance. *J Energy Storage* 2015;1:22–37. doi:10.1016/j.est.2015.04.002.
- [24] Lefebvre J, Friedemann M, Manuel G, Graf F, Bajohr S, Reimert R, et al. Renewable Power-to-Gas: A technological and economic review 2015. doi:10.1016/j.renene.2015.07.066.
- [25] Gahleitner G. Hydrogen from renewable electricity: An international review of power-to-gas pilot plants for stationary applications. *Int J Hydrogen Energy* 2013;38:2039–61. doi:10.1016/j.ijhydene.2012.12.010.

-
- [26] Reiter G, Lindorfer J. Global warming potential of hydrogen and methane production from renewable electricity via power-to-gas technology. *Int J Life Cycle Assess* 2015;20:477–89. doi:10.1007/s11367-015-0848-0.
- [27] 6th CEER benchmarking report on electricity and gas supply. 2016.
- [28] INGAS Integrated Project. Report on gas composition range in Europe. n.d.
- [29] Ministerio de Industria Turismo y Comercio. Sistema gasista. Gestión técnica. 2011.
- [30] Schiebahn S, Grube T, Robinius M, Tietze V, Kumar B, Stolten D. Power to gas: Technological overview, systems analysis and economic assessment for a case study in Germany. *Int J Hydrogen Energy* 2015;40:4285–94. doi:10.1016/j.ijhydene.2015.01.123.
- [31] Frick V, Brelloch J, Specht M. Application of ternary diagrams in the design of methanation systems. *Fuel Process Technol* 2014;118:156–60. doi:10.1016/j.fuproc.2013.08.022.
- [32] Jiao J, Wei Y, Zhao Z, Zhong W, Liu J, Li J, et al. Synthesis of 3D ordered macroporous TiO₂-supported Au nanoparticle photocatalysts and their photocatalytic performances for the reduction of CO₂ to methane. *Catal Today* 2015;258:319–26. doi:10.1016/j.cattod.2015.01.030.
- [33] Sahebdehfar S, Takht Ravanchi M. Carbon dioxide utilization for methane production: A thermodynamic analysis. *J Pet Sci Eng* 2015;134:14–22. doi:10.1016/j.petrol.2015.07.015.
- [34] Liu H, Zou X, Wang X, Lu X, Ding W. Effect of CeO₂ addition on Ni/Al₂O₃ catalysts for methanation of carbon dioxide with hydrogen. *J Nat Gas Chem* 2012;21:703–7. doi:10.1016/S1003-9953(11)60422-2.
- [35] Koschany F, Schlereth D, Hinrichsen O. On the kinetics of the methanation of carbon dioxide on coprecipitated NiAl (O) x. *Applied Catal B, Environ* 2016;181:504–16. doi:10.1016/j.apcatb.2015.07.026.
- [36] Kühn M, Streibel M, Nakaten N, Kempka T. Integrated Underground Gas Storage of CO₂ and CH₄ to Decarbonise the “Power-to-gas-to-gas-to-power” Technology. *Energy Procedia* 2014;59:9–15. doi:10.1016/j.egypro.2014.10.342.
- [37] Gutiérrez-Martín F, Rodríguez-Antón LM. Power-to-SNG technology for energy storage at large scales. *Int J Hydrogen Energy* 2016. doi:http://dx.doi.org/10.1016/j.ijhydene.2016.07.097.

References

- [38] Nastasi B, Lo Basso G. Hydrogen to link heat and electricity in the transition towards future Smart Energy Systems. *Energy* 2015;110:5–22. doi:10.1016/j.energy.2016.03.097.
- [39] Ridjan I, Mathiesen BV, Connolly D, Duić N. The feasibility of synthetic fuels in renewable energy systems. *Energy* 2013;57:76–84. doi:10.1016/j.energy.2013.01.046.
- [40] Peebles DE, Goodman DW, White JM. Methanation of carbon dioxide on nickel(100) and the effects of surface modifiers. *J Phys Chem* 1983;87:4378–87. doi:10.1021/j100245a014.
- [41] Zamani AH, Ali R, Abu Bakar WAW. Optimization of CO₂ methanation reaction over M*/Mn/Cu–Al₂O₃ (M*: Pd, Rh and Ru) catalysts. *J Ind Eng Chem* 2015. doi:10.1016/j.jiec.2015.02.028.
- [42] Kiewidt L, Thöming J. Predicting optimal temperature profiles in single-stage fixed-bed reactors for CO₂-methanation. *Chem Eng Sci* 2015;132:59–71. doi:10.1016/j.ces.2015.03.068.
- [43] Aziz MAA, Jalil AA, Triwahyono S, Mukti RR, Taufiq-Yap YH, Sazegar MR. Highly active Ni-promoted mesostructured silica nanoparticles for CO₂ methanation. *Appl Catal B Environ* 2014;147:359–68. doi:10.1016/j.apcatb.2013.09.015.
- [44] Ahmad W, Al-Matar A, Shawabkeh R, Rana A. An experimental and thermodynamic study for conversion of CO₂ to CO and methane over Cu-K/Al₂O₃. *J Environ Chem Eng* 2016;4:2725–35. doi:10.1016/j.jece.2016.05.019.
- [45] Karelovic A, Ruiz P. Mechanistic study of low temperature CO₂ methanation over Rh/TiO₂ catalysts. *J Catal* 2013;301:141–53. doi:10.1016/j.jcat.2013.02.009.
- [46] Toemen S, Abu Bakar WAW, Ali R. Effect of ceria and strontia over Ru/Mn/Al₂O₃ catalyst: Catalytic methanation, physicochemical and mechanistic studies. *J CO₂ Util* 2016;13:38–49. doi:10.1016/j.jcou.2015.11.005.
- [47] Tada S, Shimizu T, Kameyama H, Haneda T, Kikuchi R. Ni/CeO₂ catalysts with high CO₂ methanation activity and high CH₄ selectivity at low temperatures. *Int J Hydrogen Energy* 2012;37:5527–31. doi:10.1016/j.ijhydene.2011.12.122.
- [48] Abelló S, Berruero C, Montané D. High-loaded nickel-alumina catalyst for direct CO₂ hydrogenation into synthetic natural gas (SNG). *Fuel* 2013;113:598–609. doi:10.1016/j.fuel.2013.06.012.
- [49] Pan Q, Peng J, Sun T, Wang S, Wang S. Insight into the reaction route of CO₂ methanation: Promotion effect of medium basic sites. *Catal Commun*

- 2014;45:74–8. doi:10.1016/j.catcom.2013.10.034.
- [50] Rahmani S, Rezaei M, Meshkani F. Preparation of highly active nickel catalysts supported on mesoporous nanocrystalline γ -Al₂O₃ for CO₂ methanation. *J Ind Eng Chem* 2014;20:1346–52. doi:10.1016/j.jiec.2013.07.017.
- [51] Cai M, Wen J, Chu W, Cheng X, Li Z. Methanation of carbon dioxide on Ni/ZrO₂-Al₂O₃ catalysts: Effects of ZrO₂ promoter and preparation method of novel ZrO₂-Al₂O₃ carrier. *J Nat Gas Chem* 2011;20:318–24. doi:10.1016/S1003-9953(10)60187-9.
- [52] Graça I, González LV, Bacariza MC, Fernandes A, Henriques C, Lopes JM, et al. CO₂ hydrogenation into CH₄ on NiHNaUSY zeolites. *Appl Catal B Environ* 2014;147:101–10. doi:10.1016/j.apcatb.2013.08.010.
- [53] Schlereth D, Hinrichsen O. A fixed-bed reactor modeling study on the methanation of CO₂. *Chem Eng Res Des* 2014;92:702–12. doi:10.1016/j.cherd.2013.11.014.
- [54] Barbarossa V, Vanga G, Viscardi R, Gattia DM. CO₂ as Carbon Source for Fuel Synthesis. *Energy Procedia* 2014;45:1325–9. doi:10.1016/j.egypro.2014.01.138.
- [55] Su X, Xu J, Liang B, Duan H, Hou B, Huang Y. Catalytic carbon dioxide hydrogenation to methane: A review of recent studies. *J Energy Chem* 2016;0:1–13. doi:10.1016/j.jechem.2016.03.009.
- [56] Rönsch S, Schneider J, Matthischke S, Schlüter M, Götz M, Lefebvre J, et al. Review on methanation – From fundamentals to current projects. *Fuel* 2015;166:276–96. doi:10.1016/j.fuel.2015.10.111.
- [57] Ren J, Guo H, Yang J, Qin Z, Lin J, Li Z. Insights into the mechanisms of CO₂ methanation on Ni(111) surfaces by density functional theory. *Appl Surf Sci* 2015;351:504–16. doi:10.1016/j.apsusc.2015.05.173.
- [58] Westermann A, Azambre B, Bacariza MC, Graça I, Ribeiro MF, Lopes JM, et al. Insight into CO₂ methanation mechanism over NiUSY zeolites: An operando IR study. *Appl Catal B Environ* 2015;174–175:120–5. doi:10.1016/j.apcatb.2015.02.026.
- [59] Ren J, Qin X, Yang J-Z, Qin Z-F, Guo H-L, Lin J-Y, et al. Methanation of carbon dioxide over Ni–M/ZrO₂ (M=Fe, Co, Cu) catalysts: Effect of addition of a second metal. *Fuel Process Technol* 2015;137:204–11. doi:10.1016/j.fuproc.2015.04.022.
- [60] Mills GA, Steffgen FW. Catalytic Methanation. *Catal Rev* 1974;8:159–210.

References

- doi:10.1080/01614947408071860.
- [61] Pandey D, Deo G. Effect of support on the catalytic activity of supported Ni–Fe catalysts for the CO₂ methanation reaction. *J Ind Eng Chem* 2015;33:99–107. doi:10.1016/j.jiec.2015.09.019.
- [62] Yaccato K, Carhart R, Hagemeyer A, Lesik A, Strasser P, Volpe AF, et al. Competitive CO and CO₂ methanation over supported noble metal catalysts in high throughput scanning mass spectrometer. *Appl Catal A Gen* 2005;296:30–48. doi:10.1016/j.apcata.2005.07.052.
- [63] Wan Abu Bakar WA, Ali R, Mohammad NS. The effect of noble metals on catalytic methanation reaction over supported Mn/Ni oxide based catalysts. *Arab J Chem* 2015;8:632–43. doi:10.1016/j.arabjc.2013.06.009.
- [64] Ross JRH. Chapter 4 – Catalyst Preparation. *Heterog. Catal.*, 2012, p. 65–96. doi:10.1016/B978-0-444-53363-0.10004-0.
- [65] Younas M, Loong Kong L, Bashir MJK, Nadeem H, Shehzad A, Sethupathi S. Recent Advancements, Fundamental Challenges, and Opportunities in Catalytic Methanation of CO₂. *Energy & Fuels* 2016;acs.energyfuels.6b01723. doi:10.1021/acs.energyfuels.6b01723.
- [66] Worstell J. Chapter 3 – Catalyst Deactivation. *Adiabatic Fixed-Bed React.*, 2014, p. 35–65. doi:10.1016/B978-0-12-801306-9.00003-0.
- [67] Lehner M, Tichler R, Steinmüller H, Koppe M. *Power-to-gas: technology and business models*. vol. 39. Springer; 2014.
- [68] Schildhauer TJ, Biollaz SMA. Reactors for Catalytic Methanation in the Conversion of Biomass to Synthetic Natural Gas (SNG). *Chimia (Aarau)* 2015;69:603–7. doi:10.2533/chimia.2015.603.
- [69] Olivo A, Trevisan V, Ghedini E, Pinna F, Bianchi CL, Naldoni A, et al. CO₂ photoreduction with water: Catalyst and process investigation. *J CO₂ Util* 2015;12:86–94. doi:10.1016/j.jcou.2015.06.001.
- [70] Tahir M, Tahir B, Amin NAS, Muhammad A. Photocatalytic CO₂ methanation over NiO/In₂O₃ promoted TiO₂ nanocatalysts using H₂O and/or H₂ reductants. *Energy Convers Manag* 2016;119:368–78. doi:10.1016/j.enconman.2016.04.057.
- [71] Li H, Wu X, Wang J, Gao Y, Li L, Shih K. Enhanced activity of Ag-MgO-TiO₂ catalyst for photocatalytic conversion of CO₂ and H₂O into CH₄. *Int J Hydrogen Energy* 2016;41:8479–88. doi:10.1016/j.ijhydene.2016.03.194.

- [72] Linic S, Christopher P, Ingram DB. Plasmonic-metal nanostructures for efficient conversion of solar to chemical energy. *Nat Mater* 2011;10:911–21. doi:10.1038/nmat3151.
- [73] Zhang X, Chen YL, Liu R-S, Tsai DP. Plasmonic photocatalysis. *Rep Prog Phys* 2013;76:46401. doi:10.1088/0034-4885/76/4/046401.
- [74] Clavero C. Plasmon-induced hot-electron generation at nanoparticle/metal-oxide interfaces for photovoltaic and photocatalytic devices. *Nat Photonics* 2014;8:95–103. doi:10.1038/nphoton.2013.238.
- [75] Peiris S, McMurtrie J, Zhu H-Y. Metal nanoparticle photocatalysts: emerging processes for green organic synthesis. *Catal Sci Technol* 2016;6:320–38. doi:10.1039/C5CY02048D.
- [76] Kale MJ, Kale MJ, Avanesian T, Christopher P. Direct Photocatalysis by Plasmonic Nanostructures Direct Photocatalysis by Plasmonic Nanostructures. *ACS Catal* 2014;4:116–28. doi:10.1021/cs400993w.
- [77] Baffou G, Quidant R. Nanoplasmonics for chemistry. *Chem Soc Rev* 2014;43:3898–907. doi:10.1039/c3cs60364d.
- [78] Cybula A, Klein M, Zaleska A. Methane formation over TiO₂-based photocatalysts: Reaction pathways. *Appl Catal B Environ* 2015;164:433–42. doi:10.1016/j.apcatb.2014.09.038.
- [79] Collado L, Reynal A, Coronado JM, Serrano DP, Durrant JR, De la Peña O'Shea VA. Effect of Au surface plasmon nanoparticles on the selective CO₂ photoreduction to CH₄. *Appl Catal B Environ* 2015;178:177–85. doi:10.1016/j.apcatb.2014.09.032.
- [80] Jain PK, Huang X, El-Sayed IH, El-Sayed MA. Noble metals on the nanoscale: Optical and photothermal properties and some applications in imaging, sensing, biology, and medicine. *Acc Chem Res* 2008;41:1578–86. doi:10.1021/ar7002804.
- [81] Göeken KL, Subramaniam V, Gill R. Enhancing spectral shifts of plasmon-coupled noble metal nanoparticles for sensing applications. *Phys Chem Chem Phys* 2015;17:422–7. doi:10.1039/c4cp03739a.
- [82] Kosmulski M. The pH dependent surface charging and points of zero charge. VI. Update. *J Colloid Interface Sci* 2014;426:209–12. doi:10.1016/j.jcis.2014.02.036.
- [83] García-García I, Acha E, Bizkarra K, Martínez de Ilarduya J, Requies J, Cambra JF. Hydrogen production by steam reforming of m-cresol, a bio-oil model compound, using catalysts supported on conventional and unconventional supports. *Int J*

References

- Hydrogen Energy 2015;40:14445–55. doi:10.1016/j.ijhydene.2015.07.155.
- [84] Teoh WY, Amal R, Madler L. Flame spray pyrolysis: An enabling technology for nanoparticles design and fabrication. *Nanoscale* 2010;2:1324–47. doi:10.1039/C0nr00017e.
- [85] Lovell E, Scott J, Amal R. Ni-SiO₂ Catalysts for the Carbon Dioxide Reforming of Methane: Varying Support Properties by Flame Spray Pyrolysis. *Molecules* 2015;20:4594–609. doi:10.3390/molecules20034594.
- [86] Mei B, Pougin A, Strunk J. Influence of photodeposited gold nanoparticles on the photocatalytic activity of titanate species in the reduction of CO₂ to hydrocarbons. *J Catal* 2013;306:184–9. doi:10.1016/j.jcat.2013.06.027.
- [87] Mäki-Arvela P, Murzin DY. Effect of catalyst synthesis parameters on the metal particle size. *Appl Catal A Gen* 2013;451:251–81. doi:10.1016/j.apcata.2012.10.012.
- [88] Anbuvaran M, Ramesh M, Viruthagiri G, Shanmugam N, Kannadasan N. Synthesis, characterization and photocatalytic activity of ZnO nanoparticles prepared by biological method. *Spectrochim Acta Part A Mol Biomol Spectrosc* 2015;143:304–8. doi:10.1016/j.saa.2015.01.124.
- [89] López-Fonseca R, Jiménez-González C, de Rivas B, Gutiérrez-Ortiz JI. Partial oxidation of methane to syngas on bulk NiAl₂O₄ catalyst. Comparison with alumina supported nickel, platinum and rhodium catalysts. *Appl Catal A Gen* 2012;437–438:53–62. doi:10.1016/J.APCATA.2012.06.014.
- [90] Alihosseinzadeh A, Nematollahi B, Rezaei M, Lay EN. CO methanation over Ni catalysts supported on high surface area mesoporous nanocrystalline γ -Al₂O₃ for CO removal in H₂-rich stream. *Int J Hydrogen Energy* 2015;40:1809–19. doi:10.1016/j.ijhydene.2014.11.138.
- [91] Li G, Hu L, Hill JM. Comparison of reducibility and stability of alumina-supported Ni catalysts prepared by impregnation and co-precipitation. *Appl Catal A Gen* 2006;301:16–24. doi:10.1016/j.apcata.2005.11.013.
- [92] Richardson J., Scates R., Twigg M. X-ray diffraction study of the hydrogen reduction of NiO/ α -Al₂O₃ steam reforming catalysts. *Appl Catal A Gen* 2004;267:35–46. doi:10.1016/j.apcata.2004.02.022.
- [93] Wu Y, Yan A, He Y, Wu B, Wu T. Ni-Ag-O as catalyst for a novel one-step reaction to convert ethane to ethylene oxide. *Catal Today* 2010;158:258–62. doi:10.1016/j.cattod.2010.03.041.

- [94] Gao Z, Cui L, Ma H. Selective methanation of CO over Ni/Al₂O₃ catalyst: Effects of preparation method and Ru addition. *Int J Hydrogen Energy* 2016;41:5484–93. doi:10.1016/j.ijhydene.2016.02.085.
- [95] Gao J, Jia C, Li J, Zhang M, Gu F, Xu G, et al. Ni/Al₂O₃ catalysts for CO methanation: Effect of Al₂O₃ supports calcined at different temperatures. *J Energy Chem* 2013;22:919–27. doi:10.1016/S2095-4956(14)60273-4.
- [96] Zhao C, Yu Y, Jentys A, Lercher JA. Understanding the impact of aluminum oxide binder on Ni/HZSM-5 for phenol hydrodeoxygenation. *Appl Catal B Environ* 2013;132–133:282–92. doi:10.1016/j.apcatb.2012.11.042.
- [97] Seo JG, Youn MH, Chung JS, Song IK. Effect of calcination temperature of mesoporous nickel–alumina catalysts on their catalytic performance in hydrogen production by steam reforming of liquefied natural gas (LNG). *J Ind Eng Chem* 2010;16:795–9. doi:10.1016/j.jiec.2010.05.010.
- [98] Gousi M, Andriopoulou C, Bourikas K, Ladas S, Sotiriou M, Kordulis C, et al. Green diesel production over nickel–alumina co-precipitated catalysts. *Appl Catal A Gen* 2017;536:45–56. doi:10.1016/j.apcata.2017.02.010.
- [99] Debecker DP, Stoyanova M, Rodemerck U, Gaigneaux EM. Preparation of MoO₃/SiO₂–Al₂O₃ metathesis catalysts via wet impregnation with different Mo precursors. *J Mol Catal A Chem* 2011;340:65–76. doi:10.1016/J.MOLCATA.2011.03.011.
- [100] Zhao H, Bennici S, Cai J, Shen J, Auroux A. Effect of vanadia loading on the acidic, redox and catalytic properties of V₂O₅–TiO₂ and V₂O₅–TiO₂/SO₄²⁻ catalysts for partial oxidation of methanol. *Catal Today* 2010;152:70–7. doi:10.1016/j.cattod.2009.08.005.
- [101] Montero C, Ochoa A, Castaño P, Bilbao J, Gayubo AG. Monitoring Ni⁰ and coke evolution during the deactivation of a Ni/La₂O₃– α -Al₂O₃ catalyst in ethanol steam reforming in a fluidized bed. *J Catal* 2015;331:181–92. doi:10.1016/j.jcat.2015.08.005.
- [102] Scirè S, Crisafulli C, Maggiore R, Mini O S, Galvagno S. Influence of the support on CO₂ methanation over Ru catalysts: an FT-IR study. *Catal Letters* 1998;51:41–5.
- [103] Bang Y, Han SJ, Seo JG, Youn MH, Song JH, Song IK. Hydrogen production by steam reforming of liquefied natural gas (LNG) over ordered mesoporous nickel–alumina catalyst. *Int J Hydrogen Energy* 2012;37:17967–77. doi:10.1016/j.ijhydene.2012.09.057.
- [104] Wang T, Zhang H, Yan Y. High efficiency of isopropanol combustion over cobalt

References

- oxides modified ZSM-5 zeolite membrane catalysts on paper-like stainless steel fibers. *J Solid State Chem* 2017;251:55–60. doi:10.1016/j.jssc.2017.04.003.
- [105] Pawelec B, Navarro RM, Campos-Martin JM, Lopez Agudo A, Vasudevan PT, Fierro JLG. Silica-alumina-supported transition metal sulphide catalysts for deep hydrodesulphurization. *Catal Today* 2003;86:73–85. doi:10.1016/S0920-5861(03)00405-X.
- [106] Barton RR, Carrier M, Segura C, Fierro JLG, Escalona N, Peretti SW. Ni/HZSM-5 catalyst preparation by deposition-precipitation. Part 1. Effect of nickel loading and preparation conditions on catalyst properties. *Appl Catal A Gen* 2017;540:7–20. doi:10.1016/j.apcata.2017.03.040.
- [107] Wang F, Xu L, Shi W. Syngas production from CO₂ reforming with methane over core-shell Ni@SiO₂ catalysts. *J CO₂ Util* 2016;16:318–27. doi:10.1016/j.jcou.2016.09.001.
- [108] Fúnez A, De Lucas A, Sánchez P, Ramos MJ, Valverde JL. Hydroisomerization in liquid phase of a refinery naphtha stream over Pt–Ni/H-beta zeolite catalysts. *Chem Eng J* 2008;136:267–75. doi:10.1016/J.CEJ.2007.03.062.
- [109] Escola J., Aguado J, Serrano D., García A, Peral A, Briones L, et al. Catalytic hydroreforming of the polyethylene thermal cracking oil over Ni supported hierarchical zeolites and mesostructured aluminosilicates. *Appl Catal B Environ* 2011;106:405–15. doi:10.1016/J.APCATB.2011.05.048.
- [110] Xia K, Lang WZ, Li PP, Long LL, Yan X, Guo YJ. The promotion effects of Ni on the properties of Cr/Al catalysts for propane dehydrogenation reaction. *Appl Catal A Gen* 2016;522:172–9. doi:10.1016/j.cej.2015.09.046.
- [111] Awadallah AE, El-Desouki DS, Aboul-Gheit NAK, Ibrahim AH, Aboul-Gheit AK. Effect of crystalline structure and pore geometry of silica based supported materials on the catalytic behavior of metallic nickel particles during methane decomposition to CO_x-free hydrogen and carbon nanomaterials. *Int J Hydrogen Energy* 2016;41:16890–902. doi:10.1016/j.ijhydene.2016.07.081.
- [112] Pan YX, Liu CJ, Shi P. Ine. *J Power Sources* 2008;176:46–53. doi:10.1016/j.jpowsour.2007.10.039.
- [113] Zhang Q, Zhang T, Shi Y, Zhao B, Wang M, Liu Q, et al. A sintering and carbon-resistant Ni-SBA-15 catalyst prepared by solid-state grinding method for dry reforming of methane. *J CO₂ Util* 2017;17:10–9. doi:10.1016/j.jcou.2016.11.002.
- [114] Borodziński A, Bonarowska M. Relation between Crystallite Size and Dispersion on Supported Metal Catalysts. *Langmuir* 1997;13:5613–20.

- doi:10.1021/la962103u.
- [115] Phung TK, Garbarino G. On the use of infrared spectrometer as detector for Temperature Programmed (TP) techniques in catalysts characterization. *J Ind Eng Chem* 2017;47:288–96. doi:10.1016/j.jiec.2016.11.045.
- [116] de Oliveira AS, Vasconcelos SJS, de Sousa JR, de Sousa FF, Filho JM, Oliveira AC. Catalytic conversion of glycerol to acrolein over modified molecular sieves: Activity and deactivation studies. *Chem Eng J* 2011;168:765–74. doi:10.1016/j.cej.2010.09.029.
- [117] Jillavenkatesa A, Dapkunas SJ, Lum L-SH. Particle Size Characterization. U.S. GOVERNMENT PRINTING OFFICE; 2001. doi:682901795.
- [118] Guimon C, Auroux A, Romero E, Monzon A. Acetylene hydrogenation over Ni–Si–Al mixed oxides prepared by sol–gel technique. *Appl Catal A Gen* 2003;251:199–214. doi:10.1016/S0926-860X(03)00318-1.
- [119] Bang Y, Han SJ, Yoo J, Choi JH, Lee JK, Song JH, et al. Hydrogen production by steam reforming of simulated liquefied natural gas (LNG) over nickel catalyst supported on mesoporous phosphorus-modified alumina xerogel. *Appl Catal B Environ* 2014;148:269–80. doi:10.1016/j.apcatb.2013.11.012.
- [120] Heracleous E, Lee AF, Wilson K, Lemonidou AA. Investigation of Ni-based alumina-supported catalysts for the oxidative dehydrogenation of ethane to ethylene: structural characterization and reactivity studies. *J Catal* 2005;231:159–71. doi:10.1016/j.jcat.2005.01.015.
- [121] Qin F, Anderegg JW, Jenks CJ, Gleeson B, Sordelet DJ, Thiel PA. The effect of Pt on Ni₃Al surface oxidation at low-pressures. *Surf Sci* 2007;601:146–54. doi:10.1016/j.susc.2006.09.014.
- [122] Jiménez-González C, Boukha Z, de Rivas B, Delgado JJ, Cauqui MÁ, González-Velasco JR, et al. Structural characterisation of Ni/alumina reforming catalysts activated at high temperatures. *Appl Catal A Gen* 2013;466:9–20. doi:10.1016/j.apcata.2013.06.017.
- [123] Wang Y, Peng J, Zhou C, Lim Z-Y, Wu C, Ye S, et al. Effect of Pr addition on the properties of Ni/Al₂O₃ catalysts with an application in the autothermal reforming of methane. *Int J Hydrogen Energy* 2014;39:778–87. doi:10.1016/j.ijhydene.2013.10.071.
- [124] Rahmani F, Haghghi M, Mohammadkhani B. Enhanced dispersion of Cr nanoparticles over nanostructured ZrO₂-doped ZSM-5 used in CO₂-oxydehydrogenation of ethane. *Microporous Mesoporous Mater* 2017;242:34–

References

49. doi:10.1016/j.micromeso.2017.01.012.
- [125] Singha RK, Yadav A, Agrawal A, Shukla A, Adak S, Sasaki T, et al. Synthesis of highly coke resistant Ni nanoparticles supported MgO/ZnO catalyst for reforming of methane with carbon dioxide. *Appl Catal B Environ* 2016;191:165–78. doi:10.1016/J.APCATB.2016.03.029.
- [126] Wang Y, Wu R, Zhao Y. Effect of ZrO₂ promoter on structure and catalytic activity of the Ni/SiO₂ catalyst for CO methanation in hydrogen-rich gases. *Catal Today* 2010;158:470–4. doi:10.1016/j.cattod.2010.07.016.
- [127] Seo Y-S, Jung Y-S, Yoon W-L, Jang I-G, Lee T-W. The effect of Ni content on a highly active Ni–Al₂O₃ catalyst prepared by the homogeneous precipitation method. *Int J Hydrogen Energy* 2011;36:94–102. doi:10.1016/J.IJHYDENE.2010.09.082.
- [128] Toemen S, Bakar WAWA, Ali R. Investigation of Ru/Mn/Ce/Al₂O₃ catalyst for carbon dioxide methanation: Catalytic optimization, physicochemical studies and RSM. *J Taiwan Inst Chem Eng* 2014;45:2370–8. doi:10.1016/j.jtice.2014.07.009.
- [129] Calzada LA, Collins SE, Han CW, Ortalan V, Zanella R. Synergetic effect of bimetallic Au-Ru/TiO₂ catalysts for complete oxidation of methanol. *Appl Catal B Environ* 2017;207:79–92. doi:10.1016/j.apcatb.2017.01.081.
- [130] Al-Asbahi BA. Influence of anatase titania nanoparticles content on optical and structural properties of amorphous silica. *Mater Res Bull* 2017;89:286–91. doi:10.1016/J.MATERRESBULL.2017.01.004.
- [131] Jin R, Sun S, Yang Y, Xing Y, Yu D, Yu X, et al. Size-dependent catalytic properties of Au nanoparticles supported on hierarchical nickel silicate nanostructures. *Dalt Trans* 2013;42:7888–93. doi:10.1039/C2DT32590J.
- [132] Casaletto MP, Longo A, Martorana A, Prestianni A, Venezia AM. XPS study of supported gold catalysts: the role of Au⁰ and Au^{+δ} species as active sites. *Surf Interface Anal* 2006;38:215–8. doi:10.1002/sia.2180.
- [133] Ulbrich AHDPS, Campedelli RR, Milani JLS, Santos JHZ dos, Casagrande O de L. Nickel catalysts based on phenyl ether-pyrazol ligands: Synthesis, XPS study, and use in ethylene oligomerization. *Appl Catal A Gen* 2013;453:280–6. doi:10.1016/j.apcata.2012.12.031.
- [134] Cárdenas-Lizana F, Gómez-Quero S, Baddeley CJ, Keane MA. Tunable gas phase hydrogenation of m-dinitrobenzene over alumina supported Au and Au–Ni. *Appl Catal A Gen* 2010;387:155–65. doi:10.1016/j.apcata.2010.08.019.
- [135] Teoh WY, Amal R, Mädler L, Pratsinis SE. Flame sprayed visible light-active Fe-

- TiO₂ for photomineralisation of oxalic acid. *Catal Today* 2007;120:203–13. doi:10.1016/j.cattod.2006.07.049.
- [136] Yeshchenko OA, Dmitruk IM, Alexeenko AA, Dmytruk AM. Optical properties of sol–gel fabricated Ni/SiO₂ glass nanocomposites. *J Phys Chem Solids* 2008;69:1615–22. doi:10.1016/J.JPCS.2007.12.002.
- [137] Vishlaghi MB, Tabriz MF, Moradi OM. Electrohydrodynamic atomization (EHDA) assisted wet chemical synthesis of nickel nanoparticles. *Mater Res Bull* 2012;47:1666–9. doi:10.1016/J.MATERRESBULL.2012.03.055.
- [138] Chiu H-K, Chiang I-C, Chen D-H. Synthesis of NiAu alloy and core–shell nanoparticles in water-in-oil microemulsions. *J Nanoparticle Res* 2009;11:1137–44. doi:10.1007/s11051-008-9506-9.
- [139] Zhou J, Duan X, Ye L, Zheng J, Li MM-J, Tsang SCE, et al. Enhanced chemoselective hydrogenation of dimethyl oxalate to methyl glycolate over bimetallic Ag–Ni/SBA-15 catalysts. *Appl Catal A Gen* 2015;505:344–53. doi:10.1016/j.apcata.2015.08.022.
- [140] Dutov V V., Mamontov G V., Sobolev VI, Vodyankina O V. Silica-supported silver-containing OMS-2 catalysts for ethanol oxidative dehydrogenation. *Catal Today* 2016;278:164–73. doi:10.1016/j.cattod.2016.05.058.
- [141] Dong L, Du Y, Li J, Wang H, Yang Y, Li S, et al. The effect of CH₄ decomposition temperature on the property of deposited carbon over Ni/SiO₂ catalyst. *Int J Hydrogen Energy* 2015;40:9670–6. doi:10.1016/j.ijhydene.2015.06.005.
- [142] Liu G, Li Y, Chu W, Shi X, Dai X, Yin Y. Plasma-assisted preparation of Ni/SiO₂ catalyst using atmospheric high frequency cold plasma jet. *Catal Commun* 2008;9:1087–91. doi:10.1016/j.catcom.2007.10.013.
- [143] Xia W-S, Hou Y-H, Chang G, Weng W-Z, Han G-B, Wan H-L. Partial oxidation of methane into syngas (H₂ + CO) over effective high-dispersed Ni/SiO₂ catalysts synthesized by a sol–gel method. *Int J Hydrogen Energy* 2012;37:8343–53. doi:10.1016/j.ijhydene.2012.02.141.
- [144] Zhang Y, Wang W, Wang Z, Zhou X, Wang Z, Liu C-J. Steam reforming of methane over Ni/SiO₂ catalyst with enhanced coke resistance at low steam to methane ratio. *Catal Today* 2015;256:130–6. doi:10.1016/j.cattod.2015.01.016.
- [145] Lippits MJ, Nieuwenhuys BE. Direct conversion of ethanol into ethylene oxide on copper and silver nanoparticles. *Catal Today* 2010;154:127–32. doi:10.1016/j.cattod.2010.03.019.

References

- [146] Stanković M, Gabrovska M, Krstić J, Tzvetkov P, Shopska M, Tsacheva T, et al. Effect of silver modification on structure and catalytic performance of Ni-Mg/diatomite catalysts for edible oil hydrogenation. *J Mol Catal A Chem* 2009;297:54–62. doi:10.1016/j.molcata.2008.09.004.
- [147] Kabir L, Mandal AR, Mandal SK. Polymer stabilized Ni–Ag and Ni–Fe alloy nanoclusters: Structural and magnetic properties. *J Magn Magn Mater* 2010;322:934–9. doi:10.1016/j.jmmm.2009.11.027.
- [148] Chen D-H, Wang S-R. Protective agent-free synthesis of Ni–Ag core–shell nanoparticles. *Mater Chem Phys* 2006;100:468–71. doi:10.1016/j.matchemphys.2006.01.027.
- [149] Xia L, Hu X, Kang X, Zhao H, Sun M, Cihen X. A one-step facile synthesis of Ag–Ni core–shell nanoparticles in water-in-oil microemulsions. *Colloids Surfaces A Physicochem Eng Asp* 2010;367:96–101. doi:10.1016/j.colsurfa.2010.06.020.
- [150] Zaleska-Medynska A, Marchelek M, Diak M, Grabowska E. Noble metal-based bimetallic nanoparticles: the effect of the structure on the optical, catalytic and photocatalytic properties. *Adv Colloid Interface Sci* 2016;229:80–107. doi:10.1016/j.cis.2015.12.008.
- [151] Samanta S, Pyne S, Sarkar P, Sahoo GP, Bar H, Bhui DK, et al. Synthesis of silver nanostructures of varying morphologies through seed mediated growth approach. *J Mol Liq* 2010;153:170–3. doi:10.1016/j.molliq.2010.02.008.
- [152] Smitha SL, Nissamudeen KM, Philip D, Gopchandran KG. Studies on surface plasmon resonance and photoluminescence of silver nanoparticles. *Spectrochim Acta Part A Mol Biomol Spectrosc* 2008;71:186–90. doi:10.1016/j.saa.2007.12.002.
- [153] Mutz B, Carvalho HWP, Mangold S, Kleist W, Grunwaldt J-D. Methanation of CO₂: Structural response of a Ni-based catalyst under fluctuating reaction conditions unraveled by operando spectroscopy. *J Catal* 2015;327:48–53. doi:10.1016/j.jcat.2015.04.006.
- [154] Milczarek G, Rebis T, Fabianska J. One-step synthesis of liginosulfonate-stabilized silver nanoparticles. *Colloids Surfaces B Biointerfaces* 2013;105:335–41. doi:10.1016/j.colsurfb.2013.01.010.
- [155] Nagaraj B, Devi LG. Silver metalized mixed phase manganese-doped titania: Variation of electric field and band bending within the space charge region with respect to the silver content. *J Mol Catal A Chem* 2014;390:142–51. doi:10.1016/j.molcata.2014.03.019.

- [156] Suryaprabha T, Sethuraman MG. Design of electrically conductive superhydrophobic antibacterial cotton fabric through hierarchical architecture using bimetallic deposition. *J Alloys Compd* 2017;724:240–8. doi:10.1016/j.jallcom.2017.07.009.
- [157] Wen Z, Duan X, Hu M, Cao Y, Ye L, Jiang L, et al. Efficient low-temperature soot combustion by bimetallic Ag–Cu/SBA-15 catalysts. *J Environ Sci* 2017. doi:10.1016/J.JES.2016.12.021.
- [158] Wang P, Huang B, Dai Y, Whangbo M-H. Plasmonic photocatalysts: harvesting visible light with noble metal nanoparticles. *Phys Chem Chem Phys* 2012;14:9813. doi:10.1039/c2cp40823f.
- [159] Kowalska E, Janczarek M, Rosa L, Juodkazis S, Ohtani B. Mono- and bi-metallic plasmonic photocatalysts for degradation of organic compounds under UV and visible light irradiation. *Catal Today* 2014;230:131–7. doi:10.1016/j.cattod.2013.11.021.
- [160] Ammendola P, Cammisa E, Chirone R, Lisi L, Ruoppolo G. Effect of sulphur on the performance of Rh–LaCoO₃ based catalyst for tar conversion to syngas. *Appl Catal B Environ* 2012;113–114:11–8. doi:10.1016/j.apcatb.2011.07.024.
- [161] ENEA consulting. The potential of Power-to-Gas. 2016.
- [162] Asociación Empresarial Eólica. Potencia Instalada 2017. <https://www.aeeolica.org/es/sobre-la-eolica/la-eolica-en-espana/potencia-instalada/>.
- [163] Yu G, Shu G, Tian H, Wei H, Liang X. Multi-approach evaluations of a cascade-Organic Rankine Cycle (C-ORC) system driven by diesel engine waste heat: Part B- techno-economic evaluations. *Energy Convers Manag* 2016;108:596–608. doi:10.1016/J.ENCONMAN.2015.10.085.
- [164] Smolinka T, Thomassen M, Oyarce A, Marchal F. MEGASTACK: Stack Design for a Megawatt Scale PEM Electrolyser. 2016.
- [165] Trambouze P, Euzen J-P. Chemical Reactors. Editions TECHNIP; 2004.
- [166] Comisión Nacional de los Mercados y la Competencia. Spanish Energy Regulator’s National Report to the European Commission 2015. 2015.
- [167] Technical Committee CEN/TC 234 “Gas Supply.” Gases from non-conventional sources — Injection into natural gas grids — Requirements and recommendations. n.d.

References

- [168] Gesalaga EF. Personal communication n.d.
- [169] Jernberg J, Nørregård Ø, Olofsson M, Persson O, Thulin M, Hulteberg C, et al. Ethanol Dehydration to Green Ethylene 2015.
- [170] Giglio E, Lanzini A, Santarelli M, Leone P. Synthetic natural gas via integrated high-temperature electrolysis and methanation: Part II— Economic analysis. *J Energy Storage* 2015;1:22–37. doi:10.1016/j.est.2015.04.002.
- [171] Mazneva E. Gazprom Said to See Its Lowest Europe Gas Price in 11 Years. Bloomberg 2015.
- [172] Le Duigou A, Bader A-G, Lanoix J-C, Nadau L. Relevance and costs of large scale underground hydrogen storage in France. *Int J Hydrogen Energy* 2017;42:22987–3003. doi:10.1016/j.ijhydene.2017.06.239.
- [173] Vienna University of Technology. Biogas to biomethane technology review. 2012.
- [174] Turton R, Bailie RC, Whiting WB, Shaeiwitz JA, Bhattacharyya D. Analysis, Synthesis and Design of Chemical Processes. Prentice Hall; 2012.
- [175] Educación MDE, Deporte CY. Boletín oficial del estado. BOLETÍN Of DEL ESTADO Miércoles 19 Julio 2014 Sec Julio 2014 Sec 2014:60502–11.
- [176] Hoffmann BS, Szklo A. Integrated gasification combined cycle and carbon capture: A risky option to mitigate CO₂ emissions of coal-fired power plants. *Appl Energy* 2011;88:3917–29. doi:10.1016/j.apenergy.2011.04.002.

Resume

Iker García García

Date of birth: 27th December 1989.

Place of birth: Eibar, Spain.

Email address: ikergarcia0@gmail.com



Research interest

- Heterogeneous catalysis
- Process design
- Localised surface plasmon resonance

Education and training

2014-Present

PhD student, Faculty of Engineering of Bilbao (UPV/EHU). Sustainable Process Engineering (SuPrEn) research group

October 2016-March 2017

Six month research stay, University of New South Wales (UNSW), Australia. Particles and Catalysis (PartCat) research group. Advisors: Dr. Jason Scott and Sci. Prof. Dr. Rose Amal

2013-2014

MSc in Advanced Materials Engineering, Faculty of Engineering of Bilbao (UPV/EHU)

2007-2013

BSc in Chemical Engineering, Faculty of Engineering of Bilbao (UPV/EHU)

Publications

Plasmonic effects on CO₂ reduction over bimetallic Ni-Au catalysts. Jessica N.G. Stanley, Iker García-García, Tom Perfrement, Emma C.L. ovell, Timothy W. Schmidt, Jason Scott, Rose Amal. *Chemical Engineering Science* (In Press, Corrected Proof).

Resume

Catalyst Deactivation and Regeneration Processes in Biogas Tri-Reforming Process. The Effect of Hydrogen Sulfide Addition. Urko Izquierdo, Iker García-García, Ángel María Gutierrez, Juan Ramón Arraibi, Victoria Laura Barrio, José Francisco Cambra and Pedro Luis Arias. *Catalysts*, 8 (2018).

Structure-activity relationships of Ni-Cu/Al₂O₃ catalysts for γ -valerolactone conversion to 2-methyltetrahydrofuran. Iker Obregón, Iñaki Gandarias, Ainhoa Ocio, Iker García-García, Nerea Alvarez de Eulate, Pedro L. Arias. *Applied Catalysis B: Environmental*, 210 (2017), 328-341.

Power-to-Gas: Storing surplus electrical energy. Study of Al₂O₃ modification. I. García-García, U. Izquierdo, V.L. Barrio, P.L. Arias, J.F. Cambra. *International Journal of Hydrogen Energy*, 41 (43) (2016), 19587-19594.

Hydrogen production by steam reforming of m-cresol, a bio-oil model compound, using catalysts supported on conventional and unconventional supports. I. García-García, E. Acha, K. Bizkarra, J. Martínez de Ilarduya, J. Requies, J.F. Cambra. *International Journal of Hydrogen Energy*, 40 (42) (2015), 14445-14455.

Contribution to conferences

Hydrogen production through reforming process of pine sawdust bio-oil - Hydrogen Power Theoretical and Engineering Solutions International Symposium (HYPOTHESIS XII)

Operating conditions and catalyst design for Power-to-Gas technology - Reunión de la Sociedad Española de Catálisis (SECAT '17)

Power-to-Gas: Storing Surplus Electrical Energy. Catalytic systems based on unconventional supports - The International Conference on Carbon Dioxide Utilisation (ICCDU XIV)

Renewable methane generation using natural supports - 3rd International Symposium on Catalysis for Clean Energy and Sustainable Chemistry (CCESC)

Hydrogen production with a microchannel reactor by tri-reforming process; catalyst development - 3rd International Symposium on Catalysis for Clean Energy and Sustainable Chemistry (CCESC)

Microreactors application in the generation of renewable energy sources with metallic and bimetallic catalytic systems - 5th International Conference on Structured Catalysts and Reactors (ICOSCAR5)

Green gas production: industrial residues as catalyst support for methanation process intensification study - 5th International Conference on Structured Catalysts and Reactors (ICOSCAR5)

Use of hydrogen for methane production: study of acidic supports - World Hydrogen Energy Conference (WHEC 2016)

Hydrogen production with a microchannel heat-exchanger reactor by single stage water-gas shift; catalyst development - World Hydrogen Energy Conference (WHEC 2016)

Power-to-Gas: Storing Surplus Electrical Energy. Study of operating conditions. - The International Conference on Carbon Dioxide Utilization (ICCDU XIII)

Storing electrical energy as synthetic natural gas using Ni based catalysts - V Iberian Symposium on Hydrogen, Fuel Cells and Advanced Batteries (HYCELTEC 2015)

Biogas reforming for hydrogen production: Activity tests with real biogas - 7th European Meeting on Chemical Industry and Environment (EMChIE 2015)

Hydrogen production by steam reforming of bio-oil model compounds - Euro-mediterranean Hydrogen Technologies Conference 2014 (EmHyTeC 2014)

